Mathematics in Industry 24
The European Consortium for Mathematics in Industry

András Bátkai
Petra Csomós
István Faragó
András Horányi
Gabriella Szépszó *Editors*

Mathematical Problems in Meteorological Modelling

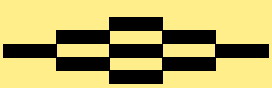

Springer

MATHEMATICS IN INDUSTRY **24**

THE EUROPEAN CONSORTIUM
FOR MATHEMATICS IN INDUSTRY

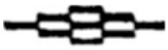

SUBSERIES

More information about this series at http://www.springer.com/series/4650

András Bátkai • Petra Csomós • István Faragó •
András Horányi • Gabriella Szépszó
Editors

Mathematical Problems in Meteorological Modelling

Springer

Editors
András Bátkai
Institute of Mathematics
Eötvös Lorand University
Budapest, Hungary

MTA-ELTE Numerical Analysis
and Large Networks Research Group
Budapest, Hungary

István Faragó
Institute of Mathematics
Eötvös Loránd University
Budapest, Hungary

MTA-ELTE Numerical Analysis
and Large Networks Research Group
Budapest, Hungary

Gabriella Szépszó
Hungarian Meteorological Service
Budapest, Hungary

Petra Csomós
Institute of Mathematics
Eötvös Loránd University
Budapest, Hungary

MTA-ELTE Numerical Analysis
and Large Networks Research Group
Budapest, Hungary

András Horányi
Solymár, Hungary

ISSN 1612-3956 ISSN 2198-3283 (electronic)
Mathematics in Industry
ISBN 978-3-319-40155-3 ISBN 978-3-319-40157-7 (eBook)
DOI 10.1007/978-3-319-40157-7

Library of Congress Control Number: 2016954078

Mathematics Subject Classification (2010): 86A10, 65L06, 62H11

Printed on acid-free paper

This Springer imprint is published by Springer Nature
The registered company is Springer International Publishing AG Switzerland

Prediction is very difficult, especially if it's about the future.

Niels Bohr

Foreword

When I first began studying pure mathematics, I could never have foreseen that I would spend the better part of my professional life in the area of meteorology. At that time, designing a proof for some conjecture seemed much more appealing than dealing with complex, high-dimensional weather forecasting models. Nevertheless, the presence of rich dynamics for already low-dimensional dynamical systems eventually piqued my curiosity for what the atmosphere, which could be considered the ultimate chaotic dynamical system, might hold within it.

In the early 1990s, people started to give some thought on how to deal with chaotic behaviour in the context of day-to-day weather forecasting. The opportunity to contribute to an operational approach that would probe the predictability of the atmosphere has been an exciting one. The Ensemble Prediction Systems, which at the time were being developed at a few places worldwide, were all designed to inform the forecasters about the occurrence of different possible weather regimes. It was already a mathematical challenge to optimally select the model runs comprising the ensemble. Given the computer capacity, it was only possible to conduct a relatively small number of model runs, compared to the model phase dimension.

During the last two decades, predictability research has produced an important shift from a deterministic to a probabilistic view in the field of weather and climate forecasting. A closer connection between ensemble forecasting and data assimilation naturally follows from this transition: the flow-dependent information that ensembles provide regarding uncertainties for certain areas can be employed to improve the use of observations in data assimilation, which in turn leads to better performing ensembles. This hybrid data assimilation approach is a promising new development that presents ample opportunities for mathematicians to excel, e.g. by exploring the role of model error.

Without a doubt, the increase in computer performance has been a decisive factor for the progress in meteorological modelling. As such, it is essential to be prepared for the next generations of computer architectures, which will most certainly require a high level of scalability for numerical models. Close interaction between computer hardware and software experts, numerical scientists and modellers would therefore seem to be a prerequisite to progress once exascale computers become the standard.

This book provides an attractive and varied introduction to topics where mathematicians and modellers from the meteorological community can cooperate with and help one another. I sincerely hope it will stimulate mathematicians to engage in solving problems which operational weather centres face now and in the near future. I would also like to warmly acknowledge the editors and contributors for their valued initiative and excellent work.

De Bilt, Netherlands Jan Barkmeijer
April 2016

Preface

Meteorological modelling, and in particular numerical weather prediction, belongs to those frontiers of research where both mathematicians and meteorologists can encounter striking new research problems. As a complex chaotic system, the atmosphere can only be modelled using a large system of nonlinear partial differential equations. Since theoretical investigations of these equations remain beyond our reach, only numerical approximative solutions are feasible. However, great strides have been made in the related mathematical disciplines in the last few years. The corresponding keywords, like big data or the environment, are also central topics in the European Union's Horizon 2020 project.

These and many other aspects are what motivated us when, in May 2014, we organized a workshop entitled "Mathematical Problems in Meteorological Modelling" at Eötvös Loránd University in Budapest. The idea was to introduce mathematicians to mathematical problems arising in meteorology and thus to spark new collaborations and research. After the informative, stimulating talks by leading experts, we decided to seek to reach a broader audience by publishing a volume where selected problems could be highlighted. Many of the contributors to this volume participated in or otherwise supported the conference. The main objective of the present volume is to highlight the beauty of the development fields covered, to demonstrate their mathematical complexity and more importantly to move mathematicians to contribute to the further success of such practical applications like weather forecasting and climate change projections.

Both the conference and this volume were made possible with the support of the MTA-ELTE Numerical Analysis and Large Networks Research Group and the European Consortium for Mathematics in Industry (ECMI). Founded more than a quarter of a century ago, the ECMI is a consortium of academic institutions and industrial companies that act cooperatively to promote and support the use of mathematical models in any activity of social or economic importance. Although traditionally meteorology has never been seen as an "industry", it nevertheless satisfies the previous definition, and one of the ECMI's key priorities is to get mathematicians involved in environmental applications.

We hope this volume can help reach this goal and reach many mathematicians. We have divided the book into three parts, moving from mathematical and numerical problems through air quality modelling to advanced applications in data assimilation and probabilistic forecasting. We are confident that many mathematicians working in numerical analysis, partial differential equations and stochastic analysis will find a source of motivation and inspiration for their future research work.

Lastly, we of course wish to warmly thank the reviewers for their valued contributions.

Budapest, Hungary — András Bátkai
Budapest, Hungary — Petra Csomós
Budapest, Hungary — István Faragó
Solymár, Hungary — András Horányi
Budapest, Hungary — Gabriella Szépszó
April 2016

Contents

Part I
Numerical Methods for Meteorological Problems

The dynamics of the atmosphere is governed by physical, chemical, and even biological processes which are commonly described by systems of time and space dependent nonlinear partial differential equations. Since this kind of mathematical description is rather complicated, the form of the equations' exact solution is usually unknown. In order to explore its properties or to compute its approximation, further mathematical methods are needed. The resulting atmospheric models are then to forecast the weather situation, the concentration of an air pollutant, or even the changes in climate. Since the computation of the forecast should not miss the events occurred in reality, it requires even faster and of course more accurate numerical treatment. These requirements stimulate the researches to elaborate on new numerical methods.

This part of the issue is devoted to the introduction and analysis of the basic ideas and methods behind atmospheric modelling. The chapters give an insight to the most commonly used numerical techniques. In order to distinguish the important features of the numerical methods themselves from the ones caused by the processes being described, the authors apply the methods to the same mathematical problems which arise in meteorology, however, in their simplified forms. Only after having showed the nice properties of a certain method, it can be applied to the more complex atmospheric problems presented in Parts II and III of the issue.

In Chap. 1, the authors analyse finite difference schemes being the most basic time discretisation method used when solving partial differential equations. They apply them to the one-dimensional shallow water equations which served as the first reliable model for large-scale atmospheric processes.

Chapter 2 introduces another discretisation method used in meteorological modelling. After giving an introduction on the mostly applied space discretisation methods, the authors focus on the combination of the semi-implicit finite difference method in time with the semi-Lagrangian approach for the nonlinear advection part, and apply it to two-dimensional shallow water equations.

Chapter 3 gives an introduction to the modelling of two-dimensional turbulence by using fractional derivatives. The main idea is to treat the shear stresses as random variables. The author present an algorithm, and apply it to a test problem.

In Chap. 4, the authors derive and show the convergence of a parallel numerical method for general nonlinear parabolic problems which usually arise in air pollution transport problems. Due to the chemical part, they face with nonlinear elliptic problems.

As seen from this short summary, Chaps. 1 and 2 treat numerical methods being the right choice when modelling the large-scale dynamics of the atmosphere, Chap. 3 deals with the modelling of turbulence occurring on much smaller scales, and Chap. 4 gives a generic treatment of problems arising in, for instance, air quality modelling. All of these fields will be covered in Parts II and III of this issue.

Chapter 1
On a Conservative Finite-Difference Method for 1D Shallow Water Flows Based on Regularized Equations

Alexander Zlotnik and Vladimir Gavrilin

Abstract We deal with the 1d shallow water system of equations and exploit its special parabolic regularization satisfying the energy balance law. We construct a three-point symmetric in space discretization such that the discrete energy balance law holds and check that it is well-balanced. The results of numerical experiments for the associated explicit finite-difference scheme are also given for several known tests to confirm its reliability and some advantages. The practical error behavior is also analyzed.

Keywords 1D shallow water equations • Discrete energy balance law • Parabolic regularization • Practical error analysis • Three-point symmetric in space discretization

1.1 Introduction

The 1d and 2d shallow water equations are widely exploited in hydrodynamics. The vast literature exists on their numerical solving, in particular, see [14] and [1, 3, 12, 15, 17–19], etc.

Several years ago a special regularization of the equations together with explicit two-level in time and symmetric in space finite-difference schemes based upon it were suggested in [5, 8]. The approach is further applied for various problems in [4, 9–11]. Previously the similar approach was developed for the more complicated Euler and Navier–Stokes equations and its practical efficiency in various

A. Zlotnik (✉)
Department of Higher Mathematics at Faculty of Economic Sciences, National Research University Higher School of Economics, Myasnitskaya 20, 101000 Moscow, Russia
e-mail: azlotnik2008@gmail.com

V. Gavrilin
Department of Mathematical Modelling, National Research University Moscow Power Engineering Institute, Krasnokazarmennaya 14, 111250 Moscow, Russia
e-mail: gavrilinva@gmail.com

A. Bátkai et al. (eds.), *Mathematical Problems in Meteorological Modelling*, Mathematics in Industry 24, DOI 10.1007/978-3-319-40157-7_1

compressible gas flow computations was demonstrated [6, 7, 16]; it is called a quasi-gas dynamic (QGD) approach. Moreover, the regularized shallow water system of equations is nothing more than a special case of the main version of the barotropic QGD system, see [20, 22].

In this chapter, following [21–23], we change the space discretization in the above mentioned schemes in order to guarantee the discrete energy balance law not available originally. We present the proof of the law and check the important property that the new discretization is well-balanced. The results of numerical experiments for the associated explicit in time finite-difference scheme are also given. We treat known tests such as a dam break (a disintegration of discontinuity) and subcritical, transcritical and supercritical flows over a hump to confirm the reliability and accuracy compared with the original scheme. In addition, the practical error behavior is analyzed as mesh refines. Here we confine ourselves by the 1d case; the 2d case should be considered in a forthcoming paper.

1.2 The 1d Shallow Water System of Equations, Its Regularization and Discretization

1.2.1. The 1d shallow water system of equations consists of the mass and momentum balance equations

$$\partial_t h + \partial_x(hu) = 0, \tag{1.1}$$

$$\partial_t(hu) + \partial_x(hu^2) + \partial_x p = \partial_x \Pi_{NS} + hF, \tag{1.2}$$

where $0 < x < X$, $t > 0$ and ∂_t and ∂_x denote the time and space derivatives. The main unknown functions are the water depth $h(x,t) > 0$ (measured from the bottom mark $b(x)$) and the velocity $u(x,t)$. The pressure, the Navier–Stokes viscous stress and the density of external force are given by

$$p = 0.5gh^2, \quad \Pi_{NS} = \mu\partial_x u, \quad F(x,t) = -g\partial_x b(x) + f(x,t), \tag{1.3}$$

where $g = \text{const} > 0$, $\mu = \mu(h) \geqslant 0$ is the viscosity coefficient (when $\mu = 0$, viscosity is ignored) and f is a perturbation of the stationary force $-g\partial_x b$. Remind also the important quantities $H = h + b$ (the water level) and hu (the discharge).

The equations are supplemented with the initial conditions

$$h(x,0) = h_0(x), \quad u(x,0) = u_0(x), \quad 0 \leqslant x \leqslant X. \tag{1.4}$$

The *regularized* 1d shallow water system of equations consists of the modified mass and momentum balance equations

$$\partial_t h + \partial_x(h(u-w)) = 0, \tag{1.5}$$

$$\partial_t(hu) + \partial_x(h(u-w)u + p) = \partial_x \Pi + h_* F. \tag{1.6}$$

Here the density of the mass flux j, the viscous stress Π and the regularized density h_* are given by

$$j = h(u - w), \quad w = \hat{w} + \frac{\tau}{h} u\partial_x(hu), \quad \hat{w} = \frac{\tau}{h}(hu\partial_x u + \partial_x p - hF), \tag{1.7}$$

$$\Pi = \mu\partial_x u + hu\hat{w} + \tau g h\partial_x(hu), \quad h_* = h - \tau\partial_x(hu), \tag{1.8}$$

where $\tau = \tau(h, u) > 0$ is the relaxation multiplier. If one puts $\tau = 0$, the system becomes the original system (1.1)–(1.3).

Note that the following simplified formula holds

$$\hat{w} = \tau\{u\partial_x u + g\partial_x(h + b) - f\}. \tag{1.9}$$

The regularized system (in equivalent form) was derived from the original one in [5, 8] in 1d and 2d cases. On the other hand, the latter system is nothing more than the special case of the main version of the barotropic QGD system of equations from [20] (its earlier version can be found in [24]) for the gas density $\rho = h$ and the pressure law $p(\rho) = 0.5g\rho^2$ with the adiabatic exponent $\gamma = 2$. In 1d this is due to formulas (1.9) and $\tau(u\partial_x p + \gamma p\partial_x u) = \tau g h\partial_x(hu)$.

For the barotropic QGD system of equations, the Petrovskii parabolicity, the energy balance law and the linearized stability of the equilibrium solutions were proved in [20, 22]; its very short derivation can be also found there. Remind that, first, the original system (1.1) and (1.2) is hyperbolic for $\mu = 0$ or of the composite hyperbolic-parabolic type for $\mu > 0$ and, second, the Petrovskii parabolicity implies a unique solvability (local in time) for the Cauchy problem in Hölder spaces, see [24] for details. These results demonstrate the dissipative nature of the barotropic system. They straightforwardly imply the corresponding results for the regularized shallow water system of equations, in particular, the following important one.

Theorem 1.1 *For the regularized shallow water equations* (1.5)–(1.8)*, the following pointwise energy balance law holds*

$$\begin{aligned} &0.5\partial_t\left\{g(h + b)^2 + hu^2\right\} + \partial_x\left\{h(u - w)\left(g(h + b) + 0.5u^2\right) - \Pi u\right\} \\ &+\mu(\partial_x u)^2 + \tau g\left\{\partial_x(hu)\right\}^2 + \tau h\left\{u\partial_x u + g\partial_x(h + b)\right\}^2 \\ &= h_* fu + \tau h\left\{u\partial_x u + g\partial_x(h + b)\right\}f. \end{aligned} \tag{1.10}$$

In the law on the left, the second term is a divergence one whereas the third (Navier–Stokes) term and fourth and fifth relaxation terms are non-negative; the property remains valid for $\tau \geqslant 0$.

For $f = 0$ and suitable boundary conditions at $x = 0, X$, for example, for the periodic ones, clearly law (1.10) implies non-increasing of the total energy in time

$$0.5\partial_t \int_0^X \{g(h+b)^2 + hu^2\}\, dx \leqslant 0. \tag{1.11}$$

Notice that, for the equilibrium solutions $h = h_S(x) > 0$ and $u = 0$, both systems (1.1)–(1.3) and (1.5)–(1.8) for $f = 0$ are reduced to the equation

$$\partial_x p(h_S) + g h_S \partial_x b = 0 \ \text{ on } \ (0, X), \tag{1.12}$$

i.e., simply to the formula $h_S(x) + b(x) \equiv C$ on $[0, X]$.

1.2.2. We define a non-uniform mesh $\bar{\omega}_h$ in space with nodes $0 = x_0 < x_1 < \cdots < x_N = X$ and steps $\Delta_i = x_i - x_{i-1}$. Let $\Delta_{\max} := \max_{1 \leqslant i \leqslant N} \Delta_i$. We also use an auxiliary (conjugate) mesh ω_h^* with nodes $x_{i+1/2} = (x_i + x_{i+1})/2$, $0 \leqslant i \leqslant N-1$, and steps $\hat{\Delta}_i = x_{i+1/2} - x_{i-1/2} = (\Delta_i + \Delta_{i+1})/2$.

For functions v given on $\bar{\omega}_h$ and y given on ω_h^*, we introduce averages, shifts of argument and difference quotients

$$[v]_{i+1/2} = 0.5(v_i + v_{i+1}),\ v_{-,i+1/2} = v_i,\ v_{+,i+1/2} = v_{i+1},\ \delta v_{i+1/2} = \frac{v_{i+1} - v_i}{\Delta_{i+1}},$$

$$[y]_i^* = \frac{\Delta_i}{2\hat{\Delta}_i} y_{i-1/2} + \frac{\Delta_{i+1}}{2\hat{\Delta}_i} y_{i+1/2},\ \ \delta^* y_i = \frac{y_{i+1/2} - y_{i-1/2}}{\hat{\Delta}_i}.$$

The operators $[\cdot]$, $(\cdot)_\pm$ and δ map functions given on $\bar{\omega}_h$ to ones defined on ω_h^* whereas $[\cdot]^*$ and δ^* map functions given on ω_h^* to those defined on $\omega_h = \{x_i\}_{i=1}^{N-1}$.

We need two difference product rules

$$\delta(uv) = \delta u \cdot [v] + [u]\delta v, \tag{1.13}$$

$$\delta^*(y[v]) = \delta^* y \cdot v + [y\delta v]^* \tag{1.14}$$

(u is given on $\bar{\omega}_h$). To reduce the amount of brackets, hereafter we suppose that, for example, $\delta u \cdot [v] = (\delta u)[v]$ (i.e., the multiplication sign $\cdot$ terminates action of preceding operators). Formula (1.14) was effectively applied, in particular, in [2]. We also exploit the formulas

$$[\delta v]_i^* = \delta^*[v]_i = \frac{v_{i+1} - v_{i-1}}{2\hat{\Delta}_i}, \tag{1.15}$$

$$[y]^* v = \big[y[v]\big]^* - 0.25\delta^*(\Delta_+^2 y \delta v). \tag{1.16}$$

Turning to [23], we first construct a three-point symmetric in space discretization to (1.5)–(1.8) and write down the semi-discrete mass and momentum balance

equations as follows

$$\partial_t h + \delta^*\big([h]([u]-w)\big) = 0, \tag{1.17}$$

$$\partial_t(hu) + \delta^*\big([h]([u]-w)[u] + [p]\big) = \delta^* \Pi + [h_* F]^* \tag{1.18}$$

on ω_h for $t > 0$. Here the following discretizations for the density of the mass flux j, the viscous stress Π and the regularized density h_* are exploited

$$j = [h]([u]-w), \quad w = \hat{w} + \frac{\tau}{[h]}\,[u]\delta(hu), \quad \hat{w} = \frac{\tau}{[h]}\big([h][u]\delta u + \delta p - [h]F\big), \tag{1.19}$$

$$\Pi = \mu\delta u + [h][u]\hat{w} + \tau g[h]\delta(hu), \quad h_* = [h] - \tau\delta(hu), \quad F = -g\delta b + f. \tag{1.20}$$

The main unknown functions h and u together with the functions p and b are defined on the main mesh $\bar{\omega}_h$ whereas the functions j, w, $\hat{w}$, Π, h_*, τ, μ and f are defined on the auxiliary mesh ω_h^*. Note that $\delta p = g[h]\delta h$ and therefore similarly to (1.9) the following formula holds

$$\hat{w} = \tau\{[u]\delta u + g\delta(h+b) - f\}. \tag{1.21}$$

We assume that $h > 0$ and derive the counterpart of the energy balance law (1.10).

Theorem 1.2 *For the semi-discrete method* (1.17)–(1.20)*, the following pointwise energy balance law holds*

$$\begin{aligned} &0.5\partial_t\big\{g(h+b)^2 + hu^2\big\} + \delta^*\big\{j\,(g(h+b) + 0.5u_-u_+) - \Pi[u] + B_\Delta\big\} \\ &\quad + \big[\mu(\delta u)^2 + \tau g\big\{\delta(hu)\big\}^2 + \tau[h]\{[u]\delta u + g\delta(h+b)\}^2\big]^* \\ &\quad = [h_* f]^* u + \big[\tau[h]\{[u]\delta u + g\delta(h+b)\}f\big]^*, \end{aligned} \tag{1.22}$$

where $B_\Delta := -0.25\Delta_+^2(\delta p + gh_*\delta b)\delta u$.

In the law on the left, all three terms under the averaging sign $[\cdot]^*$ *are non-negative; the property remains valid for* $\tau \geqslant 0$.

Proof We follow the derivation of the differential law (1.10) from [22], see also [23], and first multiply the mass balance equation (1.17) by $g(h+b)$. Since

$$\delta^* j \cdot g(h+b) = \delta^*(jg[h+b]) - \big[jg\delta(h+b)\big]^*$$

according to formula (1.14), we get

$$\partial_t(p(h) + ghb) + \delta^*(jg[h+b]) - \big[[h]g\delta(h+b)([u]-w)\big]^* = 0. \tag{1.23}$$

Next we multiply the momentum balance equation (1.18) by u. We apply the formula

$$\partial_t(hu)\cdot u = 0.5\partial_t(hu^2) + 0.5\partial_t h\cdot u^2,$$

the mass balance equation (1.17) and twice formula (1.14) to obtain:

$$\partial_t h\cdot u^2 = -\delta^*j\cdot u^2 = -\delta^*(j[u^2]) + \big[j\delta(u^2)\big]^*,$$

$$\delta^*(j[u])\cdot u = \delta^*(j[u]^2) - \big[j[u]\delta u\big]^*.$$

Then also taking into account elementary formulas

$$[u]^2 = 0.5[u^2] + 0.5u_-u_+,\ \ 0.5\delta(u^2) = [u]\delta u \tag{1.24}$$

and formula (1.15), we derive

$$0.5\partial_t(hu^2) + 0.5\delta^*(ju_-u_+) + [\delta p + gh_*\delta b]^*u - \delta^*\Pi\cdot u = [h_*f]^*u.$$

We add equality (1.23) and the last one. Formulas (1.14) and (1.16), respectively, imply

$$[\delta p + gh_*\delta b]^*\cdot u = \big[\{\delta p + g[h]\delta b - \tau\delta(hu)\cdot g\delta b\}[u]\big]^* + \delta^*B_\Delta,$$

$$-\delta^*\Pi\cdot u = -\delta^*(\Pi[u]) + [\Pi\delta u]^*,$$

with the above introduced B_Δ. Since $\delta p + g[h]\delta b = [h]g\delta(h+b)$, we obtain

$$0.5\partial_t\left\{g(h+b)^2 + hu^2\right\} + \delta^*(A + B_\Delta)$$

$$+\big[[h]g\delta(h+b)w - \tau[u]\delta(hu)\cdot g\delta b + \Pi\delta u\big]^* = [h_*f]^*u,$$

with $A := j\{g(h+b) + 0.5u_-u_+\} - \Pi[u]$.

Extracting the terms τf in the multipliers w and Π, we rewrite the last equality in the form

$$0.5\partial_t\big\{g(h+b)^2 + hu^2\big\} + \delta^*(A + B_\Delta) + \big[\mu(\delta u)^2 + \Psi(h,u)\big]^*$$

$$= [h_*f]^*u + \big[\tau\{[h]g\delta(h+b) + [h][u]\delta u\}f\big]^*, \tag{1.25}$$

where

$$\Psi(h,u) := [h]g\delta(h+b)(w+\tau f) - \tau[u]\delta(hu)\cdot g\delta b$$

$$+\{[h][u](\hat{w}+\tau f) + \tau g[h]\delta(hu)\}\delta u$$

$$= [h]g\delta(h+b)(w+\tau f) + [h][u]\delta u \cdot (\hat{w}+\tau f)$$
$$-\tau g\delta b \cdot [u]\delta(hu) + \tau g[h]\delta(hu)\cdot\delta u.$$

Applying the formulas

$$w+\tau f = \hat{w}+\tau f + \frac{\tau}{[h]}[u]\delta(hu),\ \ \hat{w}+\tau f = \tau\big\{[u]\delta u + g\delta(h+b)\big\},$$

see (1.21), we transform $\Psi(h,u)$ as follows

$$\Psi(h,u)$$
$$= \big\{[h]g\delta(h+b) + [h][u]\delta u\big\}(\hat{w}+\tau f) + \tau g\delta h\cdot[u]\delta(hu) + \tau g[h]\delta(hu)\cdot\delta u$$
$$= \tau[h]\big\{[u]\delta u + g\delta(h+b)\big\}^2 + \tau\delta(hu)\big\{g\delta h\cdot[u] + g[h]\delta u\big\}.$$

Finally, using the formula $\delta h\cdot[u] + [h]\delta u = \delta(hu)$, see (1.13), we rewrite $\Psi(h,u)$ as the sum of two squared terms and thus pass from (1.25) to the desired result (1.22). □

For $f = 0$ and suitable boundary conditions at $x = 0, X$, for example, for the periodic ones, clearly law (1.22) implies non-increasing of the total energy in time

$$0.5\partial_t \sum_{i=0}^{N-1}\big\{g(h+b)^2 + hu^2\big\}_i\hat{\Delta}_i \leqslant 0,$$

where $\hat{\Delta}_0 = (h_1 + h_N)/2$, that is the discrete counterpart of the energy inequality (1.11).

In the discrete energy balance law (1.22), the term u_-u_+ is like the geometric mean for u^2. The summand $\delta^* B_\Delta$ is the divergence mesh imbalance [additional with respect to (1.10)] with $B_\Delta = O(\Delta^2_{\max})$ for the functions of the continuous argument provided that h, $\partial_x h$, $\partial_x u$ and $\partial_x b$ are bounded.

For the equilibrium solution $h = h_S(x) > 0$ and $u = 0$, method (1.17)–(1.20) for $f = 0$ is reduced to the equations [with the help of formula (1.15)]

$$\delta^*\big\{\tau\big(\delta p(h_S) + g[h_S]\delta b\big)\big\} = 0,\ \ \big[\delta p(h_S) + g[h_S]\delta b\big]^* = 0 \ \text{ on } \ \omega_h.$$

Notice that $\delta p(h_S) + g[h_S]\delta b = g[h_S]\delta(h_S + b)$. By virtue of the first equation $\tau g[h_S]\delta(h_S+b) = C_0 \equiv \text{const}$ on ω_h^*, and next $C_0 = 0$ due to the second equation. Consequently

$$g[h_S]\delta(h_S+b) = 0 \ \text{ on } \ \omega_h^*,$$

i.e. $h_S + b \equiv \text{const}$ on $\bar{\omega}_h$. These results correspond to (1.12) and its consequence for the regularized system and mean that the method is *well-balanced* which is the known important property.

1.2.3. Let us compare our discretization and one from [5, 8, 11], for which unfortunately the energy balance law is not known. The following two terms in the momentum balance equation (1.18)

$$\delta^*[p(h)], \quad [h_* F]^* = \big[\{[h] - \tau\delta(hu)\}(-g\delta b + f)\big]^*$$

differ from those

$$\delta^* p([h]), \quad \big\{\big[[h]\big]^* - \tilde{\tau}\delta([h][u])\big\}(-g\delta^*[b] + \tilde{f}),$$

in [5, 8, 11] (generalized for the non-uniform $\bar{\omega}_h$ and written in our notation), where $\tilde{\tau}$ and $\tilde{f}$ are defined on $\bar{\omega}_h$. Moreover, inserting formula (1.21) into the second formula (1.19) leads to

$$w = \frac{\tau}{[h]}\big(2[h][u]\delta u + [u]^2\delta h\big) + \tau\big\{g\delta(h+b) - f\big\}$$

whereas in [5, 8, 11] a formula equivalent to

$$w = \frac{[\tilde{\tau}]}{[h]}\,\delta(hu^2) + [\tilde{\tau}]\big\{g\delta(h+b) - \tilde{f}\big\}$$

was applied. Since $\delta(hu^2) = 2[h][u]\delta u + [u^2]\delta h$ but $[u]^2 \not\equiv [u^2]$ [see (1.13) and (1.24)], these two formulas for w also differ.

On the other hand, inserting formula (1.21) into the first formula (1.20) gives

$$\Pi = \mu\delta u + \tau[h][u]\big\{\delta\big(g(h+b) + 0.5u^2\big) - f\big\} + \tau g[h]\delta(hu)$$

similarly to [5, 11] (up to expressions for μ, τ and f).

1.2.4. Now we define a non-uniform mesh in time with nodes $0 = t_0 < \ldots < t_M = t_{\text{fin}}$ (which are not prescribed a priori) and steps $\Delta t_m = t_{m+1} - t_m$, where t_{fin} is the given final time.

We approximate the time derivatives in the mass and momentum equations (1.15) and (1.16) by the forward differences and get *the explicit finite difference scheme*

$$\hat{h} = h - \Delta t\,\delta^*\big([h]([u] - w)\big), \tag{1.26}$$

$$\widehat{hu} = hu - \Delta t\big\{\delta^*\big([h]([u] - w)[u] + [p] - \Pi\big) - [h_* F]^*\big\} \tag{1.27}$$

on ω_h for $0 \leqslant m \leqslant M-1$, where $\hat{h}$ and $\widehat{hu}$ are the values for the upper time level. After computing them, we set $\hat{u} := \widehat{hu}/\hat{h}$ assuming that $\hat{h} > 0$. Here we also exploit the same expressions (1.19) and (1.20).

For solving the inviscid shallow water system of equations, the viscous and relaxation terms are considered as artificial regularizers with μ and τ in the form

$$\mu = \frac{4}{3}\tau[p] \ \text{ or } \ \mu = 0, \ \ \tau = \alpha\frac{\Delta}{c}, \ \ c = \sqrt{g[h]}$$

on ω_h^* like in [7, 16], where c is the counterpart for the velocity of sound and $0 < \alpha < 1$. To satisfy a stability condition of the Courant-Friedrichs-Lévy type, the time step at the current time level is chosen as

$$\Delta t = \beta \min_{1\leqslant i\leqslant N} \frac{\Delta}{|[u]_{i-1/2}| + c_{i-1/2}}$$

with $0 < \beta < 1$, and thus Δt varies from one time level to another. The scheme parameters α and β are adjusted experimentally in each problem.

Notice that, at least for the uniform space mesh, the approximation order of the semi-discrete method (1.17)–(1.20) [with respect to the regularized system (1.5)–(1.8)] is $O(\Delta^2)$ with $\Delta = X/N$ for smooth solutions but it is reduced to $O(\Delta)$ for the finite-difference scheme owing to the above choices of τ and Δt.

1.2.5. In our computations below, we use a uniform mesh in space and take $f = 0$. We investigate the convergence of functions $v = h, u$ and hu for our finite difference scheme at the final time t_{fin} as the space mesh refines; this is a standard matter, for example see [13, 15, 17], and especially important in the case of non-smooth solutions where the theoretical information is poor. In those rare cases where a sought function v_{ex} is known, we compute the average absolute value of the error on the mesh (the scaled mesh L^1-norm)

$$E_{\text{ex}}^{(N)}[v] := \frac{1}{N+1}\sum_{i=0}^{N}\left|v_{\text{ex}\,i} - v_i^{(N)}\right|, \tag{1.28}$$

where $v_{\text{ex}\,i}$ and $v_i^{(N)}$ are the exact and approximate quantities at $x_i = iX/N$.

Otherwise, we apply two formulas

$$E^{(N)}[v] := \frac{1}{N+1}\sum_{i=0}^{N}\left|v_{i\overline{N}/N}^{(\overline{N})} - v_i^{(N)}\right|, \ E_R^{(N)}[v] := \frac{1}{N+1}\sum_{i=0}^{N}\left|v_{2i}^{(2N)} - v_i^{(N)}\right|, \tag{1.29}$$

where $v^{(\overline{N})}$ is the pseudo-exact solution computed for the finer mesh with the step $\overline{\Delta} = X/\overline{N}$. Here $\overline{N}$ is a multiple of $2N$, and due to our numerical experience it is desirable that $4N \leqslant \overline{N}$. The second formula is associated to the Runge rule for the practical error estimation and is cheaper in implementation ($v^{(\overline{N})}$ is not required). We compare both of them with (1.28) if possible.

Below we plot the dependence of $\left|\ln E^{(N)}[v]\right|$ (the subscripts are omitted) on $\ln N$. Moreover, we approximate them by linear functions using the least square method and thus get the corresponding approximate error orders $p_{\mathrm{ex}}[v]$, $p[v]$ and $p_R[v]$.

1.3 Numerical Results

1.3.1. We first compute a flow in a channel of the length $X = 1500$ m. In its central part, a rectangular ledge is symmetrically located (having the height 8 m and the length 375 m), and the other bottom is flat. At the center of the channel, a dam is situated. Initially the water level $H_0(x)$ equals 20 m to the left and 15 m to the right of the dam, and the flow is at rest, i.e. the initial velocity is zero: $u_0(x) = 0$. The dam breaks at the moment $t = 0$. The open boundary conditions are imposed for h and u at the both boundaries $x = 0, X$, i.e., for example, $h_0 = h_1$ and $u_0 = u_1$ for the left boundary.

The computational results are shown in Fig. 1.1 for $t = 15$ s and $t = 60$ s, for $N = 400$; the scheme parameters are $\alpha = 0.35$ and $\beta = 0.5$. They are in a good agreement with [15] for $N = 200$ and in [11] for $N = 400$ (for other schemes).

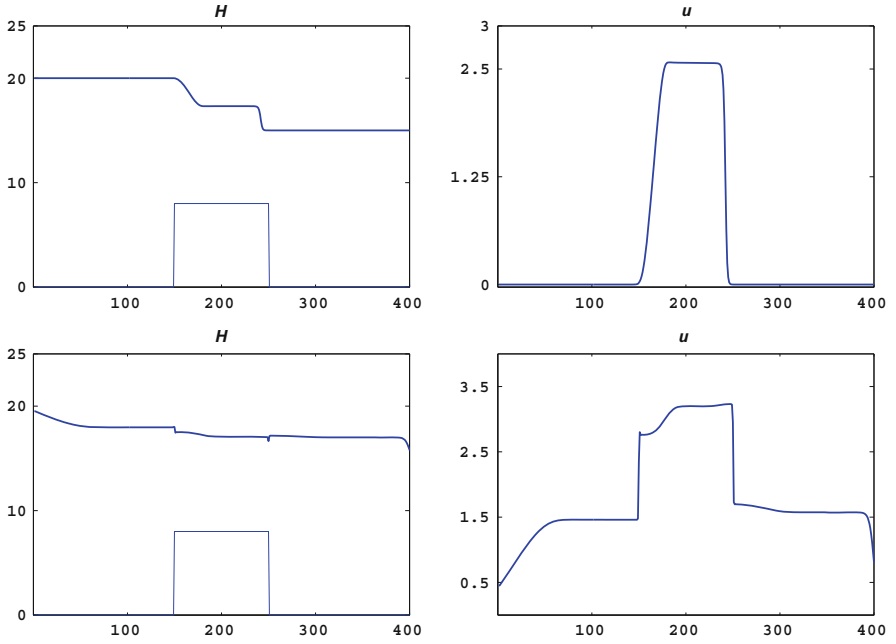

Fig. 1.1 Dam break in the channel with the rectangular ledge: H and u at $t = 15$ s (*above*) and $t = 60$ s (*below*)

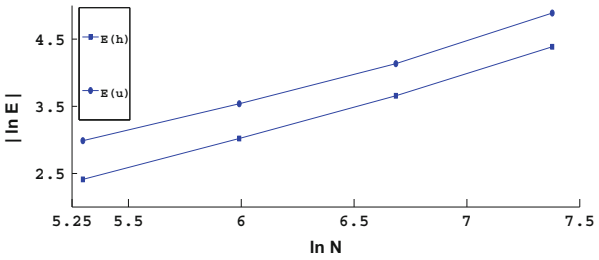

Fig. 1.2 Dam break in the channel with the rectangular ledge: $\left|\ln E^{(N)}\right|$ for h and u

In Fig. 1.2, the errors in h and u for $t = 15$ s are presented for $N = 200, 400, 800$ and 1600 as well as $\overline{N} = 6400$. We note that the error polylines are not completely linear. The error orders $p[h] \approx 0.946$ and $p[u] \approx 0.908$ are rather close to each other but both less than 1.

1.3.2. Next we consider a channel of the length $X = 25$ m with a flat bottom except for the small hump of the parabolic shape in its middle part:

$$b(x) = \begin{cases} 0.2 - 0.05(x-10)^2, & 8\,\text{m} \le x \le 12\,\text{m} \\ 0, & \text{otherwise.} \end{cases}$$

Initially the water level is constant: $H_0(x) \equiv C_H$, and the flow is at rest. The left boundary conditions are $hu|_{x=0} = C_{hu}$ for the discharge together with the open boundary condition for h, and the right boundary conditions are $H|_{x=X} = C_H$ (in general, up to a certain time moment) together with the open boundary condition for u.

This problem may seem simple but only at first glance. There are three types of flows in it: subcritical, transcritical and supercritical depending on values of the flow parameters. In what follows, examples of all three types of flows are considered. Results of computations are presented at $t_{\text{fin}} = 200$ s (at this moment the flows become stationary for the chosen values of the parameters). Note that, for these flows, the exact discharge at the final time is known: $hu \equiv C_{hu}$. As a rule, namely the computation of hu causes difficulties. The results are accurate enough for N listed below; they are comparable with those obtained in [3] (for $N = 100$), [12] (for $N = 300$) and [1, 18, 19] (for $N = 200$) by other schemes but much better for hu than in [11] (for the same N).

(a) *Subcritical flow*. This is the simplest type of flows. Here $C_H = 2$ m and $C_{hu} = 4.42\,\text{m}^2/\text{s}$ are taken. At t_{fin}, the water level is almost flat with only a small cavity above the hump.

We select $\alpha = 0.9$, $\beta = 0.2$ and $\mu = 0$. Figure 1.3 shows the water level H and the discharge hu for $N = 400$. In the vicinity of the hump edges, "hubbles"

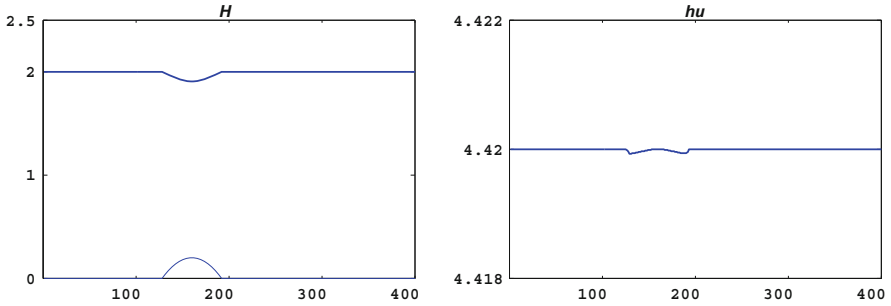

Fig. 1.3 Subcritical flow over the hump: H and hu at $t_{\text{fin}} = 200\,\text{s}$

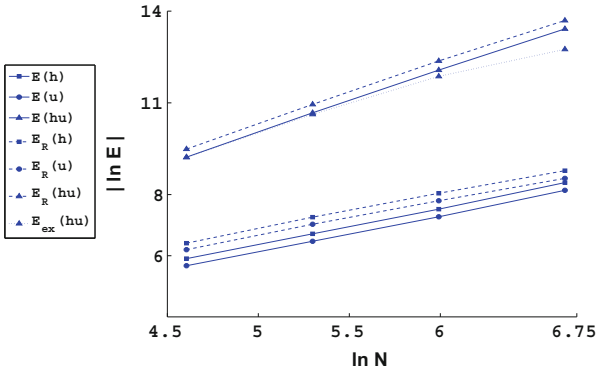

Fig. 1.4 Subcritical flow over the hump: $\left|\ln E^{(N)}\right|$ for h, u and hu

of hu values are observed (damping as N increases) but the absolute error in the discharge $E_{\text{abs}} := \max\limits_{0\le i\le N} |(hu)_i - C_{hu}| \approx 7.375\text{e-}5$ is small.

In Fig. 1.4, errors in h, u and hu are shown for $N = 100$, 200, 400 and 800 as well as $\overline{N} = 3200$. The same values are taken for two other flow types below.

The polylines of errors in h and u are more close to linear ones than for the previous problem (though this is not the case for $|\ln E_{\text{ex}}[hu]|$). Now all the orders $p[h] \approx 1.193$, $p_R[h] \approx 1.139$, $p[u] \approx 1.183$ and $p_R[u] \approx 1.121$ are all close to each other and slightly greater than 1. They are essentially less than $p_{\text{ex}}[hu] \approx 1.709$. Comparing the results by formulas (1.28) and (1.29) for hu, we see that the error orders $p_R[hu] \approx 2.023$ and $p[hu] \approx 2.017$ are close to each other but both overestimate the value $p_{\text{ex}}[hu]$.

(b) *Transcritical flow*. Here $C_H = 0.66\,\text{m}$ and $C_{hu} = 1.53\,\text{m}^2/\text{s}$ are chosen. For this and the next types of flows, the right boundary condition $H(X,t) = C_H$ is posed only for $t \le 40\,\text{s}$ whereas it is replaced by the open boundary condition for h for $t > 40\,\text{s}$. In this case, the behavior of the stationary water level H is more complicated exhibiting much more sharp change (its values on the left and right

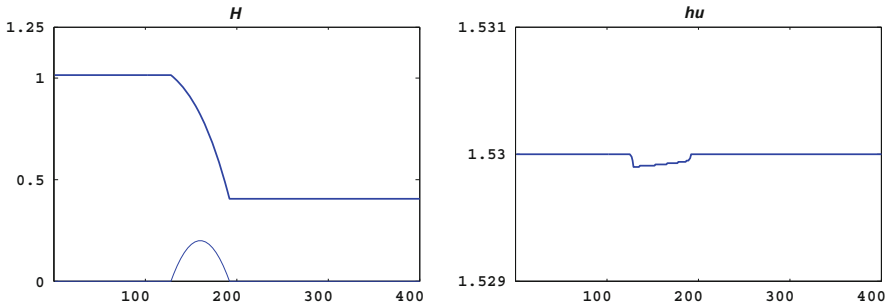

Fig. 1.5 Transcritical flow over the hump: H and hu at $t_{\text{fin}} = 200\,\text{s}$

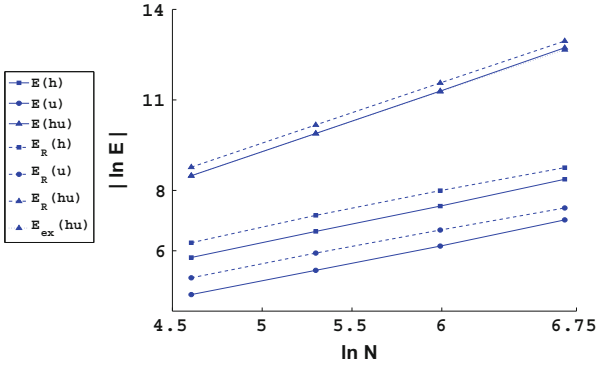

Fig. 1.6 Transcritical flow over the hump: $\left|\ln E^{(N)}\right|$ for h, u and hu

sides of the hump are very different, and there is a zone of smooth transition over the hump).

We take $\alpha = 0.9$, $\beta = 0.1$ and $\mu = 0$. Figure 1.5 shows the level H and the discharge hu at $N = 400$. Similarly to the previous case, there are "hubbles" of hu values over the hump edges (damping as N increases) but $E_{\text{abs}} \approx 9.882\text{e-}5$ is small once again.

Figure 1.6 shows the errors in h, u and hu. The polylines of errors in h and u are once again close to linear ones. Moreover, the polylines for $|\ln E_{\text{ex}}[hu]|$ and $|\ln E_R[hu]|$ are almost the same. The orders $p[h] \approx 1.243$, $p_R[h] \approx 1.196$, $p[u] \approx 1.187$ and $p_R[u] \approx 1.113$ are once again close to and slightly greater than 1 whereas all of $p_{\text{ex}}[hu] \approx 2.009$, $p[hu] \approx 2.038$ and $p_R[hu] \approx 2.010$ are much larger and close to 2 (not 1).

(c) *Supercritical flow*. Here $C_H = 0.33\,\text{m}$ and $C_{hu} = 0.18\,\text{m}^2/\text{s}$ are taken. In this case, the behavior of the stationary water level H is strongly non-monotone (its graph over the hump has a narrow sharp hollow) and more complicated than previously.

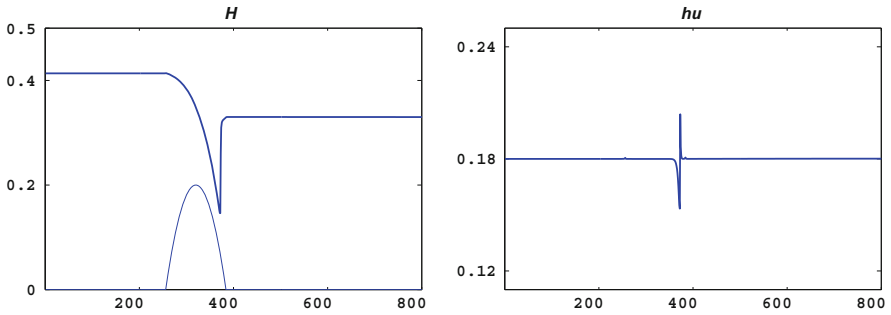

Fig. 1.7 Supercritical flow over the hump: H and hu at $t_{fin} = 200$ s

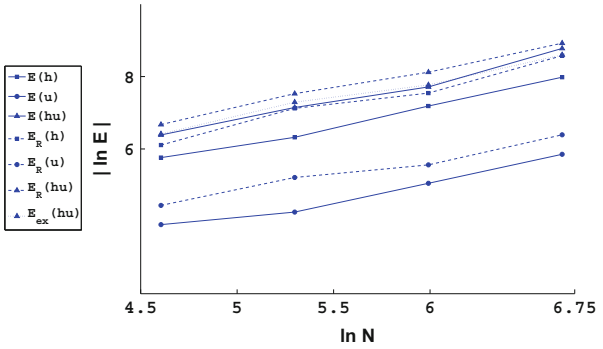

Fig. 1.8 Supercritical flow over the hump: $\left|\ln E^{(N)}\right|$ for h, u and hu

We take $\alpha = 0.8$, $\beta = 0.1$ and $N = 800$. We have checked that the presence of the Navier–Stokes-type viscosity (the term with the coefficient μ) is essential namely in the present case; the stable computations are impossible without it. From Fig. 1.7, we see that hu is now computed worse. There is a sharp oscillation near the right edge of the hump. Now $E_{\text{abs}} \approx 0.0266$ is about two orders of magnitude worse than in the previous two cases.

Figure 1.8 shows the errors in h, u and hu. Now the polylines of errors in h and u differ from linear ones. It is natural that the order $p_{\text{ex}}[hu] \approx 1.014$ is now much less and close to 1; $p_R[hu] \approx 0.950$ is slightly closer to $p_{\text{ex}}[hu]$ than $p[hu] \approx 1.116$. Other orders are $p[h] \approx 1.086$, $p_R[h] = 1.056$, $p[u] \approx 0.956$ and $p_R[u] \approx 0.895$ (two last now less than 1).

Notice that generally both formulas (1.29) give different error results but rather close error orders though the second one seems slightly more exact in the latter respect.

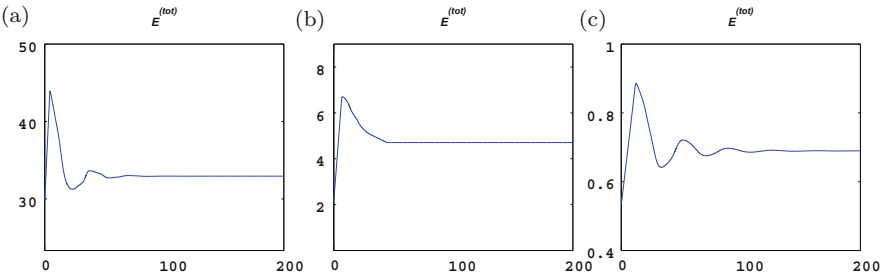

Fig. 1.9 The flow over the hump in cases (**a**)–(**c**): the mean total energy $E^{(\mathrm{tot})}$ in time

Finally, in Fig. 1.9 we present the behavior of the mean total energy

$$E^{(\mathrm{tot})} = \frac{1}{N}(0.5e_0 + \sum_{i=1}^{N-1} e_i + 0.5e_N), \quad e = 0.5g\{(h+b)^2 + hu^2\}$$

in time in all the cases (a), (b) and (c). For simplicity of comparison, it is computed for the uniform mesh in time for $N = 100$. We observe the stabilization of this quantity after one or several oscillations (with no any purely numerical oscillations).

Acknowledgements This work was supported by The National Research University Higher School of Economics' Academic Fund Program, project No. 15-09-0266 and the Russian Foundation for Basic Research, project No. 13-01-00703.

References

1. Akoh, R., Ii, S., Xia, F.: A multi-moment finite volume formulation for shallow water equations on unstructured mesh. J. Comput. Phys. **229**, 4567–4590 (2010)
2. Amosov, A.A., Zlotnik, A.A.: A study of finite-difference method for the one-dimensional viscous heat conductive gas flow equations. Part I: a priori estimates and stability. Sov. J. Numer. Anal. Math. Model. **2**(3), 159–178 (1987)
3. Benkhaldoun, F., Seaïd, M.: A simple finite volume method for the shallow water equations. J. Comput. Appl. Math. **234**, 58–72 (2010)
4. Bulatov, O.V.: Analytical and numerical Riemann solutions of the Saint-Venant equations for forward- and backward-facing step flows. Comput. Math. Math. Phys. **54**(1), 158–171 (2014)
5. Bulatov, O.V., Elizarova T.G.: Regularized shallow water equations and an efficient method for numerical simulation of shallow water flows. Comput. Math. Math. Phys. **51**(1), 160–173 (2011)
6. Chetverushkin, B.N.: Kinetic Schemes and Quasi–Gas Dynamic System of Equations. CIMNE, Barcelona (2008)
7. Elizarova, T.G.: Quasi–Gas Dynamic Equations. Springer, Dordrecht (2009)
8. Elizarova, T.G., Bulatov, O.V.: Regularized shallow water equations and a new method of numerical simulation of the open channel. Comput. Fluids. **46**, 206–211 (2011)

9. Elizarova, T.G., Saburin, D.S.: Numerical simulation of fluid oscillations in fuel tanks. Math. Models Comput. Simul. **5**, 470–478 (2013)
10. Elizarova, T.G., Istomina, M.A., Shelkovnikov, N.K.: Numerical simulation of solitary wave generation in a wind-water annular tunnel. Math. Models Comput. Simul. **4**, 552–559 (2012)
11. Elizarova, T.G., Zlotnik, A.A., Nikitina, O.V.: Modeling of one-dimensional shallow water flows on the basis of regularized equations. Preprint of Keldysh Inst. Appl. Math. **33**, 1–36 (2011) [in Russian]
12. Gallouet, T., Herard, J.M., Seguin, N.: Some approximate Godunov schemes to compute shallow-water equations with topography. Comput. Fluids. **32**, 479–513 (2003)
13. Godunov, S.K., Mazunina, Y.D., Nazarieva, M.A.: Experimental analysis of convergence of the numerical solution to a generalized solution in fluid dynamics. Comput. Math. Math. Phys. **51**, 88–95 (2011)
14. Kulikovskii, A.G., Pogorelov, N.V., Semenov, A.Y.: Mathematical Aspects of Numerical Solution of Hyperbolic Systems. Chapman & Hall/CRC Press, London (2000)
15. Noelle, S., Pankratz, N., Puppo, G., Natvig, J.R.: Well-balanced finite volume schemes of arbitrary order of accuracy for shallow water flows. J. Comput. Phys. **213**, 474–499 (2006)
16. Sheretov, Yu.V.: Continuum Dynamics Under Spatiotemporal Averaging. Regular and Chaotic Dynamics, Moscow, Ijevsk (2009) [in Russian]
17. Vignoli, G., Titarev, V.A., Toro, E.F.: ADER schemes for the shallow water equations in channel with irregular bottom elevation. J. Comput. Phys. **227**, 2463–2480 (2008)
18. Xu, K.: A well-balanced gas-kinetic scheme for the shallow-water equations with source terms. J. Comput. Phys. **178**, 533–562 (2002)
19. Zhang, S.Q., Ghidaoui, M.S., Gray, W.G., Li, N.Z.: A kinetic flux vector splitting scheme for shallow water flows. Adv. Water Resour. **26**, 635–647 (2003)
20. Zlotnik, A.A.: Energy equalities and estimates for barotropic quasi-gasdynamic and quasi-hydrodynamic systems of equations. Comput. Math. Math. Phys. **50**(2), 310–321 (2010)
21. Zlotnik, A.A.: Spatial discretization of one-dimensional quasi-gasdynamic systems of equations and the entropy and energy balance equations. Dokl. Math. **86**, 464–468 (2012)
22. Zlotnik, A.A.: On construction of quasi-gasdynamic systems of equations and the barotropic system with the potential body force. Math. Model. **24**(4), 65–79 (2012) [in Russian]
23. Zlotnik, A.A.: The space discretization of the one-dimensional barotropic quasi-gas dynamic system of equations and the energy balance equation. Math. Model. **24**(10), 51–64 (2012) [in Russian]
24. Zlotnik, A.A., Chetverushkin, B.N.: Parabolicity of the quasi-gasdynamic system of equations, its hyperbolic second-order modification, and the stability of small perturbations for them. Comput. Math. Math. Phys. **48**(3), 420–446 (2008)

Chapter 2
Discretization in Numerical Weather Prediction: A Modular Approach to Investigate Spectral and Local SISL Methods

Steven Caluwaerts, Daan Degrauwe, Fabrice Voitus, and Piet Termonia

Abstract An overview of some spatial and temporal discretization methods used in NWP is given. The authors focus on the spectral semi-implicit semi-Lagrangian scheme, which was and still is one of the most successful schemes. A Z-grid approach with an identical timestep organization as the current semi-implicit semi-Lagrangian schemes is proposed. This provides a testbed to undertake comparison studies between spectral and local spatial discretization schemes.

Keywords Dispersion • Dynamical core • Semi-implicit time discretization • Spectral spatial discretization • Z-grid

2.1 Introduction

It is obvious that accurate weather forecasts are beneficial for society. Due to the complex and multiscale nature of the weather, the only approach to predict it consists of solving the equations governing the motions in the atmosphere in a numerical way by using computers. Lewis Fry Richardson was the first to come up with the concept of numerical weather forecasting. In 1922 he published his book

S. Caluwaerts (✉)
Physics and Astronomy Department, Ghent University, Krijgslaan 281, 9000 Gent, Belgium
e-mail: steven.caluwaerts@ugent.be

D. Degrauwe
Royal Meteorological Institute, Ringlaan 3, 1180 Brussel, Belgium
e-mail: daan.degrauwe@meteo.be

F. Voitus
CNRM, Météo-France, Avenue Gaspard Coriolis, 31057 Toulouse, France
e-mail: fabrice.voitus@meteo.fr

P. Termonia
Royal Meteorological Institute, Ringlaan 3, 1180 Brussel, Belgium

Physics and Astronomy Department, Ghent University, Krijgslaan 281, 9000 Gent, Belgium
e-mail: termonia@meteo.be

A. Bátkai et al. (eds.), *Mathematical Problems in Meteorological Modelling*,
Mathematics in Industry 24, DOI 10.1007/978-3-319-40157-7_2

[36], which outlined how to make an estimate of the future weather by integrating differential equations in time. His brilliant work proposed to use a finite difference spatial discretization method to solve a set of equations describing atmospheric motion. Richardson realised that huge calculation power was needed to forecast the weather at the pace the weather is evolving. The advent of the first computers in the forties made these computational resources available and numerical weather forecasts became a reality [7]. Since then increasing computer power and a better understanding of meteorological processes fuelled a continuous and still ongoing improvement and sophistication of numerical weather prediction (NWP) models. However, this would not have been possible without accurate and efficient numerical schemes.

The success of NWP was realised in parallel with the evolution in high performance computing (HPC). Today the scalability of NWP codes on massively parallel supercomputers is becoming one of the main issues that may affect future evolutions. The aim of this chapter is to give first an overview of numerical schemes used in NWP before focussing on the spectral semi-implicit semi-Lagrangian techniques, where scalability is felt most, and see how these schemes could be extended with local spatial discretization methods, which are expected to scale better.

This chapter is structured in the following way.

In Sect. 2.2 a non-exhaustive overview of the different choices for the numerical discretization in NWP is presented. The text is written within the context of weather modeling, but its ideas and concepts remain valid for climate models especially since there is an increasing trend towards unified modeling over all spatial and temporal scales [5, 24]. It will be clear that there does not exist one optimal discretization choice and therefore various approaches, all with (dis)advantages, are used by modeling groups. The choices are often explained by the historical background of the group or the main application of the model (e.g. tracer modeling) at the time the development was initiated.

Section 2.3 will review the merits of the so-called spectral semi-implicit (SI) semi-Lagrangian (SL) technique. It will be shown that once the choice of SI time discretization has been made, the choice for the treatment of the non-linear terms of the advection by a SL scheme follows quite naturally. The combined spectral SISL method has a long and successful history in NWP. The reasons for this are discussed and some challenges for its future applicability to atmospheric modeling are listed.

Spectral methods are defined on collocation grids, also known as Arakawa A-grids [28]. In [6] a Z-grid scheme was proposed that retains appropriate geostrophic adjustment while maintaining the A-grid. Section 2.4 will review the Z-grid method as an example of introducing local discretization methods while staying as close as possible to the code organization of the currently used spectral models. This could offer a scientific testbed for an intercomparison study between spectral and local methods while changing one discretization for another and keeping all other schemes of the model equal.

At the end, Sect. 2.5 will present some conclusions and ideas for future work.

2.2 Discretization of the Dynamical Core in NWP

In a weather model the state of the atmosphere at a certain time t is specified by a very large state vector $\mathbf{F}(t)$ containing the values of meteorological variables (e.g. wind velocity, temperature, pressure,...) at time t in all gridpoints of the 3D numerical mesh. The goal of a NWP model consists of forecasting how this state vector will evolve in time. To do so, three main components can be distinguished in a NWP model:

- The *dynamics* (or *dynamical core*) may be defined as the part of the model responsable for solving the dry, adiabatic equations, which describe the main flow in the atmosphere. This chapter concerns the discretization methods used for the solution of this dynamical core.
- All the subgrid phenomena, whose scales are too small to be represented explicitly on the chosen mesh, are taken into account by the so-called *physics*. The former includes microphysics (for precipitation), convection, turbulence, radiation,... The physics processes are coupled to the dynamics by means of a diabatic source term $\mathbf{P}(\mathbf{F}(t))$ in the dry, adiabatic equations.
- As understood already by Richardson [36], the creation of an accurate initial state of the atmosphere is a condition sine qua non for an accurate weather forecast. The *data assimilation* block combines the output of previous model forecasts and millions of observations to calculate an optimal initial state $\mathbf{F_0}$.

The physical basis of the NWP models is formed by the fundamental laws of momentum, mass and energy conservation. For the sake of simplicity we will limit the discussion in this section to the conservation of momentum. Expressed in vector form for a coordinate framework rotating with the earth, conservation of momentum can be written as:

$$\frac{\partial \mathbf{V}}{\partial t} = -\mathbf{V} \cdot \nabla \mathbf{V} - 2\boldsymbol{\Omega} \times \mathbf{V} - \frac{\nabla p}{\rho} + \mathbf{g} \tag{2.1}$$

with 3D velocity $\mathbf{V}$, density ρ and pressure p [21]. Advection (i.e. transport by the wind) is one of the main drivers for weather evolutions and is represented by $-\mathbf{V} \cdot \nabla \mathbf{V}$. Three different forces can be distinguished in Eq. (2.1): the Coriolis force $-2\boldsymbol{\Omega} \times \mathbf{V}$ with $\boldsymbol{\Omega}$ the angular velocity of the earth, the pressure gradient force $-\frac{\nabla p}{\rho}$ and gravity $\mathbf{g}$.

Symbolically one could synthesize atmospheric modeling by the following initial value problem:

$$\frac{\partial \mathbf{F}(t)}{\partial t} = \mathbf{A}(\mathbf{F}(t)) + \mathbf{M}(\mathbf{F}(t)) + \mathbf{P}(\mathbf{F}(t)) \,, \quad \mathbf{F}\,(t=0) = \mathbf{F_0} \tag{2.2}$$

with $\mathbf{A}(\mathbf{F}(t)) = -\mathbf{V} \cdot \nabla \mathbf{F}(t)$ representing advection, $\mathbf{M}$ representing the other resolved forcings (pressure gradient force, Coriolis force and gravity) and $\mathbf{P}$ the earlier mentioned tendencies of the physics. Integrating the dynamical core, the

Table 2.1 Overview of the discretization choices made in some European NWP models that are operationally in use

	Time discretization	Horizontal space discretization/grid
ICON [60] (DWD)	2 TL predictor-corrector scheme	FD-FV icosahedral-triangular on Arakawa C-grid
IFS/ARPEGE/ALADIN [1, 51] (ECMWF/Météo-France/ALADIN)	2 TL SISL	Spectral on reduced Gaussian grid, stretched grid or rectangular LAM domain
UM [14] (UK Metoffice)	2 TL SISL	FD on lat-lon Arakawa C-grid
SL-AV [55] (Russia Hydrometeor)	2 TL SISL	Partly FD, partly spectral on lat-lon Arakawa A-grid

The used abbreviations: 2 *TL* = two time level, *SISL* = semi-implicit semi-Lagrangian, *FD* = finite differences and *FV* = finite volume

scope of this chapter, could then be presented as solving:

$$\frac{\partial \mathbf{F}(t)}{\partial t} = \mathbf{A}(\mathbf{F}(t)) + \mathbf{M}(\mathbf{F}(t)) \; . \tag{2.3}$$

This section will provide an introduction about the discretization of Eq. (2.3). The numerical scheme will consist of both a time discretization and a space discretization because **A** and **M** contain spatial derivatives. The spatial operators act along the horizontal and vertical direction. Thanks to the difference in scales in the horizontal and vertical direction, the 3D numerical problem is typically split up in a complementary but rather independent 2D horizontal problem and 1D vertical problem. Largest problems with scalability are in the horizontal, we thus limit ourselves to horizontal spatial discretization. The presented methods ought to form a first introduction to this broad topic. The interested reader is referred to textbooks (e.g. [4, 8, 16]) for more exhaustive overviews of discretization approaches in NWP.

Table 2.1 presents the discretization choices made in some of the European models that are operationnaly used with ongoing research and development. The table illustrates that a broad spectrum of methods is used. All methods mentioned in Table 2.1 will be explained in this document.

2.2.1 Time Discretization of the Dynamical Core

Two main categories of time discretization schemes are used in NWP: explicit and semi-implicit schemes. In a scheme based on an *explicit* time discretization all forcing terms [right-hand side of Eq. (2.3)] are evaluated at previous times resulting in a direct update problem. By evaluating some of the forcing terms both at previous times and at the current instant of time, one obtains a *semi-implicit* scheme that

results in an elliptic problem. The choice of the time discretization scheme has an impact on:

1. the propagation properties of waves, e.g. waves can be slowed down by a semi-implicit treatment.
2. the numerical stability of the scheme, it is well known that an explicit time discretization results in a necessary condition for the timestep Δt in order to obtain a stable scheme. This so-called Courant-Friedrichs-Lewy or CFL criterion [12] reads $V_{max}\frac{\Delta t}{\Delta x} < C$ with V_{max} the velocity of the fastest propagating mode, Δx the grid mesh, Δt the timestep and C a constant depending on the used spatial discretization. Finer model resolutions will make this timestep criterion more strict.
3. the order of accuracy. An evaluation based on more instants of time will result in a higher order of accuracy. However, it would also necessitate more data storage. In NWP the timestep is mostly determined by stability and not by accuracy, which explains why often two timelevel methods with first or second order accuracy are used.

The straightforward explicit time discretization of Eq. (2.3) would be the forward Euler scheme resulting into:

$$\mathbf{F}^{+} = \mathbf{F}^{0} + \Delta t\left[\mathcal{A}\left(\mathbf{F}^{0}\right) + \mathcal{M}\left(\mathbf{F}^{0}\right)\right] , \tag{2.4}$$

with $\mathbf{F}^{+}$ and $\mathbf{F^0}$ the vectors containing the prognostic variables in all the gridpoints at time t^0 and $t^{+} = t^0 + \Delta t$ and $\mathcal{A}$ and $\mathcal{M}$ the spatially discretized operators corresponding with $\mathbf{A}$ and $\mathbf{M}$. However, this scheme turns out to be unconditionally unstable as derived for example in [8], meaning the amplitude of physically neutral waves will be amplified numerically by this scheme, independent of the choice of the timestep. In NWP other explicit temporal discretization methods are used. As an example consider the two-timelevel *predictor-corrector* scheme, also known as the second-order Runge–Kutta scheme or the Heun scheme, which could be summarized as:

$$\mathbf{F}^{*} = \mathbf{F}^{0} + \Delta t\left[\mathcal{M}\left(\mathbf{F}^{0}\right) + \mathcal{A}\left(\mathbf{F}^{0}\right)\right] \tag{2.5}$$

$$\mathbf{F}^{+} = \mathbf{F}^{0} + \frac{\Delta t}{2}\left[\mathcal{M}\left(\mathbf{F}^{0}\right) + \mathcal{M}\left(\mathbf{F}^{*}\right) + \mathcal{A}\left(\mathbf{F}^{0}\right) + \mathcal{A}\left(\mathbf{F}^{*}\right)\right] . \tag{2.6}$$

The predictor step, Eq. (2.5), uses a forward Euler scheme to find a preliminary state vector $\mathbf{F}^{*}$. During the corrector step, Eq. (2.6), $\mathbf{F}^{+}$ is calculated by interpolating the forcing over $\mathbf{F}^0$ and $\mathbf{F}^{*}$. This scheme could be evaluated easily in the sense that one does not need to solve elliptic problems. This approach is still unconditionally amplifying [16], despite having an amplification that is much weaker than the one of the forward Euler scheme. The ICON model [60] that is based on a dynamical core solving the Euler equations with a 2TL scheme is based on a stable variant of such a scheme.

As an alternative one could average the forcing terms between times t^0 and t^+. This slows down the fastest waves and permits in this way the use of longer timesteps. These schemes introduced in NWP by Robert [42] are called *implicit* time discretization schemes and result in an elliptic problem to solve

$$\mathbf{F}^+ = \mathbf{F}^0 + \frac{\Delta t}{2}\left[\mathcal{A}\left(\mathbf{F}^0\right) + \mathcal{A}\left(\mathbf{F}^+\right) + \mathcal{M}\left(\mathbf{F}^0\right) + \mathcal{M}\left(\mathbf{F}^+\right)\right]. \tag{2.7}$$

The form of Eq. (2.7) is not used as such in NWP because of its complexity, indeed the operators $\mathcal{A}$ and $\mathcal{M}$ contain non-linear terms making an implicit treatment very cumbersome. Therefore, the dynamics operator is splitted into a linear operator $\mathcal{L}$ and a non-linear residual $\mathcal{M} - \mathcal{L}$ and only the linear part is treated in an implicit way:

$$\mathbf{F}^+ = \mathbf{F}^0 + \frac{\Delta t}{2}\left[\mathcal{L}\left(\mathbf{F}^0\right) + \mathcal{L}\left(\mathbf{F}^+\right) + 2\mathcal{A}\left(\mathbf{F}^{**}\right) + 2\left(\mathcal{M} - \mathcal{L}\right)\left(\mathbf{F}^{**}\right)\right]. \tag{2.8}$$

This approach is called the *semi-implicit* (SI) or *implicit-explicit* (IMEX) method [17] and results in an Helmholtz problem:

$$\left[1 - A\left(\Delta t\right)^2 \nabla^2\right] f^+ = R, \tag{2.9}$$

with f^+ one of the prognostic fields at t^+, $\nabla^2 = \frac{\partial^2}{\partial x^2} + \frac{\partial^2}{\partial y^2}$ the Laplacian operator and A depending on the field f. The efficiency and accuracy of the solver for Eq. (2.9) will largely determine the success of the SI scheme.

Analysis shows that the waves described by the implicitly treated part $\mathcal{L}$ are significantly slowed down. The linear part $\mathcal{L}$ will be unconditionally stable and second order accurate. By carefully choosing the term $\mathcal{L}$ so that it contains the terms responsible for the fastest moving waves (e.g. sound waves in fully compressible equations), one could exploit this property to weaken the CFL-timestep criterion. The method was first illustrated in NWP in 1971 by Kwizak and Robert [25], where it was used to slow down the short scale gravity waves, resulting in an increase of the timestep by a factor 6. The non-linear part of the dynamics operator and physics could be evaluated in multiple ways (symbolized by $\mathbf{F}^{**}$), e.g. a predictor-corrector scheme as for the UM [14] or by extrapolation as for IFS [22]. Remark that the stability of the implicitly treated part is no guarantee that the scheme as a whole will be stable as explained for example in [45].

The *horizontally explicit vertically implicit* (HEVI) scheme can be considered as a member of the SI family of schemes. These days there is a trend in NWP towards unified modeling, meaning one model is used to simulate atmospheric phenomena over all scales [5]. For this purpose one can no longer use filtered equation sets (e.g. the hydrostatic primitive equations used for global NWP where the hydrostatic approximation filters out sound waves), and the fully compressible equations are gaining importance [13]. But this equation set does permit 3D

sound waves, which do not have any meteorological relevance but propagate at a high speed. In modern NWP the vertical grid spacing is varying, high up in the atmosphere the resolution is low but close to the surface the vertical grid spacing can be in the order of meters, much smaller than the horizontal resolution. If treated explicitly vertically propagating sound waves would necessitate a very short timestep. Therefore, the HEVI approach, which is an explicit scheme treating only the terms for vertical sound wave propagation implicitly, is gaining importance, e.g. the recently developed ICON model [60].

Robert [43] estimated that even in SI schemes the spatial discretization errors are 40 times larger than the temporal discretization errors, thus the timestep is still limited by stability constraints and not by accuracy. Advection processes were found to limit the maximal stable timestep. Apart from the direct evaluation of the non-linear advection terms, which was used in these days in NWP, a Lagrangian alternative, where advection was evaluated by following parcels along their trajectory, was known [19]. Because this Lagrangian approach is difficult to combine with a fixed grid, Sawyer proposed a semi-Lagrangian (SL) approach where trajectories were calculated for parcels on a uniform grid [44]. Robert showed that combining the SL treatment for advection with a SI discretization made stable integrations of the equations with even longer timesteps possible [43]. Symbolically SISL schemes can be represented as:

$$\mathbf{F}^{+} = \mathbf{F}_{D}^{0} + \frac{\Delta t}{2}\left[\mathcal{L}\left(\mathbf{F}_{D}^{0}\right) + \mathcal{L}\left(\mathbf{F}^{+}\right) + 2\left(\mathcal{M} - \mathcal{L}\right)\left(\mathbf{F}_{T}^{**}\right)\right]. \tag{2.10}$$

Remark there is no longer an evaluation of the non-linear advection terms $\mathcal{A}$. Computations at the previous time t^0 are evaluated in the departure points, found by tracking back the positions at time t^0 of parcels that are at time t^+ in the gridpoints of the fixed grid. This is symbolized by the subscript $_D$. The non-linear terms are evaluated along the SL trajectory (subscript $_T$) but different methods do exist. Remark that the SL efficiency gain by the reduction of the number of time integrations will be partly offset by the trajectory calculations and the extra communications needed to do the interpolations to departure points.

SISL schemes became popular time discretization schemes for atmospheric modeling. Table 2.1 shows that today the SISL method is used for example in IFS, SL-AV and UM.

2.2.2 Space Discretization of the Dynamical Core and Grids

In this section a brief overview of horizontal spatial discretization strategies will be given. For more information the reader is referred to the earlier mentioned textbooks. Remark that different discretization strategies could in the end lead to the same discretized equation.

Richardson used second order centered *finite differences* to approximate derivatives, e.g.

$$\frac{\partial f}{\partial x}(x_0) \approx \frac{f(x_0 + \Delta x) - f(x_0 - \Delta x)}{2\Delta x}, \tag{2.11}$$

with Δx the grid distance [36]. In fact the previous formula could be considered as a direct application of the definition of the derivative. The accuracy of Eq. (2.11) could be improved by refining the resolution or by using a higher order approximation based also on evaluations of the function f further away than one grid distance Δx. Finite difference schemes are often combined with a staggered grid formulation where different variables are evaluated in different gridpoints. This will be explained in more detail in Sect. 2.4.

Schemes based on finite difference approximations for horizontal derivatives are commonplace in NWP (e.g. second order finite differences in the Met Office UM [5], fourth order finite differences for some of the derivatives in SL-AV [55]).

A second category of spatial discretization schemes is based on an *expansion* in terms of *basis functions*. Let us illustrate this principle by solving the following equation:

$$\frac{\partial u}{\partial t} = F(u), \tag{2.12}$$

which corresponds to Eq. (2.3) written out for one field u of the state vector $\mathbf{F}$ and with $F(u)$ representing the total forcing. This method then assumes that the solution $u_N(\mathbf{r}, t)$ could be written as an expansion in basis functions $\phi_i(\mathbf{r})$ defined over the domain Ω

$$u_N(\mathbf{r}, t) = \sum_{i=1}^{N} U_i(t)\phi_i(\mathbf{r}), \tag{2.13}$$

where $U_i(t)$ represents the weight of the basis function ϕ_i and $\mathbf{r}$ the position vector. The modeling problem is now translated into finding the evolution in time of the N expansion coefficients $U_i(t)$. Using Eq. (2.13), one could define the residual R as:

$$R(\mathbf{r}, t) = \sum_{i=1}^{N} \frac{dU_i}{dt}(t)\,\phi_i(\mathbf{r}) - F\left(\sum_{i=1}^{N} U_i(t)\phi_i(\mathbf{r})\right). \tag{2.14}$$

One must strive towards a minimal R. If $R(\mathbf{r}, t) = 0$ for each position $\mathbf{r}$ and time t, the proposed solution $u_N(\mathbf{r}, t)$ would be an exact solution of Eq. (2.12). Different strategies for the minimization of the residual will result in different coefficients U_i. One could for example use the *collocation* method, which dictates the residual to be exactly equal to 0 in N gridpoints called the collocation points $\mathbf{r}_j$. However, in NWP the *Galerkin* method based on the evaluation of the residual against the N

basis functions $\phi_j(\mathbf{r})$ over the whole domain Ω, is most often used:

$$\int_\Omega \phi_j(\mathbf{r})\, R(\mathbf{r},t)\, d\mathbf{r} = 0 \;\; ; \forall j = 1,2,\ldots,N \tag{2.15}$$

or thus

$$\sum_{i=1}^{N} M_{ji} \frac{dU_i}{dt}(t) = \int_\Omega \phi_j(\mathbf{r})\, F\left(\sum_{i=1}^{N} U_i(t)\,\phi_i(\mathbf{r})\right) d\mathbf{r} \;\; ; \forall j = 1,2,\ldots,N. \tag{2.16}$$

with

$$M_{ji} = \int_\Omega \phi_i(\mathbf{r})\,\phi_j(\mathbf{r})\, d\mathbf{r}. \tag{2.17}$$

In general the update equations for the different coefficients U_i are coupled resulting in an implicit problem. However, by choosing a set of orthogonal basis functions, the mass coefficients M_{ji} become diagonal i.e.

$$M_{ji} = \int_\Omega \phi_i(\mathbf{r})\,\phi_j(\mathbf{r})\, d\mathbf{r} = \delta_{ij} \;\; ; \forall i,j = 1,2,\ldots,N, \tag{2.18}$$

which decouples Eq. (2.16) into a set of simple update equations for the expansion coefficients U_i.

One could opt for global basis functions defined over the whole domain, or local functions that are only non-zero in a limited part of the domain. The first method, called the *spectral method*, was introduced in meteorology in 1966 by again Robert [41] and permitted a highly accurate calculation of derivatives. In a global model spherical harmonics are the logical choice for the basis functions whereas for limited area forecasts double Fourier series are used [1]. Both define an orthogonal basis. The spectral method in combination with SISL time discretization became very popular due to its high accuracy and efficiency and it is still today one of the main methods (e.g. IFS [51]). Recently, questions were raised about the future applicability of the spectral method and a more thorough discussion will follow in Sect. 2.3.

A spatial discretization scheme based on the use of local basis functions only non-zero in a limited part of the domain is called a *finite element* method . A good introduction can be found in [56], which presented the first finite element scheme in NWP. Finite element methods are becoming more popular although they have a lower degree of accuracy compared to spectral methods but they need less communication and can be used in a more flexible way. There exists a whole spectrum of different subtypes: spectral elements [15], discontinuous Galerkin methods [30], mixed finite elements [11],... Until now, most of the finite element developments were undertaken in research institutes outside Europe e.g. the operational GEM model of CMC is based on a finite element discretization [35]. In

Europe there is (to the authors' knowledge) currently no operational NWP model based on finite elements.

The *finite volume approach* could be distinguished as a third main category of spatial discretizations. Its origins date back to 1959 [20] and the method was extended during the following decades but it is only quite recently that it became more commonplace in NWP, again mainly in some US research groups (e.g. [26] developed at NCAR and NASA). The finite volume method starts from the equations reformulated in their *conservative* form. In 1D this looks like

$$\frac{\partial u}{\partial t} + \frac{\partial}{\partial x} f(u) = S(u,x), \tag{2.19}$$

with $f(u)$ the flux determining the reaction of the flow to gradients and $S(u,x)$ a source term. By assuming a division of the grid in different elements, one could spatially integrate the conservative equations over each element. By assuming a 1D-element $[x_{i-1/2}, x_{i+1/2}]$ around x_i, integrating Eq. (2.19) over this element results in:

$$\frac{d}{dt}\int_{x_{i-1/2}}^{x_{i+1/2}} u(x,t)\,dx + f\left(u\left(x_{i+1/2},t\right)\right) - f\left(u\left(x_{i-1/2},t\right)\right) = \int_{x_{i-1/2}}^{x_{i+1/2}} S(u,x)\,dx. \tag{2.20}$$

Time integration from t^n to $t^{n+1} = t + \Delta t$ leads to:

$$\int_{x_{i-1/2}}^{x_{i+1/2}} u\left(x,t^{n+1}\right)dx - \int_{x_{i-1/2}}^{x_{i+1/2}} u\left(x,t^{n}\right)dx + \int_{t^n}^{t^{n+1}} f\left(u\left(x_{i+1/2},t\right)\right)dt$$
$$- \int_{t^n}^{t^{n+1}} f\left(u\left(x_{i-1/2},t\right)\right)dt = \int_{t^n}^{t^{n+1}}\int_{x_{i-1/2}}^{x_{i+1/2}} S(u,x)\,dxdt. \tag{2.21}$$

By introducing

- the average of the u field at time t^n in element $[x_{i-1/2}, x_{i+1/2}]$:

$$u_i^n = \frac{1}{\Delta x}\int_{x_{i-1/2}}^{x_{i+1/2}} u(x,t^n)\,dx \tag{2.22}$$

- the average flux through the element boundary at $x_{i-1/2}$ during $[t^n, t^{n+1}]$:

$$f_{i-1/2}^n = \frac{1}{\Delta t}\int_{t^n}^{t^{n+1}} f\left(u\left(x_{i-1/2},t\right)\right)dt \tag{2.23}$$

- the time and space averaged source term:

$$S_i^n = \frac{1}{\Delta t \Delta x} \int_{t^n}^{t^{n+1}} \int_{x_{i-1/2}}^{x_{i+1/2}} S(u,x)\, dx dt \tag{2.24}$$

one obtains for Eq. (2.21) the following update equation:

$$u_i^{n+1} = u_i^n - \frac{\Delta t}{\Delta x}\left(f_{i+1/2}^n - f_{i-1/2}^n\right) + \Delta t S_i^n. \tag{2.25}$$

This equation to find the updated cell averaged quantities is still exact. However, one needs approximations to evaluate the fluxes at the boundaries [Eq. (2.23)] and the averaged source term [Eq. (2.24)]. There exists a lot of literature on different ways to do so, but [16] is a good starting point. One of the main advantages of the finite volume method is its good conservation properties. The NASA Goddard Space Flight Center finite volume dynamical cores, which were developed for global modeling focused on transport processes, form a good illustration of this method [26].

Finally, numerical models are formulated on a *grid* covering the region of interest. For limited area models this does not pose serious problems, but gridding the sphere for global modeling is challenging. Until now the *lat-lon grid* that defines gridpoints at the intersections of meridians and latitude circles was the dominant choice for NWP. It possesses a logically rectangular structure, orthogonality and symmetry [48], but the converging meridians result in a very high resolution over the two poles as examplified in the introduction of [23]. Using a reduced grid that has less gridpoints on latitude circles closer to the poles (e.g. the reduced Gaussian grid of Hortal and Simmons [23] used for spectral models) does relax this pole problem somewhat. Due to the pole problem the CFL stability condition discourages explicit time integration on a lat-lon grid contrary to SISL discretizations, which do not suffer from this strict timestep limitation. It has been advocated that also SISL schemes may become unfeasible for high-resolution lat-lon modeling on massively parallel computer architectures where communication and not computation becomes the bottleneck. This would be due to the extensive data communication needed around the poles [48]. This explains why there is a renewed interest in alternative gridding methods for global modeling as reviewed recently in [48] and [59]. Until now the operational use of these non lat-lon grids is limited. In Table 2.1 the ICON-model, formulated on an icosahedral-hexagonal grid, is currently the only one.

2.3 Spectral SISL Discretization Schemes

After this broad overview of discretization in NWP, the focus in Sect. 2.3 will be narrowed to the spectral SISL method. The reasons for the spectral success are reviewed and at the end, currently raised issues about the spectral method are discussed.

The truncation errors caused by using finite differences for the spatial discretization were Robert's main motivation to start experimenting with the spectral method for the integration of the primitive equation [41]. The highly accurate calculations in spectral space result in wave propagation properties close to the analytical ones. However, he realised that this method was computationally very demanding, e.g. the evaluation of non-linear terms requires the calculation of triple products of basis functions, which are no longer orthogonal like the double products in Eq. (2.18):

$$M_{kji} = \int_{\Omega} \phi_i(\mathbf{r})\,\phi_j(\mathbf{r})\,\phi_k(\mathbf{r})\,d\mathbf{r} \neq \delta_{ijk} \quad ;\forall i,j,k = 1,2,\ldots,N. \tag{2.26}$$

Robert thought that the spectral formulation would not be able to challenge the gridpoint methods used for NWP [41]. However, his expectations for the use of spectral forms in weather modeling turned out to be too pessimistic. During the nineties a majority of the operational global NWP models was based on spectral schemes, e.g. IFS/ARPEGE [39] (ECMWF and France), GM [27] (Germany), GSM [34] (Japan), GEM [40] (Canada),...

Two key reasons for the success of the spectral method could be distinguished:

1. As mentioned earlier, some of the calculations (e.g. non-linear terms) are computationally very demanding in spectral space. In [18] and [33] a method, the *spectral transform method*, was introduced that proposed to evaluate this part of the computations of a spectral method in gridpoint space. With this proposal the best of two worlds is combined in the algorithmic organization of the timestep computation: derivatives are calculated in a highly accurate way in spectral space whereas non-linear terms, physics,... are evaluated efficiently in gridpoint space (e.g. [52]). Transformations every timestep back and forth between spectral and gridpoint space is the price to pay. All spectral models in NWP make use of this transform approach.
2. Ritchie showed that the spectral method could be combined with SISL time discretizations paving the way to long timestep spectral schemes [38]. Moreover, the elliptic problem, Eq. (2.9), characteristic for the SI approach becomes trivial in spectral space, because the spherical harmonics (or double Fourier functions for LAMs) are eigenfunctions of the Laplacian; by using the spectral method you get the SI nearly for free. The SL treatment avoids an explicit evaluation of the large non-linear advection terms and increases the timestep even further, improving the efficiency of the method. This explains why to the authors' knowledge spectral schemes are always combined with SISL.

Spectral SISL schemes dominated global NWP models from the nineties on. By replacing the spherical harmonics by double Fourier series and by periodisation of the in general non-periodic fields, this approach was succesfully extended to LAMs, e.g. ALADIN [1].

Since some years concern has been expressed by some communities about the applicability of the spectral method in the future, and some institutes using spectral models before, switched to other discretization methods (e.g. ICON [60] and GEM

[10]). One could distinguish two concerns about the spectral SISL method as it is used today:

- **Scientific issues:** The most fundamental scientific limitation of spectral methods seems to be the global character of the basis functions. It is impossible to include non horizontally-homogeneous coefficients in the linear operator $\mathcal{L}$ in Eq. (2.10), because this would introduce triple products [Eq. (2.26)] of basis functions in the elliptic equation and thus make the calculations very complex. This is in contrast with more local discretization schemes (FD, FE,...), which permit reference states depending on the horizontal position in the implicit calculations (e.g. a horizontally varying orography or reference temperature). Being limited to horizontally-homogeneous coefficients could lead to large non-linear residuals, which are a potential source of instabilities. As an example the use of a homogeneous background state may lead to a decrease in accuracy when used over steep slopes in future high resolution models.
- **Technological issues:** A trend towards massively parallel high performance computing (HPC), which makes data movement costly in terms of wall-clock time and energy, is observed. As this evolution is expected to continue and if there would be no new technology to speed up communication, NWP modelers should reflect on the communication needs of their schemes. A distinction should be made between two kinds of communications. Some numerical methods (e.g. derivative calculations with finite differences or SL advection) need only *local* communication of data from nearby points. By adapting the computer topology to the grid, local communication becomes quite inexpensive and the code could scale well. However, if global communication is needed the topology of the computers can not avoid data communication between distant cores. For such problems the communication will become more problematic if more cores are used. For the transforms back and forth between spectral and gridpoint space the spectral transform method needs so-called transpositions. This comprises that all data of one latitude or longitude have to be collected on one processor thus necessitating poorly scalable global communication. Reducing the need for global communication is one of the motivations in [57] to study the impact of solving the spectral part with a coarser resolution than the gridpoint part.

Although the viability of the spectral method has been questioned already in [9], it is still today one of the main NWP approaches. This illustrates the difficulty to estimate the future of a modeling approach. However, it is sure that it will be challenging to find a highly scalable and flexible alternative that retains the success properties (e.g. high accuracy, no grid imprinting,...) of the spectral method.

2.4 Study of Local SISL Z-Grid Schemes

Local (finite differences or finite element) discretization schemes should not suffer from the two issues raised in the previous section, thereby it would be interesting to make a scientifically clean comparison between spectral and local methods. Here

we use the example of the Z-grid method to illustrate how the spectral discretization could be complemented by a local method while keeping the timestep structure equal to the one of the spectral transform method described in the previous section.

First the Z-grid scheme is introduced in Sect. 2.4.1, then its raison d' être being its ability to represent accurately wave propagation is reviewed. In Sect. 2.4.3 it is explained how to combine a SISL time discretization with the Z-grid method with a timestep organization equal to what is used in IFS/ARPEGE/ALADIN. And finally, there is a short discussion about the computational aspects of SISL Z-grid schemes combined with finite differences or finite elements.

2.4.1 The Z-Grid Approach

Because of the complexity of the equations solved in NWP, new schemes are first examined by studying its impact on the less complex shallow water equations (SWE) as motivated in [2]. The 2D Cartesian SWE on an f-plane, meaning the Coriolis constant f is assumed constant, look like:

$$\frac{du}{dt} = -\frac{\partial \phi}{\partial x} + fv \tag{2.27}$$

$$\frac{dv}{dt} = -\frac{\partial \phi}{\partial y} - fu \tag{2.28}$$

$$\frac{d\phi}{dt} = -\phi \left(\frac{\partial u}{\partial x} + \frac{\partial v}{\partial y} \right) , \tag{2.29}$$

with

$$\frac{d}{dt} = \frac{\partial}{\partial t} + u\frac{\partial}{\partial x} + v\frac{\partial}{\partial y} , \tag{2.30}$$

u and v the wind velocity components in the x- and y-direction and ϕ the geopotential. The wave solutions of these SWE have very similar properties to their counterparts for the complete set of equations used for atmospheric modeling as nicely demonstrated in [2]. Equations (2.27)–(2.29) represent the *momentum formulation* of the SWE.

It is possible to reformulate Eqs. (2.27)–(2.29) in terms of divergence D and relative vorticity ζ,

$$D = \frac{\partial u}{\partial x} + \frac{\partial v}{\partial y} \tag{2.31}$$

$$\zeta = \frac{\partial v}{\partial x} - \frac{\partial u}{\partial y} , \tag{2.32}$$

resulting in

$$\frac{dD}{dt} = -u\left(\frac{\partial D}{\partial x} + \frac{\partial \zeta}{\partial y}\right) - v\left(\frac{\partial D}{\partial y} - \frac{\partial \zeta}{\partial x}\right) - \nabla^2\left(\phi + \frac{u^2+v^2}{2}\right) + \zeta(f+\zeta) \tag{2.33}$$

$$\frac{d\zeta}{dt} = -(\zeta + f)\, D \tag{2.34}$$

$$\frac{d\phi}{dt} = -\Phi D\,. \tag{2.35}$$

Schemes based on the *vorticity-divergence* formulation are denoted as *Z-grid* schemes.

2.4.2 Geostrophic Adjustment of Z-Grid Schemes

In [48] some important constraints are listed for NWP schemes. Among others representing the process of geostrophic adjustment appropriately is one of them. An atmospheric situation that violates this equilibrium, will try to restore geostrophic balance by radiating inertia-gravity (IG) waves [21]. An inappropriate treatment of these waves could disturb the energy redistribution corresponding with the propagation of these waves.

In what follows we focus on the impact of the spatial discretization on the wave properties by using the 2D SWE. Due to its highly accurate calculation of derivatives, the spectral method guarantees an appropriate representation of geostrophic adjustment. But using finite differences, finite elements or finite volumes could seriously alter the wave behaviour as illustrated for example in [28].

For geostrophic adjustment studies one uses Eqs. (2.27)–(2.29) linearized around a reference state at rest with geopotential Φ ($u = u'$, $v = v'$, $\phi = \Phi + \phi'$):

$$\frac{\partial u'}{\partial t} = -\frac{\partial \phi'}{\partial x} + f v' \tag{2.36}$$

$$\frac{\partial v'}{\partial t} = -\frac{\partial \phi'}{\partial y} - f u' \tag{2.37}$$

$$\frac{\partial \phi'}{\partial t} = -\Phi\left(\frac{\partial u'}{\partial x} + \frac{\partial v'}{\partial y}\right)\,, \tag{2.38}$$

where u', v' and ϕ' represent perturbations to the reference state. By introducing a spatial discretization in Eqs. (2.36)–(2.38), assuming a wavelike behaviour for these

Table 2.2 Responses of the second order finite differences, linear finite-elements and spectral spatial discretization of a wave like Eq. (2.39)

	Second order FD	Linear FE	Spectral
p	1	$\frac{1}{3}\,(2 + cos(k\Delta x))$	1
p_x	$\frac{i}{\Delta x} sin(k\Delta x)$	$\frac{i}{\Delta x} sin(k\Delta x)$	ik
p_{xx}	$\frac{2}{(\Delta x)^2}\,(cos(k\Delta x) - 1)$	$\frac{2}{(\Delta x)^2}\,(cos(k\Delta x) - 1)$	$-k^2$

fields

$$x = \hat{X} e^{i(kx+ly+\omega t)} \text{ with } x = u', v' \text{ or } \phi' \,, \tag{2.39}$$

with $\hat{X}$ the amplitude, ω the frequency, k and l the wavenumber,[1] and exact time derivation, one finds:

$$i\omega p\hat{U} = -p_x\hat{\Phi} + fp\hat{V} \tag{2.40}$$

$$i\omega p\hat{V} = -p_y\hat{\Phi} - fp\hat{U} \tag{2.41}$$

$$i\omega p\hat{\Phi} = -\Phi\left(p_x\hat{U} + p_y\hat{V}\right) \,. \tag{2.42}$$

The spatial derivatives $\frac{\partial}{\partial x}$ and $\frac{\partial}{\partial y}$ are replaced by the responses p_x and p_y of the discretized derivative operator on a wavelike field like Eq. (2.39) [46]. Remark that even in the absence of a spatial derivation a response p is written; this is needed for example for Galerkin schemes with non orthogonal basis functions, e.g. the finite element scheme with bilinear basis functions. Table 2.2 shows the responses for second order finite differences, linear finite elements and spectral (Fourier) discretization.

The three equations Eqs. (2.40)–(2.42) define three wave solutions allowed by the discretized 2D SWE on a f-plane. One could solve this set of equations to find the frequency ω in function of the wavenumbers k and l (and thus wavelength) of the waves:

$$\omega_{ro} = 0 \tag{2.43}$$

$$\omega_{ig} = \pm\sqrt{f^2 - \frac{\Phi}{p^2}\left(p_x^2 + p_y^2\right)} \,. \tag{2.44}$$

The first frequency ω_{ro} corresponds with a so-called stationary Rossby wave. By filling in $\omega_{ro} = 0$ in Eqs. (2.40) and (2.41), one will retrieve the geostrophic relation between wind and geopotential. The inertia-gravity waves have a frequency ω_{ig}

[1] The wavenumbers are related to the wavelengths in the x and y-direction λ_x and λ_y by $k = \frac{2\pi}{\lambda_x}$ and $l = \frac{2\pi}{\lambda_y}$.

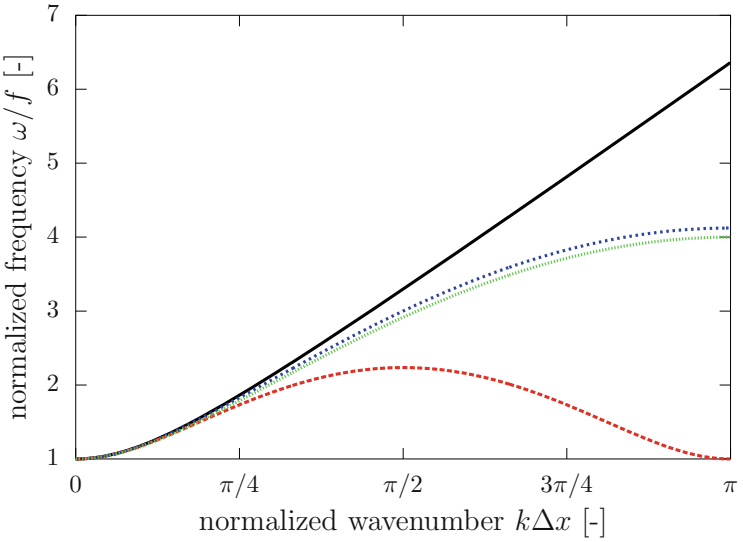

Fig. 2.1 1D dispersion relation ($l = 0$) of the IG-wave propagating in the positive x-direction for exact time derivatives and with $\sqrt{\Phi}/(f\Delta x) = 2$: spectral (*black*), A-grid second order FD (*red*), C-grid second order FD (*green*) and Z-grid second order FD (*blue*) spatial discretization

depending on the wavenumber. This is represented in Fig. 2.1 for the second order finite differences (red) and spectral (black) discretization. The spectral discretization completely agrees with the analytical dispersion relation. Indeed its responses in Table 2.2 agree with the exact responses. However, the second order finite difference dispersion relation is bending towards 0 for $k\Delta x$ going to π. This will correspond to a negative group velocity of the shortest scale waves, which is considered unacceptable, because it leads to rapidly propagating short scale noise in the opposite direction. It turns out that all finite difference and finite element discretization suffer from this problem independent of the order of the method. Apart from using a spectral method two other approaches that give appropriate geostrophic adjustment exist [48]:

1. Solving the SWE in momentum formulation on a *staggered* grid formulation where the velocity variables and geopotential are defined on different gridpoints. Arakawa proposed different staggered grids, but the *C-grid* is generally considered as the best one [28]. When the momentum formulation is solved on an unstaggered grid, it is called the *A-grid* approach. C-grids are operationally used in ICON and UM, see Table 2.1.
2. Applying the discretization on the Z-grid formulation of the SWE does also result in appropriate geostrophic adjustment as reported in [58]. This could be demonstrated by considering the version of Eqs. (2.33)–(2.35) linearized by

assuming $D = D'$, $\zeta = \zeta'$, $\phi = \Phi + \phi'$:

$$\frac{\partial D'}{\partial t} = -\nabla^2 \phi' + f\zeta' \tag{2.45}$$

$$\frac{\partial \zeta'}{\partial t} = -fD' \tag{2.46}$$

$$\frac{\partial \phi'}{\partial t} = -\Phi D' \ . \tag{2.47}$$

Wavelike solutions will now obey:

$$\omega_{ro} = 0 \tag{2.48}$$

$$\omega_{ig} = \pm \sqrt{f^2 - \frac{\Phi}{p}\left(p_{xx} + p_{yy}\right)} \ . \tag{2.49}$$

The dispersion curves of the second order finite differences combined with the C-grid and Z-grid discretization (green and blue in Fig. 2.1) do indeed no longer suffer from this bending. The previous geostrophic adjustment discussion was illustrated by using second order accurate space discretization. Increasing the order of accuracy does influence the dispersion relations but it does not change its qualitative properties, e.g. the negative group velocity will remain independent of the order of the method.

A good way to understand the practical impact of numerical dispersion behaviour consists of integrating a strongly ageostrophic initial state with different discretization schemes. The initial state

$$\phi'(x) = \phi_0 \ \mathrm{sgn}\,(x - x_0) \tag{2.50}$$

$$u'(x) = 0 \tag{2.51}$$

$$v'(x) = 0 \tag{2.52}$$

will evolve towards geostrophic balance by radiating away IG waves as explained in [21]. Figure 2.2 shows the results of the A-grid, C-grid and Z-grid second order finite difference simulations after 40 timesteps. An integration based on the spectral discretization is used as reference. In Fig. 2.2a it can be seen that all schemes result in IG waves propagating away from the discontinuity. Zooming in at $x = x_0$, Fig. 2.2b reveals that for the reference, the C-grid and Z-grid scheme the shortest waves are standing still in agreement with the flattening of ω for k going to $\frac{\Delta x}{\pi}$ in Fig. 2.1. For the A-grid scheme even waves with wavelengths around $4\Delta x$ are standing still again in agreement with the zero group velocity $\frac{\partial \omega}{\partial k}$ around $k\Delta x = \frac{\pi}{2}$ for the A-grid scheme in Fig. 2.1. Figure 2.2c zooms in on part of the domain where the long waves are dominant and reveals for the A-grid a superposition of very short scale noise on the longer waves again in agreement with Fig. 2.1. Thus the

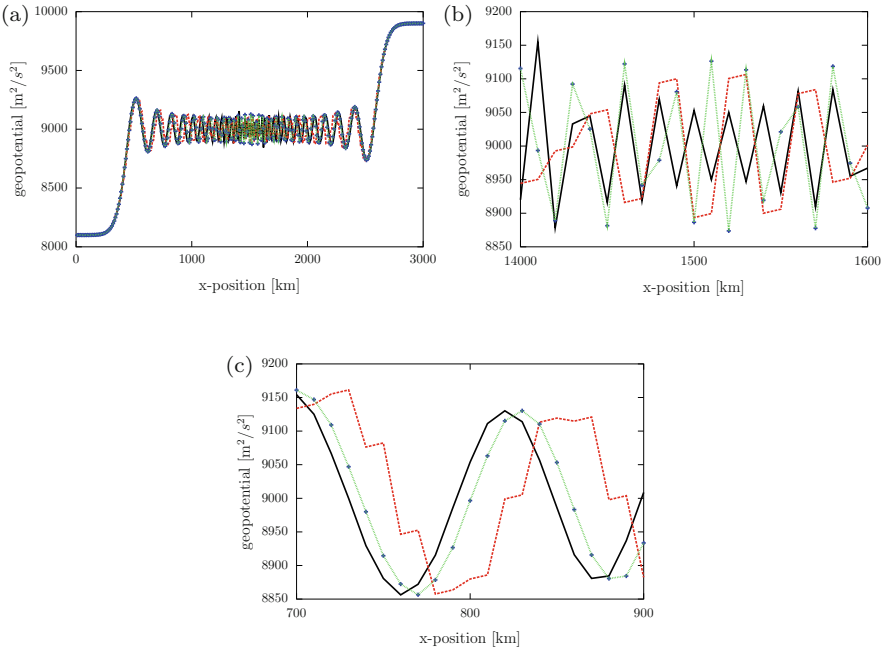

Fig. 2.2 Geopotential field $\Phi + \phi'$ of 1D geostrophic adjustment test for linearized SWE with $f = 0$, $\Delta t = 300\,\mathrm{s}$, $\Delta x = 10\,\mathrm{km}$, $\Phi = 9000\,\mathrm{m}^2/\mathrm{s}^2$ and $x_0 = 1500\,\mathrm{km}$. The legend is the same as in Fig. 2.1. Remark that the *green* C-grid and the *blue* Z-grid curve are nearly identical: (**a**) general overview (**b**) zoom in around x_0 and (**c**) zoom in at longer scale waves

fingerprint of the inappropriate A-grid dispersion is clearly visible in this numerical test. However, the relevance on operational weather forecasts, where diffusion, truncation, interpolations to departure points in SL schemes, physics,... influence the shortest scales, is unknown.

To study the propagation properties of Rossby modes, which are very important for synoptic meteorology, one needs to analyse the β-plane 2D SWE where the Coriolis parameter f is no longer constant. Neta showed that Z-grid schemes do represent this well [31].

The Z-grid and C-grid approach seem to be very similar based on Figs. 2.1 and 2.2. However, concerning wave properties the Z-grid has some advantages over the C-grid:

- For the evaluation of Coriolis terms the C-grid formulation needs some averaging and special care is needed to not impact the Rossby waves [53].
- The good IG-wave dispersion are unconditional for the Z-grid approach, but for C-grid they depend on the relative importance of the Coriolis terms. The dispersion curve of the C-grid for $\sqrt{\Phi}/(f\Delta x) = 0.1$ shows similar problems as the A-grid (not shown) [37].

2.4.3 SISL Z-Grid Schemes

In the previous subsection it was shown that both the C-grid and Z-grid approach result in appropriate dispersion. To exploit the long timesteps of the SISL approach, the staggered C-grid does need extra trajectory calculations compared to unstaggered methods. However, the Z-grid framework permits the use of a finite differences or finite element method on an unstaggered grid while retaining appropriate geostrophic adjustment. Contrary to the staggered formulations, the Z-grid method does not increase the computational cost of SL advection. The price to pay consists of solving a Poisson equation every timestep

$$\nabla^2 u = \frac{\partial D}{\partial x} - \frac{\partial \zeta}{\partial y} \tag{2.53}$$

$$\nabla^2 v = \frac{\partial \zeta}{\partial x} + \frac{\partial D}{\partial y} \tag{2.54}$$

to retrieve the wind velocities from the relative vorticity and divergence.

To circumvent the evaluation of the non-linear terms in the divergence equation Eq. (2.33), one could construct the discrete divergence equation from the SISL discretized momentum equations Eqs. (2.27) and (2.28) instead of discretizing Eq. (2.33). This formed the basis of the SISL Z-grid schemes proposed earlier, e.g. [47], [49] and [54].

This approach is surprisingly similar to what is done in the spectral SISL model of IFS/ARPEGE/ALADIN, which also uses divergence and vorticity although for a different reason. The wind vector components u and v are discontinuous at the poles and therefore not appropriate to use in a spherical harmonics decomposition [50]. This explains why spectral methods are often applied on equations formulated in terms of divergence and vorticity, which are true scalars [3].

As a result the organisation of the SISL Z-grid timestepping is similar to the SISL spectral timestepping (a good overview can be found in Table 2 of [52]) except for

- the elliptic problem and calculation of derivatives, which is done now in finite element space or with finite differences instead of in spectral space.
- the need to solve a non-trivial Poisson problem to retrieve the wind velocities from divergence and vorticity if finite elements or finite differences are used.

This analogy could be employed to use the IFS/ARPEGE/ALADIN model as a testbed to compare spectral SISL and finite differences or finite element Z-grid SISL schemes.

Recently, the importance of using the same operators at t^+ and t^0 in an implicit discretization was pointed at in [6], e.g. the operator $\mathcal{L}$ must be discretized in the same way at both times in Eq. (2.8). If not, the dispersion relation of the resulting IG waves may become unphysical for part of the spectrum.

At first sight this analysis could seem meaningless, why would one construct an asymmetric scheme? However, it is easy to introduce inadvertently asymmetries

especially if one needs some manipulation of equations. As one illustration, remember that in the Z-grid approach, to circumvent the evaluation of the extra non-linear terms in Eq. (2.33), the discrete divergence equation is constructed starting from the time discretized momentum equations Eqs. (2.27) and (2.28). For a two timelevel SISL scheme the discrete divergence equation writes as:

$$D^+ + \frac{\Delta t}{2}\nabla^2\phi^+ - \frac{f\Delta t}{2}\zeta^+ = \frac{\partial R_u}{\partial x} + \frac{\partial R_v}{\partial y} \tag{2.55}$$

with

$$R_u = u_D^0 - \frac{\Delta t}{2}\left(\frac{\partial \phi}{\partial x}\right)_D^0 + \frac{f\Delta t}{2}v_D^0 \tag{2.56}$$

$$R_v = v_D^0 - \frac{\Delta t}{2}\left(\frac{\partial \phi}{\partial y}\right)_D^0 - \frac{f\Delta t}{2}u_D^0. \tag{2.57}$$

To not overload the notations, the primes are omitted in the previous equations. Mind that for the complete model equations the right-hand sides of Eqs. (2.56) and (2.57) include: non-linear residuals evaluated explicitly, physics, SL trajectory computations and interpolations. In the spectral transform method this is done in gridpoint space, which is exactly identical to what is done in the Z-grid approach. The only difference resides in the method to calculate the derivatives in Eqs. (2.56) and (2.57).

Whereas the construction of Eq. (2.55) seems logical, an asymmetry has been introduced: at time t^+ the Laplacian $\nabla^2 = \frac{\partial^2}{\partial x^2} + \frac{\partial^2}{\partial y^2}$ of the geopotential appears whereas at that time t^0 first order derivatives are taken twice $\frac{\partial}{\partial x}\frac{\partial}{\partial x} + \frac{\partial}{\partial y}\frac{\partial}{\partial y}$. The previous does not result in an asymmetry if one evaluates the operators in a spectral way. However, for most spatial discretizations the operations will be no longer symmetrical as illustrated in Table 2.2, where $p_x^2 \neq p_{xx}$ for second order finite differences or linear finite elements.

In [6] two potential sources of asymmetries were distinguished in SI Z-grid schemes and solutions were proposed:

1. the evaluation of *the second order derivatives of the geopotential* as explained in the previous section. The symmetry could be restored by evaluating the Laplacian in the implicit part as taking twice first order derivatives. However, the scheme then comes down to an A-grid scheme and as explained earlier the geostrophic adjustment will be no longer appropriate. A better way to remove the asymmetry consists of using in Eqs. (2.56) and (2.57) first order derivatives for the geopotential of the form $\left(\frac{\partial}{\partial x}\right)^{-1}\frac{\partial^2}{\partial x^2}$ and $\left(\frac{\partial}{\partial y}\right)^{-1}\frac{\partial^2}{\partial y^2}$.
2. *the retrieval of the wind velocities* from divergence D and relative vorticity ζ. In Eq. (2.55) the divergence D^+ and relative vorticity ζ^+ in the implicit part correspond with $\frac{\partial u^0}{\partial x} + \frac{\partial v^0}{\partial y}$ and $\frac{\partial v^0}{\partial x} - \frac{\partial u^0}{\partial y}$ in the explicit part. One must construct

the diagnostic equations to calculate the wind in accordance with the previous and obtains:

$$\left(\frac{\partial}{\partial x}\frac{\partial}{\partial x}+\frac{\partial}{\partial y}\frac{\partial}{\partial y}\right)u=\frac{\partial D}{\partial x}-\frac{\partial \zeta}{\partial y} \tag{2.58}$$

$$\left(\frac{\partial}{\partial x}\frac{\partial}{\partial x}+\frac{\partial}{\partial y}\frac{\partial}{\partial y}\right)v=\frac{\partial D}{\partial y}+\frac{\partial \zeta}{\partial x}, \tag{2.59}$$

where the operator in the left hand side must be discretized as twice a first order derivative and not as 1 s order derivative.

Taking into account the previous recommendations results in a symmetric SISL Z-grid scheme. However, the solution described for the geopotential asymmetry, which was proposed in [6], is expensive because it necessitates another inversion problem. As shown hereafter, there is a more practical way to remove this asymmetry. The direct discretization of the divergence equation Eq. (2.33) is avoided due to the presence of extra non-linear terms compared to the momentum equations. However, none of these non-linear terms is related to the geopotential. This means that the following discretization should also work:

$$D_A^+ + \frac{\Delta t}{2}\nabla^2\phi_A^+ - \frac{f\Delta t}{2}\zeta_A^+ = \frac{\partial R_u}{\partial x}+\frac{\partial R_v}{\partial y}-\frac{\Delta t}{2}\nabla^2\phi_D^0 \tag{2.60}$$

with

$$R_u = u_D^0 + \frac{f\Delta t}{2}v_D^0 \tag{2.61}$$

$$R_v = v_D^0 - \frac{f\Delta t}{2}u_D^0\,. \tag{2.62}$$

In this way the Laplacian of the geopotential $\nabla^2\phi$ appears both at time t^+ and t^0 and symmetry is guaranteed.

To summarize, using the Z-grid approach in a SISL way with finite difference or finite elements does not seem to pose any problems except that care needs to be taken not to introduce asymmetries. The calculations needed during one timestep show an equal organization as in the currently used spectral SISL models. This modularity could be exploited to investigate further finite difference or finite element SISL Z-grid schemes within an existing NWP framework.

2.4.4 Computational Aspects

As explained in Sect. 2.2 the SI schemes gain efficiency by allowing long timestep integrations at the cost of solving an Helmholtz problem every timestep. Moreover, if the Z-grid approach is used, the wind retrieval from vorticity and divergence

adds two more Poisson problems [Eqs. (2.58) and (2.59)]. By using a spectral space discretization highly accurate solutions for these elliptic problems can be obtained efficiently. However, Fourier and Legendre transforms back and forth are needed every timestep. SI schemes combined with local spatial discretization methods like finite differences, finite elements,... do translate these elliptic equations into algebraic problems:

$$\mathbf{Ax} = \mathbf{B} \tag{2.63}$$

with $\mathbf{A}$ a $(N \times N)$ matrix, $\mathbf{x}$ the $(N \times 1)$ column vector of unknowns, $\mathbf{B}$ the $(N \times 1)$ column vector containing known values and N the number of unknowns. The local way to approximate derivative operators is reflected into the sparse structure of the matrix $\mathbf{A}$. In Fig. 2.3 the non-zero elements of the $\mathbf{A}$ matrices for the Helmholtz equation and the Poisson equation are shown for a second order finite difference discretization on a 10×10 grid (thus $N = 100$). It can be seen that in general every

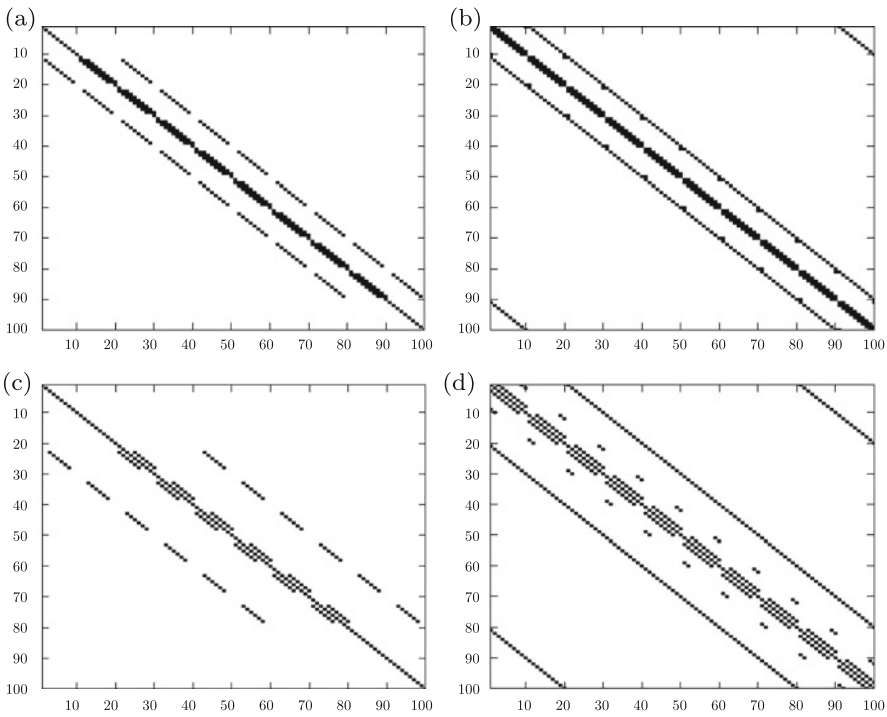

Fig. 2.3 Non-zero elements of the sparse $\mathbf{A}$ matrices for a 10×10 domain and for a second order finite difference discretization. On the *left* we have the matrices in the case that the boundaries values are imposed, at the *right* we have the matrices for periodic boundaries. (**a**) and (**b**) represent the structure of the $\mathbf{A}$ matrix corresponding with the Helmholtz problem Eq. (2.9) whereas (**c**) and (**d**) represent the Poisson problem Eqs. (2.58) and (2.59)

row consists of five non-zero elements, e.g. in the Helmholtz equation Eq. (2.9) the second order finite difference Laplacian in a point is indeed calculated based on the values in the point itself and its four closest neighbours. By employing higher order methods the matrix **A** will contain more non-zero values. Remark that the structure of **A** connects all gridpoints, this means that solution methods for this problem do also need communication.

The boundary conditions and the used grid will influence the exact form of the **A** matrices. Figure 2.3a and c represent the matrices obtained if one assumes that the boundary values are known already (e.g. LAM forecast with boundary values specified by a run on a larger domain) whereas for (b) and (d) periodic boundary conditions were assumed. It would be interesting to study the impact of the boundary conditions on the conditioning of the **A** matrices.

Assuming that 1 day global models will be used at 1 km resolution, the matrix dimension N is estimated by Müller and Scheichl [29] to be around 10^{10}. It is clear that scalable algorithms well adapted to the massively parallel computer architecture used will be needed to make SI NWP feasible on these scales. Müller and Scheichl [29] recently presented an overview of efficient and scalable solution methods used for the elliptical problems resulting from a SI time discretization in atmospheric modeling. Contrary to the direct spectral solution of elliptic problems, local spatial discretization methods will in general need iterative solvers. Two main solver types could be distinguished and both are used in NWP: Krylov and multigrid solvers. It seems that some of these solution methods scale reasonably well as demonstrated for example by Notay and Napov [32], which tested a particular multigrid solver for Poisson problems on machines consisting of up to 373,000 cores. The promising conclusion in [29] stated that (semi-) implicit methods do not limit scalability.

2.5 Conclusion and Outlook

A non-exhaustive overview of both temporal and spatial discretization schemes used in NWP is presented. It is reviewed that the transform method made the combination of a spectral spatial discretization and a SISL time scheme very attractive. The spectral SISL scheme forms today the fundament of the dynamical core of some of the main European models.

Some claim this approach may become less attractive for scientific and/or technological reasons. To investigate this, a testbed to compare spectral and local methods within a code organization otherwise identical is necessary. It is shown that the Z-grid approach could be employed to introduce a local method, finite differences or finite elements, within the existing timestep framework of the spectral SISL models. The only differences would be the Helmholtz solver, the derivative calculations and the extra Poisson solver. This modular approach could allow a scientific comparison between spectral and local spatial discretization methods.

Two important issues related to the use of the SISL Z-grid scheme were discussed:

1. To obtain within a SI time discretization appropriate geostrophic adjustment, special care must be taken to maintain symmetry between the explicit and implicit part of the calculations. This constraint is valid for all SI schemes but is shown to become particularly relevant for Z-grid schemes because this method needs some manipulations of equations to construct the discretized equations.
2. The SISL Z-grid approach will necessitate to solve both a Poisson and Helmholtz problem every timestep. To be operationally attractive, it is thus crucial to develop an efficient sparse matrix solver for elliptic problems that scales well on massively parallel machines. Some recent studies showed promising results.

Finally, it would be valuable to understand the impact and thus importance of the quality of geostrophic adjustment within a real model test. The effect of poor geostrophic adjustment is well known for simplified equation sets. However, its impact on real atmospheric modeling is unknown. As an example the A-grid is generally considered as not appropriate in NWP. However, only the shortest waves show an inappropriate propagation. One could argue that the physics and not the dynamics is dominant on these scales. If this would turn out to be true local discretization methods combined with SISL on the A-grid could be an alternative.

The authors believe that the Z-grid approach is worth more investigations because it may help us in better understanding some scientific and technological questions and forms a promising alternative for current day spectral SISL dynamical cores.

Acknowledgements The authors gratefully acknowledge the anonymous reviewer for his/her comments and suggestions, which substantially improved the manuscript.

References

1. ALADIN International Team: The ALADIN project: mesoscale modelling seen as a basic tool for weather forecasting and atmospheric research. WMO Bull. **46**, 317–324 (1997)
2. Arakawa, A.: Adjustment mechanisms in atmospheric models. J. Meteorol. Soc. Jpn. **75B**, 155–179 (1997)
3. Bourke, W.: An efficient, one-level, primitive-equation spectral model. Mon. Weather Rev. **100**, 683–691 (1972)
4. Boyd, J.P.: Chebyshev and Fourier Spectral Methods, p. 688. Dover, New York (2001)
5. Brown, A., Milton, S., Cullen, M., Golding, B., Mitchell, J., Shelly, A.: Unified modeling and prediction of weather and climate. A 25-year journey. Bull. Am. Meteorol. Soc. **93**, 1865–1877 (2012)
6. Caluwaerts, S., Degrauwe, D., Termonia, P., Voitus, F., Beńard, P., Geleyn, J.F.: Importance of temporal symmetry in spatial discretization for geostrophic adjustment in semi-implicit Z-grid schemes. Q. J. R. Meteorol. Soc. **141**, 128–138 (2015)
7. Charney, J.G., Fjörtoft, R., Von Neumann, J.: Numerical integration of the barotropic vorticity equation. Tellus **2**, 237–254 (1950)
8. Coiffier, J.: Fundamentals of Numerical Weather Prediction, p. 340. Cambridge University Press, Cambridge (2011)

9. Côté, J., Staniforth, A.: An accurate and efficient finite-element global model of the shallow water equations. Mon. Weather Rev. **118**, 2707–2717 (1990)
10. Côté, J., Gravel, S., Méthot, A., Patoine, A., Roch, M., Staniforth, A.: The operational CMC-MRB global environmental multiscale (GEM) model. Part 1: design considerations and formulation. Mon. Weather Rev. **126**, 1373–1395 (1998)
11. Cotter, C.J., Shipton, J.: Mixed finite elements for numerical weather prediction. J. Comput. Phys. **231**, 7076–7091 (2012)
12. Courant, R., Friedrichs, K.O., Lewy, H..: Uber die Partielen Differenzengleichungen der Mathematischen Physik. Math. Ann. **100**, 32–74 (1928)
13. Davies, T., Staniforth, A., Wood, N., Thuburn, J.: Validity of anelastic and other equation sets as inferred from normal-mode analysis. Q. J. R. Meteorol. Soc. **129**, 2761–2775 (2003)
14. Davies, T., Cullen, M., Malcolm, A., Mawson, M., Staniforth, A., White, A., Wood, N.: A new dynamical core for the Met Office's global and regional modelling of the atmosphere. Q. J. R. Meteorol. Soc. **131**, 1759–1782 (2005)
15. Dennis, J., Edwards, J., Evans, K., Guba, O., Lauritzen, P., Mirin, A., St-Cyr, A., Taylor, M., Worley, P.: CAM-SE: A scalable spectral element dynamical core for the community atmosphere model. Int. J. High Perform. Appl. **26**, 74–89 (2011)
16. Durran, D.R.: Numerical Methods for Fluid Dynamics with applications to Geophysics, p. 516. Springer, Berlin (2010)
17. Durran, D., Blossey, P.: Implicit-explicit multistep methods for fast-wave-slow-wave problems. Mon. Weather Rev. **140**, 1307–1325 (2012)
18. Eliasen, E., Machenhauer, B., Rasmussen E.: On a numerical method for integration of the hydrodynamical equations with a spectral representation of the horizontal fields. Report no 2. Institut for Teoretisk Meteorologi, University of Copenhagen (1970)
19. Fjortoft, R.: On a numerical method of integrating the barotropic vorticity equation. Tellus **4**, 179–194 (1952)
20. Godunov, S.K.: A difference scheme for numerical computation of discontinuous solutions of equations in fluid dynamics. Mat. Sb. **47**, 271 (1959)
21. Holton, J.R.: An Introduction to Dynamic Meteorology, p. 535. Elsevier, Amsterdam/Academic, New York (2004)
22. Hortal, M.: The development and testing of a new two-time level semi-Lagrangian scheme (SETTLS) in the ECMWF forecast model. Q. J. R. Meteorol. Soc. **128**, 1671–1687 (2002)
23. Hortal, M., Simmons, A.J.: Use of reduced Gaussian grids in spectral models. Mon. Weather Rev. **119**, 1057–1074 (1991)
24. Hurrell, J., Meehl, G., Bader, D., Delworth, T., Kirtman, B., Wielicki, B.: A unified modeling approach to climate system prediction. Bull. Am. Meteorol. Soc. **90**, 1819–1832 (2009)
25. Kwizak, M., Robert, A.: A semi-implicit scheme for grid point atmospheric models of the primitive equations. Mon. Weather Rev. **99**, 32–36 (1971)
26. Lin, S.: A vertically Lagrangian finite-volume dynamical core for global models. Mon. Weather Rev. **132**, 2293–2307 (2004)
27. Majewski, D., Liermann, D., Prohl, P., Ritter, B., Buchhold, M., Hanisch, T., Paul G., Wergen W., Baumgardner, J.: The operational global isocahedral-hexagonal gridpoint model GME: description and high-resolution tests. Mon. Weather Rev. **130**, 319–338 (2002)
28. Mesinger, F., Arakawa, A.: Numerical methods used in atmospheric models. GARP Publications, Series No. 17 1. World Meteorological Organisation, Geneva (1976)
29. Müller, E., Scheichl R.: Massively parallel solvers for elliptic partial differential equations in numerical weather and climate prediction. Q. J. R. Meteorol. Soc. **140**, 2605–2624 (2014)
30. Nair, D., Thomas, S., Loft, R.: A discontinuous Galerkin global shallow water model. Mon. Weather Rev. **133**, 876–888 (2005)
31. Neta, B.,Williams, R.: Rossby wave frequencies and group velocities for finite element and finite difference approximations to the vorticity-divergence and the primitive forms of the shallow water equations. Mon. Weather Rev. **117**, 1439–1457 (1989)

32. Notay, Y., Napov, A.: A massively parallel solver for discrete Poisson-like problems. J. Comput. Phys. **281**, 237–250 (2015)
33. Orszag, S.A.: Transform method for calculation of vector-coupled sums: application to the spectral form of the vorticity equation. J. Atmos. Sci. **27**, 890–895 (1970)
34. Outline of the operational numerical weather prediction at the Japan Meteorological Agency. http://www.jma.go.jp/jma/jma-eng/jma-center/nwp/outline-nwp/index.htm (2007)
35. Qaddouri, A., Lee, V.: The Canadian global environmental multiscale model on the Yin-Yang grid system. Q. J. R. Meteorol. Soc. **137**, 1913–1926 (2011)
36. Richardson, L.F.: Weather Prediction by Numerical Process, p. 236. Cambridge University Press, Cambridge (1922)
37. Randall, D.: Geostrophic adjustment and the finite-difference shallow water equations. Mon. Weather Rev. **122**, 1371–1377 (1994)
38. Ritchie, H.: Application of the semi-Lagrangian method to a spectral model of the shallow water equations. Mon. Weather Rev. **116**, 1587–1598 (1988)
39. Ritchie, H.: Implementation of the semi-Lagrangian method in a high resolution version of the ECMWF forecast model. Mon. Weather Rev. **123**, 489–514 (1994)
40. Ritchie, H., Beaudoin, C.: Approximations and Sensitivity Experiments with a Baroclinic Semi-Lagrangian Spectral Model. Mon. Weather Rev. **122**, 2391–2399 (1994)
41. Robert, A.: The integration of a low order spectral form of the primitive meteorological equations. J. Meteorol. Soc. Jpn. **44**, 237–244 (1966)
42. Robert, A.: The integration of a spectral model of the atmosphere by the implicit method. Proc.of WMO/IUGG Symp. on NWP (1969)
43. Robert, A.: A stable numerical integration scheme for the primitive meteorological equations. Atmosphere-Ocean **19**, 35–46 (1981)
44. Sawyer, J.S.: A semi-Lagrangian method of solving the vorticity advection equation. Tellus **4**, 336–342 (1963)
45. Simmons, A., Hoskins B., Burridge, D.: Stability of the semi-implicit method of time integration. Mon. Weather Rev. **106**, 405–412 (1978)
46. Staniforth, A., Mitchell, H.: A semi-implicit finite-element barotropic model. Mon. Weather Rev. **105**, 154–169 (1977)
47. Staniforth, A., Temperton, C.: Semi-implicit semi-Lagrangian integration schemes for a barotropic finite-element regional model. Mon. Weather Rev. **114**, 2078–2090 (1986)
48. Staniforth, A., Thuburn, J.: Horizontal grids for global weather and climate prediction models: a review. Q. J. R. Meteorol. Soc. **138**, 1–26 (2012)
49. Temperton, C., Staniforth, A.: An efficient two-time level semi-Lagrangian semi-implicit integration scheme. Q. J. R. Meteorol. Soc. **113**, 1025–1039 (1987)
50. Temperton, C.: On scalar and vector transform methods for global spectral models. Mon. Weather Rev. **119**, 1303–1307 (1991)
51. Temperton, C., Hortal, M., Simmons, A.: A two-time-level semi-Lagrangian global spectral model. Q. J. R. Meteorol. Soc. **127**, 111–127 (2001)
52. Termonia, P., Hamdi, R.: Stability and accuracy of the physics-dynamics coupling in spectral models. Q. J. R. Meteorol. Soc. **133**, 1589–1604 (2007)
53. Thuburn, J., Staniforth, A.: Conservation and linear Rossby mode dispersion on the spherical C-grid. Mon. Weather Rev. **132**, 641–653 (2004)
54. Tolstykh, M.: Vorticity-divergence semi-Lagrangian shallow water model of the sphere based on compact finite differences. J. Comput. Phys. **179**, 180–200 (2002)
55. Tolstykh, M., Shashkin, V.: Vorticity-divergence mass-conserving semi-Lagrangian shallow-water model using the reduced grid on the sphere. J. Comput. Phys. **231**, 4205–4233 (2012)
56. Wang, H., Halpern, P., Douglas, J., Dupont, T.: Numerical solutions of the one-dimensional primitive equations using Galerkin approximations with localized basis functions. Mon. Weather Rev. **100**, 738–746 (1972)
57. Wedi, N.: Increasing horizontal resolution in numerical weather prediction and climate simulations: illusion or panacea. Philos. Trans. R. Soc. **372**, 1–12 (2014)

58. Williams, R.T.: On the formulation of finite-element prediction models. Mon. Weather Rev. **109**, 463–466 (1981)
59. Williamson, D.: The evolution of dynamical cores for global atmospheric models. J. Meteorol. Soc. Jpn. **85B**, 241–269 (2007)
60. Zangl, G., Reinert, D., Ripodas, P., Baldauf, M.: The ICON (ICOsahedral Non-hydrostatic) modelling framework of DWD and MPI-M: description of the non-hydrostatic dynamical core. Q. J. R. Meteorol. Soc. **141**, 563–579 (2015)

Chapter 3
Turbulence Modeling Using Fractional Derivatives

Béla J. Szekeres

Abstract We propose a new two-dimensional turbulence model in this work. The main idea of the model is that the shear stresses are considered to be random variables and we assume that their differences with respect to time are Lévy-type distributions. This is a generalization of the classical Newton's law of viscosity. We tested the model on the classical Backward Facing Step benchmark problem. The simulation results are in a good accordance with real measurements.

Keywords Backward facing step • Fractional derivative • Turbulence

3.1 Introduction

Turbulence is a velocity fluctuation of the mean flow in fluid dynamics. For this phenomenon there is no any exact definition, we can hardly quantify it and its numerical simulation is also challenging. Its study has a long history, it is enough to refer to the famous wish of Albert Einstein: "After I die, I hope God will explain turbulence to me."

Our study is based on the Navier–Stokes equations as a widely accepted model for fluid dynamics. Starting from this point there are many variant ways to modeling this phenomenon, for example the direct numerical simulation, the large eddy simulation and modeling with the Reynolds averaged equations. We propose here a new two-dimensional model and a new way for modeling turbulence. We consider the quantity obtained from the Newton's law of viscosity as a special expected value for the shear stresses. According to our approach, in the simulation we should take into account not only the actual velocity field but also the history of the velocity field to calculate this expected value.

We generalize the Navier–Stokes equation, using this hypothesis and get a two-dimensional probabilistic–deterministic model.

B.J. Szekeres (✉)
Department of Applied Analysis and Computational Mathematics, Eötvös Loránd University, Budapest, Hungary

MTA-ELTE Numerical Analysis and Large Networks Research Group, Budapest, Hungary
e-mail: szbpagt@cs.elte.hu

A. Bátkai et al. (eds.), *Mathematical Problems in Meteorological Modelling*,
Mathematics in Industry 24, DOI 10.1007/978-3-319-40157-7_3

3.2 Preliminaries

The Navier–Stokes equations for incompressible fluids in two space dimensions can be given as

$$\frac{\partial v_x}{\partial t} + v_x\frac{\partial v_x}{\partial x} + v_y\frac{\partial v_x}{\partial y} = \frac{1}{\rho}\Big(\frac{\partial \sigma_x}{\partial x} + \frac{\partial \tau_{yx}}{\partial y}\Big) \tag{3.1}$$

$$\frac{\partial v_y}{\partial t} + v_x\frac{\partial v_y}{\partial x} + v_y\frac{\partial v_y}{\partial y} = \frac{1}{\rho}\Big(\frac{\partial \sigma_y}{\partial x} + \frac{\partial \tau_{xy}}{\partial y}\Big) \tag{3.2}$$

$$\frac{\partial v_x}{\partial x} + \frac{\partial v_y}{\partial y} = 0. \tag{3.3}$$

Here the terms σ_x, σ_y denote the tensile stresses, τ_{xy}, τ_{yx} denote the shear stresses, ρ the fluid density and $\mathbf{v} = (v_x, v_y)$ the velocity vector. According to the Newton's law of viscosity we additionally have

$$\tau_{ij} = \mu\Big(\frac{\partial v_j}{\partial i} + \frac{\partial v_i}{\partial j}\Big), \quad i,j \in \Big\{x,y\Big\}. \tag{3.4}$$

The tensile stresses are given as

$$\sigma_i = -P + \mu\tau_{ii} = -P + 2\mu\frac{\partial v_i}{\partial i}, \quad i \in \Big\{x,y\Big\}. \tag{3.5}$$

Let us introduce the notations $p := \frac{P}{\rho}$ for the pressure and $\nu := \frac{\mu}{\rho}$ for the kinematic viscosity. Using (3.4), (3.5) in (3.1) we can make it explicit, to obtain the classical Navier–Stokes equations

$$\frac{\partial v_x}{\partial t} + v_x\frac{\partial v_x}{\partial x} + v_y\frac{\partial v_x}{\partial y} = -\frac{\partial p}{\partial x} + \nu\Delta v_x \tag{3.6}$$

$$\frac{\partial v_y}{\partial t} + v_x\frac{\partial v_y}{\partial x} + v_y\frac{\partial v_y}{\partial y} = -\frac{\partial p}{\partial y} + \nu\Delta v_y \tag{3.7}$$

$$\text{div } \mathbf{v} = 0. \tag{3.8}$$

3.3 Results

3.3.1 The Fractional Newton's Law of Viscosity

We first assume in our model that the stear stresses are random variables. The physical interpretation of this assumption is that by measuring we can observe an average viscosity only. It is also assumed that the number of small changes in the

shear stresses compared to the number of large changes is not so high: the stress is supposed to arise from a Lévy type distribution. Note that a similar observation was made by Mandelbrot [7] by examining the cotton prices over a certain time period. In this subsection we give a mathematical formalization of the above model using fractional order differentiation.

To work with fractional order differentiation we need the following definition (see, e.g., [10]).

Definition 3.1 For each $q \in [0, 1)$ and $a \in \mathbb{R}$ we say that f is q-times differentiable if the following limit exists:

$$\frac{1}{\Gamma(1-q)} \frac{\partial}{\partial t} \int_a^t \frac{f(s)}{(t-s)^q} \, \mathrm{ds} =: {}_a D^q f(t). \tag{3.9}$$

In [10] the authors investigated the accuracy of the approximation of (3.9):

$${}_a D^q f(t) \approx [{}_a D_h^q] f(t) := \Big(\frac{t-a}{N}\Big)^{-q} \sum_{k=0}^{N-1} \binom{q}{k} (-1)^k f\big(t - k\frac{t-a}{N}\big). \tag{3.10}$$

Using the fractional order derivatives in (3.9) we introduce the following generalization of (3.4):

$$\tau_{ij}(t, \cdot) = \nu \Big[{}_{t-T} D^q \Big(\frac{\partial v_j}{\partial i}(t, \cdot) + \frac{\partial v_i}{\partial j}(t, \cdot) \Big) \Big], \quad 0 \le q < 1, \quad i, j \in \Big\{ x, y \Big\}. \tag{3.11}$$

We modify the equations for the tensile stresses accordingly to obtain

$$\sigma_i(t, \cdot) = -p(t, \cdot) + \tau_{ii}(t, \cdot), \quad i \in \Big\{ x, y \Big\}. \tag{3.12}$$

Using the notation in (3.9) and substituting (3.11) and (3.12) into (3.6) we arrive at the fractional Navier–Stokes equations

$$\frac{\partial v_x}{\partial t} + v_x \frac{\partial v_x}{\partial x} + v_y \frac{\partial v_x}{\partial y} = -\frac{\partial p}{\partial x} + {}_{t-T} D^q \Big(\nu \Delta v_x \Big) \tag{3.13}$$

$$\frac{\partial v_y}{\partial t} + v_x \frac{\partial v_y}{\partial x} + v_y \frac{\partial v_y}{\partial y} = -\frac{\partial p}{\partial y} + {}_{t-T} D^q \Big(\nu \Delta v_y \Big) \tag{3.14}$$

$$\operatorname{div} \mathbf{v} = 0. \tag{3.15}$$

We call α as a stability parameter and T the fluid memory. These parameters specify the Lévy type distribution, which describes the wobbling of the shear stresses.

We need the following two theorems, the second one is discussed in [8] and we proved the first one in the Appendix. For this we recall that for $\alpha \in \mathbb{R}$ and $j \in \mathbb{N}$ we define $\binom{\alpha}{j} = \frac{\alpha(\alpha-1)\ldots(\alpha-j+1)}{j!}$.

Theorem 3.1 *For each $\alpha \in \mathbb{C}$ and $h = 1/N$ the following is true:*

$$\lim_{N\to\infty} \sum_{j=0}^{N-1} \binom{\alpha}{j} \frac{(-1)^j}{h^\alpha} = \frac{1}{\Gamma(1-\alpha)}. \tag{3.16}$$

Theorem 3.2 *For any $\alpha \in [0,1)$ and $j \in \mathbb{Z}^+$ we have $\binom{\alpha}{j}(-1)^j < 0$ and the following equality holds:*

$$\sum_{j=0}^{\infty} \binom{\alpha}{j} (-1)^j = 0. \tag{3.17}$$

Let $f : \mathbb{R} \to \mathbb{R}$ α-times differentiable by means of Definition 3.1 and it is approximated using (3.10). For simplicity we assume that $T := 1$, then the following estimations are valid

$$\begin{aligned} {}_{t-1}D^\alpha f(t) &\approx \Big(\frac{1}{N}\Big)^{-\alpha} \sum_{k=0}^{N-1} \binom{\alpha}{k} (-1)^k f\big(t - \frac{k}{N}\big) \\ &\approx \Big(\frac{1}{N}\Big)^{-\alpha} \sum_{k=1}^{N-1} \binom{\alpha}{k} (-1)^{k+1} \Big[f(t) - f\big(t - \frac{k}{N}\big)\Big] \\ &= \frac{1}{\Gamma(1-\alpha)} \sum_{k=1}^{N-1} \Gamma(1-\alpha) \Big(\frac{1}{N}\Big)^{-\alpha} \binom{\alpha}{k} (-1)^{k+1} \Big[f(t) - f\big(t - \frac{k}{N}\big)\Big]. \end{aligned} \tag{3.18}$$

Let

$$p_k = \Gamma(1-\alpha) \Big(\frac{1}{N}\Big)^{-\alpha} \binom{\alpha}{k} (-1)^{k+1}. \tag{3.19}$$

According to Theorem 3.2 we have $p_k > 0$, and Theorem 3.1 gives that

$$\lim_{N\to\infty} \sum_{k=1}^{N-1} p_k = 1. \tag{3.20}$$

Consequently, the values $\{p_k\}_{k\in\mathbb{N}}$ define a probability density function, and the limit distribution is Lévy type. We can also conclude that the generalization (3.11) of the Newton's law can be considered as the expected value of the variation of the shear stresses, where the distribution function is defined by the values p_k. This serves as a motivation for our model.

Note that the standard Newton's law corresponds to the case $q = 0$ in (3.11), which can be interpreted as the distribution of the variation is Gaussian, and then the shear stresses are independent from the earlier stress values.

3.3.2 The Algorithm

To discretize (3.13) we use the method of the work [4], which is a finite difference approximation on a staggered grid. The semidiscretization results then in the following ODE:

$$\begin{aligned} \mathbf{u}_t + L_h(\mathbf{u})\mathbf{u} + \operatorname{grad}_h p &= \mathbf{0} \\ \operatorname{div}_h \mathbf{u} &= 0, \end{aligned} \tag{3.21}$$

where $L_h(\mathbf{u}) = D_h(\mathbf{u}) - \nu[{}_{t-T}D_h^{\alpha}]\Delta$, $D_h(\mathbf{u})\mathbf{u}$ is the approximation of the nonlinear terms, div_h is the discrete divergence, grad_h is the discrete gradient operator, ν is the viscosity parameter and $[{}_{t-T}D_h^{\alpha}]$ defined in (3.10).

We solve then Eq. (3.21) using a simple predictor-corrector algorithm. We start from an initial velocity field $\mathbf{u}^0$ and an initial value for the pressure and apply the time step τ. The main steps of the algorithm are the following.

1. Solve the first equation in (3.21) for $\mathbf{w}$:

$$\frac{\mathbf{w} - \mathbf{u}^n}{\tau} + L_h(\mathbf{u}^n)\mathbf{w} + \operatorname{grad}_h p^n = 0. \tag{3.22}$$

2. Solve the following equation for q:

$$\operatorname{div}_h \operatorname{grad}_h q = \frac{1}{\tau}\mathbf{w}. \tag{3.23}$$

3. Compute the pressure values $p^{n+1} = q + p^n$.
4. Compute the velocity vector $\mathbf{u}^{n+1} = \mathbf{w} - \tau \operatorname{grad}_h q$.

3.3.3 The Test Problem

To test our simulation we use the real measurements of the work [6] and we also compare our results with other numerical predictions. We choose a classical benchmark problem, the Backward Facing Step. The geometric setup of this problem is shown in Fig. 3.1. We set the fluid memory T $= 2.5$ s, and the time step $\tau = 0.005$ s. It is sufficient to assume this fluid memory because for N $= 500$ and $\alpha = 0.2$ we have $1 - \sum_{k=1}^{N} p_k = 2 \cdot 10^{-4}$.

The fluid flows into the channel on the upper part of the left hand side of the channel and it flows out at the right hand side. We set the geometric parameters to $H = 1$ cm, $L = 10$ cm, $h = 0.5$ cm and $\nu = \frac{2}{3} \cdot 10^{-5}\ \frac{\mathrm{m}^2}{s}$ and use the the Reynolds number $\mathrm{Re} = \frac{4h v_{\max}}{3\nu}$. With these the exact boundary conditions are the following:

- $x = 0, y \in [H - h, h]$ (inflow section): $v_y = 0$ and $v_x = -\frac{4(H-y)(H-h-y)}{h^2} v_{\max}$,

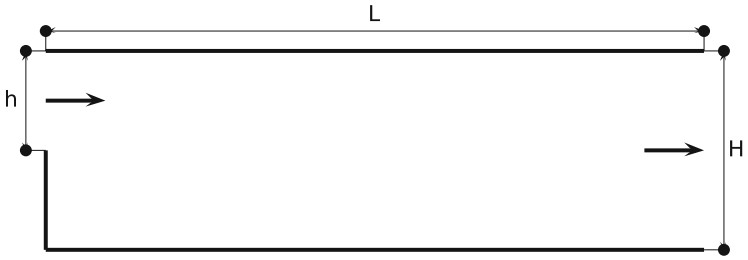

Fig. 3.1 The Backward Facing Step problem

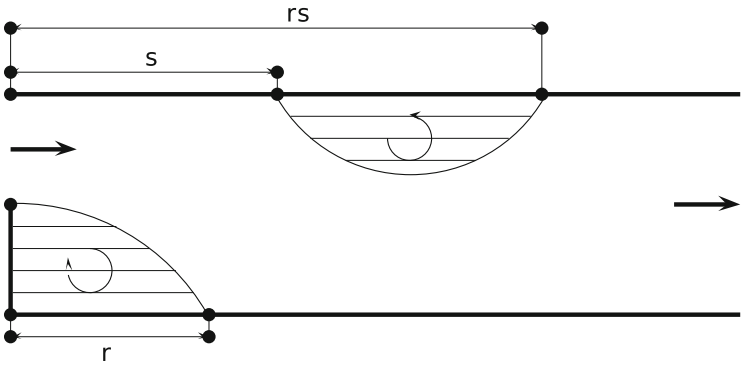

Fig. 3.2 Reattachment lengths r, s and rs. The subdomains of the computational domain with $v_x < 0$ are shaded

- $x = L$ (outflow section): $\frac{\partial v_x}{\partial x} = \frac{\partial v_y}{\partial x} = 0$ and $p = 0$,
- on the remaining part of the boundary: $v_x = v_y = 0$.

We notice that one can take also a channel before the inlet stage, because it has some effect on the velocity field [1]. Focusing to the simplest version of the problem we do not use this inlet channel. Whenever the problem seems to be easy, many recent calculations underpredict certain well-measurable quantities, the location of the so-called reattachment lengths r, s and rs. The corresponding error rate is about $5 - 15\,\%$. For a visualization of the reattachment lengths we refer to Fig. 3.2.

An important advance of our model is that we can predict this quantity very precisely for different Reynolds number by choosing the parameter α properly. We made some comparison with other predictions and summarized the results in Tables 3.1, 3.2, and 3.3.

For the computations we divided the domain into 300×30 elementary cells. Implementing then the algorithm in Sect. 3.3.2 we found that the numerical method converges to a stationary solution. The simulated time was 30 s using a number of 6000 time steps both for the Eqs. (3.6) and (3.13).

We also tested our model on a similar benchmark problem using a different parameter set $H = 1\,\text{cm}$, $L = 12\,\text{cm}$, $h = 0.6\,\text{cm}$ and $\nu = 8 \cdot 10^{-6}\,\frac{\text{m}^2}{\text{s}}$, with the

Table 3.1 Summarized results for the reattachment lengths with Re = 800

	Experimental results		Computed results					
	Length on	Exp. [6]	Lee, Mateescu [6]	Gartling [3]	Kim, Moin [5]	Sohn [9]	Present study, NNS	Present study, FNS, ($\alpha = 0.06$)
Lower wall	r/H	6.45	6.0	6.1	6.0	5.8	6.11	6.43
Upper wall	s/H	5.15	4.80	4.85	–	–	5.08	5.33

FNS fractional Navier–Stokes, *NNS* classical Navier–Stokes

Table 3.2 Numerical results for the reattachment lengths with Re = 1000

	Experimental results		Computed Results	
	Length on	Exp. [6]	Present study, NNS	Present study, FNS, ($\alpha = 0.17$)
Lower wall	r/H	7.5	6.68	7.46
Upper wall	s/H	6.5	5.51	6.16

FNS fractional Navier–Stokes, *NNS* classical Navier–Stokes

Table 3.3 Numerical results for the reattachment lengths with Re = 1200

	Experimental results		Computed results	
	Length on	Exp. [6]	Present study, NNS	Present study, FNS, ($\alpha = 0.24$)
Lower wall	r/H	8.5	7.16	8.50
Upper wall	s/H	7.5	5.93	7.06

FNS fractional Navier–Stokes, *NNS* classical Navier–Stokes

Table 3.4 Summarized results for the reattachment lengths with Re = 2425

	Reattachment length ratio r/H					
Reynolds number	Exp. [2]	$k-\epsilon$ [2]	RNG $k-\epsilon$ [2]	SA [2]	SST [2]	Present study, FNS, $\alpha = 0.4$
2425	9.2	6.3	6.93	8.54	9.4	9.06

FNS fractional Navier–Stokes, *NNS* classical Navier–Stokes

Reynolds number Re = 2425. We made some comparison with other predictions with different turbulence models and measurements [2] and summarized the results in Table 3.4.

3.4 Conclusion

We introduced a new turbulence model in this work by assuming that the variations of shear stresses are random variables and their distributions are Lévy-type. In this way we use two new parameter for the governing equations: the fluid memory and a stability parameter. The most important task in the practical computations was to choose correctly the stability parameter, while the length of the memory is not so

important in numerical calculations. We could predict well the reattachment lengths in a classical benchmark problem by a proper setting of the stability parameter, this we made with a simple trial and error procedure by hand.

We observed that for small Reynolds numbers the choice of parameter $\alpha = 0$, which corresponds to the classical Navier–Stokes equations, gives good accordance with the real measurements. If only the Reynolds number is increased and consequently, the flow becomes turbulent, the parameter α has to be also increased. For example, if $\mathrm{Re} = 800$, we found that the choice $\alpha = 0.06$ is optimal for the simulation. This corresponds to the fact, that turbulent flows can be described rather statistically than explicitly, and in the long run we can consider the present model also a statistical one.

Our future aim is to find experimentally the values α corresponding to the Reynolds number. It would also be important to compare this result with numerical experiments on further test problems.

Acknowledgements The author acknowledges the financial support of the Hungarian National Research Fund OTKA (grant K112157) and the useful advice for Ferenc Izsák and Gergő Nemes.

Appendix

Proof (Theorem 3.1) Let $\alpha \in \mathbb{C}$ be any fixed complex number. Let x be a real or complex number such that $|x| < 1$, then

$$(1-x)^{\alpha} = \sum_{N=0}^{\infty} (-1)^N \binom{\alpha}{N} x^N. \tag{3.24}$$

It is easy to see that

$$(1-x)^{\alpha-1} = \frac{(1-x)^{\alpha-1}}{1-x} = \sum_{N=0}^{\infty} \left(\sum_{k=0}^{N} (-1)^k \binom{\alpha}{k} \right) x^N. \tag{3.25}$$

On the other hand

$$(1-x)^{\alpha-1} = \sum_{N=0}^{\infty} (-1)^N \binom{\alpha-1}{N} x^N, \tag{3.26}$$

whence equating the coefficients of x^{N-1}, we obtain

$$\begin{aligned} \sum_{k=0}^{N-1} (-1)^k \binom{\alpha}{k} &= (-1)^{N-1} \binom{\alpha-1}{N-1} \\ &= \binom{N-\alpha-1}{N-1} = \frac{\Gamma(N-\alpha)}{\Gamma(N)\Gamma(1-\alpha)}. \end{aligned} \tag{3.27}$$

Thus

$$\lim_{N\to\infty} N^{\alpha} \sum_{k=0}^{N-1} (-1)^k \binom{\alpha}{k} = \lim_{N\to\infty} \frac{N^{\alpha}\Gamma(N-\alpha)}{\Gamma(N)\Gamma(1-\alpha)} \\ = \frac{1}{\Gamma(1-\alpha)} \lim_{N\to\infty} \frac{N^{\alpha}\Gamma(N-\alpha)}{\Gamma(N)} = \frac{1}{\Gamma(1-\alpha)}, \tag{3.28}$$

where we have used Stirling's formula (or the known asymptotics for gamma function ratios) in the last step.

References

1. Adams, E.W., Johnston, J.P.: Effects of the separating shear layer on the Reattachment length and wall shear stress. Exp. Fluids **6**, 493–499 (1988)
2. Anwar-ul-Haque, Ahmad, F., Yamada, S., Chaudhry, S.R.: Assessment of turbulence models for turbulent flow over backward facing step. Proc. World Congr. Eng. **1**, 1340 (2007)
3. Gartling, D.K.: A test problem for outflow boundary conditions—flow over a backward-facing step. Int. J. Numer. Methods Fluids **11**, 953–967 (1990)
4. Harlow, F.H., Welch, E.J.: Numerical calculation of time-dependent viscous incompressible flow with free surface. Phys. Fluids **8**(12), 2182–2189 (1965)
5. Kim, J., Moin, P.: Application of a fractional-step method to incompressible Navier-Stokes equations. J. Comput. Phys. **59**, 308–323 (1985)
6. Lee, T., Mateescu, D.: Experimental and numerical investigation of 2-D backward-facing step flow. J. Fluids Struct. **12**, 703–716 (1998)
7. Mandelbrot, B.: The variation of certain speculative prices. J. Bus. **36**(4), 394–419 (1963)
8. Meerschaert, M., Tadjeran, C.: Finite difference approximations for fractional advection-dispersion flow equations. J. Comput. Appl. Math. **172**(1), 65–77 (2004)
9. Sohn, J.: Evaluation of FIDAP on some classical laminar and turbulent benchmarks. Int. J. Numer. Methods Fluids **8**, 1469–1490 (1988)
10. Tuan, Vu.K., Gorenflo, R.: Extrapolation to the limit for numerical fractional differentiation. Z. Angew. Math. Mech. **75**, 646–648 (1995)

Chapter 4
A Parallel Numerical Solution Approach for Nonlinear Parabolic Systems Arising in Air Pollution Transport Problems

János Karátson and Balázs Kovács

Abstract The subject of this chapter is the numerical treatment of nonlinear parabolic systems, which arise in various mathematical models of time-dependent reaction-convection-diffusion transport systems. Such coupled nonlinearities frequently arise in environmental modeling, in particular, in the study of the transport of air pollutants, and these systems may consist of a huge number of equations. In this chapter we extend our previously developed approach, based on operator preconditioning, to problems with mixed boundary conditions and localized interface conditions. The mixed boundary conditions allow that the flux is prescribed on a part of the boundary, whereas the presence of interface conditions allows the inclusion of a localized reaction on some subdomain modelled by a curve or polygon. The overall method consists of four parts: time discretization, space discretization, outer iteration for the nonlinear systems and inner iteration for the linearized systems. The preconditioning step arises in the last part, in which the preconditioning matrix has a block-diagonal structure due to the used uncoupled equivalent operator preconditioning. The auxiliary problems can thus be solved in parallel and with a cost proportional to that of a single PDE, further, the method exhibits mesh independent superlinear convergence of the preconditioned iteration.

Keywords Air pollution • Nonlinear parabolic systems • Parallel numerical solution • Transport problems

J. Karátson (✉)
Department of Applied Analysis and Computational Mathematics, Eötvös Loránd University, Budapest, Hungary

MTA-ELTE Numerical Analysis and Large Networks Research Group, Budapest, Hungary

Department of Analysis, Technical University; Budapest, Hungary
e-mail: karatson@cs.elte.hu

B. Kovács
MTA-ELTE Numerical Analysis and Large Networks Research Group, Pázmány Péter st. 1/C, H-1117 Budapest, Hungary
e-mail: koboaet@cs.elte.hu

A. Bátkai et al. (eds.), *Mathematical Problems in Meteorological Modelling*, Mathematics in Industry 24, DOI 10.1007/978-3-319-40157-7_4

4.1 Introduction

The subject of this chapter is the numerical treatment of nonlinear parabolic systems, which arise in various situations in the mathematical modeling of time-dependent reaction-convection-diffusion transport systems, in particular those describing meteorological phenomena and the effect of air pollution [5, 6, 12–14]. Such systems normally lead to large-scale and computationally complicated problems, hence it is important to develop efficient and mathematically solid numerical solution algorithms.

We consider systems which contain nonlinear coupling in the reaction terms, further, involving mixed boundary conditions and localized interface conditions as well. That is, in the general case we consider a system of the form

$$\left.\begin{aligned} \tfrac{\partial u_i}{\partial t} - \operatorname{div}(K_i \nabla u_i) + \mathbf{b}_i \cdot \nabla u_i + R_i(x, u_1, \dots, u_\ell) &= f_i \\ K_i \nabla u_i \cdot \nu\big|_{\Gamma_N \times \mathbf{R}^+} &= \gamma_i \\ u_i\big|_{\Gamma_D \times \mathbf{R}^+} &= g_i \\ [K_i \nabla u_i \cdot \nu]_{\Gamma_{int} \times \mathbf{R}^+} &= \varrho_i \\ [u_i]_{\Gamma_{int} \times \mathbf{R}^+} &= 0 \\ u_i\big|_{t=0} &= u_i^{(0)} \end{aligned}\right\} \quad (i = 1, \dots, \ell), \tag{4.1}$$

where $t \geq 0$ is the time variable and x is the space variable in a d-dimensional bounded domain Ω (where $d = 1, 2$ or 3). A precise formulation of the conditions and notations of the problem will be given in the next section. Such coupled nonlinearities frequently arise in environmental modeling, in particular, in the study of the transport of air pollutants, where u_i are concentrations of chemical species. These systems may consist of a huge number of equations, e.g. in [13] a model with more than 70 chemical reaction is analysed in details, but larger models can also occur. We have considered such problems with only Dirichlet boundary conditions and without interface conditions in [9]. Thereby a compound algorithm was defined and its efficiency was demonstrated by numerical tests.

Our goal is to extend the approach of [9] to problems with mixed boundary conditions and interface conditions. The mixed boundary conditions allow that the flux is prescribed on a part of the boundary, whereas the presence of interface conditions allows the inclusion of a localized reaction on some subdomain modelled by a curve or polygon. Similarly as in [9], we first apply time-discretization, thus a coupled elliptic system has to be solved on each time level. Since the system of ODEs that stems from the chemical part is generally stiff, the usage of implicit time-discretization schemes is inevitable, hence a nonlinearity appears in the elliptic problems. We propose an outer-inner iteration (outer damped inexact Newton method with inner preconditioned conjugate gradient, CG, method) for

solving the FEM discretization of the nonlinear elliptic problems. The main part of this method is preconditioning using the discretization of an ℓ-tuple of independent scalar elliptic operators as preconditioner. This implies that the preconditioning matrix has a block-diagonal structure, and the auxiliary problems can be solved with a cost proportional to that of a single PDE, in contrast to solving the linearized PDE systems. The advantages of such operator preconditioning is discussed in [2]. In particular, the usage of independent scalar operators as preconditioner allows parallelization of the method, which was illustrated for linear elliptic systems in [10].

We note that when similar problems are handled numerically on computers, a very popular and often used approach in this field involves some kind of splitting technique (for example, the Marchuk-Strang splitting). Thereby the problem is split into proper subproblems. In our method no splitting is used, since the role of separation to subproblems is played by the above mentioned preconditioning via parallel scalar operators.

The description of the method will consist of four parts: time discretization, space discretization, outer iteration for the nonlinear systems and inner iteration for the linearized systems. The preconditioning step arises in the last part, and we derive mesh independent superlinear convergence of the preconditioned iteration.

4.2 The Numerical Solution Process and its Convergence

We consider system (4.1) under the following conditions.

Assumptions 4.1

1. (Domain:) the domain Ω is a bounded polytope in $\mathbf{R}^d$ with Lipschitz boundary; $\Gamma_N, \Gamma_D \subset \partial\Omega$ are disjoint subsets, relatively open with respect to $\partial\Omega$ and with piecewise C^1 boundary, such that $\partial\Omega = \overline{\Gamma}_D \cup \overline{\Gamma}_N$, further, the interface $\Gamma_{int} \subset \Omega$ is a piecewise C^1 surface lying in Ω. Here ν is the outward normal vector and $[.]_{\Gamma_{int}}$ denotes the jump (i.e., the difference of the limits from the two sides of the interface Γ_{int}) of a function.
2. (Smoothness:) for any $i = 1, \dots, \ell$, $K_i \in L^\infty(\Omega)$, $\boldsymbol{b}_i \in C^1(\overline{\Omega})^d$, $f_i \in L^2(\Omega)$, g_i is the trace of a Dirichlet lift $\tilde{g}_i \in H^1(\Omega)$, $\gamma_i \in L^2(\Gamma_N)$ and $\varrho_i \in L^2(\Gamma_{int})$. Further, the function $R = (R_1, \dots, R_\ell) : \Omega \times \mathbf{R}^\ell \to \mathbf{R}^\ell$ is measurable and bounded w.r. to the variable $x \in \Omega$ and C^1 in the variable $\xi \in \mathbf{R}^\ell$.
3. (Boundedness from below:) there is $m > 0$ such that $K_i \geq m$ holds for all $i = 1, \dots, \ell$, further, using the notation $R'_\xi(x, \xi) := \frac{\partial R(x,\xi)}{\partial \xi}$, there exists $\alpha \in \mathbf{R}$ such that

$$R'_\xi(x, \xi)\, \eta \cdot \eta - \frac{1}{2} \left(\max_i \operatorname{div} \boldsymbol{b}_i(x) \right) |\eta|^2 \geq \alpha\, |\eta|^2 \tag{4.2}$$

for any $(x, \xi) \in \Omega \times \mathbf{R}^\ell$ and $\eta \in \mathbf{R}^\ell$.

4. (Local Lipschitz continuity:) let $3 \le p$ (if $d = 2$) or $3 \le p \le 6$ (if $d = 3$), then there exist constants $c_1, c_2 \ge 0$ such that for any (x, ξ_1) and $(x, \xi_2) \in \Omega \times \mathbf{R}^l$,

$$\left\| R'_\xi(x, \xi_1) - R'_\xi(x, \xi_2) \right\| \le \left(c_1 + c_2 \, (\max\, |\xi_1|, |\xi_2|)^{p-3} \right) |\xi_1 - \xi_2|.$$

First let us formulate our problem using a vector notation, i.e. we set for brevity

$$\boldsymbol{u} := \boldsymbol{u}(x, t) = (u_1(x, t), u_2(x, t), \ldots, u_\ell(x, t)),$$

which satisfies the semilinear parabolic system

$$\begin{aligned} \frac{\partial \boldsymbol{u}}{\partial t} - \operatorname{div}(\boldsymbol{K} \nabla \boldsymbol{u}) + \boldsymbol{b} \cdot \nabla \boldsymbol{u} + \boldsymbol{R}(x, \boldsymbol{u}) &= \boldsymbol{f}, \\ \boldsymbol{K} \nabla \boldsymbol{u} \cdot \nu \big|_{\Gamma_N \times \mathbf{R}^+} &= \boldsymbol{\gamma}, \\ \boldsymbol{u} \big|_{\Gamma_D \times \mathbf{R}^+} &= \boldsymbol{g}, \\ [\boldsymbol{K} \nabla \boldsymbol{u} \cdot \nu]_{\Gamma_{int} \times \mathbf{R}^+} &= \boldsymbol{\varrho}, \\ [\boldsymbol{u}]_{\Gamma_{int} \times \mathbf{R}^+} &= 0 \\ \boldsymbol{u} \big|_{t=0} &= \boldsymbol{u}^{(0)}. \end{aligned} \tag{4.3}$$

The numerical solution starts by using Röthe's method, see [7], where the PDE system is first discretized in time, in general by a Runge–Kutta method, but in our situation it is proper to use the implicit (backward) Euler method. Then the resulting nonlinear equation will be discretized by finite elements and solved by an iterative method combined with a preconditioning process (as an inner iteration).

4.2.1 Time Discretization

First we apply time discretization on the continuous level to system (4.3). For stability reasons we apply the implicit Euler method. The convergence for general time discretizations of quasilinear Cauchy problems is found e.g. in the paper [11]. For ease of presentation we use constant step size τ. (We denote $v^n := v(., n\tau)$ for any continuous function.)

This results in the following nonlinear elliptic system on each time level, for $n \geq 1$:

$$\begin{aligned} -\tau \ \mathrm{div}\left(\boldsymbol{K}\nabla \boldsymbol{u}^{n+1}\right) + \tau \boldsymbol{b}\cdot\nabla \boldsymbol{u}^{n+1} + \tau \boldsymbol{R}(x,\boldsymbol{u}^{n+1}) + \boldsymbol{u}^{n+1} &= \tau \boldsymbol{f}^{n+1} + \boldsymbol{u}^{n}, \\ \boldsymbol{K}\,\nabla \boldsymbol{u}^{n+1}\cdot \nu\big|_{\Gamma_N} &= \boldsymbol{\gamma}^{n+1}, \\ \boldsymbol{u}^{n+1}\big|_{\Gamma_D} &= \boldsymbol{g}^{n+1}, \\ \left[\boldsymbol{K}\,\nabla \boldsymbol{u}^{n+1}\cdot \nu\right]_{\Gamma_{int}} &= \boldsymbol{\varrho}^{n+1}, \\ \left[\boldsymbol{u}^{n+1}\right]_{\Gamma_{int}} &= 0. \end{aligned} \tag{4.4}$$

4.2.2 FEM Discretization in Space

First, the weak formulation of the problem is done after homogenization of the boundary conditions (i.e. we set $u_i \rightarrow u_i - \tilde{g}_i$, where $\tilde{g}_i$ is the Dirichlet lift for g_i). Defining the Sobolev space

$$H^1_D(\Omega) := \{u \in H^1(\Omega) : \ u_{|\Gamma_D} = 0\}$$

that corresponds to the decomposition to Γ_N and Γ_D, we will use the product space $H^1_D(\Omega)^\ell$ for system (4.1). Thereby we use the following nonlinear operator: for any $\boldsymbol{u} \in H^1_D(\Omega)^\ell$ let

$$\begin{aligned} \langle F(\boldsymbol{u}), \boldsymbol{v}\rangle_{H^1_D(\Omega)^\ell} &= \int_\Omega \sum_{i=1}^{\ell} \Big(\tau K_i\,\nabla u_i^{n+1}\cdot\nabla v_i + \tau\left(\mathbf{b}_i\cdot\nabla u_i^{n+1}\right) v_i \\ &\qquad + \tau R_i(x,\boldsymbol{u}^{n+1}) v_i + u_i^{n+1} v_i\Big) \\ &= \int_\Omega \Big(\tau \boldsymbol{K}\,\nabla \boldsymbol{u}^{n+1}\cdot\nabla \boldsymbol{v} + \tau\left(\mathbf{b}\cdot\nabla \boldsymbol{u}^{n+1}\right)\cdot \boldsymbol{v} \\ &\qquad + \tau \boldsymbol{R}(x,\boldsymbol{u}^{n+1})\cdot \boldsymbol{v} + \boldsymbol{u}^{n+1}\cdot \boldsymbol{v}\Big) \qquad \left(\boldsymbol{v} \in H^1_D(\Omega)^\ell\right). \end{aligned}$$

The weak form of the right hand side can be represented as follows, where for simplicity we define

$$\Gamma := \Gamma_N \cup \Gamma_{int},$$

and we extend the functions γ_i and ϱ_i to Γ as constant zero on the other component. Thus for all $\boldsymbol{v} \in H_D^1(\Omega)^\ell$ we let

$$\begin{aligned}\langle B, \boldsymbol{v}\rangle_{H_D^1(\Omega)^\ell} &= \int_\Omega \sum_{i=1}^{\ell} \Big(\tau f_i^{n+1} v_i + u_i^n v_i\Big)\mathrm{d}x + \tau \int_\Gamma \sum_{i=1}^{\ell} \Big(\gamma_i v_i + \varrho_i v_i\Big)\mathrm{d}\sigma \\ &= \int_\Omega \Big(\tau \boldsymbol{f}^{n+1} \cdot \boldsymbol{v} + \boldsymbol{u}^n \cdot \boldsymbol{v}\Big) + \tau \int_\Gamma \sum_{i=1}^{\ell} \Big(\boldsymbol{\gamma} \cdot \boldsymbol{v} + \boldsymbol{\varrho} \cdot \boldsymbol{v}\Big)\mathrm{d}\sigma.\end{aligned} \tag{4.5}$$

Therefore (4.4) is equivalent to the following abstract operator equation:

$$\langle F(\boldsymbol{u}), \boldsymbol{v}\rangle_{H_D^1(\Omega)^\ell} = \langle B, \boldsymbol{v}\rangle_{H_D^1(\Omega)^\ell} \qquad (\boldsymbol{v} \in H_D^1(\Omega)^\ell) \tag{4.6}$$

We consider the FEM discretization of (4.6) over a quasi-uniform triangulation of the domain Ω, i.e. regular triangular finite elements are used in the two-dimensional case, while tetrahedral finite elements are needed in the three-dimensional case. The maximal meshwidth is denoted by h. The corresponding finite element space $V_h \subset V = H_D^1(\Omega)$ is spanned by continuous, piecewise linear basis functions $\varphi_1, \varphi_2, \ldots, \varphi_N$ that are continuous on Ω and linear on each finite element, vanising on Γ_D, and $\varphi_j(x_k) = \delta_{jk}$ holds for each node x_k (not sitting on Γ_D). Then the finite element solution to (4.6) can be simply written as $\boldsymbol{u}_h \in V_h^\ell$ satisfying

$$\langle F(\boldsymbol{u}_h), \boldsymbol{v}_h\rangle_{H_D^1(\Omega)^\ell} = \langle B, \boldsymbol{v}_h\rangle_{H_D^1(\Omega)^\ell} \qquad (\boldsymbol{v}_h \in V_h^\ell).$$

The convergence of FEM discretization is well-known, see e.g. [3].

4.2.3 Outer Iteration: Damped Newton's Method

The operator $F_h : V_h^\ell \to V_h^\ell$ and the function $\mathbf{g}_h \in V_h^\ell$ are defined by the identities

$$\langle F_h(\boldsymbol{u}_h), \boldsymbol{v}_h\rangle_{H_0^1} = \langle F(\boldsymbol{u}_h), \boldsymbol{v}_h\rangle_{H_0^1} \qquad \left(\boldsymbol{v}_h \in V_h^\ell\right),$$

$$\langle \mathbf{g}_h, \boldsymbol{v}_h\rangle_{H_0^1} = \int_\Omega \mathbf{g} \cdot \boldsymbol{v}_h \qquad \left(\boldsymbol{v}_h \in V_h^\ell\right)$$

via the Riesz representation theorem, thus the problem can be written as a nonlinear algebraic system

$$F_h(\boldsymbol{u}_h) = \mathbf{g}_h. \tag{4.7}$$

We apply the damped inexact Newton method (DIN) for the iterative solution of problem (4.7). The construction of the DIN method and the related convergence results are well-known, for completeness we briefly summarize them as follows.

Algorithm 4.2.1 (DIN) *Let $\boldsymbol{u}_0 \in V_h^\ell$ be arbitrary. The sequence $(\boldsymbol{u}_n) \subset V_h^\ell$ is constructed as follows:*

- *Denoting the residual by $\mathbf{r}_h = \mathbf{g}_h - F_h(\boldsymbol{u}_n)$, the vector $\mathbf{p}_n$ is the approximate solution of problem $F_h'(\boldsymbol{u}_n)\mathbf{p}_n = \mathbf{r_h}$, i.e.*

$$\left\| F_h'(\boldsymbol{u}_n)\mathbf{p}_n - \mathbf{r_h} \right\|_{H_0^1} \leq \delta_n \left\| \mathbf{r}_h \right\|_{H_0^1} \quad \text{with } 0 < \delta_n \leq \delta_0 < 1,$$

- $\sigma_n = \min \left\{ 1, \dfrac{1-\delta_n}{(1+\delta_n)^2} \cdot \dfrac{K^2}{L \left\| F_h(\boldsymbol{u}_n) - \mathbf{g}_h \right\|_{H_0^1}} \right\}$,
- $\boldsymbol{u}_{n+1} = \boldsymbol{u}_n + \sigma_n \mathbf{p}_n$.

Under suitable smoothness, growth and coercivity conditions the following theorem holds, for the proof see [4, Theorem 5.12] in a more general setting.

Theorem 4.1 *If $\delta_n \leq c \cdot \left\| F_h(\boldsymbol{u}_n) - \mathbf{g}_h \right\|_{H_0^1}^\gamma$ with some $0 < \gamma \leq 1$, then the convergence is locally of order $1+\gamma$, that is the convergence is linear for n_0 steps until $\left\| F_h(\boldsymbol{u}_n) - \mathbf{g}_h \right\|_{H_0^1}^\gamma \leq \varepsilon$, where $\varepsilon \leq (1-\delta_0)\frac{K^2}{2L}$ (here and in the definition of σ_n the constant L comes from the Lipschitz continuity of F'), and further on (as $\sigma_n \equiv 1$)*

$$\left\| \boldsymbol{u}_n - \boldsymbol{u}_h \right\|_{H_0^1} \leq d_1 q^{(1+\gamma)^{n-n_0}}$$

with some $d_1 > 0$, $0 < q < 1$.

4.2.4 Inner Iteration: Preconditioned CG Method Using Equivalent Operator Preconditioning

In each step the construction of $\boldsymbol{u}_n$ requires the approximate solution of the linearized problem

$$F_h'(\boldsymbol{u}_n)\mathbf{p}_h = \mathbf{r}_h. \tag{4.8}$$

Applying the previously mentioned homogenization and linearization, and dividing by τ, it is easy to see that the linearized system is equivalent to the FEM solution in

V_h^ℓ of a linear elliptic system of the following structure:

$$\left.\begin{aligned} -\operatorname{div}(K_i\,\nabla p_i) + \mathbf{b}_i\cdot\nabla p_i + \sum_{j=1}^{\ell}\hat{R}_{ij}p_j &= \hat{f}_i \\ K_i\,\nabla p_i\cdot\nu\big|_{\Gamma_N} &= \hat{\gamma}_i \\ p_i\big|_{\Gamma_D} &= 0 \\ [K_i\,\nabla p_i\cdot\nu]_{\Gamma_{int}} &= \hat{\varrho}_i \\ [p_i]_{\Gamma_{int}} &= 0 \end{aligned}\right\} \qquad (i=1,\dots,\ell), \tag{4.9}$$

where the coefficients of the p_j are

$$\hat{R}_{ij}(x) := \partial_j R_i\big(x,\, \boldsymbol{u}_n(x) + \tilde{g}_i(x)\big) + \frac{1}{\tau}\delta_{ij}$$

(where δ_{ij} denotes the Kronecker symbol). The weak form of problem (4.9) on the continuous level is

$$\begin{aligned} &\int_\Omega \sum_{i=1}^{\ell}\Big(K_i\,\nabla p_i\cdot\nabla v_i + (\mathbf{b}_i\cdot\nabla p_i)\,v_i + \sum_{j=1}^{\ell}\hat{R}_{ij}p_j v_i\Big) \\ &= \int_\Omega \sum_{i=1}^{\ell}\hat{f}_i v_i\,\mathrm{d}x + \int_\Gamma \sum_{i=1}^{\ell}\Big(\hat{\gamma}_i v_i + \hat{\varrho}_i v_i\Big)\mathrm{d}\sigma \qquad (\boldsymbol{v}_h\in V_h^\ell). \end{aligned} \tag{4.10}$$

Denoting by $\mathbf{c}$ and $\mathbf{d}$ the coefficient vectors of $\mathbf{p}_h$ and $\mathbf{r}_h$ with respect to the FEM basis $\{\phi_1,\dots,\phi_N\}$, and by $\mathbf{L}_h^{(n)}$ the stiffness matrix corresponding to the left-hand side of (4.9), Eq. (4.8) turns into the linear algebraic system

$$\mathbf{L}_h^{(n)}\mathbf{c} = \mathbf{d}. \tag{4.11}$$

The theory of equivalent operators (cf. [2]) can be applied to the auxiliary linear problem (4.9) which can be solved by a proper CG type method using a suitable preconditioner. We propose the CGN method for the nonsymmetric system (4.9), see e.g. [2]. Letting $\eta_i \in L^\infty(\Omega)$, $\eta_i \geq 0$ be suitable functions, we introduce the symmetric linear elliptic operators

$$S_i p_i := -\operatorname{div}(K_i\,\nabla p_i) + \eta_i p_i \qquad (i=1,\dots,\ell) \tag{4.12}$$

in $H_D^1(\Omega)$, and then define the ℓ-tuple of independent elliptic operators

$$S\mathbf{p} = \big(S_1 p_1\ S_2 p_2\ \dots\ S_\ell p_\ell\big) \tag{4.13}$$

as preconditioning operator. The preconditioning matrix for the discrete system (4.11) is defined as the stiffness matrix $\mathbf{S}_h$ of S in $H_0^1(\Omega)^\ell$. Then we apply the CGN algorithm for the preconditioned system

$$\mathbf{S}_h^{-1}\mathbf{L}_h^{(n)}\mathbf{c} = \tilde{\mathbf{d}}, \tag{4.14}$$

where $\tilde{\mathbf{d}} := \mathbf{S}_h^{-1}\mathbf{d}$. According to the main idea of preconditioning, system (4.14) is equivalent to (4.11), but the spectrum of the matrix $\mathbf{S}_h^{-1}\mathbf{L}_h^{(n)}$ is much more clustered than the spectrum of $\mathbf{L}_h^{(n)}$. Therefore, when we apply the CGN algorithm for system (4.14), we obtain fast convergence, which will be analyzed below. Altogether, in each Newton step the linearized system (4.9) is preconditioned by the discretization of independent (i.e. decoupled) symmetric scalar elliptic operators. This means that the preconditioning matrix $\mathbf{S}_h$ has a block-diagonal structure. This enables parallel computation of the solution of the auxiliary problems in the CGN, which was demonstrated for a linear elliptic test system in [10]. Moreover, combining the convergence results for the CGN and the DIN Algorithm 4.2.1, the combined iteration provides mesh independent convergence, with superlinear convergence rate for both the inner and outer iterations. This was given in Theorem 4.1 for the outer iteration, and it can be derived as follows for the inner iteration.

Theorem 4.2

(1) The left-hand side of Eq. (4.10) *can be represented as*

$$\int_\Omega \sum_{i=1}^{\ell} \left(K_i \nabla p_i \cdot \nabla v_i + (\mathbf{b}_i \cdot \nabla p_i)\, v_i + \sum_{j=1}^{\ell} \hat{R}_{ij} p_j v_i \right) = \langle (I+Q)\boldsymbol{p}, \boldsymbol{v} \rangle_{H_D^1(\Omega)^\ell},$$

for any $\boldsymbol{p}, \boldsymbol{v} \in H_D^1(\Omega)^\ell$, where $Q : H_D^1(\Omega)^\ell \to H_D^1(\Omega)^\ell$ is a compact linear operator and I is the identity on $H_D^1(\Omega)^\ell$.

(2) The right-hand side of Eq. (4.10) *can be represented as*

$$\int_\Omega \sum_{i=1}^{\ell} \hat{f}_i v_i \mathrm{d}x + \int_\Gamma \sum_{i=1}^{\ell} \left(\hat{\gamma}_i v_i + \hat{\varrho}_i v_i \right) \mathrm{d}\sigma = \langle \boldsymbol{r}, \boldsymbol{v} \rangle_{H_D^1(\Omega)^\ell} \qquad (\boldsymbol{v} \in H_D^1(\Omega)^\ell)$$

for a proper element $\boldsymbol{r} \in H_D^1(\Omega)^\ell$.

Proof

(1) Let us introduce the weighted inner product

$$\langle \boldsymbol{u}, \boldsymbol{v} \rangle_{H_D^1(\Omega)^\ell} := \int_\Omega \sum_{i=1}^{\ell} \left(K_i \nabla u_i \cdot \nabla v_i + \eta_i u_i v_i \right)$$

in the space $H_D^1(\Omega)^\ell$, which is equivalent to the standard one. Defining Q via

$$\langle Q\boldsymbol{p}, \boldsymbol{v} \rangle_{H_D^1(\Omega)^\ell} := \int_\Omega \sum_{i=1}^{\ell} \left((\mathbf{b}_i \cdot \nabla p_i)\, v_i + \sum_{j=1}^{\ell} \hat{R}_{ij} p_j v_i - \eta_i p_i v_i \right) \quad (\boldsymbol{p}, \boldsymbol{v} \in H_D^1(\Omega)^\ell),$$

the representation is obvious under the used weighted inner product. The compactness of Q follows from the fact that it is the sum of the weak forms of first and zeroth order scalar operators, for which the compactness was shown under the similar form in [1].

(2) The continuous embedding of $L^2(\Omega)$ and $L^2(\Gamma)$ into $H^1_D(\Omega)$ implies that each term in the right-hand side of (4.10) is a bounded linear functional on $H^1_D(\Omega)$ w.r.t the variable v_i. Hence the sum of these terms is a bounded linear functional on $H^1_D(\Omega)^\ell$ w.r.t the variable $\boldsymbol{v}$. Then the Riesz representation theorem yields the existence and uniqueness of the proper element $\boldsymbol{r} \in H^1_D(\Omega)^\ell$.

Theorem 4.3 *Let us apply the CGN algorithm for system* (4.14) *under the* $\mathbf{S}_h$*-inner product* $\langle .,. \rangle_{\mathbf{S}_h}$. *Then the residual errors satisfy*

$$\left(\frac{\|r_k\|_{\mathbf{S}_h}}{\|r_0\|_{\mathbf{S}_h}} \right)^{1/k} \leq \varepsilon_k \tag{4.15}$$

where

$$\varepsilon_k := \frac{2}{km^2} \sum_{i=1}^{k} \Big(\big|\lambda_i(Q^* + Q)\big| + \lambda_i(Q^*Q) \Big) \to 0 \quad \text{as } k \to \infty \tag{4.16}$$

(with Q *being the compact operator above, and* m *being the ellipticity constant of* $I + Q$*), and* ε_k *is a sequence independent of* V_h.

Proof Due to Theorem 4.3, we can rewrite Eq. (4.10) as

$$(I + Q)\boldsymbol{p} = \boldsymbol{r} \tag{4.17}$$

in $H^1_D(\Omega)^\ell$, i.e. an operator equation with a compact preturbation of the identity. Similarly, since we have the decomposition

$$\mathbf{L}_h^{(n)} = \mathbf{S}_h + \mathbf{Q}_h^{(n)}$$

(where respectively $\mathbf{S}_h^{(n)}$ and $\mathbf{Q}_h^{(n)}$ are the stiffness matrices for the weighted inner product and compact operator Q, defined in Theorem 4.3), we obtain that (4.14) can be rewritten as

$$(\mathbf{I}_h + \mathbf{S}_h^{-1}\mathbf{Q}_h^{(n)})\,\mathbf{c} = \tilde{\mathbf{d}}$$

(where $\tilde{\mathbf{d}} := \mathbf{S}_h^{-1}\mathbf{d}$). That is, we obtain a proper projection of (4.17) in V_h^ℓ, and Proposition 7.5 of [2] yields the desired convergence result.

4.3 Some Examples in Air Pollution Models

Systems of the type (4.1) typically arise in air pollution models, involving diffusion, convection and chemical reactions related to the polluting materials (pollutants), see e.g. [12, 13]. A simplified model involving the 10 main arising pollutants involves the following vector, describing the concentrations of the considered species:

$$\boldsymbol{u} = \left(u_{\mathrm{NO}_2}, u_{\mathrm{O}_3}, u_{\mathrm{NO}}, u_{\mathrm{O}_2}, u_{\mathrm{O}^1\mathrm{D}}, u_{\mathrm{H}_2\mathrm{O}}, u_{\mathrm{OH}}, u_{\mathrm{CO}}, u_{\mathrm{H}}, u_{\mathrm{HO}_2}\right)^T.$$

Then the reaction terms, given through the coordinate functions of R, are as follows:

$$\begin{aligned}
R_{\mathrm{NO}_2}(\boldsymbol{u}) = & -J_1 u_{\mathrm{NO}_2} u_{hv} + k_2 u_{\mathrm{NO}} u_{\mathrm{O}_3} - k_5 u_{\mathrm{OH}} u_{\mathrm{NO}_2} + k_8 u_{\mathrm{HO}_2} u_{\mathrm{NO}} \\
R_{\mathrm{O}_3}(\boldsymbol{u}) = & \ J_1 u_{\mathrm{NO}_2} u_{hv} - k_2 u_{\mathrm{NO}} u_{\mathrm{O}_3} - J_3 u_{\mathrm{O}_3} u_{hv} + k_9(T) u_{\mathrm{O}^1\mathrm{D}} u_M \\
R_{\mathrm{NO}}(\boldsymbol{u}) = & \ J_1 u_{\mathrm{NO}_2} u_{hv} - k_2 u_{\mathrm{NO}} u_{\mathrm{O}_3} - k_8 u_{\mathrm{HO}_2} u_{\mathrm{NO}} \\
R_{\mathrm{O}_2}(\boldsymbol{u}) = & \ k_2 u_{\mathrm{NO}} u_{\mathrm{O}_3} + J_3 u_{\mathrm{O}_3} u_{hv} \\
R_{\mathrm{O}^1\mathrm{D}}(\boldsymbol{u}) = & \ J_3 u_{\mathrm{O}_3} u_{hv} - k_4 u_{\mathrm{O}^1\mathrm{D}} u_{\mathrm{H}_2\mathrm{O}} - k_9(T) u_{\mathrm{O}^1\mathrm{D}} u_M \\
R_{\mathrm{H}_2\mathrm{O}}(\boldsymbol{u}) = & -k_4 u_{\mathrm{O}^1\mathrm{D}} u_{\mathrm{H}_2\mathrm{O}} + k_{10} u_{HCHO} u_{\mathrm{OH}} \\
R_{\mathrm{OH}}(\boldsymbol{u}) = & \ 2k_4 u_{\mathrm{O}^1\mathrm{D}} u_{\mathrm{H}_2\mathrm{O}} - k_5 u_{\mathrm{OH}} u_{\mathrm{NO}_2} - k_6 u_{\mathrm{OH}} u_{\mathrm{CO}} + k_8 u_{\mathrm{HO}_2} u_{\mathrm{NO}} \\
& - k_{10} u_{HCHO} u_{\mathrm{OH}} \\
R_{\mathrm{CO}}(\boldsymbol{u}) = & -k_6 u_{\mathrm{OH}} u_{\mathrm{CO}} + k_{10} u_{HCHO} u_{\mathrm{OH}} + J_{11} u_{HCHO} u_{hv} \\
& + J_{12} u_{HCHO} u_{hv} \\
R_{\mathrm{H}}(\boldsymbol{u}) = & \ k_6 u_{\mathrm{OH}} u_{\mathrm{CO}} - k_7(T) u_{\mathrm{H}} u_{\mathrm{O}_2} u_M \\
R_{\mathrm{HO}_2}(\boldsymbol{u}) = & \ k_7(T) u_{\mathrm{H}} u_{\mathrm{O}_2} u_M - k_8 u_{\mathrm{HO}_2} u_{\mathrm{NO}} + k_{10} u_{HCHO} u_{\mathrm{OH}} \\
& + 2J_{11} u_{HCHO} u_{hv}.
\end{aligned}$$

Here k_j are the reaction rates, and the photolysis rates are defined as

$$J_j = a_j e^{-b_j \sin(\theta)^{-1}}.$$

Let us list some possible situations covered by our system (4.1). This shows that our given numerical algorithm can be used for the computation of the desired concentrations. The initial conditions have the same general form

$$u_i\big|_{t=0} = u_i^{(0)}$$

as in (4.1) in each problem below, hence it is omitted in the formulas.

Example 4.3.1. Dirichlet boundary conditions in 2D:

$$\left.\begin{aligned} \tfrac{\partial u_i}{\partial t} - \operatorname{div}(K_i \nabla u_i) + \mathbf{b}_i \cdot \nabla u_i + R_i(x, u_1, \dots, u_\ell) &= f_i \\ u_i\big|_{\partial\Omega\times\mathbf{R}^+} &= g_i \end{aligned}\right\} \qquad (i = 1, \dots, \ell). \tag{4.18}$$

In this case the values of concentrations are given from a larger-scale model on the boundary of the considered, typically rectangular domain. The exact boundary conditions are of course unknown in real situations, therefore these values should be taken from a model treated on a much larger spatial domain. Some kind of interpolation may be needed because the larger models are normally handled on the coarser grids, see details in [13]. This model was studied in [9], and the efficiency of the similar approach was demonstrated by numerical test, involving a rotating wind field test problem taken from [5].

Example 4.3.2. Mixed boundary conditions in 3D:

$$\left.\begin{aligned} \tfrac{\partial u_i}{\partial t} - \operatorname{div}(K_i \nabla u_i) + \mathbf{b}_i \cdot \nabla u_i + R_i(x, u_1, \dots, u_\ell) &= f_i \\ K_i \nabla u_i \cdot \nu\big|_{\Gamma_N\times\mathbf{R}^+} &= 0 \\ u_i\big|_{\Gamma_D\times\mathbf{R}^+} &= g_i \end{aligned}\right\} \qquad (i = 1, \dots, \ell). \tag{4.19}$$

Here Ω is a 3D rectangle, Γ_N is the union of the horizontal faces of the domain and there the flux is assumed to be zero, i.e. no horizontal transmission occurs, whereas Γ_D has the same role as in the previous example.

Example 4.3.3. Mixed boundary conditions in 2D, point source:

$$\left.\begin{aligned} \tfrac{\partial u_i}{\partial t} - \operatorname{div}(K_i \nabla u_i) + \mathbf{b}_i \cdot \nabla u_i + R_i(x, u_1, \dots, u_\ell) &= f_i \\ K_i \nabla u_i \cdot \nu\big|_{\Gamma_N\times\mathbf{R}^+} &= \gamma_i \\ u_i\big|_{\Gamma_D\times\mathbf{R}^+} &= g_i \end{aligned}\right\} \qquad (i = 1, \dots, \ell). \tag{4.20}$$

Here Γ_D is a small circle inside Ω representing a chimney which is a(n almost) point source of the pollution, g_i are given large values, and Γ_N is the outer boundary where the flux is given.

Example 4.3.4. Dirichlet boundary conditions in 2D and interface conditions on a curve:

$$\left.\begin{aligned} \tfrac{\partial u_i}{\partial t} - \operatorname{div}(K_i \nabla u_i) + \mathbf{b}_i \cdot \nabla u_i + R_i(x, u_1, \dots, u_\ell) &= f_i \\ u_i\big|_{\partial\Omega\times\mathbf{R}^+} &= g_i \\ [K_i \nabla u_i \cdot \nu]_{\Gamma_{int}\times\mathbf{R}^+} &= \varrho_i \\ [u_i]_{\Gamma_{int}\times\mathbf{R}^+} &= 0 \end{aligned}\right\} \qquad (i = 1, \dots, \ell), \tag{4.21}$$

Here Example 4.3.1 is completed such that the diffusion coefficient is different on the two sides of an interior curve Γ_{int} that separates two subregions, e.g. the boundary of a lake.

In addition, our results might be extended to include reaction terms also on the interface Γ_{int}, which we did not do for simplicity. Then one can consider problems like

$$\left.\begin{aligned} \tfrac{\partial u_i}{\partial t} - \operatorname{div}(K_i \nabla u_i) + \mathbf{b}_i \cdot \nabla u_i + R_i(x, u_1, \ldots, u_\ell) &= f_i \\ u_i\big|_{\partial\Omega\times\mathbf{R}^+} &= g_i \\ [K_i \nabla u_i \cdot \nu + s_i(x, u_1, \ldots, u_\ell)]_{\Gamma_{int}\times\mathbf{R}^+} &= \varrho_i \\ [u_i]_{\Gamma_{int}\times\mathbf{R}^+} &= 0 \end{aligned}\right\} \quad (i = 1, \ldots, \ell), \tag{4.22}$$

in which given chemical reactions, described by functions s_i, take place on the interior curve as considered e.g. in [8]. Such a curve can model a localized site of catalysis, or a polluted highway etc. The formal conditions for the functions s_i are similar as for R_i.

Finally we note that it is not the goal of this chapter to include computer tests, since we have focused on the general approach to construct methods for a class of problems. It will be the subject of forthcoming papers to implement such algorithms for specific problems like in the above examples. We expect as similarly efficient behaviour for such problems as found in the tests for the pure Dirichlet problem in our cited paper [9].

Acknowledgements This research was supported by the by the Hungarian Scientific Research Fund OTKA, no. 112157.

References

1. Axelsson, O., Karátson, J.: Mesh independent superlinear PCG rates via compact-equivalent operators. SIAM J. Numer. Anal. **45**(4), 1495–1516 (2007)
2. Axelsson, O., Karátson, J.: Equivalent operator preconditioning for elliptic problems. Numer. Algoritm. **50**, 297–380 (2009)
3. Ciarlet, P.G.: The Finite Element Method for Elliptic Problems. Society for Industrial and Applied Mathematics, Philadelphia (2002)
4. Faragó, I., Karátson, J.: Numerical Solution of Nonlinear Elliptic Problems via Preconditioning Operators: Theory and Applications. Advances in Computation, vol. 11. NOVA Science Publishers, New York (2002)
5. Georgiev, K., Zlatev, Z.: Implementation of sparse matrix algorithms in an advection-diffusion-chemistry module. J. Comput. Appl. Math. **236**, 342–353 (2011)
6. Hov, Ø., Zlatev, Z., Berkowicz, R., Eliassen, A., Prahm, L.P.: Comparison of numerical techniques for use in air pollution models with non-linear chemical reactions. Atmos. Environ. **23**, 967–983 (1989)
7. Kacur, J.: Method of Rothe in Evolution Equations, Bd. 80. Teubner-Texte zur Mathematik, Leipzig (1985)

8. Kandilarov, J.D., Vulkov, L.G.: Analysis of immersed interface difference schemes for reaction–diffusion problems with singular own sources. Comput. Methods Appl. Math. **3**, 253–273 (2003)
9. Karátson, J., Kurics, T.: A preconditioned iterative solution scheme for nonlinear parabolic systems arising in air pollution modeling. Math. Model. Anal. **18**, 641–653 (2013)
10. Karátson, J., Kurics, T., Lirkov, I.: NMA 2006. In: Boyanov, T. et al. (eds.) A Parallel Algorithm for Systems of Convection-Diffusion Equations. Lecture Notes in Computer Science, vol. 4310, pp. 65–73. Springer, New York (2007)
11. Lubich, Ch., Ostermann, A.: Runge–Kutta approximation of quasilinear parabolic equations. Math. Comput. **64**, 601–627 (1995)
12. Tomlin, A., Berzins, M., Ware, J., Smith, J., Pilling, M.J.: On the use of adaptive gridding methods for modelling chemical transport from multi-scale sources. Atmos. Emiron. **31**, 2945–2959 (1997)
13. Zlatev, Z.: Computer Treatment of Large Air Pollution Models. Kluwer Academic Publishers, Dordrecht/Boston/London (1995)
14. Zlatev, Z., Dimov, I.: Computational and Numerical Challenges in Air Pollution Modelling. Studies in Computational Mathematics. Elsevier Science, Boston (2006)

Part II
Air Quality Modelling

Atmospheric modelling covers the modelling of air quality as well. To demonstrate its importance, it is enough to mention the growing air pollution in metropolises, the toxic emission of industrial areas and power plants, the danger of radioactive gases after an accident in a nuclear power plant, but even the natural hazards, such as the drift of ash after a volcanic eruption. In all of these cases the fast and accurate forecast of the pollutant's trajectory is indispensable. Air quality models have their own difficulties when solving the corresponding partial differential equations, moreover, they are usually coupled with a numerical weather prediction model which provides the actual weather situation and the values of meteorological variables being of interest for computing the pollutant's trajectory and the chemical reactions taking place on its way. The main difficulty of solving air pollution transport models is the mathematical description of the complicated chemical reactions, which lead to nonlinear coupling between the equations. This part of the issue is devoted to present several numerical methods aiming at overcoming this and other challenges.

Chapter 5 deals with atmospheric dispersion processes which occur on several temporal and spatial scales with the complexity of chemistry ranging from passive tracers (e.g., dust) to chemically active species. The authors give an introduction to and analyse the two basic groups of atmospheric dispersion models: the Eulerian (deterministic) and the Lagrangian (stochastic) ones.

Chapter 6 treats the hydrodynamic modelling of industrial pollutants spreading in the atmosphere. An efficient methodology for the numerical solution of the problems is elaborated under real weather conditions. The results of numerical experiments, weather forecast, and the modelling of pollutants in the atmosphere verify this approach.

Chapter 7 gives a coordinate transformation which transforms differential problems imposed on unbounded domains to bounded ones. One of the main advantages of this approach is that by its application the numerical solution preserves the required qualitative property of non-negativity of the pollutants' concentration.

Chapter 8 considers the impact of climatic changes on pollution levels. The climatic changes might be linked to the increased frequency of extreme events in

many different areas. One of the most important consequences is the clear trend for global increase of the temperature. The chapters' results indicate that the climatic changes will lead to an increase of the pollution levels related to ozone in many parts of Europe.

As seen from the summary above, the chapters are mainly devoted to the efficient selection of numerical algorithms being appropriate to the given problem. Thus, the improvement of the existing numerical schemes as well as the development of new and even more efficient methods are still extremely important for the applications, such as air quality modelling. Hence, the chapters in Part II show how numerical methods, such those presented in Part I, are applied for modelling the transport and climatic changes of air pollution in real situations.

Chapter 5
Eulerian and Lagrangian Approaches for Modelling of Air Quality

Ádám Leelőssy, Tamás Mona, Róbert Mészáros, István Lagzi, and Ágnes Havasi

Abstract Simulation of the dispersion, chemical and physical transformations of air pollutants in the atmosphere is one of the most important and challenging tasks in environment science. Computations should be fast and the results should be precise to be used in decision support. There are two main approaches to solve atmospheric transport equations that describe the spatiotemporal variation of the concentrations of the air pollutants. These are Eulerian and Lagrangian models, and usually both models can be used in simulations. However, there are some cases where one of them can perform better than the other one. An appropriate choice and usage of a proper approach should be crucial to obtain sufficiently accurate results in a cost-efficient way.

Keywords Air quality • Atmospheric transport equation • Eulerian model • Lagrangian model • Operator splitting

5.1 Introduction

The aim of the application of air quality models is usually twofold. First is to estimate the concentration of air pollutants arising from emission sources. In this case we use models that have a better spatial and temporal representativeness than

Á. Leelőssy • T. Mona • R. Mészáros
Department of Meteorology, Eötvös Loránd University, Budapest, Hungary
e-mail: leelossyadam@gmail.com; motpaat@caesar.elte.hu; mrobi@nimbus.elte.hu

I. Lagzi
Department of Physics, Budapest University of Technology and Economics, Budapest, Hungary
e-mail: istvanlagzi@gmail.com

Á. Havasi (✉)
Department of Applied Analysis and Computational Mathematics, Eötvös Loránd University, Budapest, Hungary

MTA-ELTE Numerical Analysis and Large Networks Research Group, Budapest, Hungary
e-mail: havasia@cs.elte.hu

A. Bátkai et al. (eds.), *Mathematical Problems in Meteorological Modelling*,
Mathematics in Industry 24, DOI 10.1007/978-3-319-40157-7_5

a monitoring network and based on this information a load of air pollutants can be estimated (e.g., photochemical air pollution). Second is to predict the dispersion of air pollutants to mitigate a possible damage of air pollutants on environment and human health (e.g., accidental release).

Dispersion of air pollutants in the atmosphere can be described by the atmospheric transport equation (ATE). Mathematically, ATE is a set of second-order partial differential equations and it has the form:

$$\frac{\partial c_i}{\partial t} = -\mathrm{div}(\mathbf{u}c_i) + \mathrm{div}(\mathbf{K} \cdot \mathrm{grad}(c_i)) + R_i + E_i + D_i \tag{5.1}$$

where c_i is the concentration of the i-th air pollutant, $\mathbf{u}$ is the three-dimensional wind field and $\mathbf{K}$ is the matrix of the turbulent diffusion. The first term in the equation describes the effect of advection (wind field). The second term incorporates the mass transport due to turbulence occurring in the atmosphere. R_i denotes chemical reaction and radioactive decay (in case of radionuclides). E_i and D_i describe the emission sources and deposition processes in the atmosphere, respectively.

To estimate and predict the transport and transformation of air pollutants, ATE should be solved numerically. The solution of ATE (equipped with appropriate initial and boundary conditions) provides the spatiotemporal variation of the concentrations of air pollutants. There are two types of models that can be used, namely the Lagrangian and the Eulerian models [18].

The aim of this chapter is to provide a brief introduction to dispersion modelling and to show a few case studies for Eulerian and Lagrangian models. We will discuss the advantages and drawbacks of these two approaches.

5.2 Eulerian Models

The main idea in Eulerian models is to solve numerically the ATE (5.1) with the corresponding initial and boundary conditions in a fixed coordinate frame. As a result we obtain the space and time dependent concentration function $c = c(t, x, y, z)$. There are several numerical methods to solve this system. Usually, a grid is defined on the space domain of interest, and the spatial derivatives are discretized over the grid. As a result of the spatial discretization, at each grid-point we obtain a system of ordinary differential equations (ODE's) for the unknown, time-depending functions approximating the concentrations at the given point. (This procedure is called semi-discretization.) The obtained system of ODE's with the corresponding initial values (i.e., a Cauchy problem) is then solved numerically.

An example of Eulerian models is the Danish Eulerian Model (DEM), which has been developed at the National Environmental Research Institute of Denmark (NERI) [30]. The spatial domain of this model covers the whole of Europe. All important chemical species (sulphur pollutants, nitrogen pollutants, ammonia-ammonium, ozone, as well as many radicals and hydrocarbons) can be studied by this model. The chemical reactions are described by using the well-known

condensed CBM IV scheme. Today 56 chemical species are involved in the model, but its latest version, called UNI-DEM [1–3, 31], is able to treat 168 different species.

The advantages of the Eulerian approach are as follows:

- All physical and chemical processes can be taken into account, since the full transport equations, describing all the important physical and chemical processes, are solved.
- It is straightforward to use these models in 3-D.

The disadvantages are:

- Eulerian models lead to huge computational tasks. For example, in the case of a 10 km × 10 km horizontal resolution and 10 vertical layers in the Danish Eulerian Model, the number of grid points is several million. Moreover, if a time step of 2.5 s is used, then for a 1 year long run more than 12 million time steps are to be taken. By such a high resolution, discretization of the transport equations leads to a huge system of (non-linear) equations.
- It is not possible to study directly relationships between sources and receptor points (areas). This latter disadvantage can be overcome by using long sequences of scenarios, which, however, is rather time-consuming. Another possibility is to use inverse Eulerian transport models for the identification of source regions on global and continental scales.

The numerical treatment of large Eulerian models requires extra care [32]. The equations to be solved are rather complicated, since the right-hand sides of the equations contain terms of different mathematical properties. If some off-the-shelf numerical method is applied directly to the system, we cannot obtain a sufficiently accurate numerical solution within reasonable computational time. Therefore, operator splitting is usually applied [6]. During this procedure the right-hand side of the original system is divided into a few simple terms, and the corresponding systems—which are connected to each other through the initial conditions—are solved one after the other in each time step of the numerical integration. In this manner, we replace the original model with one in which the different sub-processes take place successively in time. This de-coupling procedure allows us to solve a few simpler systems instead of the original, complicated one. For example, in the DEM the subsystems describe the horizontal advection (5.2), the horizontal diffusion (5.3), the chemical reactions to which also emissions are added (5.4), the deposition (5.5) and the vertical exchange (5.6):

$$\frac{\partial c_i^{(1)}}{\partial t} = -\frac{\partial (u c_i^{(1)})}{\partial x_1} - \frac{\partial (v c_i^{(1)})}{\partial x_2}, \tag{5.2}$$

$$\frac{\partial c_i^{(2)}}{\partial t} = \frac{\partial}{\partial x_1}\left(k_1 \frac{\partial c_i^{(2)}}{\partial x_1}\right) + \frac{\partial}{\partial x_2}\left(k_2 \frac{\partial c_i^{(2)}}{\partial x_2}\right), \tag{5.3}$$

$$\frac{\partial c_i^{(3)}}{\partial t} = E_i(\mathbf{x}) + R_i(\mathbf{x}, c_1^{(3)}, \ldots, c_m^{(3)}), \tag{5.4}$$

$$\frac{\partial c_i^{(4)}}{\partial t} = -\sigma_i c_i^{(4)}, \tag{5.5}$$

$$\frac{\partial c_i^{(5)}}{\partial t} = -\frac{\partial (w c_i^{(5)})}{\partial x_3} + \frac{\partial}{\partial x_3}\left(k_3 \frac{\partial c_i^{(5)}}{\partial x_3}\right), \tag{5.6}$$

for $i = 1, \ldots, m$, where m denotes the number of chemical species, and the superscripts refer to the number of the given sub-problem. Assume that some approximation to the concentration vector $(c_1, \ldots, c_m)$ at the beginning of the time step has been found. The first system is solved by using this vector as a starting vector. The obtained solution will serve as the initial vector in the treatment of the second system and so on. The solution of the fifth system is accepted as an approximation to the concentration vector at the end of the time step.

The DEM splitting is based on a separation of the different physical processes of the air pollution transport and a separation of the vertical and horizontal directions for advection and diffusion. An alternative of the DEM splitting is the so-called physical splitting, where the sub-operators belong to the five basic air pollution processes, and there is no directional separation. In spite of the commonly used terminology, the DEM splitting is also based on a physical principle: the distinction of the vertical and horizontal directions is natural in shallow atmospheres, and makes it easier to switch on to the 2-D version of the model.

There are two approaches that can be used to increase the accuracy of the numerical solution and to resolve problems arising from the steep concentration gradient especially near a point source. These are nested and adaptive grids. Nested grid is static and uses a finer resolution subgrid near the point source. In the simulations using adaptive gridding, the density of grid cells changes in space and time according to a user defined algorithm that identifies regions of high numerical error. There are two types of adaptive gridding strategies, *h*-refinement and *r*-refinement [10]. In *h*-refinement the number of grid cells changes spatiotemporally according to an algorithm. However, in *r*-refinement—in contrast to the previous case—the number of grid cells remains constant, but the characteristic grid size changes (grid relocation). Both techniques have been successfully applied in air quality modeling [10, 15, 16]. Figure 5.1 shows an example of the usage of an *h*-refinement in case of an accidental release from the Paks Nuclear Power Plant (NPP) [15].

In this example, the grid cells are refined and coarsened by an algorithm that calculates the difference between the low and high order solutions thus providing a measure for spatial error. A refinement indicator for the *j*th cell is defined by a scaled error $serr_j$:

$$serr_j = \frac{e_j(t)}{atol/A_j + rtol \cdot c_j} \tag{5.7}$$

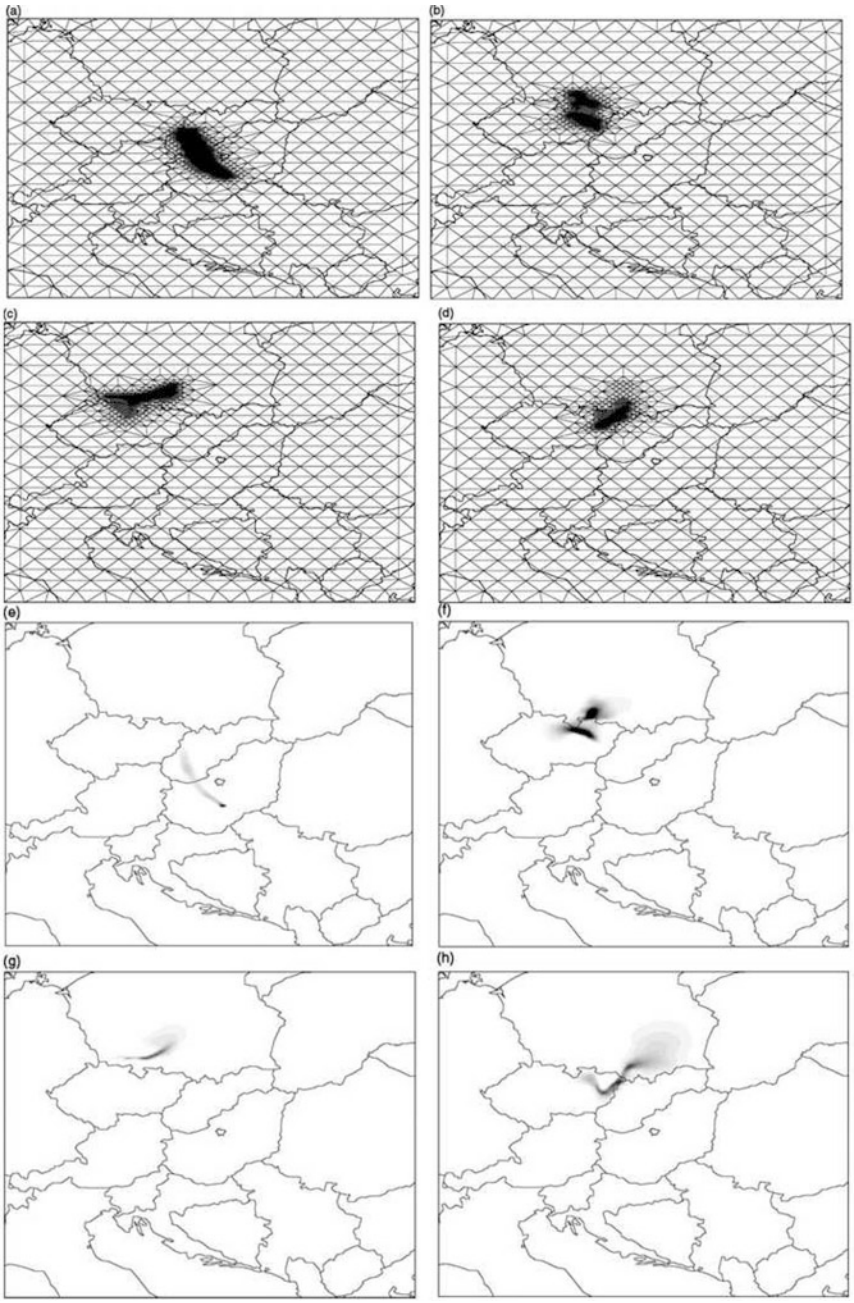

Fig. 5.1 Evolution of mesh structure in the surface layer ((**a**), (**b**), (**c**), (**d**)) and the activity of the ^{131}I ((**e**), (**f**), (**g**), (**h**)) in an accidental release simulation from the Paks NPP using an *h*-refinement. Reprinted from Lagzi et al. [15] with kind permission of Elsevier. Simulation started from 2 August 1998, at 0.00. (**a**)–(**d**) The adaptive mesh at $t_0 + 12$, $t_0 + 24$, $t_0 + 36$, $t_0 + 48$ h; (**e**)–(**h**) activity in the surface layer at t_0 $t_0 + 12$, $t_0 + 24$, $t_0 + 36$, $t_0 + 48$ h

where *atol* and *rtol* are the absolute and relative error tolerances, respectively, $e_j(t)$ is the local error estimate of the radionuclide over element j, c_j is the concentration of radionuclide over grid cell j and A_j is the area of jth cell.

There is a continuous plume from the point source in the first 12 h, because a continuous release was assumed for that time period. After the first 12 h, the plume is separated from the point source. It can be seen that the region of higher grid resolution continuously follows the path of the contaminated air. Typically the grid size in the simulation changed from $\sim$ 106 to 6.6 km by the adaptation routine allowing better spatial resolution in areas with high numerical error. It should be noted that always an extra computational time is required for adaptive gridding, because the mathematical algorithm should estimate numerical errors.

5.3 Lagrangian Models

Contrary to the deterministic partial differential equations of Eulerian models, the Lagrangian approach is based on stochastic ordinary differential equations to estimate the solution of the dispersion equation, see e.g. [8, 25]. Instead of the Eulerian concentration field, the model variables are position vectors of elementary units of the pollutant, often referred to as "particles" or "puffs". Model equations are equations of motion for each particle:

$$\frac{d\mathbf{v}}{dt} = \mathbf{g} - k(\mathbf{v} - \mathbf{v_a} - \mathbf{v_t}), \tag{5.8}$$

where $\mathbf{v}$ is the particle velocity vector, $\mathbf{v_a}$ is the grid-scale wind ("advection"), and $\mathbf{v_t}$ is the subgrid-scale wind fluctuation ("turbulence"). Sedimentation is taken into account with the $\mathbf{g}$ gravitational acceleration, and k is a function of the particle size, density and fluid viscosity, usually calculated based on Stokes' law. In case of gas tracers, the "particle" is only theoretical and thus particle size has no physical relevance. In this case, particle motion is assumed to follow the streamlines:

$$\mathbf{v} = \mathbf{v_a} + \mathbf{v_t}. \tag{5.9}$$

The grid-scale wind $\mathbf{v_a}$ is obtained from numerical weather prognostic model outputs, however, in a Lagrangian model, particle locations do not fit on the regular grid of meteorological data. This requires interpolation of meteorological fields for every particle location at every timestep, which can become the costliest part of a Lagrangian simulation.

The Lagrangian approach provides an intuitive way of simulation by following the pathway of the pollutants through the atmosphere from the source to the receptor. However, these trajectories are stochastic due to turbulent motions, and therefore different particles can follow significantly different trajectories even with equal initial conditions. The turbulent velocities are assumed to follow a Markov

process described by the Langevin equation, where the deviations of velocities σ_i and Lagrangian timescales of autocorrelation T_{Li} are parameterized based on precomputed Monin–Obukhov length and planetary boundary layer height [25]:

$$\mathrm{d}v_{t,i} = \frac{-v_{t,i}}{T_{L,i}}\mathrm{d}t + \sqrt{\frac{2}{T_{L,i}}}\sigma_i \mathrm{d}W, \tag{5.10}$$

where $\mathrm{d}W$ is the incremental component of a Wiener process with zero mean and $\mathrm{d}t$ variance.

The ODEs are usually integrated with a simple first-order method. Higher-order solvers are applicable, however, numerical error is also limited by the order of meteorological data interpolation [8]. The Δt computational timesteps are adjusted based on the vertical Lagrangian timescale T_{Lw} to provide sufficient temporal resolution for the calculation of vertical turbulence, the turbulent process with the shortest timescale. For most applications, the setting $\Delta t = 0.1T_{Lw}$ is a reasonable selection of the timestep [25].

The timescale T_{Lw} defines the strength of autocorrelation of vertical turbulent motions, and is in principle calculated from parameterizations. However, to save computational time, autocorrelation is often underestimated with a manually defined Δt, which results in a weaker representation of turbulence, but provides an acceptable approximation for large-scale simulations [25]. For computational representation of the Wiener process in the Langevin equation, normally distributed pseudorandom numbers are generated with the Mersenne-Twister algorithm. Random number generation contributes to the computational cost, and becomes a significant issue in parallel simulations, especially on GPUs [23].

The concentration field can be estimated from the spatial distribution of a large number of particles, treated as probability distribution of random variables. Depending on the scale, splitting the released mass of pollutants among 1000–10,00,000 particles can provide an acceptable accuracy in concentration results.

Trajectory models have been used to simulate the transport of pollution from industrial accidents [17], the dispersion of radioactive pollution originating from Fukushima [20, 26], and volcanic ash clouds like the one from Eyjafjallajökull [5, 13]. Another application of Lagrangian simulations is the atmospheric transport of wind-driven vectors of diseases. Trajectory models provided important information during the foot-and-mouth disease epidemics [11, 22].

Lagrangian simulations are popular tools of source identification and to explore source-receptor sensitivities [9, 26]. Backward trajectories are a plausible way to follow the atmospheric transport process from the receptor to the possible source points. This method has important applications in several fields of environmental modeling, like source identification in air quality protection [14, 21] as well as continental to global scale airmass climatology, aerosol or precipitation source estimation [7, 28].

5.3.1 Puff Models

Besides their position, each particle represents an amount of mass (or activity in case of radioactive materials) that changes through deposition and chemical reactions. These ODEs are solved at each timestep after the equations of motion. However, as each particle is treated independently, only local effects (in-particle reactions, simple decay and deposition) can be taken into account. The easiest and computationally cheapest way of concentration forecast with Lagrangian models is the puff approach that merges Gaussian and Lagrangian turbulence approach. Puff models regard particles as independent pollutant plumes, "puffs" with an extended volume. These puffs grow in size due to turbulent mixing in the atmosphere, with an inner concentration field following the normal distribution. This approach calculates grid-scale turbulence in Lagrangian, and subgrid-scale turbulence in Gaussian way [27]:

$$c(x_1, x_2, x_3) = \frac{1}{(2\pi)^{\frac{3}{2}}} \sum_{i=1}^{N} \frac{m_i}{\sigma_{1,i}\sigma_{2,i}\sigma_{3,i}} \times \\ \times \exp\left(\frac{-(x_{1,i}-x_1)^2}{2\sigma_{1,i}^2} + \frac{-(x_{2,i}-x_2)^2}{2\sigma_{2,i}^2} + \frac{-(x_{3,i}-x_3)^2}{2\sigma_{3,i}^2} \right), \tag{5.11}$$

where c is the concentration at a given location, m_i is the mass represented by the ith particle, $(x_{1,i}, x_{2,i}, x_{3,i})$ is the particle location and N is the number of particles. The σ deviations are functions of atmospheric turbulence, and calculated from timestep to timestep through additional ODEs. Despite the new equations, the puff approach requires significantly smaller number of puffs to estimate the concentration field, which largely accelerates the simulation.

Puff models merge the advantages of Lagrangian trajectories with Gaussian speed and simplicity of simulations. Therefore they are widely used in regulatory models in environmental protection and risk assessment [12, 19]. One of the most popular Lagrangian models, HYSPLIT is also often used in puff mode for dispersion simulations [17]. HYSPLIT improved the simple puff approach with separating horizontal and vertical mixing schemes. It also provides a "top-hat puff" method, using a horizontally normally distributed, vertically uniformly mixed puff [8].

5.3.2 Trajectory Models

Concentration field can be estimated from calculation of density based on a large number of single particle locations and their representative masses:

$$c(kernel) = \frac{\sum_{i=1}^{K} m_i}{V_{kernel}} \tag{5.12}$$

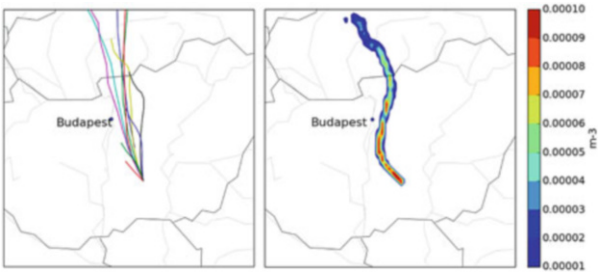

Fig. 5.2 Trajectory and concentration results of a Lagrangian model 24 h after the beginning of the Bugac wildfire in Hungary, 29 April 2012

where the concentration is assumed to be homogeneous within a kernel, and calculated with the total mass represented by all K particles within the kernel divided by the kernel volume. The density is usually calculated on a rectangular kernel that provides concentration output similar to that of an Eulerian model [8].

A large advantage of Lagrangian models, however, is that model integration requires no spatial discretization, thus the calculation of concentration values on a grid is only a diagnostic step. The primary model results are independent of the output grid, and concentrations can be obtained on different grids without rerunning the model. It allows a flexible grid setup with increased near-source resolution or non-rectangular grids [25]. The kernel shape and size can be user-defined [8], estimated from meteorological parameters or with clustering of particles. This makes Lagrangian models especially suitable for near-source simulations, where large gradients would require an extremely fine mesh in an Eulerian model [4]. An example of primary trajectory results and the derived concentration field is presented in Fig. 5.2.

Chemical reactions among different pollutants depend on their concentration at each timestep, which is not a prognostic variable in a Lagrangian model. Simple chemical processes, like deposition or decay can be modeled locally within each particle, however, for cases with complex chemistry, capabilities of Lagrangian models are limited and they are often coupled or replaced with Eulerian models [24].

As particle densities are calculated independently at each grid point, computational cost can be largely reduced if only a few receptor points are taken into account. This is an efficient solution if calculating the concentration field for the whole domain is unnecessary, especially in source-receptor sensitivity studies, e.g. the impact of factories or dust sources on the air quality of cities or environmental protection areas [29].

5.4 Conclusion

Atmospheric dispersion processes occur on several temporal and spatial scales with the complexity of chemistry ranging from passive tracers (e.g. dust) to non-linear interaction of millions of reactants (e.g. urban air). Therefore, significantly different modeling approaches have been developed to handle this wide range of environmental problems. In the present work, we have briefly introduced the two main groups of atmospheric dispersion models: the Eulerian (deterministic) and the Lagrangian (stochastic) approach. While both model types solve the atmospheric transport equation, their fitness for a particular purpose is very different. In general, Eulerian models are more appropriate for handling complex chemistry and detailed time- and space-continuous emission inventories. They are easily coupled either one-way or two-way with numerical weather prognostic models. On the other hand, Lagrangian models are usually applied for backward simulations, to explore source-receptor relationships and for near-source concentration estimations.

A more detailed comparison is presented in Table 5.1.

Both type of atmospheric dispersion models have important applications in environmental science and policy making. Regulatory and decision support models have saved several lives and large value of property in recent events like the Fukushima nuclear accident or the foot-and-mouth disease epidemics. On the other

Table 5.1 Comparison of Eulerian and Lagrangian dispersion models

	Eulerian	Lagrangian
Turbulence	Deterministic	Stochastic
Prognostic variable	Concentration field	Particle location vectors
Discretization	Discrete in space and time	Discrete in time, continuous in space
Chemistry	Complex chemistry can be easily treated in the model	Chemical reactions require an extra diagnostic step at each timestep
Meteorological models	Possibility of integration with numerical weather prognostic models	Meteorological data must be interpolated to each particle location at each time step
Emission data	Handling source data from continuous large-scale emission inventories	Mostly applied for point or area emissions bounded in space and time
Resolution	Numerical solution and computational cost is highly dependent on mesh resolution	Numerical solution is independent of the output grid, might depend on input data resolution
Output	Concentration is prognostic variable, output grid is the same as computational mesh	Primary model results are particle locations. Kernels for concentration are either user-defined or calculated in a diagnostic way

(continued)

Table 5.1 (continued)

	Eulerian	Lagrangian
Near-source treatment	Large near-source errors due to cell averaging	Numerical solution is continuous in space, near-source output kernels can be refined without extra computational cost
Source-receptor studies	Inverse modelling and source-receptor relationships require extensive model modifications and/or diagnostics	Simple calculation of source-receptor sensitivities and backward trajectories
Main area of applications	Regulatory models with complex chemistry and/or continuous releases (e.g. urban areas)	Fast response regulatory models with simple chemistry (e.g. nuclear accidents, volcanic ash)
		Source-receptor sensitivity studies, source identification
	Integrated atmospheric chemistry transport models	Airmass identification, exploration of atmospheric transport pathways on climatological scales

hand, the better understanding of large-scale atmospheric transport pathways of aerosols and greenhouse gases has become a key priority in environmental modeling from urban air quality protection to climate change. With the improvement of computational performance and the increasing scientific interest in atmospheric transport processes, the range of atmospheric dispersion model applications is largely widening. Therefore, understanding of modeling principles and finding the best model for the particular purpose as well as further development of both Eulerian and Lagrangian dispersion models is of a high importance.

Acknowledgements The authors acknowledge the support of the Hungarian Research Fund (K104666, K109109 and K116506).

References

1. Alexandrov, V., Owczarz, W., Thomsen, P.G., Zlatev, Z.: Parallel runs of large air pollution models on a grid of SUN computers. Math. Comput. Simul. **65**, 557–577 (2004)
2. Ambelas Skjøth, C., Bastrup-Birk, A., Brandt, J., Zlatev, Z.: Studying variations of pollution levels in a given region of Europe during a long time-period. Syst. Anal. Model. Simul. **37**, 297–311 (2000)
3. Bastrup-Birk, A., Brandt, J., Uria, I., Zlatev, Z.: Studying cumulative ozone exposures in Europe during a 7-year period. J. Geophys. Res. **102**, 23917–23035 (1997)

4. Brandt, J., Mikkelsen, T., Thykier-Nielsen, S., Zlatev, Z.: Using a combination of two models in tracer simulations. Math. Comput. Model. **23**, 99–115 (1996)
5. Dacre, H.F., Grant, A.L.M., Hogan, R.J., Belcher, S.E., Thomson, D.J., Devenish, B.J., Marenco, F., Hort, M.C., Haywood, J.M., Ansmann, A., Mattis, I., Clarisse, L.: Evaluating the structure and magnitude of the ash plume during the initial phase of the 2010 Eyjafjallajökull eruption using lidar observations and NAME simulations. J. Geophys. Res.-Atmos. **116** (2011). doi:10.1029/2011JD015608
6. Dimov, I., Faragó, I., Havasi, Á., Zlatev, Z.: Different splitting techniques with application to air pollution models. Int. J. Environ. Pollut. **32**(2), 174–199 (2008)
7. Dirmeyer, P.A., Brubaker, K.L.: Characterization of global hydrologic cycle from a back-trajectory analysis of atmospheric water vapor. J. Hydrometeorol. **8**, 20–37 (2007)
8. Draxler, R.R., Hess, G.D.: An overview of the HYSPLIT-4 modelling system for trajectories, dispersion and deposition. Aust. Meteorol. Mag. **47**, 295–308 (1998)
9. de Foy, B., Burton, S.P., Ferrare, R.A., Hostetler, C.A., Hair, J.W., Wiedinmyer, C., Molina, L.T.: Aerosol plume transport and transformation in high spectral resolution lidar measurements and WRF-Flexpart simulations during the MILAGRO field campaign. Atmos. Chem. Phys. **11**, 3543–3563 (2011)
10. Garcia-Menendez, F., Odman, M.T.: Adaptive grid use in air quality modelling. Atmosphere **2**, 484–509 (2011)
11. Garner, M.G., Hess, G.D., Yang, X.: An integrated modelling approach to assess the risk of wind-borne spread of foot-and-mouth disease virus from infected premises. Environ. Model. Assess. **11**, 195–207 (2006). doi:10.1007/s10666-005-9023-5
12. Ghannam, K., El-Fadel, M.: Emissions characterization and regulatory compliance at an industrial complex: an integrated MM5/CALPUFF approach. Atmos. Environ. **69**, 156–169 (2013)
13. Haszpra, T., Tél, T.: Volcanic ash in the free atmosphere: a dynamical systems approach. J. Phys. Conf. Ser. **333** (2011). doi:10.1088/1742-6596/333/1/012008
14. Koracin, D., Vellore, R., Lowenthal, D.H., Watson, J.G., Koracin, J., McCord, T., DuBois, D.W., Chen, L.-W.A., Kumar, N., Knipping, E.M., Wheeler, N.J.M., Craig, K., Reid, S.: Regional source identification using lagrangian stochastic particle dispersion and HYSPLIT backward-trajectory models. J. Air Waste Manage. **61**, 660–672 (2011)
15. Lagzi, I., Kármán, D., Tomlin, A.S., Turányi, T., Haszpra, L.: Simulation of the dispersion of nuclear contamination using an adaptive Eulerian grid model. J. Environ. Radioact. **75**, 59–82 (2004)
16. Lagzi, I., Tomlin, A.S., Turányi, T., Haszpra, L.: Modelling photochemical air pollutant formation in Hungary using an adaptive grid technique. Int. J. Environ. Pollut. **36**, 44–58 (2009)
17. Leelőssy, A., Ludányi, E.L., Kohlmann, M., Lagzi, I., Mészáros, R.: Comparison of two Lagrangian models: a case study for the chemical accident in Rouen, 21–22 January 2013. Időjárás **117**, 435–450 (2013)
18. Leelőssy, A., Molnár, F. Jr., Izsák, F., Havasi, Á., Lagzi, I., Mészáros, R.: Dispersion modeling of air pollutants in the atmosphere: a review. Cent. Eur. J. Geosci. **6**, 257–278 (2014)
19. Levy, J.I., Spengler, J.D., Hlinka, D., Sullivan, D., Moon, D.: Using CALPUFF to evaluate the impacts of power plant emissions in Illinois: model sensitivity and implications. Atmos. Environ. **36**, 1063–1075 (2002)
20. Long, N.Q., Truong, Y., Hien, P.D., Binh, N.T., Sieu, L.N., Giap, T.V., Phan, N.T.: Atmospheric radionuclides from the Fukushima Dai-ichi nuclear reactor accident observed in Vietnam. J. Environ. Radioact. **111**, 53–58 (2012)
21. McGowan, H., Clark, A.: Identification of dust transport pathways from Lake Eyre, Australia using HYSPLIT. Atmos. Environ. **42**, 6915–6925 (2008)
22. Mikkelsen, T., Alexandersen, S., Astrup, P., Champion, H.J., Donaldson, A.I., Dunkerley, F.N., Gloster, J., Sorensen, J.H., Thykier-Nielsen, S.: Investigation of airborne foot-and-mouth disease virus transmission during low-wind conditions in the early phase of the UK 2001 epidemic. Atmos. Chem. Phys. **3**, 2101–2110 (2003)

23. Molnár, F. Jr., Szakály, T., Mészáros, R., Lagzi, I.: Air pollution modelling using a Graphics Processing Unit with CUDA, Comput. Phys. Commun. **181**, 105–112 (2010)
24. Oettl, D., Uhrner, U.: Development and evaluation of GRAL-C dispersion model, a hybrid Eulerian-Lagrangian approach capturing NO-NO2-O3 chemistry. Atmos. Environ. **45**, 839–847 (2011)
25. Stohl, A., Forster, C., Frank, A., Seibert, P., Wotava, G.: Technical note: the Lagrangian particle dispersion model FLEXPART version 6.2. Atmos. Chem. Phys. **5**, 2461–2474 (2005)
26. Stohl, A., Seibert, P., Wotawa, G., Arnold, D., Burkhart, J.F., Eckhardt, S., Tapia, C., Vargas, A., Yasunari, T.J.: Xenon-133 and caesium-137 releases into the atmosphere from the Fukushima Dai-ichi nuclear power plant: determination of the source term, atmospheric dispersion and deposition. Atmos. Chem. Phys. **12**, 2313–2343 (2012)
27. Thykier-Nielsen, S., Deme, S., Mikkelsen, T.: Description of the atmospheric dispersion module RIMPUFF. RODOS(WG2)-TN(98)-02 (1999)
28. Warneke, C., Froyd, K.D., Brioude, J., Bahreini, R., Brock, C.A., Cozic, J., de Gouw, J.A., Fahey, D.W., Ferrare, R., Holloway, J.S., Middlebrook, A.M., Miller, L., Montzka, S., Schwarz, J.P., Sodemann, H., Spackman, J.R., Stohl, A.: An important contribution to springtime Arctic aerosol from biomass burning in Russia. Geophys. Res. Lett. **37** (2010). doi:10.1029/2009GL041816
29. Zhou, Y., Levy, J.I., Hammitt, J.K., Evans, J.S.: Estimating population exposure to power plant emissions using C ALPUFF: a case study in Beijing. China Atmos. Environ. **37**, 815–826 (2003)
30. Zlatev, Z.: Computer Treatment of Large Air Pollution Models. Kluwer Academic Publisher, Dordrecht-Boston-London (1995)
31. Zlatev, Z.: Impact of future climate changes on high ozone levels in European suburban areas. Clim. Chang. **101**, 447–483 (2010)
32. Zlatev, Z., Dimov, I.: Computational and Numerical Challenges in Environmental Modelling. Elsevier, Amsterdam (2006)

Chapter 6
Hydrodynamic Modeling of Industrial Pollutants Spreading in Atmosphere

Vitaliy A. Prusov and Anatoliy Y. Doroshenko

Abstract An efficient methodology for numerical solving problems of hydrodynamic modeling of spreading atmospheric pollutants from towering stationary sources of emissions under real weather conditions is described. The methodology is based on the "one-way interaction" approach, implemented on embedded grids and characterized by high accuracy and low computational expenses. The results of numerical experiments, weather forecast and modeling of impurities in the atmosphere are presented.

Keywords Hydrodynamic modeling • Atmospheric processes • Air pollution • Numerical methods

6.1 Introduction

Emissions from industrial plants often are stationary and focused in a particular place. Suspended impurities from these emissions are distributed by air flows depending on wind direction, turbulence intensity and atmospheric stratification. Studying the role of atmospheric physical-chemical and kinetic processes in the spreading of the aerosol particles, the transformation of trace gas components of natural and anthropogenic origin has begun yet in the second half of the last century. In that time the data of massive observations made in the inhabited localities were

V.A. Prusov
Department of Geography of Kyiv National University by Taras Shevchenko, Kyiv, Ukraine

Academician Glushkov prosp. 2a, Kyiv, Ukraine

Ukrainian Hydrometeorological Institute, Nauki prosp. 37, Kyiv, Ukraine
e-mail: vitaliy@softick.com

A.Y. Doroshenko (✉)
Department of Informatics and Computer Engineering of National Technical University of Ukraine, "Kyiv Polytechnic Institute", Peremohy prosp. 37 building 18, Kyiv, Ukraine

Institute of Software Systems of National Academy of Sciences of Ukraine, Academician Glushkov prosp. 40, building 5, Kyiv, Ukraine
e-mail: doroshenkoanatoliy2@gmail.com

A. Bátkai et al. (eds.), *Mathematical Problems in Meteorological Modelling*,
Mathematics in Industry 24, DOI 10.1007/978-3-319-40157-7_6

compiled and statistically analyzed to identify the role of meteorological conditions and other factors influencing the level of pollution. As indicators of air pollution there were average and maximum permissible concentration, the frequency of concentrations exceeding the maximum permissible concentration and the duration of increased levels of air pollution.

According to [1], the impurity distribution in space near a source point is described by a Gaussian law. The discrepancy between the experimental and calculated values of concentrations at a considerable distance from the emission source has been unsuccessfully tried to eliminate by introducing a dependence of the horizontal component of the diffusion coefficient on the distance from the source. To describe the distribution of atmospheric pollutant concentrations it is often used logarithmic normal law (LNL) [2] used long ago in a number of papers (e.g. [3]). It was found that 75 % of the points of the probability distribution lay near the straight line. This suggested that the distribution of the impurity concentration in the atmosphere obeys LNL and in this connection the implementation of such a distribution was considered as a criterion of verification of the observational concentrations of impurities in a tested region.

Statistical analysis of the occurrence repeatability of specific pollutant concentration values, as well as the average values of the concentrations of impurities, without relying on LNL have found application in [4, 5]. Some methods of statistical analysis studied multiple correlation, i.e. accounting impact of a combination of factors. However, as the practice of their application has shown, detecting the main factors was not always possible and the effectiveness of this approach was limited. Therefore, the researchers essentially concerned studying correlation between the impurity concentration at one or several locations and individual factors, excluding the effect of other factors.

In the analysis of random fields in various meteorological studies sometimes there was used the method of decomposition of the initial information on statistically orthogonal system of functions [6]. It allows calculating the impurity scattering in the atmosphere, as a rule, at open and extra-urban areas in the presence of a relatively small number of sources of air pollution.

Constructing a detailed field of concentrations, especially in unfavorable weather conditions, is obviously much easier to carry out with hydrodynamic models than by calculation being based on empirical data [7–12]. Advanced computer technologies have led to the inclusion in the task of modeling the laws of propagation of impurities and the characteristics of their spatial and temporal distribution of meteorological aspects that are associated primarily with the simulation of atmospheric convection and diffusion [13–23].

Objectives of environmental monitoring require the use of modern high-performance computing resources due to the need to process large amount of data, particularly, in sorting and preprocessing for further use in complex numerical algorithms related to the transport of pollutants in the environment. Creating models of estimation of concentration fields and source parameters, using observational data and model representations of pollution spreading from a lot of sources of emissions, would monitor more reliably the main parameters of anthropogenic

pollution areas [9]. This approach makes it possible to determine the information content of the observing systems and to optimize the position and the number of sampling points. The task of identifying relevant sources of pollution is important as its decision can determine the contribution of individual sources (companies, cities, countries) in air pollution or soil at a given point. This should be considered when creating new sources of pollution while commissioning of new industrial enterprises and the management of existing emissions to the total amount that does not exceed the established norms.

This chapter presents an efficient methodology developed by the authors in Ukrainian Hydro-meteorological Institute and Institute of Software Systems of National Academy of Sciences of Ukraine, for numerical solving problems of hydrodynamic modeling of spreading of atmospheric pollutants from towering stationary sources of emissions under real weather conditions. The numerical method developed here for meteorological processes of regional scale differs from existing ones by high accuracy of the fourth order, low computational expenses and excellent stability property.

The methodology is based on the "one-way interaction" approach [24–27]. Since late 1960s researchers have seen importance of use of sufficiently fine computational grids in regional models of forecasting meteorological phenomena. It was proposed to do forecasting within "telescopic" scheme of the system of successively smaller areas with increasing resolution where one-way interaction method is obtained in the case of models when unsteady boundary conditions are taken from the "near-field" system of larger grid. Likely reasoned formulation of meteorological conditions in the "near-field" allows to linearize the problems of pollution near the sources of emissions and to solve it analytically for a virtually unlimited number of sources.

The main advantages of the presented model of regional atmospheric processes and its use for modeling pollutants spreading in atmosphere, what differ it from other models, are high accuracy and low cost numerical method obtained from combining the concept of "one-way interaction" and interpolation techniques.

6.2 General Hydrodynamic Model of Air Circulation

Contemporary ecology, that studies among others the state of atmosphere of Earth, is to a great extent an important subdiscipline of continuum mechanics closely related to many other sections of physics. Purely statistical methods being used in theoretical research of meteorological processes in the first half of twentieth century could not represent adequately substantially nonlinear properties of atmospheric processes and that is why were unsuccessful. They have been replaced by hydrodynamic methods which have given rise numerical modeling of complex problems with ecological-meteorological one as a top application.

Modern nonlinear theory of continuous media based on the approach of Newton liquid allows presenting a very complicated problem as the system of equations cor-

responding physical laws that are well tested in many applied areas of hydrodynamics. In general case these laws are mathematically expressed by following equations:

- Continuity

$$\frac{d\rho}{dt} + \rho\nabla \cdot \boldsymbol{V} = 0; \tag{6.1}$$

- hydrodynamics in vector form

$$\frac{d\boldsymbol{V}}{dt} + 2\Omega \times \boldsymbol{V} = \frac{1}{\rho}\nabla p + \boldsymbol{g} + \nabla \cdot \vec{\tau}_n; \tag{6.2}$$

- spreading heat in the atmosphere

$$\frac{d\theta}{dt} = \nabla \cdot (k_T \nabla\theta - F_{rad}) + \left(\frac{p_{00}}{p}\right)^{R/C_p} \frac{L}{C_p} Q_H; \tag{6.3}$$

- spreading specific humidity

$$\frac{dq}{dt} = \nabla \cdot (k_d \nabla q) + Q_H; \tag{6.4}$$

- spreading condensed moisture (water content)

$$\frac{d\delta}{dt} = \nabla \cdot (k_d \nabla \delta) - Q_H; \tag{6.5}$$

- distribution of concentrations of suspended impurities

$$\frac{ds}{dt} = \nabla \cdot (k_d \nabla \mathrm{s}) - S_s - J_s; \tag{6.6}$$

- state

$$p = R\rho T. \tag{6.7}$$

Following denotations are accepted in the system of Eqs. (6.1), (6.2), (6.3), (6.4), (6.5), (6.6), and (6.7): t is time; ρ is the air density; $\vec{\tau}_n$ is friction tension tensor when moving air, T is the absolute temperature of air; $\theta = T(p_{00}/p)^{R/C_p}$ is the potential temperature of air; p is the atmospheric pressure of air, p_{00} is the atmospheric pressure on the underlying surface; R is the universal gas constant for dry air; C_p is the specific heat capacity at a constant pressure; q is the specific humidity (mass of water vapor in a unit of mass of air); δ is the specific water content (mass of the condensate moisture in a unit of mass of air); s is the concentration of impurities in air; Ω is the angular velocity of Earth rotation; $\boldsymbol{g} = (0, 0, g)$ is the acceleration

of gravity; k_T is the molecular coefficient of heat conductivity; k_d is the molecular coefficient; F_{rad} is the density of radiation stream of energy, depending on factors of absorption, radiation, reflection and dispersion; L is the latent heat of evaporation; Q_H is the change of specific humidity q and specific water content δ in a volume unit of air in those parts of atmosphere where phase transitions of the first kind take place (evaporation and condensation, melting and crystallization, sublimation and desublimation); S_s is the change of concentration of impurities in a volume unit of air moving in that part of atmosphere where chemical reactions take place; J_s is the speed of washing out of impurities by precipitation.

Except the denotations above in the system of Eqs. (6.1), (6.2), (6.3), (6.4), (6.5), (6.6), and (6.7) other generally accepted dependences are used:

$$\operatorname{div} \boldsymbol{V} = \nabla \cdot \boldsymbol{V} = \frac{\partial \mathrm{v}_1}{\partial x_1} + \frac{\partial \mathrm{v}_2}{\partial x_2} + \frac{\partial \mathrm{v}_3}{\partial x_3} = \frac{\partial \mathrm{v}_j}{\partial x_j} \quad (j = 1,\ 2,\ 3)\,;$$

$$\operatorname{grad} \Phi = \nabla \Phi = i \partial \Phi / \partial x_i \quad (i = 1,\ 2,\ 3)\,;$$

$$\frac{d\mathcal{R}}{dt} = \frac{\partial \mathcal{R}}{\partial t} + \mathrm{v}_1 \frac{\partial \mathcal{R}}{\partial x_1} + \mathrm{v}_2 \frac{\partial \mathcal{R}}{\partial x_2} + \mathrm{v}_3 \frac{\partial \mathcal{R}}{\partial x_3} \equiv \frac{\partial \mathcal{R}}{\partial t} + \mathrm{v}_i \frac{\partial \mathcal{R}}{\partial x_i} \quad (i = 1, 2, 3)\,;$$

$$\operatorname{div} \vec{\tau}_n = \nabla \cdot \vec{\tau}_n = \frac{\partial \vec{\tau}_1}{\partial x_1} + \frac{\partial \vec{\tau}_2}{\partial x_2} + \frac{\partial \vec{\tau}_3}{\partial x_3} = \frac{\partial \vec{\tau}_j}{\partial x_j} \quad (j = 1,\ 2,\ 3)\,;$$

$$\left(\operatorname{div} \vec{\tau}_n\right)_i = \left(\nabla \cdot \vec{\tau}_n\right)_i = \frac{\partial \vec{\tau}_{i1}}{\partial x_1} + \frac{\partial \vec{\tau}_{i2}}{\partial x_2} + \frac{\partial \vec{\tau}_{i3}}{\partial x_3} = \frac{\partial \vec{\tau}_{ij}}{\partial x_j} \quad (j = 1,\ 2,\ 3)\,,$$

where $\boldsymbol{V} = (\mathrm{v}_1, \mathrm{v}_2, \mathrm{v}_3)$ is the velocity of moving continuous environment, $\boldsymbol{X} = (x_1, x_2, x_3)$ are the coordinates of an elementary volume of air; for short, in every equality above there is carried out adding up on a twice repetitive index in a monomial.

The system of Eqs. (6.1), (6.2), (6.3), (6.4), (6.5), (6.6), and (6.7) describes the turbulent streams of impulse, heats and the masses, and also elements characterizing the sources (sinks) of mass and energies due to phase transformations of atmospheric moisture and radiation processes. Direct involving of these micro- and meso-scale processes into the model of circulation of atmosphere is unreasonable for two major reasons.

First, not all these processes can be described by means of exact differential equations. The actual picture of turbulent flows of impulse, heats and the masses in a boundary layer, phase and radiation processes in the real atmosphere is extremely complicated. It depends on geometrical and optical features of the underlying surface, vertical gradients of heat and humidity, convective motions in layers with moisture-adiabatic instability and in inverse layers. It depends also on the structure of clouds, plenty of gaseous and fine-grained constituents of air with different spectral properties of absorption, radiation, dispersions of and others.

Contemporary mathematical models of atmosphere cannot adequately reproduce all this multiparameter stochastic picture of turbulent, phase and radiation processes.

Second, numerical realization of the model would require diminishing step of a grid to the size which would entail the increase of general amount of points of the grid in the areas of decision and, consequently, numeral integration of the model would be unreal even for the most powerful modern computers. Therefore processes of interaction of atmosphere and the underlying surface, radiant and phase heat exchange, convection and formation of clouds attribute to subscale processes, and solving problem of modelling subscale processes is of great importance.

6.3 A Model of Turbulence

An initial point for mathematical description of atmospheric processes in the most general case, including turbulent processes, is acceptability for their interpretation by the system of Eqs. (6.1), (6.2), (6.3), (6.4), (6.5), (6.6), and (6.7) that describes instantaneous motion of atmospheric air. In recent years there is increasing application of modelling turbulence based on the method of direct numerical simulation (DNS). Basic assumption of DNS is that Eqs. (6.1), (6.2), (6.3), (6.4), (6.5), (6.6), and (6.7) adequately describe not only laminar but also turbulent processes. Accordingly, within the framework of this approach, calculation of turbulent processes is performed by the direct (without some preliminary averaging) numerical solving Eqs. (6.1), (6.2), (6.3), (6.4), (6.5), (6.6), and (6.7). In doing so regardless of the process is two-dimensional or three-dimensional, stationary or non-stationary, three-dimensional non-stationary Eqs. (6.1), (6.2), (6.3), (6.4), (6.5), (6.6), and (6.7) must be used since turbulence is fundamentally the three-dimensional and non-stationary phenomenon. In addition, for exact enough decision of all spatial-temporal scales for turbulence DNS suggests three-dimensional non-stationary computation on grids fine enough even in those cases when the purpose of computation is determining only parameters of averaging processes. Because of extreme computational complexity of this approach its practical realization in solving intricate problems of dynamic meteorology is actually not feasible. So seemingly, during the nearest decades as a basic working instrument for solving applied problems of dynamic meteorology there will be semi-empiric methods of RANS (Reynolds Averaged Navier–Stokes) based on use of averaged on Reynolds equations of Navier–Stokes in combination with different semi-empiric models of turbulence.

One of the families of turbulence models widely used in practice is based on conception of eddy viscosity and turbulent diffusion. Following Boussinesq [28], Reynolds' tensions are determined as product of the eddy viscosity and constituents of the tensor of averaged speeds of deformation:

$$-\overline{\mathrm{v}_i'\mathrm{v}_j'} = \nu_t \left(\frac{\partial \overline{\mathrm{v}_i}}{\partial x_j} + \frac{\partial \overline{\mathrm{v}_j}}{\partial x_i} \right) - \frac{2}{3}\delta_{ij}k. \tag{6.8}$$

Equation (6.8) itself does not involve the turbulence model and only characterizes the structure of such model; the basic task here is the task of definition of the function ν_t. Unlike the coefficient of molecular viscosity ν, the coefficient ν_t is determined by the state of turbulence and is not connected with properties of liquid. It can vary greatly from point to point dependently on the type of flow.

The model of turbulent viscosity suggests that the transfer of amount of motion takes place like the transfer due to molecular motion. Exposed to criticism as physically groundless, this model, however, is used widely as it allows getting fully acceptable results in meteorological practice. By direct analogy with the turbulent transfer of amount of motion the concept of turbulent diffusion supposes following relation of the transfer of substance $\mathfrak{H}$ (masses, heats, moistures or admixtures) and the gradient of this substance $\overline{\mathfrak{H}}$:

$$-\overline{u_j'\mathfrak{H}'} = d_t \frac{\partial \overline{\mathfrak{H}}}{\partial x_j}, \tag{6.9}$$

where d_t is the coefficient of turbulent diffusion. Like turbulent viscosity d_t is not intrinsic property of environment and depends on the state of turbulence. According to the hypothesis of Reynolds about an analogy on the turbulent transfer of mass or heat and amount of motion, following relation takes place:

$$d_t = \frac{\nu_t}{\sigma_t}. \tag{6.10}$$

The quantity σ_t is called the turbulent number of Prandtl or Schmidt. Unlike the coefficients of turbulent diffusion and turbulent viscosity σ_t poorly changes both within the limits of the stream and from a process to another process. Therefore the value of σ_t is accepted in a number of models as a constant, near to 1, though it experiences influence of floatation and curvature of the stream lines. Consequently, the basic problem of turbulence closure is a method of determining the coefficient of turbulent viscosity ν_t.

An important merit of turbulent viscosity models is their relative simplicity, clarity and computational efficiency. Within the framework of Boussinesq's approach the closure problem is reduced to determining one scalar value (of turbulent viscosity) instead of six components of the tensor $\vec{\tau}_n$.

There are a few different models of turbulence [29–31]. These models have a different degree of complexity, beginning from the simple one in which ν_t, k_T, k_d are expressed through local descriptions of averaged fields of velocity, temperatures and concentrations, up to complicated enough models that include equations of transfer for characteristic velocities and linear scales of turbulent flows.

The most widely used in hydrodynamic models has become a semi-empiric model known in scientific community as (k–ε) model of turbulence [30]. Its practical use showed satisfactory results in the process of modelling complicated three-dimensional flows including recirculation ones at the same values of empiric constants. However, application of (k–ε) model of turbulence in dynamic meteorol-

ogy leads to difficult problems at integrating differential equations, that constitute the basis of (k–ε) model, where there is a necessity to formulate initial and border conditions for variables k and ε along with ordinary requirements to the variables of averaged motion (i.e. to the meteorological values). It is mostly not a trivial task, especially at setting initial conditions for k and ε, as meteorological values of the averaged motion are not exact. This problem remains also in the case of other models which are combinations of density of kinetic energy of turbulence k and scale of length l like $f = k^{\alpha} l^{\beta}$.

One way to remove the problem of formulation of initial and border conditions in the model of turbulence is the method which allows changing value of eddy viscosity ν_t by independent differential equation describing the transfer of this value. In papers [29, 32–37] some modifications of this model of turbulence are offered in which connection between turbulent viscosity and parameters of averaged flow is set directly by non-stationary nonlinear equation for turbulent viscosity ν_t:

$$\frac{\partial \nu_t}{\partial t} + u_j \frac{\partial \nu_t}{\partial x_j} = D_{\nu_t} + G_{\nu_t} - \varepsilon_{\nu_t}, \quad j = 1, 2, 3, \tag{6.11}$$

where D_{ν_t} is diffusion of turbulent viscosity ν_t; G_{ν_t} is a generation of ν_t due to a wind shear and forces of floatation; ε_{ν_t} is the decay of ν_t due to dissipation process.

Presently the most popular model with one Eq. (6.11) is the model [37] in which instead of eddy viscosity ν_t a relative variable $\tilde{\upsilon} = \nu_t / f_{\upsilon 1}$ is used where $f_{\upsilon 1} = \bar{\tilde{\upsilon}}^3 / \left(\bar{\tilde{\upsilon}}^3 + C_{\upsilon 1}^3\right)$, $\bar{\tilde{\upsilon}} = \tilde{\upsilon}/\nu$, $C_{\upsilon 1} = 0.71$. Diffusion of turbulent viscosity $\tilde{\nu}$ looks like

$$D_{\nu_t} = \frac{1}{\sigma} \frac{\partial}{\partial x_j} \left[(\nu + \tilde{\nu}) \frac{\partial \tilde{\upsilon}}{\partial x_j} \right], \quad \sigma = \frac{2}{3};$$

or

$$D_{\nu_t} = \frac{1}{\sigma} \left\{ \frac{\partial}{\partial x_j} \left[(\nu + \tilde{\upsilon}) \frac{\partial \tilde{\upsilon}}{\partial x_j} \right] + c_{b2} \frac{\partial \tilde{\upsilon}}{\partial x_j} \frac{\partial \tilde{\upsilon}}{\partial x_j} \right\}, \quad c_{b2} = 0,622,$$

as turbulent viscosity is not a fundamental physical entity and it is not subject to obligations of conservation laws.

In the member describing a generation of $\tilde{\upsilon}$ the derivative of velocity is replaced by an invariant tensor expression $G_{\nu_t} = c_{b1} \tilde{S} \tilde{\upsilon}$ where $\tilde{S} = S + \tilde{\upsilon} f_{\upsilon 2} / \left(\chi^2 d^2\right)$, $S = \sqrt{2\Omega_{ij}\Omega_{ij}}$, $\Omega_{ij} = \left(\partial \mathrm{v}_i / \partial x_j - \partial \mathrm{v}_j / \partial x_i\right)/2$, $\chi = 0.41$, d is the distance from a solid surface, $f_{\upsilon 2} = 1 - \bar{\tilde{\upsilon}} / \left(1 + \bar{\tilde{\upsilon}} f_{\upsilon 1}\right)$.

Dissipative member ε_{ν_t} on right side of (6.11) is determined by following expression

$$\varepsilon_{\nu_t} = \left(c_{w1} f_w - \frac{c_{b1}}{k^2} f_{t2} \right) \left(\frac{\tilde{\upsilon}}{d_w} \right)^2,$$

in which d_w is the height of the first calculated level above the underlying surface; k is Carman's constant;

$$f_w = \xi \cdot \left(\frac{1 + c_{w3}^6}{\xi^6 + c_{w3}^6} \right)^{1/6}, \; \xi = \varepsilon \left[1 + c_{w2} \left(\varepsilon^5 - 1 \right) \right], \; \varepsilon = \frac{\tilde{v}}{\tilde{S} k^2 d_w^2}.$$

The function f_{t2}, providing suppression of the so-called "spontaneous" or "numerical" transition from laminar to turbulent motion mode in the boundary layer, is determined by the expression

$$f_{t2} = \mathrm{c}_{t3} \cdot \exp\left(-\mathrm{c}_{t4} \chi^2 \right).$$

The most complete model of Spalart and Allmaras [37] contains in the right side of (6.11) the term $f_{t1} \Delta U^2$, intended to initiate the laminar-turbulent transition in given point, is calculated by means of the formulas:

$$f_{t1} = \mathrm{c}_{t1} \xi_t \cdot \exp\left[-\mathrm{c}_{t2} \frac{\xi_t^2}{\Delta U^2} \left(d_w^2 + \xi_t d_t^2 \right) \right],$$

$$\xi_t = \min\left(0, 1; \; \frac{\Delta U}{\varpi_t} l_t \right), \quad \varpi_t = \omega_{W,trip},$$

$$d_t^2 = \left(x - x_{trip} \right)^2 + \left(y - y_{trip} \right)^2 + \left(z - z_{trip} \right)^2,$$

$$\Delta U = \left| V - V_{trip} \right|.$$

Here the bottom index of "trip" relates to quantities determined in that point on the line of transition which is on minimum distance from the examined point of flow; $l_t = \left(\Delta x^2 + \Delta y^2 \right)^{1/2}$ is the diagonal length of the cell of the grid on the streamlined surface in this point, and U is equal to the module of the difference of vectors of speed in the examined point and the point of transition (in the case of motionless underlying surface $\Delta U = |V|$)).

The empiric constants of model are equal:

$$\sigma = 2/3; k = 0,41; \; c_{b1} = 0,1355; \; c_{b2} = 0,622;$$

$$c_{w1} = \frac{c_{b1}}{k^2} + \frac{1 + c_{b2}}{\sigma}; \; c_{w2} = 0,3; \; c_{w3} = 2;$$

$$c_{t1} = 1; \; c_{t2} = 2; \; c_{t3} = 1,2; \; c_{t4} = 0,5.$$

Border terms to Eq. (6.11) are set as follows. The modified turbulent viscosity, as well as true one, must apply in zero, $\tilde{v} = 0$, on the solid underlying surface. On an input area of the lateral border of calculation area there must be set boundary

condition of the first kind for $\tilde{v}$, and on an output area the value of $\tilde{v}$ should be extrapolated on the border from the internal points of the area.

When calculating motion of atmospheric air under an inverse layer the choice of value of $\tilde{v}$ on the external border of the inverse layer is carried out as follows. If a point (line) of transition from laminar to turbulent motion mode is known from the preliminary calculation of vertical profile of temperature, then $\tilde{v}$ on the external border of inverse layer of calculation area becomes equal to some small value (about 10^{-3} of molecular viscosity) the exact account of which does not matter. Thus, due to the "trip" term in Eq. (6.11), a transition from laminar to turbulent flow mode takes place in the small vicinity of a given point (line) of transition.

In those cases when position of transit point (lines) is unknown beforehand but an inverse layer is however present, so that it is possible to disregard the laminar area of boundary layer on the laying surface, it is possible to use "fully turbulent" approach to description of the transition. In this case on the external border of the inverse layer of calculation area a high enough level of $\tilde{v}$ ($\tilde{v} = (1 \div 5)\,\nu$) is set, and Eq. (6.11) provides the rapid (during a few steps of grid) transition to the developed turbulent flow in the boundary layer.

Note, finally, that for "diagnostics" of the state of boundary layer during carrying out calculation it is useful to exploit the so-called index of turbulence the value of which in the developed turbulent boundary layer is near by 1. The index of turbulence is calculated with the formula from [37]

$$i = \frac{1}{kv^*}\frac{\partial \tilde{v}}{\partial n},$$

where "speed of friction" in general case of three-dimensional flow is calculated as $v^* = \sqrt{\nu\omega}$ (ω is the module of rotationality in the examined point on a laying surface).

When modelling of squall winch (the eddy of horizontal axis) and tornado (the eddy of vertical axis), curvature of lines of flow and rotation of flow have substantial influence on turbulence characteristics and can result both in its significant intensification or suppression. Within the framework of the examined model special amendments are needed for their account. The most successful from such amendments, presumably, there is amendment of Spalart and Shur [38–40] that takes into account single nature of effects of curvature of lines and rotation of flow and is applicable, generally speaking, to any linear model.

Within the framework of model (6.11) a generating member G_ν is modified by multiplying by an empiric function

$$f_{r1} = \frac{2r^*\,(1 + c_{r1})}{1 + r^*}\,[1 - c_{r3}\mathrm{arctg}\;(c_{r2}\tilde{r})] - c_{r1},$$

which depends on two parameters r^* and $\tilde{r}$ being, respectively, the measure of curvature of lines and rotation of flow. Expressions for these parameters look like:

$$r^* = \left|\frac{S}{\omega}\right|, \quad \tilde{r} = \frac{2\omega_{ik}S_{jk}(DS/Dt)_{ij}}{D^4}.$$

Here $(DS/Dt)_{ij}$ is corresponding component of complete derivative with respect to time of the tensor of speeds of deformations, and a value of D is determined by expression:

$$D^2 = \frac{1}{2}\left(S^2 + \omega^2\right),$$

where

$$S = \left(2S_{ij}S_{ij}\right)^{1/2}, \quad S_{ij} = \frac{1}{2}\left(\frac{\partial u_i}{\partial x_j} + \frac{\partial u_j}{\partial x_i}\right),$$

$$\omega = \left(2\omega_{ij}\omega_{ij}\right)^{1/2}, \quad \omega_{ij} = \frac{1}{2}\left(\frac{\partial u_i}{\partial x_j} - \frac{\partial u_j}{\partial x_i}\right).$$

Three new constants included in the last expressions have next values:

$$c_{r1} = 1, c_{r2} = 12, c_{r3} = 1.$$

6.4 A Model of Cloud and Precipitation

If atmosphere is saturated by water vapor then the terms of stability of dry atmosphere take place only for moist air which moves to a higher temperature area (goes down), because amount of moisture, which the examined volume can contain, as a rule, increases at heating (lowering). Vice versa, in the air which moves to a lower temperature area (raises) the amount of moisture, which can be hold in a volume, diminishes, what results in the processes of condensation (crystallizations) and heat release. As a consequence the floatation of an air volume increases in comparison to that which would be observed in absence of condensation (crystallizations). The condensation, which results to cloudiness and precipitation refers to be the nondeterministic process, and therefore is described as prognostic and circulation patterns in the atmosphere models by means of parameterization.

To derive the parameterization equations we represent the temperature T, specific humidity q and the specific conductivity of δ as a sum:

$$T = \tilde{T} + \grave{T}, \quad q = \tilde{q} + \grave{q}, \quad \delta = \tilde{\delta} + \grave{\delta},$$

where $\tilde{T}$, $\tilde{q}$ and $\tilde{\delta}$ are variables whose values are changed due to convection-diffusion processes and which are described by following homogeneous equations:

$$\frac{d\tilde{\theta}}{dt} = \nabla \cdot \left(k_T \nabla \tilde{\theta} - F_{rad} \right), \tag{6.3′}$$

$$\frac{d\tilde{q}}{dt} = \nabla \cdot (k_d \nabla \tilde{q}) \tag{6.4′}$$

$$\frac{d\delta}{dt} = \nabla \cdot (k_d \nabla \delta) ; \tag{6.5′}$$

$\grave{T}$, $\grave{q}$ and $\grave{\delta}$ are variables whose values are changed solely due to moisture phase transitions of the first kind and are described by the equations:

$$\frac{\partial \grave{\theta}}{\partial t} = \left(\frac{p_{00}}{p} \right)^{R/C_p} \frac{L}{C_p} Q_H, \tag{6.3″}$$

$$\frac{\partial \grave{q}}{\partial t} = Q_H, \tag{6.4″}$$

$$\frac{\partial \grave{\delta}}{\partial t} = -Q_H . \tag{6.5″}$$

Changing the amount of saturated water vapor per unit of volume per time unit (the rate of condensation) Q_H we define follows:

$$Q_H = \begin{cases} 0, & \text{if } \ q < q_s; \\ -\frac{\partial q_s}{\partial t} & \text{otherwise,} \end{cases}$$

where q_s is the specific humidity at saturation.

For the equilibrium of the system "water – water vapor or ice – water vapor" it is necessary, that the vapor pressure in air would correspond to saturation. Dependence of pressure of the saturated vapor E on temperature T in differential form can be given on the basis of thermodynamics laws, described by equation of Clausius-Clapeyron

$$\frac{dE}{dT} = \frac{LE}{R_w T^2} \ \frac{\mathrm{dE}}{\mathrm{dT}} = \frac{\mathrm{LE}}{\mathrm{R}_\Pi \mathrm{T}^2} = \frac{\mathrm{LE}}{1,6\mathrm{RT}^2}, \tag{6.12}$$

where $R_w = 461.50$ J kg^{-1} kcal^{-1} is the universal gas constant for water vapor.

For determination of pressure of the saturated vapor over water we will perform integration of (6.12) from the temperature $T_0 = 273.15$ K and corresponding value

of pressure of the saturated vapor $E_0 = 6.1078$ of Mb to some values T and E. Accepting the first approach approximation as $L = const$, we will get

$$\ln \frac{E}{E_0} = -\frac{L}{1.6R}\left(\frac{1}{T} - \frac{1}{T_0}\right) = \frac{L}{1.6RT_0}\frac{T - T_0}{T}, \tag{6.13a}$$

or

$$E = E_0 \exp\left(C_w \frac{T - T_0}{T}\right), \tag{6.13b}$$

where $C_W = \frac{L}{1,6RT_0}$.

When determining the dependence of resilience of the saturated steam on temperature over ice E_i it is necessary to take the heat of sublimation $L_s = L + L_m$ instead of heat of evaporation L, where $L_m = 335.008$ J kg^{-1}, is a heat of melting of ice. Then like (6.13a) we will get:

$$\ln \frac{E_i}{E_0} = -\frac{L + L_m}{1.6R}\left(\frac{1}{T} - \frac{1}{T_0}\right) = \frac{L + L_m}{1.6RT_0}\frac{T - T_0}{T}, \tag{6.14a}$$

or performing the same transformation as above, we will find

$$E_i = E_0 \exp\left(C_i \frac{T - T_0}{T}\right), \tag{6.14b}$$

where

$$C_i = \frac{L + L_m}{1,6RT_0}.$$

Now we will find the difference between the saturated vapor resilience over overcooled water E and the saturated vapor resilience over ice E_i at the same temperature. This difference, in view of (6.13b) and (6.14b) can be written as:

$$\Delta E = E_0 \left[\exp\left(C_w \frac{T - T_0}{T}\right) - \exp\left(C_i \frac{T - T_0}{T}\right)\right].$$

To find extreme of the function $\Delta E(T)$ we hold differentiation left and right sides of the resulting equation with respect to T and equate $\partial\ (\Delta \mathrm{E})\ /\partial \mathrm{T}$ to zero:

$$\frac{T_0 E_0}{T^2}\left[C_w \exp\left(C_w \frac{T - T_0}{T}\right) - C_i \exp\left(C_i \frac{T - T_0}{T}\right)\right] = 0.$$

Factor T_0E_0/T^2 is not equal to zero, so the expression in square brackets is equal to zero. Hence we obtain:

$$T = T_0\left[1 - \frac{\ln(C_w/C_i)}{C_i - C_w}\right]^{-1}. \tag{6.15}$$

The result is that when $C_W = 19.80$ and $C_i = 22.46$ maximum value of the difference $\Delta E(T)$ is about 0.269 Mb and corresponds to the point with the temperature $T \approx 260.4$ K or $t \approx -12.6$ °C. Subsequently, the value of this temperature we will take as the critical temperature below of which the condensation process is replaced by crystallization.

We will assume that the change of the temperature of some elementary volume of moist air, in which steam is reached saturation state q_s and condensation (or crystallization) takes place, occurs without the exchange of heat between the dedicated air mass and the environment. Assume also that the condensation (or crystallization) products are still left inside the considered volume element of air. Then its total moisture content does not change but only its ratio in the gas and the condensed water vapor phases. In other words we will consider only the case of the moist-adiabatic process in which the temperature change associated with the change in humidity $dq_s(p, T)$ in saturated air, according to the first law of thermodynamics, is described by the equation $c_p d\grave{T} - \frac{1}{\rho}dp + Ldq_s = 0$ which can be converted to

$$\frac{c_p\grave{T}}{\grave{\theta}}d\grave{\theta} + Ldq_s = 0.$$

From this ovseration we obtain

$$d\grave{\theta} = -\frac{L}{c_{ps}}\left(\frac{p_{00}}{p}\right)^{R_s/c_{ps}} dq_s, \tag{6.16}$$

where $c_{ps} = 4R_s$ is the specific heat of water vapor at constant pressure.

Here, as in the system of equations for the mathematical model of the atmospheric circulation, L is the latent heat of vaporization, which is calculated by the formula [41]

$$L = (2500.8 - 2.3t) \times 10^3 \text{ J} \cdot \text{kg}^{-1}. \tag{6.17a}$$

At temperature being $t < -12.6$ °C, when the ice is formed instead of water, q_s is replaced by the corresponding value for ice q_i, and instead of the latent heat of vaporization we introduce the latent heat of sublimation [41]:

$$L = 2.839 \times 10^6 - 3.6(t + 35)^2 \text{ J} \cdot \text{kg}^{-1}. \tag{6.17b}$$

In general, when the value of q_s is changing, the value of coefficient

$$A = -\frac{L}{c_{ps}}\left(\frac{p_{00}}{p}\right)^{R_s/c_{ps}}$$

In the Eq. (6.16) is also changing. But for a fixed value q_s coefficient A is a number that does not depend on dq_s. From the calculus it is known that if $A \neq 0$, that is if $d\grave{\theta} \neq 0$, then the differentiability of $\grave{\theta}$ at q_s means that the main part of the increase of the function $\Delta\grave{\theta}$ at q_s is a linear function with respect to $\Delta\grave{q}$. The increase and the differential are equivalent infinitesimal when $\Delta\grave{q} \to 0$. Thus, the differential Eq. (6.16) can be written as

$$\Delta\grave{\theta} = -\frac{L}{c_{ps}}\left(\frac{p_{00}}{p}\right)^{R_s/c_{ps}}\Delta q_s + \alpha\left(\Delta q_s\right). \tag{6.18}$$

where $\alpha\left(\Delta q_s\right) = 0\left(\Delta q_s\right)$ when $\Delta q_s \to 0$.

The Eq. (6.18) allows determining the amount of change in temperature if we know the amount of change of humidity $\Delta q_s = q - q_s$, which occurs as a result of phase transitions in the wet air when water vapor is saturated to q_s.

Many experimental research efforts carried out in laboratory and in vivo indicate, that to condensate water vapor in the atmosphere the vapor resilience in the air e is needed to be greater than the vapor resilience E over the surface being formed by new phase particles, and that there should be fine particles in the air that could serve as nuclei of condensation. And droplets formed at the nuclei can grow to form cloud droplets only with oversaturation, i.e., when the relative air humidity $f = e/E$ will be greater than 1. For the crystallization process in the presence of ice crystals oversaturation must be determined with respect to the surface of the ice. Since the vapor resilience over the ice is less than over the water, then at low negative temperatures oversaturation can occur at a relative humidity in the air less than 1 with respect to the flat surface of the overcooled water.

We introduce the so-called critical relative humidity f_{cr} above which there will always be the condensation of water vapor in the atmosphere. We associate f_{cr} with a ratio of saturated vapor resilience over ice E_i and the same quantity over overcooled water E at the same temperature:

$$f_{cr} = E_i(T)/E(T). \tag{6.19}$$

The values of E and E_i calculated by formulas (6.13b) and (6.14b) do not coincide with the experimental data. On the basis of the experimental data presented in the Smithsonian meteorological tables there have been offered empirical formulas [42]. According to these tables saturation vapor resilience $E(T)$—the pressure of saturated water vapor—over a flat surface water at temperatures in the range of ± 40 °C can be calculated by the formula

$$E(T) = \gamma \exp\left[(0.08006T - 20.047) / (0.00412T - 0.12476)\right] \tag{6.20}$$

The value of the factor γ in (6.20) considered to atmospheric conditions is within $1 \div 1.006$, and can be found using the following equation:

$$\gamma = 1 + p\left[4.5 + 0.0006(T - T_0)^2\right] \cdot 10^{-6}. \tag{6.21}$$

Saturated vapor tension $E_i(T)$ above the flat surface of ice at temperatures ranging from 0 to −40 °C satisfies the condition

$$\mathrm{E}_i(T) = E(T) \exp\left(0.00422T - 1.15206\right). \tag{6.22}$$

Values calculated by formulae (6.20) and (6.22) coincide with values from Smithsonian meteorological tables №94 and №96 accordingly [42] providing absolute error 0.0002 mbar within temperature range of −40 to +40 °C. Substituting equalities (6.20) and (6.22) into (6.19) we obtain:

$$f_{cr} = \mathrm{E}_i(T)/E(T) = \exp\left(0.00422T - 1.15206\right). \tag{6.23}$$

It can be seen from the resulting dependence that the relative humidity f_{cr} significantly increases with temperature. For example, at the temperature $t = 0$ °C relative humidity $f_{cr} = 1$ and at $t = -30$ °C it drops to values $f_{cr} = 0.88$. In numerical simulation of clouds we will take that saturation, i.e. condensation (at $t \geq -12.6$ °C) or crystallization (at $t < -12.6$ °C) of water vapor occurs when the relative humidity is greater than or equal to f_{cr} value calculated using the formula (6.23).

In this connection let us return to the question of calculating the amount of change in the specific humidity Δq_s, which is part of the Eq. (6.18), for moist air in which water vapor is reached saturation. We will carry out following chain of elementary transformations:

$$\begin{aligned}\Delta q_s = q - q_s &= \xi\left[\frac{e}{p - (1-\xi)\,e} - \frac{E}{p - (1-\xi)\,E}\right] \\ &= \xi\frac{E}{p - (1-\xi)\,E}\left[\frac{e}{E}\frac{p - (1-\xi)\,E}{p - (1-\xi)\,e} - 1\right] \approx \xi\frac{E}{p - (1-\xi)\,E}\left(f - f_{cr}\right),\end{aligned} \tag{6.24}$$

where $\xi = R/R_w = 0.62197$ and take into account that indeed there is always $p >> e$ and $p >> E$.

When calculating the temperature change by the formula (6.18) and changes in specific humidity by the formula (6.24) occurring as a result of phase transitions in the humid air in which water vapor reached a state of saturation, it is necessary to take into account that a change in temperature leads to a change in the conditions of saturation. Hence, these calculations should be performed using the method of successive approximations (iterations).

From the system of Eqs. (6.3″), (6.4″), and (6.5″) and the equality $Q_H = -\partial q_s/\partial t$ it follows:

$$\frac{\partial \grave{\theta}}{\partial t} = -\left(\frac{p_{00}}{p}\right)^{R/C_p} \frac{L}{C_p} \frac{\partial q_s}{\partial t},$$

$$\frac{\partial \grave{q}}{\partial t} = -\frac{\partial q_s}{\partial t},$$

$$\frac{\partial \grave{\delta}}{\partial t} = \frac{\partial q_s}{\partial t}.$$

Integrating this system of equations in the interval $t = \left[0, t_{pr}\right]$, we find that the temperature, specific humidity and specific conductivity will change during the time t_{pr}, respectively, by an amount of:

$$\Delta \grave{\theta} = -\left(\frac{p_{00}}{p}\right)^{R/C_p} \frac{L}{C_p} \Delta q_s, \quad \Delta \grave{q} = -\Delta q_s, \quad \Delta \grave{\delta} = \Delta q_s. \tag{6.25}$$

In constructing a mathematical model of precipitation we will assume that independently of the origin of clouds and cloud systems (frontal, convective, orographic, etc.), there are known the power of clouds (vertical dimension) h_{cl} and the rate of change of the specific water content $\partial \acute{\delta}/\partial t$. Expected rainfall I, dropped from a single column of clouds during the period of time t_{pr}, is estimated by the formula:

$$I = \int_0^{t_{pr}} \int_0^{h_{cl}} \frac{\partial \acute{\delta}}{\partial t} dx_3 dt. \tag{6.26}$$

Integrating (6.26) with respect to t in the interval $t = \left[0, t_{pr}\right]$, we obtain for $\Delta \grave{\delta} = \Delta q_s$:

$$I = \int_0^{h_{cl}} \Delta q_s dx_3. \tag{6.27}$$

6.5 Numerical Method for Solving the Non-stationary Problem with a Prehistory Based on Interpolation with Multiple Nodes

Consider the global atmospheric circulation in the macro-scale area $\wp(r)$ that is determined by the vector of discrete values $\Re\,(r, t) = (\mathrm{v}_1, \mathrm{v}_2, \mathrm{v}_3, p, \theta, q, \delta, s, \nu_t)$ of

analysis and forecast prepared on the basis of this macro-scale model. To distinguish the time grid from the spatial grid, the value assigned to the individual points of time will be marked by superscripts, and the values specified in the nodes of the spatial grid will be marked by subscripts. As before, the state vector $\Re(r,t)$ in the field $\wp(r)$ is defined by vector of discrete values $\Re\left(r,t^{\eta}\right) = \Re^{\eta}(r)$ at time points $t = t^{\eta}$ $(\eta = 0,\ 1,..,n)$, $\tau^{\eta} = t^{\eta} - t^{\eta-1}$ is the step of the increment. Thus, to determine the state of the atmosphere in a limited area $\overline{\wp}$ at $\forall t \in \left[t^{n-1},\ t^{n}\right]$ we need to solve the problem which in the vector representation has the form:

$$\frac{\partial \Re\left(r,t\right)}{\partial t} = D\Re\left(r,t\right),\ \ \forall t \in \left[t^{n-1},\ t^{n}\right], \forall r \in \overline{\wp} \tag{6.28}$$

$$\Re\left(r,t^{\eta}\right) = \Re^{\eta}(r),\ \ \eta = 0,\ 1,..,n$$

where

$$D\Re\left(r,t\right) = \frac{\partial}{\partial x_i}\left[\left(\frac{\nu + \nu_t}{\sigma}\right)\frac{\partial \mathcal{R}}{\partial x_i}\right] - \mathrm{v}_i\frac{\partial \mathcal{R}}{\partial x_i} + F.$$

Suppose that in the area $\wp(r)$ of coordinate system $r = (x_1, x_2, x_3)$ the independent continuous variables x_1, x_2, x_3 take the values: $\alpha_1 \le x_1 \le \alpha_2$, $\beta_1 \le x_2 \le \beta_2$, and $\varsigma_1 \le x_3 \le \varsigma_2$. The spatial grid ϖ_H in this area is formed by the decomposition of segments $[\alpha_1, \alpha_2]$, $[\beta_1, \beta_2]$ and $[\varsigma_1, \varsigma_2]$ into a set of I–1 elements $\Delta(x_1)_i$, J–1 elements $\Delta(x_2)_j$ and elements K–1 of $\Delta(x_3)_k$ respectively. Values of the vector $\Re(r,t)$ at the nodes of this grid ϖ_H are:

$$\begin{aligned}
(x_1)_i &= \alpha_1 + \sum_{\lambda=1}^{i-1}\Delta(x_1)_{\lambda},\ 1 \le i \le I;\\
(x_2)_j &= \beta_1 + \sum_{\lambda=1}^{j-1}\Delta(x_2)_{\lambda},\ 1 \le j \le J;\\
(x_3)_k &= \varsigma_1 + \sum_{\lambda=1}^{k-1}\Delta(x_3)_{\lambda},\ 1 \le k \le K
\end{aligned} \tag{6.29}$$

at the time $t = t^{\eta}$ $(\eta = 0,\ 1,..,n)$ that we will denote as $\Re^{\eta}_{i,j,k}$.

We define in the macroscale area $\wp(r)$ a mesoscale area solutions $\overline{\wp}(r)$ with horizontal dimensions $\overline{\alpha}_1 \le x_1 \le \overline{\alpha}_2$, $\overline{\beta}_1 \le x_2 \le \overline{\beta}_2$ such that $\overline{\alpha}_1 \ge \alpha_1$, $\overline{\alpha}_2 \le \alpha_2$, $\overline{\beta}_1 \ge \beta_1$, $\overline{\beta}_2 \le \beta_2$. Hence $\overline{G}(r) \subset G(r)$. In the field of small-scale solutions $\overline{G}(r)$ we construct a fine-grained grid $\overline{\varpi}_h$ by dividing the area $\overline{G}$ into a set of $N_1 - 1$ elements of $\Delta\overline{(x_1)}_i$, $N_2 - 1$ elements of $\Delta\overline{(x_2)}_j$ and $N_3 - 1$ elements of $\Delta\overline{(x_3)}_k$.

We will construct a vector $\{r_{ijk}\}$ defining a continuous variable r only at the points $i \ \ (1 \le i \le N_1), j \ \ (1 \le j \le N_2), k \ \ (1 \le k \le N_3)$. As a result, we obtain:

$$\begin{aligned}
(x_1)_i &= \overline{\alpha}_1 + \sum_{\lambda=1}^{i-1} \Delta\overline{(x_1)}_\lambda, \ 1 \le i \le N_1; \\
(x_2)_j &= \overline{\beta}_1 + \sum_{\lambda=1}^{j-1} \Delta\overline{(x_2)}_\lambda, \ 1 \le j \le N_2; \\
(x_3)_k &= \overline{\varsigma}_1 + \sum_{\lambda=1}^{k-1} \Delta\overline{(x_3)}_\lambda, \ 1 \le k \le N_3.
\end{aligned} \tag{6.30}$$

Then, to determine the state of the atmosphere in a point r_{ijk} of the grid $\overline{\varpi}_h$ in a bounded domain $\overline{\wp}$ at $\forall t \in \left[t^{n-1}, \ t^n\right]$ it is necessary to solve the problem:

$$\frac{\partial \Re_{ijk}}{\partial t} = \Lambda \Re_{ijk}, \forall t \in \left[t^{n-1}, \ t^n\right], \tag{6.31}$$

$$\Re_{ijk}\left(t^\eta\right) = \Re_{ijk}^\eta, \forall r_{ijk} \in \overline{\varpi}_h, \ \eta = 0, \ 1, .., n, \tag{6.32}$$

where Λ is the difference representation of the differential operator D, and $\Lambda\Re_{ijk}$ is the numerical value of the right-hand side of Eq. (6.28) at a point r_{ijk} in the grid $\overline{\varpi}_h$ of the area $\overline{\wp}$.

For results below we accept following convention: *the initial value problem (6.28) for the ordinary differential equation with specific values i, j, k and the initial value problem (6.31)–(6.32) for the differential-difference equation with the same values i, j, k are equivalent.*

With this convention finding values $r_{ijk}(t)$ within the interval $\left[t^{n-1}, t^n\right]$ can be solved as a problem of interpolation "with multiple nodes" (using Hermit polynomial) because function values $\mathcal{R}_{ijk} = \mathcal{R}_{ijk}\left(t^\eta\right)$ and the value of its derivative $\Lambda\left(\mathcal{R}_{ijk}\left(t^\eta\right)\right) = \partial\mathcal{R}_{ijk}/\partial t\big|_{t=t^\eta}$ at the points $t = t^\eta \ \ (\eta = 1, 2, \ldots, n)$ are known.

To reduce the bulkiness of the formulas cited below we introduce the notation $f_n \equiv f\left(t^n\right) = \mathcal{R}_{ijk}\left(t^n\right), f_n^{(1)} = \partial\mathcal{R}_{ijk}/\partial t\big|_{t=t^n}$.

Hermit interpolation polynomial

$$P_{2n}(t) = \sum_{i=1}^{n}\sum_{\alpha=0}^{p-1} \frac{f_i^{(\alpha)}}{\alpha!} \cdot \frac{\omega_n^p(t)}{(t-t^i)^p} \sum_{j=0}^{p-1-\alpha} C_j^i \left(t-t^i\right)^{j+\alpha},$$

constructed by values $f_i^{(\alpha)}$, $i = 1, 2, \ldots, n, \alpha = 0,\ 1, \ldots, p$ of the function $f(t)$ and its derivatives of order p, satisfying the condition

$$\frac{d^\alpha P(t)}{dt^\alpha} = \left.\frac{d^\alpha f(t)}{dt^\alpha}\right|_{t=t^i},\ i = 1, 2, \ldots, n,\ \alpha = 0,\ 1,$$

looks like

$$P_{2n}(t) = \sum_{i=1}^{n} \frac{\omega^2(t)}{\left[(t-t^i)\,\omega_i'\right]^2} \left\{ \left[1 - \left(t-t^i\right)\frac{\omega_i''}{\omega_i'}\right] f_i^{(0)} + \left(t-t^i\right) f_i^{(i)} \right\}, \tag{6.33}$$

where $\omega_i(t) = \left(t-t^1\right)\cdot\left(t-t^2\right)\ldots\left(t-t^n\right)$.

It is known (see e.g. [43]) the uniqueness of such the polynomial $P_{2n}(t)$, satisfying the conditions listed above, as well as the order of error when interpolating with Hermite polynomial of degree n. Naturally, the increase in the value of n increases the cost of the solution especially concerning modeling atmospheric circulation and/or weather forecast. So, the choice of a particular value of n strongly depends on the nature of the problem being solved. It is hardly advisable to use large values of n in cases of methods that are applicable to the limited value of n and when it is not expected significant improvement of results.

For $n = 3$ the interpolation polynomial (6.33) takes the form:

$$\begin{aligned} P_6(t) = {} & \left(\tfrac{t^3-t}{t^3-t^2}\right)^2 \left(\tfrac{t-t^2}{t^3-t^2}\right)^2 \left[\left(1+\tfrac{3}{4}\right)\left(\tfrac{t-t^2}{t^3-t^2}\right) f_1^{(0)} + \tfrac{1}{4}\left(t-t^1\right) f_1^{(1)}\right] \\ & + \left(\tfrac{t^3-t}{t^3-t^2}\right)^2 \left(\tfrac{t-t^1}{t^2-t^1}\right)^2 \left[f_2^{(0)} + \left(t-t^2\right) f_2^{(1)}\right] \\ & + \left(\tfrac{t-t^1}{t^2-t^1}\right)^2 \left(\tfrac{t-t^2}{t^3-t^2}\right)^2 \left[\left(1-\tfrac{3}{4}\right)\left(\tfrac{t-t^2}{t^3-t^2}\right) f_3^{(0)} - \tfrac{1}{4}\left(t^3-t\right) f_3^{(1)}\right], \end{aligned}$$

and for $n = 2$ it is further to be simplified to the form

$$\begin{aligned} P_4(t) = {} & \left(\tfrac{t^2-t}{t^2-t^1}\right)^2 \left[\left(1+2\tfrac{t-t^2}{t^3-t^2}\right) f_1^{(0)} + \left(t-t^1\right) f_1^{(1)}\right] \\ & + \left(\tfrac{t-t^1}{t^2-t^1}\right)^2 \left[\left(1+2\tfrac{t^2-t}{t^2-t^1}\right) f_2^{(0)} + \left(t^2-t\right) f_2^{(1)}\right]. \end{aligned}$$

Everybody can make sure that the last formula gives accurate results for the functions depending on the cube argument. For functions depending on the argument in the fourth degree, the maximum error of the interval $(0, 1)$ is equal to -0.0625. Note that maximum error of interpolation using the formula Bessel with the same number of given values of functions f_i is equal to -0.5625.

The main advantages of interpolation formulas (6.33) built on the basis of given values of the function f_i and its derivatives $f_i^{(\alpha)}$, $i = 1, 2, \ldots, n, \alpha = 0,\ 1, \ldots, p$ are:

- they have a greater accuracy than any formula that use only the value f_i;

- for the interpolation over the interval $\left[t^{n-1}, t^n\right]$ they do not require the data outside the right boundary of the interpolation interval and therefore can be used for the rightmost interval;

value function and its derivatives $f_i^{(\alpha)}$, $i = 1, 2, \ldots, n$, $\alpha = 0,\ 1, \ldots, p$ can be defined on a nonuniform grid t^i.

6.6 Interpolating Functions, Specified in Macro-Scale Grid Nodes, into the Meso-Scale Grid

Nodes of vertical grids of macro-scale prediction models usually are defined in standard geopotential surfaces: sea level, 850, 700, 500, ... hPa. This grid is too coarse for meso-scale problems, especially in the boundary layer of the atmosphere where there are all the processes of turbulent exchange.

We divide the height $x_3 = H$ of the area of meso-scale solution of the problem $\overline{G}(r)$ on two levels $z_0 \le x_3 \le h$ and $h \le x_3 \le H$ where z_0 is roughness of the underlying surface and h is the height agreed as the height of the atmospheric boundary layer where the atmospheric pressure is 850 hPa.

Values of meteorological variables at all nodes of meso-scale horizontal grid $\overline{\varpi}_h$ and in the segment $h \le x_3 \le H$ of vertical interval computational grid can be interpolated by one of the known schemes of polynomial splines. Obviously, there is no interpolation formulas which would provide both the solution uniqueness and the required accuracy for the problem of interpolation on the interval $z_0 \le x_3 \le h$. Therefore interpolation of meteorological data given in macro-scale grid nodes into meso-scale grid will be based on the model of a vertical column of the atmosphere.

We introduce a nondegenerate coordinate transformation associated with the geometry of the domain of solving the problem

$$x = x_1,\ y = x_2,\ \sigma = H\left[x_3 - F\left(x_1, x_2\right)\right] / \left[H - F\left(x_1, x_2\right)\right], \tag{6.34}$$

where $F = F\left(x_1, x_2\right)$ is the equation of the profile (relief) of the underlying surface, H is the height of the top layer. Coordinate transformation (6.34) maps the area of solving the problem to the rectangular prism whose height is H. The inverse transformation is given by the relations:

$$x_1 = x,\ x_2 = y,\ x_3 = F\left(x_1, x_2\right) + \sigma\left[H - F\left(x_1, x_2\right)\right] / H.$$

Communication between the operators of the first derivatives with respect to coordinates in the old (x_1, x_2, x_3) and new (x, y, σ) variables can be expressed by known formulas:

$$\frac{\partial}{\partial x_1} = \frac{\partial}{\partial x} - \frac{\partial F}{\partial x}\frac{H-\sigma}{H-F}\frac{\partial}{\partial \sigma}, \quad \frac{\partial}{\partial x_2} = \frac{\partial}{\partial y} - \frac{\partial F}{\partial y}\frac{H-\sigma}{H-F}\frac{\partial}{\partial \sigma}, \quad \frac{\partial}{\partial x_3} = \frac{H}{H-F}\frac{\partial}{\partial \sigma}. \tag{6.35}$$

We take following processes as the main factors influencing the interaction of the atmosphere with the underlying surface: turbulent exchange; forced convective motions generated by the relief of the underlying surface; free convective motions caused by the lifting force of Archimedes. Let the components of the velocity v_1, v_2, v_3 relate to the coordinates as follows: v_1 is in the direction of increasing x (East direction), v_2 is in the direction of increasing y (North direction), v_3 is in the direction of growth of σ (the direction opposite to the gravitational force, i.e. upwards). Then, introducing the notation

$$\sigma = H\frac{x_3 - F(x,y)}{H - F(x,y)}, \quad \overline{w} = \frac{H}{H - F(x,y)}\left[v_3 - \frac{H-\sigma}{H}\left(v_1\frac{\partial F}{\partial x} + v_2\frac{\partial F}{\partial y}\right)\right] \tag{6.36}$$

and considering the area $\overline{G}(r)$ to have quite justifiable horizontal homogeneity of meteorological fields in the free atmosphere, we obtain the system of equations of the form:

$$\begin{aligned}
&\frac{\partial v_1}{\partial t} + \overline{w}\frac{\partial v_1}{\partial \sigma} = \frac{H^2}{(H-F)^2}\frac{\partial}{\partial \sigma}\left[(\nu + \nu_t)\frac{\partial v_1}{\partial \sigma}\right] + f\left(v_2 - v_g\right) - g\frac{H-\sigma}{H}\frac{\partial F}{\partial x},\\
&\frac{\partial v_2}{\partial t} + \overline{w}\frac{\partial v_2}{\partial \sigma} = \frac{H^2}{(H-F)^2}\frac{\partial}{\partial \sigma}\left[(\nu + \nu_t)\frac{\partial v_2}{\partial \sigma}\right] - f\left(v_1 - v_g\right) - g\frac{H-\sigma}{H}\frac{\partial F}{\partial y},\\
&\frac{\partial v_3}{\partial t} + \overline{w}\frac{\partial v_3}{\partial \sigma} = \frac{H^2}{(H-F)^2}\frac{\partial}{\partial \sigma}\left[(\nu + \nu_t)\frac{\partial v_3}{\partial \sigma}\right] - \frac{H}{H-F}\frac{g}{\theta}\frac{\partial \theta}{\partial \sigma}\Delta\sigma,\\
&\frac{\partial \theta}{\partial t} + \overline{w}\frac{\partial \theta}{\partial \sigma} = \frac{H^2}{(H-F)^2}\frac{\partial}{\partial \sigma}\left[(\nu + \nu_t)\frac{\partial \theta}{\partial \sigma} - F_{rad}\right] - \left(\frac{p_{00}}{p}\right)^{R/C_p}\frac{L}{C_p}Q_H,\\
&\frac{\partial q}{\partial t} + \overline{w}\frac{\partial q}{\partial \sigma} = \frac{H^2}{(H-F)^2}\frac{\partial}{\partial \sigma}\left[(\nu + \nu_t)\frac{\partial q}{\partial \sigma}\right] + Q_H,\\
&\frac{\partial \delta}{\partial t} + \overline{w}\frac{\partial \delta}{\partial \sigma} = \frac{H^2}{(H-F)^2}\frac{\partial}{\partial \sigma}\left[(\nu + \nu_t)\frac{\partial \delta}{\partial \sigma}\right] - Q_H,
\end{aligned} \tag{6.37}$$

where t plays the role of an iteration parameter.

We construct the vertical grid comprising $M < N_3$ counting levels with uneven distribution of the grid step size as following

$$z = \frac{x_3}{h} = 1 - \frac{\ln\left\{\left[\beta + 1 - (x_3/h)\right]/\left[\beta - 1 + (x_3/h)\right]\right\}}{\ln\left[(\beta+1)/(\beta-1)\right]} \tag{6.38}$$

The values of β are in the range of $1 < \beta < \infty$. The proposed formula allows to place as greater the number of nodes near the $z = x_3/h = 0$ as the value of β is closer to 1.

Equation (6.37) apply to all interior points of the vertical layer $0 < x_3 < h$ and the boundary conditions are imposed at the boundary points $x_3 = z_0$ and $x_3 = h$. At the level of $x_3 = z_0$ there are formulated boundary conditions of the first kind, and at the level of $x_3 = h$ there are formulated the boundary conditions of the third kind what provides that the conditions of conjugation.

Thus, the combination of an interpolation method for filling range of $x_3 > h$ and the numerical solution of Eq. (6.37) on the interval $[0, h]$ with boundary conditions formulated above allow determining the vertical profiles of meteorological variables on the computational grid according to their values known at standard levels.

The quality of filling the vertical profiles of meteorological variables on the limited input information is shown in Fig. 6.1. Radio sounding data on standard levels at ground level, 850, 700, 500, 400, 300 hPa are shown as stars, computed filled results in inner layers are shown as a solid line. The results of filling on the segment $[0, h]$ are compared with intermediate radio sounding data, which are also plotted in the form of dots.

6.7 Approximation of Constituent Members of the Convection-Diffusion

For a discrete function $\mathcal{R}^n_{ijk} \equiv \mathcal{R}_{ijk}(t^n)$, $1 \le i \le N_1$, $1 \le j \le N_2$, $1 \le k \le N_3$, for the sake of simplicity we restrict ourselves to one-dimensional counterpart q^n_j, $j = \overline{[1,\ N_2]}$, and determine the approximate values of the partial derivative $\psi_j = (\partial q/\partial x_2)^n_j$ on the basis of following equations

$$\begin{aligned}
&\psi_{j+1} + 2\left(1 + \frac{h_j}{h_{j-1}}\right)\psi_j + \frac{h_j}{h_{j-1}}\psi_{j-1} \\
&\quad = \frac{3}{h_j}\left\{q^n_{j+1} - \left[1 - \left(\frac{h_j}{h_{j-1}}\right)^2\right]q^n_j - \left(\frac{h_j}{h_{j-1}}\right)^2 q^n_{j-1}\right\} \\
&\qquad -\frac{h_j h^2_{j-1}}{24}\left[1 - \left(\frac{h_j}{h_{j-1}}\right)^2\right]\left(\frac{\partial^4 q}{\partial x_2^4}\right)_j \quad j = 2,\ 3, \ldots, J-1,
\end{aligned} \tag{6.39}$$

obtained by expanding the function in a Taylor series in the neighborhood of the points x_{2j}, $j = \overline{[2, N_2 - 1]}$, where h_j $(j = 2,\ 3, \ldots, J)$ are grid steps and $\psi_j = (\partial q/\partial x_2)^n_j$ $(j = 2,\ 3, \ldots, J)$ are derivatives at the n-th time layer. From (6.39) one can see that these relations have the third order when $h_j \ne h_{j-1}$ and the fourth order when $h_j = h_{j-1}$. The derivatives $\psi_j = (\partial q/\partial x_2)^n_j$ that we are interested in are included in (6.39) implicitly. They can be calculated from the given values q^n_j, $j = \overline{[1, N_2]}$ by solving systems of algebraic equations with a tridiagonal matrix method.

Similarly we can get the approximate values ξ_j of the partial derivative of the second order $\left[\partial\left(\frac{\nu+\nu_t}{\sigma}\partial q/\partial x_2\right)/\partial x_2\right]^n_j$ as $(\partial\vartheta/\partial x_2)^n_j$ by representing the function $\left[\partial\left(\frac{\nu+\nu_t}{\sigma}\partial q/\partial x_2\right)/\partial x_2\right]^n_j$ as $\vartheta_j = \frac{\nu+\nu_t}{\sigma}\psi_j$.

It should be noted the main advantage of the proposed method of approximation of derivatives included in the differential equations of convective diffusion

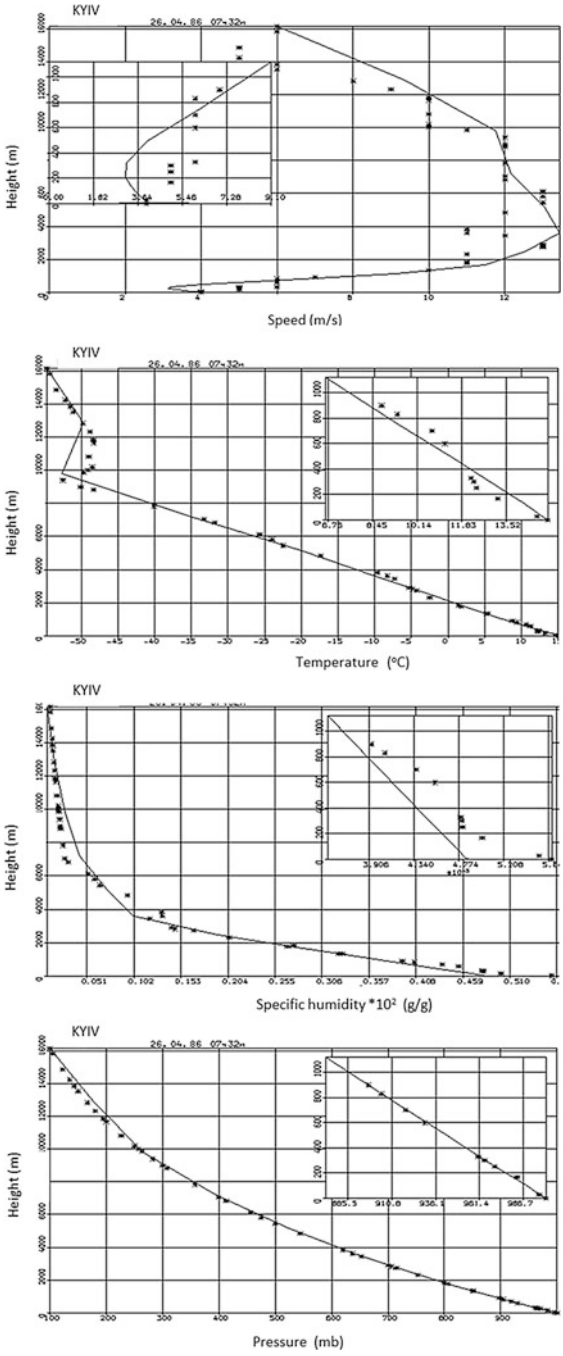

Fig. 6.1 Filling vertical profiles of meteorological variables according to the radio sounding: stared lines stand for observation data, continuous lines stand for numerical forecasting

approximation in comparison with the standard pointwise approximation. Since the solution q_j of systems of algebraic Eq. (6.39) at all points j depends on the values q at other points, it depends on x_j globally, not locally, as in the case of the standard "local three-point" difference approximations of first and second order derivatives.

The general form of difference expressions for the first-order and second-order derivatives of Eq. (6.39) can be written as:

$$A_j U_{j+1} + B_j U_j + C_j U_{j-1} = F_j,\ j = 2,\ 3, \ldots,\ N_2 - 1, \tag{6.40}$$

where

$$U = \left\{ \begin{array}{c} \psi \\ \xi \end{array} \right\},\ A_j = 1,\ B_j = 2\left(1 + \frac{h_j}{h_{j-1}}\right),\ C_j = \frac{h_j}{h_{j-1}},$$

$$F_j = \left\{ \begin{array}{l} \frac{3}{h_j}\left\{ q^n_{j+1} - \left[1 - \left(\frac{h_j}{h_{j-1}}\right)^2\right] q^n_j - \left(\frac{h_j}{h_{j-1}}\right)^2 q^n_{j-1} \right\} \\ \frac{3}{h_j}\left\{ \vartheta_{j+1} - \left[1 - \left(\frac{h_j}{h_{j-1}}\right)^2\right] \vartheta_j - \left(\frac{h_j}{h_{j-1}}\right)^2 \vartheta_{j-1} \right\} \end{array} \right\}.$$

Since $A_j > 0,\ B_j > 0,\ C_j > 0,\ B_j > A_j + C_j$, the value of rounding errors in the implementation of the tridiagonal matrix method by recurrence relations

$$U_j = E_j U_{j+1} + D_j,\ j = J - 1,\ J - 2, \ldots, 1; \tag{6.41a}$$

$$E_j = -\frac{\gamma_j}{B_j + A_j E_{j-1}},\ j = 1,\ 2, \ldots, J - 1; \tag{6.41b}$$

$$D_j = \frac{F_j - A_j D_{j-1}}{B_j + A_j E_{j-1}},\ j = 1,\ 2, \ldots, J - 1 \tag{6.41c}$$

will not grow [44]. The boundary conditions at the left boundary allow to determine the value $E_0 = 0,\ D_0 = U_1$, and boundary conditions on the right boundary make possible to determine the value of U_{N_2}.

Thus, the approximation of partial derivatives of first and second order (6.39), (6.40), and (6.41) allows to obtain very accurate (fourth order on a uniform grid) grid representation of the components of convection-diffusion equation of the members of (6.28) in coordinate direction x_2. Similarly, one can get a grid representation of components of convection-diffusion equation members of (6.28) in the coordinate directions x_1 and x_3. It remains to generate the required algebraic computation to move to the problem (6.31) and (6.32) taking in account the obtained discrete values of the terms in Eq. (6.28).

6.8 Solution of the Problem of Impurities Dispersion in the "Near Field"

Emission of impurities to the atmosphere is carried out from sources of certain geometrical size. However, these sizes are small compared to distances at which generated concentration fields are investigated. Therefore, one can take the assumption that real sources are considered dotted. This assumption allows to replace the impurity scattering problem of the tube diameter with d and height ${x_3}^0$, located at the point ${x_1}^0, {x_2}^0$, by the problem of pollution from a point source displaced from the axis of the tube at some "effective" distance $\Delta s = \left(\Delta {x_1}^2 + \Delta {x_2}^2\right)^{1/2}$ and elevated above the tube at some effective height Δx_3. In this case the law of conservation of mass implies that the average concentration of the impurities away from the mouth of the tube is proportional to r^{-2} (r is effective local radius of the cone). In this formulation of the problem point source activity is described by $\delta-$ function and, if the effective coordinates are denoted ${x_1}^{ef} = {x_1}^0 + \Delta x_1$, ${x_2}^{ef} = {x_2}^0 + \Delta x_2$, ${x_3}^{ef} = {x_3}^0 + \Delta x_3$, initial condition takes the form

$$Vq = M\delta\left(x_1 - {x_1}^{ef}\right)\delta\left(x_2 - {x_2}^{ef}\right)\delta\left(x_3 - {x_3}^{ef}\right), \tag{6.42}$$

where M is the emission of matter from a source in time unit.

For determination of effective displacements of co-ordinates of source there was used vast experimental material [44] on dependence of trajectory of central point of active part of the stream being blown out under the corner of 90° on values of the parameter

$$R = \left(\frac{\rho_q}{\rho_\infty}\right)\left(\frac{V_q}{V\infty}\right)^2, \tag{6.43}$$

where, as well as above, ρ_q, V_q are, respectively, density and speed of gas-air mixture and ρ_∞ , V_∞ are, respectively, density and speed of surrounding atmospheric air.

A sample of our experimental data is presented on the Fig. 6.2. Generalization of this experience and that of [45] allowed to get a universal empiric formula for computing effective co-ordinates of beginning of passive area of the jet ${x_1}^{ef} = {x_1}^0 + \Delta x_1$, ${x_2}^{ef} = {x_2}^0 + \Delta x_2$, ${x_3}^{ef} = {x_3}^0 + \Delta x_3$,

$$\frac{\Delta x_3}{d_j} = 1.2\frac{V_q}{V_\infty}\sqrt{\frac{\rho_q}{\rho_\infty}}\ln\left[\left(\frac{\Delta s}{d_j}\right)^{0.57} + 1,\right] \tag{6.44}$$

where d_j is the diameter of the mouth of the emission source. The effective height Δx_3 of the passive portion of the plume is determined from the condition $d\Delta x_3/ds \to 0$.

Thus, in the simulation of the processes of forming of concentration fields from stationary point source of emission there must be specified the coordinates and the

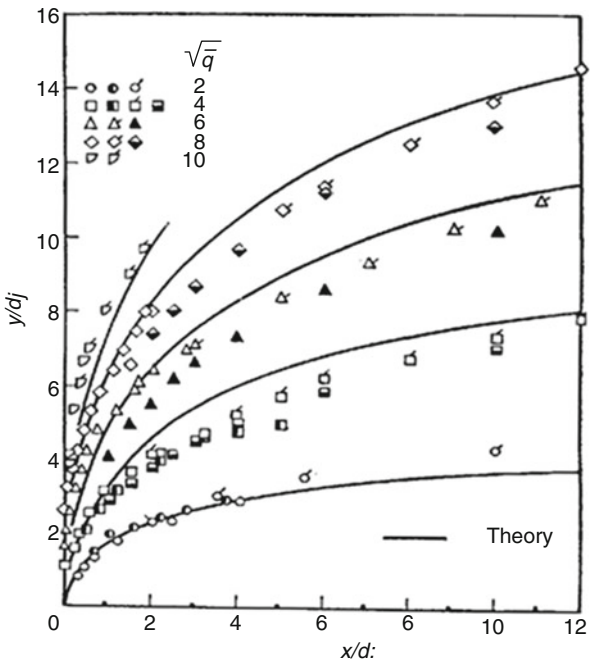

Fig. 6.2 The jet trajectories injected into the blowing air flow at various values of R

physical parameters on the passport data of industrial enterprises and then calculated by (6.44) the effective coordinates taken as the initial data for the passive area of the jet.

Spatial discretization of regional weather forecast model is very rough for the numerical solution of the problem of scattering impurities in the atmosphere, especially near emission sources. Since the point of emission sources is described by $\delta-$ function, the impurity concentration, while approaching the source, grows indefinitely and in the source point becomes infinitely large. For the corresponding approximation in the vicinity of the source requires unlimited refinement of the grid. This leads to the main problems arising in the numerical solution of the joint meteorological and environmental problems due to the fact that their scales differ by several orders of magnitude.

The current practice of analyzing observational data allows assuming fields of meteorological variables within time period of $\tau = 1$ h to be constant and locally homogeneous. It is these meteorological data averaged over this period is applied to the surface weather maps. Therefore, when $t \leq \tau$ the processes of transport and diffusion of the impurity in the atmosphere from industrial sources can be regarded as constant, so $\partial q/\partial t = 0$. At assumptions about the constancy of wind velocity $\mathbf{V} = (v_1, v_2, v_3)$ and the eddy viscosity ν_t decision problems of pollution within $t \leq \tau$ in the so-called "near-field" can be found on the basis of known analytical formulas for linear equations of convective diffusion [45]

$$s = \left[\frac{1}{2\sqrt{\pi\mu\,(t-t_0)}}\right]^3 \exp\left\{-\sum_{i=1}^{3}\left[x_i - x_i^{ef} - \mathrm{v}_i\,(t-t_0)\right]^2 / 4\mu\,(t-t_0)\right\},$$

where it is assumed that $\mu = \mu_1 \equiv \nu_1/\xi = \mu_2 \equiv \nu_2/\xi = \mu_3 \equiv \nu_3/\xi = const$, i.e. near the source of emission atmosphere is considered as of a homogeneous isotropic medium. The analytical solution assumes calculation of concentration fields from given pollution emission sources on terms $t_\eta\,(\eta = 1, 2, \ldots, n)$ with subsequent general numerical solution of meteorological and environmental problems (6.31) and (6.32) inside the interval $[t_{n-1}, t_n]$ [46].

Examples of numerical experiments on weather forecast and simulation of distribution in the atmosphere are presented elsewhere [46].

6.9 Conclusion

Presented mathematical model of regional atmospheric processes and its use for modeling pollutants spreading in atmosphere is based on the concept of "one-way interaction" and is characterized by high efficiency and accuracy of computation provided by:

- solving ordinary differential equations of the first order, which are obtained from the original equations of the model, is performed by interpolating with multiple nodes with Hermite polynomial of the fifth order;
- difference approximation of the spatial derivatives of first and second order contained in the operators of convective diffusion is carried out on the 3-point pattern using the finite-difference operators of the fourth order.

The initial and boundary conditions for a regional task are defined by the vector of discrete values of the analysis and prediction of meteorological variables derived from the numerical solution of the macro-scale problem. The accuracy of interpolating theses values at the nodes of the regional grid is consistent with the accuracy of the numerical method of the regional forecast.

Formulation of additional conditions in the environmental task is performed by calculating the concentration fields of impurities generated from a priori known number of point sources of a given power, based on the method of separation of variables and fundamental solutions of linear equations of convective diffusion. It has been justified the use of the linear convective diffusion equation with constant coefficients as the model of impurity outspread in the so-called "near-field" where within 1 h period the values of meteorological variables remain constant.

The high efficiency and accuracy of the proposed numerical method for solving equations of convective diffusion have been justified in Ukrainian Hydrometeorological Center for simulating the formation of the fields of pollution in the atmosphere from given number of stationary sources of impurity under real weather conditions [11]. It appeared that proposed here mathematical models and numerical

methods allow solving the problem of monitoring and controlling the state of the atmosphere experienced the impact of man-made industrial enterprises provided their normal work. These models can be used in the control of transboundary transport of pollutants in the atmosphere.

References

1. Oke, T.R.: Boundary Layer Climates, 2nd edn. Routledge, London (1987)
2. Gumbel, E.J.: Statistics of Extremes. Columbia University Press, New York (1958)
3. Larsen, R.I.: Parameters of aerometric measurements for air pollution. Am. Ind. Hyg. Assoc. Quart. **22**, 97–101 (1961)
4. Berlyand, M.E.: On distribution of air pollutants in urban environments. Meteorol. Hydrol. **3**, 45–57 (1970) (in Russian)
5. Sonkin. L.R., Chalikov, D.V.: On the processing and analysis of observations of air pollution in cities. In: Proc. Voeikov Main Geophysical Observatory **207**, 51–55 (in Russian) (1968)
6. Yudin, M.I.: Atmospheric Diffusion and Air Pollution. Izdatelstvo inostrannoy literatury, Moscow (in Russian) (1962)
7. Berkowicz, R., Olesen, J.R., Torp, U.: The Danish Gaussian air pollution model (OLM): description, test and sensitivity analysis, in view of regulatory applications. In: De Wispelaere, V.C., Schiermeier, F.A., Gillani, N.V. (eds.) Air Pollution Modeling and Its Application, pp. 453–481. Plenum, New York (1986)
8. Doroshenko, A.Y., Prusov, V.A.: Methods of efficient modeling and forecasting regional atmospheric processes. In: Faragó, I., Havasi, Á, Georgiev, K. (eds.) Advances in Air Pollution Modeling for Environmental Security, NATO Science Series, vol. 54, 143–152. Springer Netherlands, Leiden (2005)
9. Marchuk, G.I.: Mathematical Modeling in Environmental Issues. Nauka, Moscow (1982) (in Russian)
10. Martin, D.O.: An urban diffusion model for estimating long-term average values of air quality. Air Pollut. Contr. QI Assoc. **21**, 16–19 (1971)
11. Prusov, V., Doroshenko, A.: Modeling and forecasting atmospheric pollution over region. Annales Univ. Sci. Budapest **46**, 47–64 (2003)
12. Zannetti, P.: Air Pollution Modeling—Theories, Computational Methods and Available Software. Van Nostrand Reinhold, New York (1990)
13. Aloyan, A.E.: Modeling Dynamics and Kinetics of Gas Impurities and Aerosols in Atmosphere. Nauka, Moscow (2008) (in Russian)
14. Baranova, M.E., Gavrilov, A.S.: Methods of computational monitoring of atmospheric pollution of megacities. Yestestvennye i Tekhnicheskie Nauki **4**, 221–225 (2008) (in Russian)
15. Carlslaw, D.C., Beevers, S.D.: Development of an urban inventory for road transport emissions of NO_2 and comparison with estimates derived from ambient measurements. Atmos. Environ. **39**, 2049–2059 (2005)
16. Carruters, D., Dyster, S., McHugh, C.: Factors affecting inter-annual variability of NOx and NO_2 concentration from single point sources. Clean Air Environ. Prot. **33**(1), 15–20 (2003)
17. Kochergin, S.V., Kochergin, V.S.: Identification of turbulent diffusion coefficients in the transfer model of passive admixture. Sistemy Kontrol'a Okruzhayushchei Sredy **14**, 111–113 (2010) (in Russian)
18. Kozhevnikova, M.F., Levenets, V.V., Rolik, I.L.: Identification of pollution sources: computational methods. Voprosy Atomnoy Nauki i Tekhniki. Series: Vacuum, Pure Materials, Superconductors **19**(6), 149–156 (in Russian) (2011)
19. GPistocchi, A., Galmarini, S.: Evaluation of a simple spatially explicit model of atmospheric transport of pollutants in Europe. Environ. Model Assess. **15**, 37–51 (2010)

20. Prevedouros, K., MacLeod, M., Jones, K.C., Sweetmana, A.: Modelling the fate of persistent organic pollutants in Europe: parameterization of a gridded distribution model. Environ. Pollut. **128**, 251–261 (2004)
21. Semenchyn, E.A., Kuziakina, M.V.: Stochastic Methods for Solving Inverse Problems in the Mathematical Model of Atmospheric Diffusion. Fizmatgiz, Moscow (2012) (in Russian)
22. Stepanenko, S.N., Voloshyn, V.G., Tiptsov, S.V.: Solution of turbulent diffusion equation for stationary point source. Ukr. Hydrometeorological J. **3**, 1–24 (in Russian) (2008)
23. Venkatram, A., Karamchandani, P., Goldstein, P.R.: The development and application of a simplified ozone modelling system (SOMS). Atmos. Environ. **28**(22), 3365–3678 (1994)
24. Gauntlett, D.J., Leslie, L.M., McGregor, J.L., Hincksman, D.R.: A limited area nested numerical weather prediction model: formulation and preliminary results. Quart. J. R. Met. Soc. **104**, 103–117 (1978)
25. Hill, G.E.: Grid telescoping in numerical weather prediction. J. Appl. Meteorol. **7**, 29–38 (1968)
26. Miyakoda, K., Rosati, A.: One-way nested grid models: the interface condition and the numerical accuracy. Mon. Weather Rev. **105**, 1092–1107 (1977)
27. Sundstrom, A.: Theoretical and practical problems in formulating boundary conditions for a limited-area model. Report DM-9, Dept. Meteor., University of Stockholm, Sweden (1973)
28. Boussinesq, J.: Theorie de l'ecoulement tourbillant. Mem. Pres. Acad. Sci. **XXIII**, 46 (1877)
29. Blackadar, A.K.: The vertical distribution of wind and turbulence exchange in a neutral atmosphere. J. Geophys. Res. **105**, 6453–6468 (2000)
30. Bradshaw, P., Cebeci, T., Whitelaw, J.H.: Engineering Calculation Methods for Turbulent Flow. Academic, New York (1981)
31. Doms, G., Shättler, U., Schraff, C.: A Description of the Nonhydrostatic Regional COSMO-Model, User's Guide. http://www.cosmo-model.org. Accessed 9 Sep 2015 (2008)
32. Durbin, P.A., Mansour, N.N., Yang, Z.: Eddy viscosity transport model for turbulent flow. Phys. Fluids **6**(2), 1007–1015 (1994)
33. Guliaev, A.N., Kozlov, V.E., Sekundov, A.N.: To creation of universal monoparametrical model for turbulent viscosity. Mekanika Zhidkosti i Gaza **4**, 69–76 (1993) (in Russian)
34. Nee, V.W., Kovasznay, L.S.G.: Simple phenomenological theory of turbulent, shear flows. Phys. Fluids **12**, 473–484 (1969)
35. Prusov, V.A., Romaniuk, A.P.: Mathematical model of turbulence for stratified environments. Proc. Ukrainian Hydrometeorological Institute **246**, 35–45 (in Russian) (1998)
36. Prusov, V.A., Solohub, T.A.: Model of vertical column of horizontally homogeneous atmosphere. Proc. Ukrainian Hydrometeorological Institute **259**, 61–73 (in Ukrainian) (2011)
37. Spalart, P.R., Allmaras, S.R.: A One-equation turbulence model for aerodynamic flows. La Recherche Aerospatiale **1**, 5–21 (1994)
38. Shur, M., Strelets, M., Travin, A., Spalart, P.R.: Turbulence modeling in rotating and curved channels: assessment of the Spalart-Shur correction term. AIAA J. **38**(5), 784–792 (2000)
39. Dacles-Mariani, J., Zilliac, G.G., Chow, J.S., Bradshaw, P.: Numerical/experimental study of a wingtip vortex in the near field. AIAA Journal **33**(9), 1561–1568 (1968)
40. Spalart, P.R., Shur, M.L.: On the sensitization of simple turbulence models to rotation and curvature. Aerosp. Sci. Technol. **1**(5) 297–302 (1997)
41. Gill, A.E.: Atmosphere-Ocean Dynamics, vol. 1. Academic, London (1982)
42. List, R.J.: Smithsonian Meteorological Tables, 6th edn. Smithson, Inst., Washington (1951)
43. Bakhvalov, N.: Numerical Methods. Nauka, Moscow (1975) (in Russian)
44. Godunov, S.K., Riaben'kii, V.S.: Difference Schemes (Introduction to the Theory). Nauka, Moscow (1973) (in Russian)
45. Schetz, J.: Injection and Mixing in Turbulent Flow (Progress in Astronautics and Aeronautics). American Institute of Aeronautics, Reston (1980)
46. Prusov, V., Doroshenko, A.: Simulation of Natural and Anthropogenic Processes in the Atmosphere. Naukova Dumka, Kyiv (2006) (in Ukrainian)

Chapter 7
Coordinate Transformation Approach for Numerical Solution of Environmental Problems

Tatiana Chernogorova, Ivan Dimov and Lubin Vulkov

Abstract We consider numerical solution of 1D and 2D advection-diffusion equations that arise, among others, in environmental modeling. Since the problems are posed on the unbounded domains we use coordinate transformations to confine the computational region. Well-posedness of the new problems and properties of the solution are studied. Finite volume difference schemes (FVDS) are discussed. Positive splitting numerical method is proposed.

Keywords Advection-diffusion equations • Air-pollution • Difference scheme • Non-negativity preservation • Splitting • Transformation • Unbounded domain

7.1 Introduction

Many problems of air pollution transport are described by partial differential equations on unbounded domains and must be treated numerically. The process of pollutant transport and diffusion in the atmosphere (and, in the water, as well) is described by advection-diffusion equations [4, 8, 12]. For this kind of problems the main difficulty is the unboundedness of the domain. Standard numerical methods, such as the finite difference and finite element methods, cannot be applied directly to these problems. In this chapter we discuss the coordinate transformation method, first proposed in [7] according to our best knowledge. What

T. Chernogorova (✉)
Faculty of Mathematics and Informatics, University of Sofia, Sofia, Bulgaria
e-mail: chernogorova@fmi.uni-sofia.bg

I. Dimov
Institute of Information and Communication Technologies, Bulgarian Academy of Sciences, Sofia, Bulgaria
e-mail: ivdimov@bas.bg

L. Vulkov
Faculty of Natural Sciences and Education, University of Rousse, Rousse, Bulgaria
e-mail: lvalkov@uni-ruse.bg

A. Bátkai et al. (eds.), *Mathematical Problems in Meteorological Modelling*, Mathematics in Industry 24, DOI 10.1007/978-3-319-40157-7_7

type of coordinate transformation is suitable? It should satisfy the following basic requirements:

- *the reduced problem is well-posed*, i.e. the reduced problem has a unique solution and the solution depends continuously on the boundary value (and initial value);
- the solution of reduced problem *is the same as the solution of the original problem, or it is a good approximation of the solution of the original problem*;
- *the bounded computational domain should be as small as possible*, in order to reduce the computational work and memory requirement.

Let us consider one-to-one transform, the parameter a is a positive scaling factor and $l > 0$ is arbitrary but fixed:

$$z = g(\xi; a),\ a > 0,\ \xi \in \Omega = (0, l) \text{ or } (-l, l),\ z \in D = (0, +\infty) \text{ or } (-\infty, \infty),$$

such that

$$z' = g'_{\xi}(\xi; a) > 0, \quad a > 0, \quad \xi \in \Omega$$

and

$$g(-l, a) = 0,\ g(l; a) = +\infty \text{ if } D = (0, +\infty);\ g(\pm l; a) = \pm\infty \text{ if } D \in (-\infty, \infty).$$

Several typical mappings that have been proposed and used in practice are of the above type, see e. g. [11] and the references there in. In the present chapter we will use the logarithmic mapping

$$z = \frac{1}{2a} \log\left(\frac{l+\xi}{l-\xi}\right), \quad \xi \in \Omega = (0, l) \Leftrightarrow \xi = l\frac{e^{2az} - 1}{e^{2az} + 1}, \quad z \in (0, \infty). \tag{7.1}$$

The convection-diffusion equations of the environmental models describe physical and chemical processes. The numerical approximations must reproduce their behavior adequately. For example, considering the process of pollutant transport and diffusion in the atmosphere (and in the water, as well) the concentration of pollutants cannot be negative, so that the numerical method is required to have the so called *property of non-negativity preservation* [3, 6].

The chapter is organized as follows. The next Sect. 7.2 presents some theoretical and numerical results for a 1D model of the convection-diffusion problem. In Sect. 7.3 we discuss the well-posedness and non-negativity of the solution of a non-stationary 2D problem. Positive numerical method is proposed in Sect. 7.4. Finally, Sect. 7.5 summarizes our conclusions.

The present contribution is based on the previously published contribution [2].

7.2 A Stationary Model of Air Pollution

The stationary model of determining the *concentration of pollutants* described in [3] is reduced to the following *problem*:

$$u\frac{\partial\varphi}{\partial x} - w_g\frac{\partial\varphi}{\partial z} - \frac{\partial}{\partial z}\left(v(z)\frac{\partial\varphi}{\partial z}\right) + \sigma\varphi = 0, \quad x > 0,\ z > 0, \tag{7.2a}$$

$$u\varphi(0,z) = Q\delta(z-H), \quad z > 0, \tag{7.2b}$$

$$\frac{\partial\varphi}{\partial z}(x,0) = \alpha\varphi(x,0),\ x > 0,\ \lim_{z\to\infty}\varphi(x,z) = 0, \quad x > 0, \tag{7.2c}$$

where $\delta(z)$ denotes the Dirac delta function and $\alpha = const \geq 0$ is a coefficient characterizing the reflection and adsorption of the bedding surface. Equation (7.2a) is *parabolic advection-diffusion equation*, where x plays the role of the time variable. To problem (7.2a)–(7.2c) we apply transformation (7.1) taking for clarity $l = 1$ and using the notation $\psi(x,\xi) \equiv \varphi(x, z(\xi))$, namely:

$$L\psi \equiv v(\xi)\frac{\partial\psi}{\partial x} - \frac{\partial}{\partial\xi}\left(p(\xi)\frac{\partial\psi}{\partial\xi} + q(\xi)\psi\right) + (\sigma + r(\xi))\psi = 0, \tag{7.3a}$$

$$(x,\xi) \in Q_X \equiv (0,X)\times(0,1),$$

$$p(\xi) = a^2(1-\xi^2)^2\mu(\xi), \quad q(\xi) = a(1-\xi^2)[2a\xi\mu(\xi) + w_g],$$

$$r(\xi) = 2a^2(1-3\xi^2)\mu(\xi) + 2a^2\xi(1-\xi^2)\frac{\partial\mu(\xi)}{\partial\xi} - 2aw_g\xi,$$

$$v(\xi)\psi(0,\xi) = Q\delta\left(\xi-\xi_H\right), \quad \xi\in\Omega,\ \ \xi_H = \frac{e^{2aH}-1}{e^{2aH}+1}, \tag{7.3b}$$

$$l_0\psi = a\frac{\partial\psi}{\partial\xi}(x,0) - \alpha\psi(x,0) = 0, \ \ x\in(0,X), \tag{7.3c}$$

$$l_1\psi = \psi(x,1) = 0, \ \ x\in(0,X). \tag{7.3d}$$

Further, to handle the degeneracy in Eq. (7.3a) at $\xi = 1$, we introduce the weighted inner product and corresponding norm on $L_{2,w}(\Omega)$ by

$$(u,v)_{0,w} = \int_0^1 (1-\xi)^2 uv d\xi, \quad \|v\|_{0,w} = \sqrt{(v,v)_w} = \left(\int_0^1 (1-\xi)^2 v^2 d\xi\right)^{1/2}.$$

The space of all weighted square-integrable functions is defined as $L_{2,w}(\Omega) = \{v : \|v\|_{0,w} < \infty\}$. By using a standard argument it is easy to show that the pair $(L_{2,w}(\Omega),(\cdot,\cdot)_w)$ is a Hilbert space. Using $L_2(\Omega)$ and $L_{2,w}(\Omega)$, we define the following weighted Sobolev space

$$H^1_w(\Omega) := \{v\in L_2(\Omega),\ v'\in L_{2,w}(\Omega)\}, \quad v' = \partial v/\partial\xi$$

with the corresponding inner product. Also, it is easy to prove that the pair $(H_w^1(\Omega), (\cdot,\cdot)_{H_w^1})$ is a Hilbert space with the norm

$$\|v\|_{1,w} := \{\|v'\|_{0,w}^2 + \|v\|_2^2\}^{1/2} = \{\big((1-\xi)^2 v', v'\big) + (v, v)\}^{1/2}.$$

For $\psi, \chi \in H_w^1(\Omega)$ we define the bilinear form

$$A(\psi, \chi; x) := \int_0^1 \left[p(\xi)\frac{\partial \psi}{\partial \xi}\frac{\partial \chi}{\partial \xi} + q(\xi)\psi\frac{\partial \chi}{\partial \xi} + (\sigma + r(\xi))\psi\chi \right] d\xi \tag{7.4}$$
$$+a(\alpha\mu(0) + w_g)\psi(x,0)\chi(0).$$

For reason of computations we will assume that the condition (7.3b) is regularized

$$v(\xi)\psi(0,\xi) = \psi_0(\xi), \quad \xi \in \Omega \tag{7.5}$$

and at least $\psi_0 \in L_2(\Omega)$. Find $\psi \in L^\infty((0,X); H_w^1) \cap C((0,X); L_2(\Omega))$ satisfying the initial condition (7.5) such that for all $\chi \in H_w^1(\Omega)$

$$\int_0^1 v\frac{\partial \psi}{\partial x}\chi d\xi + A(\psi, \chi; x) = 0 \ \text{ a. e. in } (0,X).$$

Theorem 7.1 ([2]) *Let $\psi_0 \in L^\infty((0,X); H_w^1) \cap C((0,X); L_2(\Omega))$. There exists a unique solution $\psi \in H_w^1(\Omega)$ to problem (7.3a), (7.5), (7.3c), (7.3d).*

Let $V(Q_X)$ be the Banach space consisting of all functions $f \in H_w^{0,1}(Q_X) = C((0,X); H_w^1(\Omega))$ having finite norm

$$\|f\|_{V_2(Q_X)} = sup_{0\le x\le X}\|f(x,\cdot)\|_{L_2(\Omega)} + \left[\int_{Q_X}(1-\xi)^2\left(\frac{\partial f}{\partial \xi}\right)^2 d\xi dx\right]^{1/2}.$$

A function $\psi \in V(Q_X)$ is said to satisfy weakly (7.3a), (7.5), (7.3c), (7.3d) if for any non-negative function $\eta \in H_w^{1,1}(Q_X) = H^1((0,T); H_w^1(\Omega))$

$$\int_0^1 v(\xi)\psi(x,\xi)\eta(\xi,x)d\xi - \int_0^1 v(\xi)\psi_0(\xi)\eta(0,\xi)d\xi - \iint\limits_{Q_x} v\psi\eta_x d\xi dx$$
$$+\int_0^x A(\psi, \eta; s)ds \ge 0$$

for almost every $x \in (0,X)$. Here $Q_x = (0,x)\times\Omega$.

Theorem 7.2 ([2]) *Let* $\psi(x,\xi)$ *be in* $V(Q_X)$ *and satisfy* (7.3a)–(7.3d). *Then* $\psi(x,\xi) \geq 0$ *in* Q_X.

Let the interval $[0,1]$ be subdivided into N intervals $I_i = [\xi_i, \xi_{i+1}]$, $i = 1,2,\ldots,N$ with $0 = \xi_1 < \xi_2 < \ldots < \xi_N < \xi_{N+1} = 1$ and $h_i = \xi_{i+1} - \xi_i$ for $i = 1,2,\ldots,N$. We set $\xi_{i-1/2} = 0.5(\xi_{i-1} + \xi_i)$, $\xi_{i+1/2} = 0.5(\xi_i + \xi_{i+1})$, $\hbar_i = \xi_{i+1/2} - \xi_{i-1/2}$ for $i = 2,3,\ldots,N$ [10]. In order to discretize with respect to x we introduce the mesh $0 = x_1 < x_2 < \ldots < x_j < x_{j+1} < \ldots < x_{M+1} = X$, $\Delta x_j = x_{j+1} - x_j$. Then in [2] the weighted θ-scheme is derived for the solution of the problem (7.3a), (7.5), (7.3c), (7.3d)

$$-\left[\frac{v_1}{\Delta x_j}\frac{h_1}{2} + \theta e_{1,1}\right]\psi_1^{j+1} + \theta e_{1,2}\psi_2^{j+1} = \left[-\frac{v_1}{\Delta x_j}\frac{h_1}{2} + (1-\theta)e_{1,1}\right]\psi_1^j$$

$$-(1-\theta)e_{1,2}\psi_2^j, \quad \psi_{N+1}^{j+1} = 0,$$

$$\theta e_{i,i-1}\psi_{i-1}^{j+1} - \left[\frac{v_i}{\Delta x_j}\hbar_i + \theta e_{i,i}\right]\psi_i^{j+1} + \theta e_{i,i+1}\psi_{i+1}^{j+1} = -(1-\theta)e_{i,i-1}\psi_{i-1}^j$$

$$+\left[-\frac{v_i}{\Delta x_j}\hbar_i + (1-\theta)e_{i,i}\right]\psi_i^j - (1-\theta)e_{i,i+1}\psi_{i+1}^j, \quad i = 2,3,\ldots,N,$$

$$e_{1,1} = \frac{(1-\xi_{3/2}^2)b_{3/2}\left(\frac{1+\xi_1}{1-\xi_1}\right)^{\frac{\alpha_1}{2}}}{\left(\frac{1+\xi_2}{1-\xi_2}\right)^{\frac{\alpha_1}{2}} - \left(\frac{1+\xi_1}{1-\xi_1}\right)^{\frac{\alpha_1}{2}}} + a\left(\alpha\mu(\xi_1) + w_g\right) + \frac{h_1}{2}\left(\sigma + r(\xi_1)\right),$$

$$e_{1,2} = \frac{(1-\xi_{3/2}^2)b_{3/2}\left(\frac{1+\xi_2}{1-\xi_2}\right)^{\frac{\alpha_1}{2}}}{\left(\frac{1+\xi_2}{1-\xi_2}\right)^{\frac{\alpha_1}{2}} - \left(\frac{1+\xi_1}{1-\xi_1}\right)^{\frac{\alpha_1}{2}}}, \quad e_{i,i-1} = \frac{(1-\xi_{i-1/2}^2)b_{i-1/2}\left(\frac{1+\xi_{i-1}}{1-\xi_{i-1}}\right)^{\frac{\alpha_{i-1}}{2}}}{\left(\frac{1+\xi_i}{1-\xi_i}\right)^{\frac{\alpha_{i-1}}{2}} - \left(\frac{1+\xi_{i-1}}{1-\xi_{i-1}}\right)^{\frac{\alpha_{i-1}}{2}}},$$

$$e_{i,i+1} = \frac{(1-\xi_{i+1/2}^2)b_{i+1/2}\left(\frac{1+\xi_{i+1}}{1-\xi_{i+1}}\right)^{\frac{\alpha_i}{2}}}{\left(\frac{1+\xi_{i+1}}{1-\xi_{i+1}}\right)^{\frac{\alpha_i}{2}} - \left(\frac{1+\xi_i}{1-\xi_i}\right)^{\frac{\alpha_i}{2}}}, \quad e_{i,i} = \frac{(1-\xi_{i+1/2}^2)b_{i+1/2}\left(\frac{1+\xi_i}{1-\xi_i}\right)^{\frac{\alpha_i}{2}}}{\left(\frac{1+\xi_{i+1}}{1-\xi_{i+1}}\right)^{\frac{\alpha_i}{2}} - \left(\frac{1+\xi_i}{1-\xi_i}\right)^{\frac{\alpha_i}{2}}}$$

$$+\frac{(1-\xi_{i-1/2}^2)b_{i-1/2}\left(\frac{1+\xi_i}{1-\xi_i}\right)^{\frac{\alpha_{i-1}}{2}}}{\left(\frac{1+\xi_i}{1-\xi_i}\right)^{\frac{\alpha_{i-1}}{2}} - \left(\frac{1+\xi_{i-1}}{1-\xi_{i-1}}\right)^{\frac{\alpha_{i-1}}{2}}} + \hbar_i\left(\sigma + r(\xi_i)\right), \quad i = 2,3,\ldots,N-1;$$

$$e_{N,N-1} = \frac{(1-\xi_{N-1/2}^2)b_{N-1/2}\left(\frac{1+\xi_{N-1}}{1-\xi_{N-1}}\right)^{\frac{\alpha_{N-1}}{2}}}{\left(\frac{1+\xi_N}{1-\xi_N}\right)^{\frac{\alpha_{N-1}}{2}} - \left(\frac{1+\xi_{N-1}}{1-\xi_{N-1}}\right)^{\frac{\alpha_{N-1}}{2}}}, \quad e_{N,N+1} = \frac{1}{2}(1-\xi_{N+1/2}^2)$$

$$\times \left(\bar{c}_{N+1/2} + b_{N+1/2}\right), \; e_{N,N} = \frac{1}{2}(1-\xi_{N+1/2}^2)\left(\bar{c}_{N+1/2} - b_{N+1/2}\right)$$
$$+\frac{(1-\xi_{N-1/2}^2)b_{N-1/2}\left(\frac{1+\xi_N}{1-\xi_N}\right)^{\frac{\alpha_{N-1}}{2}}}{\left(\frac{1+\xi_N}{1-\xi_N}\right)^{\frac{\alpha_{N-1}}{2}} - \left(\frac{1+\xi_{N-1}}{1-\xi_{N-1}}\right)^{\frac{\alpha_{N-1}}{2}}} + \hbar_N\left(\sigma + r(\xi_N)\right).$$

Theorem 7.3 (Corollary in [2]) *Let $Q > 0$. Then for $0 < \theta \leq 1$ and $\tau = \max_{1\leq j\leq M} \triangle x_j$ sufficiently small, the discrete solution $\{\psi_i^{j+1}\}$ is nonnegative.*

7.3 A Non-stationary Two-Dimensional Problem

The model is based on the time-dependent advection-diffusion equation:

$$\frac{\partial C}{\partial t} + u(z)\frac{\partial C}{\partial x} - w_s\frac{\partial C}{\partial z} = k_x(z)\frac{\partial^2 C}{\partial x^2} + \frac{\partial}{\partial z}\left(k_z(z)\frac{\partial C}{\partial z}\right) + f(x,z) \tag{7.6}$$

on $(-\infty,\infty)\times(z^0,1)$ and subjected to the boundary and initial conditions

$$C(\pm\infty,z,t) = 0, \quad \left(k_z(z)\frac{\partial C}{\partial z} + w_s C\right)_{z=z^0,1} = 0, \quad C(x,z,0) = 0, \tag{7.7}$$

where C is the concentration of the pollutant, z^0 is the boundary roughness height, w_s is the setting velocity and $f(x,z) = \delta(x)\delta(z-z_p)$, i.e. a point source is located at $(x,z) = (0,z_p)$.

Following the transformation (7.1) the model becomes

$$\frac{\partial C}{\partial t} + u(z)a(1-\xi^2)\frac{\partial C}{\partial \xi} - a^2 k_\xi(z)(1-\xi^2)\left[(1-\xi^2)\frac{\partial^2 C}{\partial \xi^2} - 2\xi\frac{\partial C}{\partial \xi}\right]$$
$$= \frac{\partial}{\partial z}\left(k_z(z)\frac{\partial C}{\partial z}\right) + w_s\frac{\partial C}{\partial z} + \delta(\xi)\delta(z-z_p), \tag{7.8a}$$
$$l^{\pm}(C) \equiv C(\pm 1,z,t) = 0, \tag{7.8b}$$
$$l_{z^0,1}(C) \equiv \left[k_z(z)\frac{\partial C}{\partial z} + w_s C\right]_{z=z^0,1} = 0, \tag{7.8c}$$
$$C(\xi,z,0) = C_0(\xi,z) = 0. \tag{7.8d}$$

The parabolic equation (7.8a) belongs to the second order PDEs with *non-negative characteristic form* [9]. The main character of such kind of equations is the *degeneracy*. It can easily be seen that at $\xi = \mp 1$ Eq. (7.8a) degenerates into two

parabolic one-dimensional equations:

$$\frac{\partial C}{\partial t} = \frac{\partial}{\partial z}\left(k_z(z)\frac{\partial C}{\partial z}\right) + w_s\frac{\partial C}{\partial z}, \quad (z,t) \in (z^0,1)\times(0,T].$$

We rewrite Eq. (7.8a) in divergent form:

$$\frac{\partial C}{\partial t} - LC + p(\xi,z)C = f_R(\xi,z) \quad \text{for } (\xi,z,t) \in Q_T = \Omega\times(0,T], \tag{7.9}$$

$$LC = \nabla\cdot(\mathbf{A}\nabla C + \mathbf{b}C), \quad \Omega = (-1,1)\times(z^0,1),$$

$$\mathbf{A} = \begin{pmatrix} a_{11} & 0 \\ 0 & a_{22}\end{pmatrix}, \quad a_{11} = a^2k_\xi(z)(1-\xi^2)^2, \qquad a_{22} = k_z(z),$$

$$\begin{pmatrix} b_1(\xi,z) \\ b_2\end{pmatrix} = \begin{pmatrix} (1-\xi^2)a\left(2\xi a k_\xi(z) - u(z)\right) \\ w_s\end{pmatrix},$$

$$p(\xi,z) = 2a^2k_\xi(z)(1-3\xi^2) + 2\xi a u(z),$$

and $f_R(\xi,z)$ is a regularization of the delta function $\delta(\xi)\delta(z-z_p)$.

We introduce the inner product and corresponding norm on $L_{2,w}(\Omega)$ by

$$(u,v)_w := \iint_\Omega (1-\xi^2)^2 uv\,d\xi dz, \ \|v\|_{0,w} = \sqrt{(v,v)_w} = \left(\iint_\Omega (1-\xi^2)^2 v^2\,d\xi dz\right)^{\frac{1}{2}}.$$

Using $L_2(\Omega)$ and $L_{2,w}(\Omega)$ we define the following weighted Sobolev space:

$$H^1_w(\Omega) := \left\{ v \in L_2(\Omega), \ \frac{\partial v}{\partial \xi} \in L_{2,w}(\Omega) \ \text{ and } \ \frac{\partial v}{\partial z} \in L_2(\Omega)\right\}.$$

It is also easy to prove that $H^1_w(\Omega)$ is a Hilbert space with the norm

$$\|v\|_{1,w} := \left[\int_\Omega \left(v^2 + (1-\xi^2)^2\left(\frac{\partial v}{\partial \xi}\right)^2 + \left(\frac{\partial v}{\partial z}\right)^2\right) d\xi dz\right]^{1/2}.$$

Next, for $C, \eta \in H^1_w(\Omega)$ define the bilinear form

$$\mathcal{A}(C,\eta) \equiv \int_\Omega \left(a_{11}\frac{\partial C}{\partial \xi}\frac{\partial \eta}{\partial \xi} + a_{22}\frac{\partial C}{\partial z}\frac{\partial \eta}{\partial z} + b_1 C\frac{\partial \eta}{\partial \xi} + b_2 C\frac{\partial \eta}{\partial z} + pC\eta\right) d\xi dz.$$

The following variational problem corresponding to (7.9) and (7.8b)–(7.8d): find $C \in H_w^1(\Omega)$ satisfying the initial condition (7.8d) such that for all $\eta \in H_w^1(\Omega)$

$$\int_\Omega \frac{\partial C}{\partial t}\eta d\xi dz + \mathcal{A}(C,\eta) = \int_\Omega f_R \eta d\xi dz, \quad \text{a. e. in } (0,T].$$

Theorem 7.4 ([1]) *There exists a unique solution* $C \in H_w^1(\Omega)$ *to problem* (7.9), (7.8b)–(7.8d).

Let $V_2(Q_T)$ be the Banach space consisting of all functions in $H_w^{1,0}(Q_T) = C((0,T); H_w^1(\Omega))$ having finite norm

$$\|v\|_{V_2(Q_T)} = \sup_{0\le t\le T} \|v(\cdot,\cdot;t)\|_{L_2(\Omega)} + \left(\int_0^T \|v\|_{H_w^1(\Omega)}(t)dt\right)^{1/2}.$$

Theorem 7.5 ([1]) *Let* $C(\xi,z,t)$ *be in* $V_2(Q_T)$ *and satisfy integral identity above. Then* $C(\xi,z,t) \ge 0$ *in* Q_T.

Further a FVDS for approximation of the problem (7.8a)–(7.8d) (that is an extension to the 1D scheme in the previous section) is constructed and analyzed in [1].

7.4 Positive Splitting Numerical method

Four types splitting procedures for air pollution models are defined and studied numerically in [5].

On the base of the considerations of Sects. 7.2 and 7.3 we will propose a positive splitting numerical method for the 2D non-stationary model of air pollution [4]

$$\frac{\partial \varphi}{\partial t} = \frac{\partial}{\partial x}\left(k_x(x,z)\frac{\partial \varphi}{\partial x}\right) + \frac{\partial}{\partial z}\left(k_z(x,z)\frac{\partial \varphi}{\partial z}\right) - u\frac{\partial \varphi}{\partial x} - (w - w_g)\frac{\partial \varphi}{\partial z} - \sigma\varphi,$$
$$x > 0,\ z > 0,\ 0 < t \le T,$$

$$u\varphi(t,0,z) = Q\delta(z-H), \quad \frac{\partial \varphi}{\partial z}(t,x,0) = \alpha\varphi(t,x,0),$$
$$\lim_{x\to\infty} \varphi(t,x,z) = 0, \quad \lim_{z\to\infty} \varphi(t,x,z) = 0,$$
$$\varphi(0,x,z) = 0.$$

Here φ is the concentration of pollutants, (u,w) are the components of the wind velocity, $w_g = const > 0$ is the falling velocity of the pollutants by gravity,

$\sigma = const \geq 0$ is the transformation coefficient of pollutants and k_x, k_z are the horizontal and vertical diffusion coefficients.

After logarithmic transformations

$$x = \frac{1}{2a}\log\left(\frac{1+\xi}{1-\xi}\right), \quad \xi \in (0,1) \quad \Leftrightarrow \xi = \frac{e^{2ax}-1}{e^{2ax}+1}, \quad x \in (0,\infty),$$

$$z = \frac{1}{2b}\ln\left(\frac{1+\eta}{1-\eta}\right), \quad \eta \in (0,1) \quad \Leftrightarrow \eta = \frac{e^{2bz}-1}{e^{2bz}+1}, \quad z \in (0,\infty),$$

function $\psi(t,\xi,\eta) = \varphi(t,x(\xi),z(\eta))$ satisfies the following equation and additional conditions:

$$\frac{\partial\psi}{\partial t} = a^2\left(1-\xi^2\right)^2 k_x\frac{\partial^2\psi}{\partial\xi^2} + a\left(1-\xi^2\right)\left[a\left(1-\xi^2\right)\frac{\partial k_x}{\partial\xi} - 2a\xi k_x - u\right]\frac{\partial\psi}{\partial\xi}$$
$$+b^2\left(1-\eta^2\right)^2 k_z\frac{\partial^2\psi}{\partial\eta^2} + b\left(1-\eta^2\right)\left[b\left(1-\eta^2\right)\frac{\partial k_z}{\partial\eta} - 2b\eta k_z - \left(w-w_g\right)\right]\frac{\partial\psi}{\partial\eta}$$
$$-\sigma\psi \tag{7.10a}$$

$$u\psi(t,0,\eta) = Q\delta\left(\eta - \frac{e^{2bH}-1}{e^{2bH}+1}\right), \quad \eta \in [0,1], \quad t \in [0,T], \tag{7.10b}$$

$$b\frac{\partial\psi}{\partial\eta}(t,\xi,0) = \alpha\psi(t,\xi,0), \quad \xi \in [0,1], \quad t \in [0,T], \tag{7.10c}$$

$$\psi(t,1,\eta) = 0, \quad \eta \in [0,1], \quad t \in [0,T], \tag{7.10d}$$

$$\psi(t,\xi,1) = 0, \quad \xi \in [0,1], \quad t \in [0,T], \tag{7.10e}$$

$$\psi(0,\xi,\eta) = 0. \tag{7.10f}$$

Following the same line as in the previous section, the well-posedness of the differential problem (7.10a)–(7.10f) and the non-negativity of its solution can be studied.

For the problem (7.10a)–(7.10f) we construct a splitting method. Let us introduce a uniform mesh in the interval $[0,T]$: $\bar{\omega}_\tau = \{t_j = j\tau,\ j = 0,1,\ldots,M\}$. Problem (7.10a)–(7.10f) can be reduced to consequently solving (in the rows and columns of a two-dimensional mesh, introduced in the unit square) the following 1D problems, in which the differential equation is written in divergent form:

Problem A:

$$L_1\psi_1 \equiv \frac{1}{2}\frac{\partial\psi_1}{\partial t} - \frac{\partial}{\partial\xi}\left(p_1(\xi,\eta)\frac{\partial\psi_1}{\partial\xi} + q_1(\xi,\eta)\psi_1\right) + \left(0.5\sigma + r_1(\xi,\eta)\right),$$
$$\xi \in [0,1], \quad \eta \in [0,1], \quad t_j < t \leq t_{j+1/2},$$

$$u\psi_1(t,0,\eta) = Q\delta\left(\eta - \frac{e^{2bH}-1}{e^{2bH}+1}\right), \quad \psi_1(t,1,\eta) = 0,$$
$$\psi_1(0,\xi,\eta) = 0, \quad \psi_1(t_{j+1},x,z) = \psi_2(t_{j+1},x,z),$$

where

$$p_1(\xi,\eta) = a^2(1-\xi^2)^2 k_x(\xi,\eta), \quad q_1(\xi,\eta) = a(1-\xi^2)\left[2a\xi k_x(\xi,\eta) - u\right],$$
$$r_1(\xi,\eta) = 2a^2(1-3\xi^2)k_x(\xi,\eta) + 2a^2\xi\left(1-\xi^2\right)\frac{\partial k_x(\xi,\eta)}{\partial\xi} + 2au\xi;$$

Problem B:

$$L_2\psi_2 \equiv \frac{1}{2}\frac{\partial\psi_2}{\partial t} - \frac{\partial}{\partial\eta}\left(p_2(\xi,\eta)\frac{\partial\psi_2}{\partial\eta} + q_2(\xi,\eta)\psi_2\right) + \left(0.5\sigma + r_2(\xi,\eta)\right),$$
$$\xi \in [0,1], \quad \eta \in [0,1], \quad t_{j+1/2} < t \le t_{j+1},$$

$$\psi_2(t_{j+1/2},x,z) = \psi_1(t_{j+1/2},x,z),$$
$$b\frac{\partial\psi_2}{\partial\eta}(t,\xi,0) = \alpha\psi_2(t,\xi,0), \quad \psi_2(t,\xi,1) = 0,$$

where

$$p_2(\xi,\eta) = b^2(1-\eta^2)^2 k_z(\xi,\eta), \quad q_2(\xi,\eta) = b(1-\eta^2)\left[2b\eta k_z(\xi,\eta) - \left(w - w_g\right)\right],$$
$$r_2(\xi,\eta) = 2b^2(1-3\eta^2)k_z(\xi,\eta) + 2b^2\eta\left(1-\eta^2\right)\frac{\partial k_z(\xi,\eta)}{\partial\eta} + 2b(w-w_g)\eta.$$

For approximation of the problems A and B one can apply the FVDS method from Sect. 7.2.

7.5 Conclusions

We have briefly discussed a 1D coordinate transformation often used in computation of differential problems on unbounded domains. We theoretically investigated one 1D and another 2D problem transformed on finite domains using appropriate weighted numerical methods that preserve the non-negativity of the solution of the differential problem (= concentrations of pollutants in environmental models). We continue our theoretical investigations of the positive splitting numerical method and will present various computational results in a forthcoming paper.

As a future plan, it will be interesting to consider extensions of the present results to nonlinear convection-diffusion problems including real models, for example, the Unified Danish Eulerian Model.

Acknowledgements We would like to thank the anonymous referee for the valuable comments and helpful suggestions to improve an earlier version of the manuscript.

This work was partially supported by the Bulgarian Fund of Sciences under Grants No. FNI I 02/9-2014 "Theoretical and Numerical Investigation of Nonlinear Mathematical Models" and No. FNI I 02/20-2014 "Efficient Parallel Algorithms for Large-Scale Computational Problems".

References

1. Chernogorova, T., Vulkov, L.: Finite volume difference scheme for a model of settling particle dispersion from an elevated source in a open-channel flow. Comput. Math. Appl. **67**, 2099–2111 (2014)
2. Chernogorova, T., Vulkov, L.: Fitted finite volume positive difference scheme for a stationary model of air pollution. Numer. Algor. **70**(1), 171–189 (2015)
3. Dang, Q.A., Ehrhardt, M.: Adequate numerical solution of air pollution problems by positive difference schemes on unbounded domains. Math. Comput. Model. **44**, 834–856 (2006)
4. Dimov, I., Zlatev, Z.: Computational and numerical challenges in environmental modeling. Elsevier, Amsterdam (2006)
5. Dimov, I., Farago, I., Havasi, A., Zlatev, Z.: Different splitting techniques with applications to air pollution models. Int. J. Environ. Pollut. **32**(2), 174–199 (2008)
6. Farago, I., Korotov, S., Szabo, T.: Non-negativity preservation of the discrete nonstationary heat equation in 1D and 2D. J. Appl. Math. **3**, 60–81 (2010)
7. Grosh, C.E., Orszag, S.A.: Numerical solution of problems in unbounded regions: coordinates transforms. J. Comput. Physics. **25**, 273–296 (1977)
8. Marchuk, G.I.: Mathematical models in environmental problems. Studies in Mathematics and Its Applications, vol. 16. North Holland, Amsterdam (1986)
9. Oleinik, O.A., Radkevich, E.V.: Second Order Equations with Nonnegative Characteristic Form. AMS/Plenum Press, New York (1973)
10. Samarskii, A.A.: The Theory of Difference Schemes. Marcel Dekker, New York (2001)
11. Shen, J., Wang, L.: Some recent advances on methods for unbounded domains. Commun. Comput. Phys. **5**, 195–241 (2009)
12. Zlatev, Z., Havasi, A., Farago, I.: Influence of climatic changes on pollution levels in Hungary and its surrounding countries. Atmosphere **2**, 201–221 (2011)

Chapter 8
Impact of Climatic Changes on Pollution Levels

Zahari Zlatev, István Faragó, and Ágnes Havasi

Abstract The climatic changes are already causing more and more extreme weather events in many different areas of the Earth. One of the most important consequences of these changes, which has different impacts, is the clear trend for global increase of the temperature. This increase has also some influence on the pollution levels, mainly because (a) many of the damaging pollutants participate in chemical reactions which depend strongly on the temperature and (b) the pollution levels depend also on the natural (biogenic) emissions, which in general are increased when the temperature becomes higher. Therefore, some pollution levels, which are not very dangerous at present, could become harmful in the near future. This is why the influence of the climate changes on the pollution levels should be studied carefully.

Some results related to the influence of the climatic changes on some critical levels related to ozone concentrations are reported in this chapter. The mathematical tool applied in this investigation is a large-scale air pollution model developed and used to study pollution levels in Europe. The model is described by a system of partial differential equations. The discretization of this system leads to huge computational tasks and it is difficult to handle it even when some of the fastest computers are used. Several difficult tasks must be resolved in the efforts to make the model tractable on the computers available at present. It is necessary to resolve the following four tasks: (A) to apply advanced numerical methods, (B) to introduce some splitting techniques, (C) to parallelize the computational process and (D) to exploit the cache memories efficiently.

Z. Zlatev (✉)
Department of Environmental Science, Aarhus University, Frederiksborgvej 399,
P.O. 358, 4000 Roskilde, Denmark
e-mail: zz@envs.au.dk

I. Faragó • Á. Havasi
Department of Applied Analysis and Computational Mathematics,
Eötvös Loránd University, Budapest, Hungary

MTA-ELTE Numerical Analysis and Large Networks Research Group,
Budapest, Hungary
e-mail: faragois@cs.elte.hu; havasia@cs.elte.hu

A. Bátkai et al. (eds.), *Mathematical Problems in Meteorological Modelling*,
Mathematics in Industry 24, DOI 10.1007/978-3-319-40157-7_8

Some results, which are obtained when the four requirements (A)–(D) are satisfied, are presented and analysed in the chapter. The results show clearly that the climatic changes will lead to some increase of pollution levels, thus these could become dangerous for human beings.

Keywords Air pollution modelling • EU ozone directive • Non-linear system of partial differential equations • Operator splitting • UNI-DEM

8.1 Introduction

Increased temperatures in different parts of the Earth would certainly lead to some changes of the concentrations of many of the damaging chemical species (see the conclusions drawn in [10, 30]). There are two major reasons for the increase of the pollution levels: (1) the chemical reactions, in which the pollutants are involved, depend on the temperature and (2) the relative parts of the natural (biogenic) emissions in the sums of all emissions (human-made + natural) are becoming bigger in many areas when the temperature is higher. This is why the global warming will in general cause some increase of the dangerous effects of the concentrations of pollutants in the atmosphere on human beings, animals and plants. Therefore, the relationship between the global increase of the temperature and the pollution levels should be carefully studied. In this chapter the area of interest is both Europe as a whole and also some specific parts of it. The major topics discussed in the chapter are (a) the influence of the climate changes on the pollution levels in some European areas, (b) the changes of the pollution levels that are due to a **combination** of the warming effect with some other important factors and (c) the contribution of air pollution transported from some European countries to other countries. The study was carried out by using 14 elaborated scenarios. Most of the selected scenarios were also discussed in [11, 12, 34, 37, 42, 43]. These scenarios were run over a long time period (consisting of 16 consecutive years) with a powerful large-scale mathematical tool for studying complex environmental problems, the Unified Danish Eulerian Model (UNI-DEM), which is fully described in [2, 4, 6, 31, 33–39, 41–43]. It should additionally be mentioned here that this air pollution model was used in several other advanced studies which were related to (1) the Balkan Peninsula [43], (2) Bulgaria [38, 39], (3) Denmark [6, 32, 37, 41], (4) England [1], (5) Europe [4, 6, 11, 12, 32, 34–36], (6) Hungary [20, 21, 42] and (7) the North Sea [18]. A previous version of UNI-DEM was additionally used in some inter-comparisons of several well-known European large-scale air pollution models [19, 28].

Three climatic scenarios are introduced in Sect. 8.2. The particular model used in the computations, UNI-DEM is briefly described in Sect. 8.3. The complexity of the computational process when the effects due to climatic changes are studied is discussed in Sect. 8.4. In Sect. 8.5 it is explained why (A) the inter-annual variations of the meteorological conditions and (B) the relations between human-

made (anthropogenic) and natural (biogenic) emissions must be taken into account. Numerical result are presented in Sect. 8.6. Some concluding remarks are given in the last section, Sect. 8.7.

8.2 Development of Three Climatic Scenarios

The total number of scenarios used during this study is 14. Not all of the results obtained by using these scenarios are presented here, but most of them are taken into account when conclusions are drawn. All scenarios are fully discussed in [11, 34, 37, 42, 43]. It should also be mentioned here that some of the principles as well as some of the data reported in [7–10, 13, 14, 16, 19, 22–25, 28] were applied during the preparation of the 14 scenarios.

For this study the climatic scenarios are most important and these scenarios will be shortly discussed in this section. The results from the IPCC SRES A2 Scenario were used in the preparation of the climatic scenarios. Some other and more general conclusions from the reports [23, 30], as for example the statement that "the diurnal temperature range in the future will be reduced in the land areas" were also taken into account. This will be explained in the remaining part of this section when the three climatic scenarios will be discussed. The major rules, which are actually applied in the development of these scenarios, are sketched below.

8.2.1 Climate Scenario 1 (Taking into Account Only the Future Changes of the Temperatures)

The predicted annual changes of the temperature according to the IPCC SRES A2 Scenario, see [23], are used to produce the first climatic scenario (it should be mentioned that according to the newest conclusions, [30], the changes are accelerating and becoming greater, but this fact is only indicating that the pollution levels will become even higher than those that are shown in Sect. 8.6). The changes of the temperature in Europe resulting from the IPCC SRES A2 Scenario are shown in Fig. 8.1. Consider any cell of the grid used to create the plot shown in Fig. 8.1 and assume that this cell is located in a region in Fig. 8.1 where the increase of the temperature is in the interval $[a, b]$. The temperature in the chosen cell at hour n (n being any hour in the interval from 1989 to 2004) is increased by an amount $a + c(n)$, where $c(n)$ is randomly generated and uniformly distributed in the interval $[0, b - a]$ so that the mathematical expectation of the increase of the annual mean of the temperature at any cell of the space domain is $(b - a)/2$. This means that (a) only temperatures are varied in this scenario and (b) **the mean value of the annual change** of the temperature at a given point will tend to be the same as that prescribed by the IPCC SRES A2 Scenario.

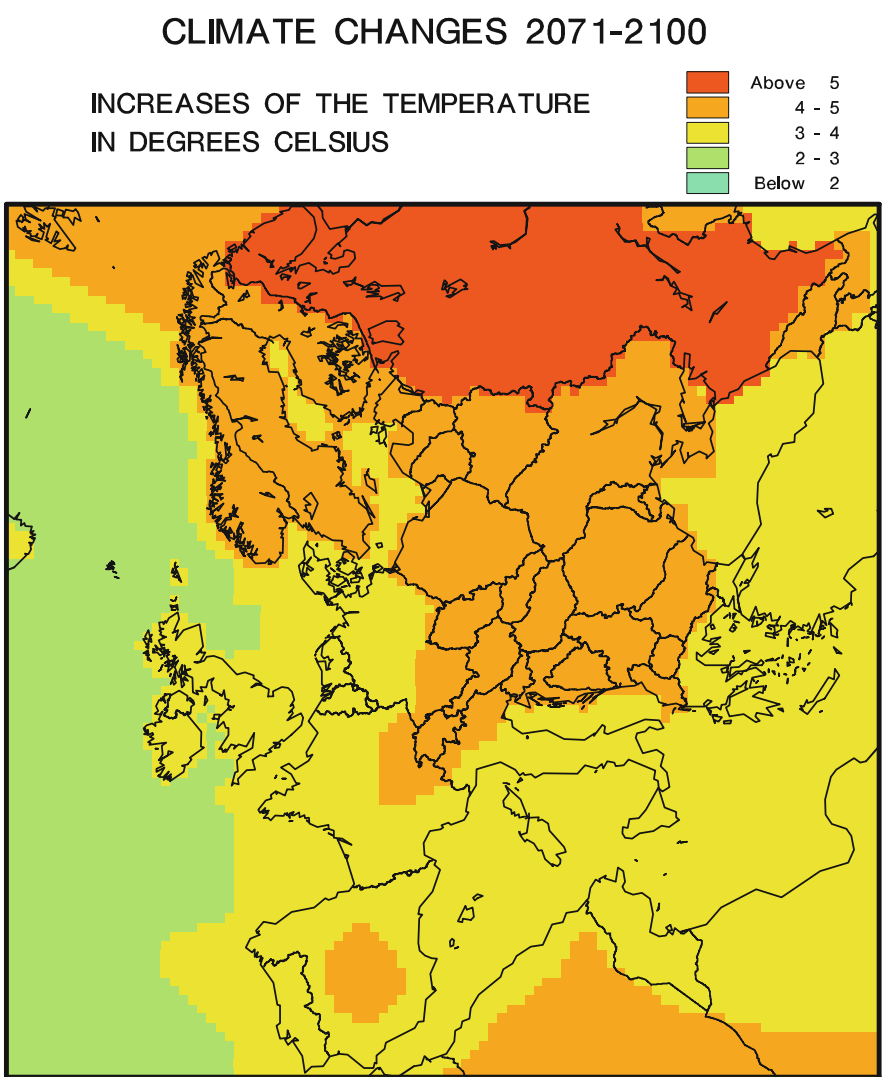

Fig. 8.1 Temperature changes in Europe according to the IPCC Scenario SRES A2 from [22]

8.2.2 Climate Scenario 2 (Taking into Account Some Additional Factors)

The extreme cases will become even stronger in the future climate; see Table 9.6 on p. 575 in [23]. It is expected that: (a) there will be higher maximum temperatures and more hot days over the land areas, (b) there will be higher minimum temperatures, fewer cold days and fewer frost days over nearly all land areas and (c) the diurnal

temperature range will be reduced over land areas. In order to satisfy these three requirements, the conditions (a)–(c) taken from [23], we increased the temperatures during the night-time with a factor larger than the factor by which the day-time temperatures were increased. In this way the second and the third requirements are satisfied. The first requirement is satisfied as follows: during the summer periods the day-time temperatures are increased by a larger amount in hot days. All these changes are carried out only over land. Furthermore, the temperatures are varied in such a way that the annual means of the changes remained the same, at all cells, as those in the first climatic scenario (i.e., the same as those prescribed in the IPCC SRES A2 Scenario). We also reduced (by 10 %) the cloud covers over land during the summer periods.

8.2.3 Climate Scenario 3 (Taking into Account More Additional Factors)

It is also expected, as shown in Table 9.6 on p. 575 in [23], that there will be more intense precipitation events but increased summer drying and associated risk of drought. We increased the precipitation events during winter (both over land and over water). During summer, the precipitation events in the continental parts of Europe were reduced. Similar changes in the humidity data were made. The cloud covers during winter were increased (by 10 %), while the same cloud covers as those in the second climatic scenario were applied in the third climatic scenario during summer. Again, as in the previous two climatic scenarios, the mathematical expectation of the annual means of the changes of the temperature remains the same as the predictions made in the IPCC SRES A2 Scenario.

8.2.4 Some Remarks Related to the Climatic Scenarios

The major purpose with the three climatic scenarios can be explained as follows. It is highly desirable to be able to compare **directly** the pollution levels (which are obtained by using the predicted future temperatures) with **the present state** of the pollution levels. We fixed the transport and varied only the temperatures and several quantities closely related to the temperature in the efforts to achieve this aim. For the sake of simplicity, assume, as was done in Climatic Scenario 1, that only the temperature is varied. Then it becomes very clear that the approach discussed in this chapter has an important advantage: it allows us to compare directly the present pollution levels with the pollution levels obtained with the increased temperature. Since the temperature is the only parameter that is varied, all changes of the ozone levels are clearly caused by the increased temperature levels (the increase of the temperature is the most important factor of the future climate changes and all other effects can be considered as consequences of the global warming process).

It is obvious that the same direct comparison can be performed also if the emissions and some other parameters are also varied (the important issue being **to keep the transport the same during the comparisons**).

We shall not discuss here the creation of the other eleven scenarios in spite of the fact that some of them will be used in the next sections. Most of the remaining scenarios are traditionally used (as, for example, the scenarios based on variations of the emissions). Moreover, when the other scenarios are used, it will be clear how these are created. Some short explanations will be given (when results calculated by some of the other scenarios will be presented) if there will be some danger for misunderstanding.

It is possible to apply another approach; meteorological data (including here wind fields) that are obtained by a climatic model can be used in our model. Such an action implies a requirement to run a big climatic model. However some difficulties will unavoidably appear. The major problem is that it is not very clear in advance how to compare directly the results so found with the results obtained with the Basic Scenario (the scenario in which the actual meteorological data and emission sources are used), because the changes will be caused both by the increased temperature and by the different transport of the pollutants. On the other side, it will be possible to draw other useful conclusions by performing runs over sufficiently long time-periods. It must also be emphasized that the computational difficulties (which will be discussed in Sect. 8.4) would be enormous when the fine discretization (10 km $\times$ 10 km surface cells) that is applied by us is to be preserved.

The computational problems and the problems related to the enormous amount of data that are needed and must be kept and updated in the available computers will become even more challenging if the air pollution model is fully coupled with a climatic model. The advantage of such an approach will be the possibility to investigate also the feedback from the increased pollution levels to the climatic changes. At present it is not possible to resolve this very interesting and challenging problem on the whole European domain when **fine spatial resolution** is to be used. However, the computers are becoming more and more powerful and it will hopefully be possible to resolve the last two problems in the near future.

Some more details about the use of other approaches in the study of the impact of future climatic changes on air pollution levels can be found in [7, 10, 24] as well as in some of the references given in these three papers.

8.3 Presentation of the Mathematical Model

It was stated in Sect. 8.1 that the Unified Danish Eulerian Model (UNI-DEM) is used to calculate results with the different scenarios developed for this study. This model is described mathematically by a non-linear system of partial differential equations (PDEs). Five important physical and chemical processes are taken into account during the derivation of the system of PDEs. These processes are: (a) horizontal transport (advection), (b) horizontal diffusion, (c) non-linear chemical reactions plus

emission sources, (d) dry and wet deposition and (e) vertical exchange. The non-linear system of PDEs is written in the following form:

$$\begin{aligned}\frac{\partial c_i}{\partial t} &= -u\frac{\partial c_i}{\partial x} - v\frac{\partial c_i}{\partial y} + \frac{\partial}{\partial x}\left(K_x\frac{\partial c_i}{\partial x}\right) + \frac{\partial}{\partial y}\left(K_y\frac{\partial c_i}{\partial y}\right)\\ &+Q_i(t,x,y,z,c_1,c_2,\ldots,c_q) + E_i(t,x,y,z) - (k_{i1}+k_{i2})c_i\\ &-w\frac{\partial c_i}{\partial z} + \frac{\partial}{\partial z}\left(K_z\frac{\partial c_i}{\partial z}\right), \quad i = 1,2,\ldots,q. \end{aligned} \tag{8.1}$$

The first two terms in the right-hand-side of Eq. (8.1) describe the horizontal advection, while the next two represent the horizontal diffusion. The terms in the second row of this equation are describing the chemical reactions, the emissions sources in the model domain and the deposition respectively. The vertical processes, vertical advection and vertical deposition, are given in the third row of Eq. (8.1). The number of equations in the system of PDEs represented by Eq. (8.1) is equal to the number q of the chemical species which are to be studied by the model. The concentrations of the chemical species at point (x, y, z) of the spatial domain and at time t are denoted by $c_i = c_i(t, x, y, z)$. The notation $u = u(t, x, y, z)$, $v(t, x, y, z)$ and $w(t, x, y, z)$ is used for the wind velocities along the Ox, Oy and Oz axes respectively. The diffusivity coefficients are $K_x = K_x(t, x, y, z)$, $K_y = K_y(t, x, y, z)$ and $K_z = K_z(t, x, y, z)$ (the first two of them being normally non-negative constants, while the third one is a function, the calculation of which is rather complicated; see, for example, [29, 31]). The deposition rates are denoted by $k_{i1} = k_{i1}(t, x, y, z)$ for the dry deposition and $k_{i2} = k_{i2}(t, x, y, z)$ for the wet deposition. The non-linear terms $Q_i(t, x, y, z, c_1, c_2, \ldots, c_q)$ in the second line of Eq. (8.1) describe the chemical reactions. Finally, the terms $E_i(t, x, y, z)$ are describing emission sources, including both human-made (anthropogenic) emissions and natural (biogenic) emissions.

The spatial domain is a parallelepiped and the parameters N_x, N_y and N_z are used in the discretization (N_x, N_y and N_z being the numbers of grid-points along the three coordinate axes). For the runs carried out in connection with this study $N_x = N_y = 480$ and $N_z = 10$ are used. The grids in the horizontal planes are equidistant; actually this leads to 10 km × 10 km horizontal cells. In the vertical direction the grid is not equidistant; the distance between the grid-points are small close to the surface and become larger and larger when the height is increased. The size of the surface horizontal plane (the bottom of the spatial domain) is 4800 km × 4800 km and it is covering the whole of Europe together with parts of the Atlantic Ocean, Arctic, Asia and Africa. The number of chemical species used in most of the runs is $N_s = q = 56$. The number of equations that are to be handled at each time-step is equal to $N_x \times N_y \times N_z \times N_s = 142{,}518{,}376$ when this choice is made. A run over a time-period of 1 year with a time stepsize $\Delta t = 2.5$ s will result in $N_t = 213{,}120$ time-steps. These figures indicate very clearly that the arising computational tasks are enormous. Therefore, the following three conditions must be satisfied; it is necessary (a) to select fast but sufficiently accurate numerical methods, (b) to exploit efficiently the caches of the available computer and (c) to

parallelize carefully the code in the efforts to make it tractable on the available computer architectures. It should be mentioned that it may be impossible to handle some very large environmental models on the computers available at present even when the above three conditions are satisfied. Therefore, it is also necessary to use appropriate splitting procedures. UNI-DEM is split (as described in [2, 36]) into the following three sub-models and an attempt to select optimal numerical algorithms for every sub-model is carried out:

$$\frac{\partial c_i^{(1)}}{\partial t} = -w\frac{\partial c_i^{(1)}}{\partial z} + \frac{\partial}{\partial z}\left(K_z\frac{\partial c_i^{(1)}}{\partial z}\right), \tag{8.2}$$

$$\frac{\partial c_i^{(2)}}{\partial t} = -u\frac{\partial c_i^{(2)}}{\partial x} - v\frac{\partial c_i^{(2)}}{\partial y} + \frac{\partial}{\partial x}\left(K_x\frac{\partial c_i^{(2)}}{\partial x}\right) + \frac{\partial}{\partial y}\left(K_y\frac{\partial c_i^{(2)}}{\partial y}\right), \tag{8.3}$$

$$\frac{\partial c_i^{(3)}}{\partial t} = Q_i(t, x, y, z, c_1^{(3)}, c_2^{(3)}, \ldots, c_q^{(3)}) + E_i(t, x, y, z) - (k_{i1} + k_{i2})c_i^{(3)}. \tag{8.4}$$

The vertical exchange, the combination of the horizontal transport (the advection) with the horizontal diffusion and the chemical reactions together with the emission sources in the studied domain and the deposition terms are described in the right-hand-sides of Eqs. (8.2), (8.3), (8.4), respectively. There are three major advantages of the splitting procedure: (A) the large problem (1) is replaced by long sequences of small problems, which can be handled independently of each other, (B) the small problems can be treated in parallel (i.e., parallel tasks appear in a natural way; moreover, the amount of data needed during the treatment of each of the small tasks is not large, which implies that these data will often stay in cache while the small tasks are handled and (C) optimal numerical methods can be applied in the numerical solution of each of the three sub-models. It should be added that the particular splitting procedure described by (2), (3) and (4) does not require extra and artificial boundary conditions. It is fair to mention here that there is also one drawback: the accuracy of the splitting procedures is normally low (if the above three sub-models are handled in a sequential way, then the order of accuracy is one).

The first sub-model consists of $N_x \times N_y \times N_s$ independent tasks (the tasks along each vertical grid-line and each of the chemical species are independent). The spatial derivatives in the first sub-model are discretized (along the vertical grid-lines) by linear finite elements, while the θ-method with $\theta = 0.75$ is used in the time-steps.

The second sub-model is decoupled into $N_z \times N_s$ separate tasks (the task related to each grid-plane and to each chemical species are independent). The spatial derivatives are discretized by applying finite elements, while predictor-corrector schemes with several different correctors are used (with a stability control check) in the time-steps.

The third sub-model is containing $N_x \times N_y \times N_z$ independent tasks (the tasks related to the grid-points of the spatial domain are independent; the chemical species react with each other at a given grid-point, but do not react with chemical species from the neighbouring grid-points). The chemical part is the most difficult and time-consuming sub-model. Different methods for the treatment of the third model were tested extensively in [32, 36].

The above short discussion indicates very clearly that there are indeed a lot of parallel tasks, which appear in a quite natural way when splitting procedures are used. Unfortunately, these tasks are not well-balanced. Some of them, the tasks which arise in the first and the third sub-models, are too small (and, thus, bigger tasks must be created by combining several of them), others (the tasks arising in the second sub-model) are too big and some search for finding well-balanced parallel sub-tasks have to be carried out. Different ways for resolving the additional problems arising during the parallelization of the model are discussed in [2, 17, 26, 27].

Much more details about the computer treatment of UNI-DEM can be found [32, 36]. It should be mentioned that some other numerical methods, as, for example, those applied in [40] for spectroscopic models, can also be applied in air pollution models.

8.4 Additional Computational Difficulties Arising in the Climatic Runs

The great computational difficulties arising when a large-scale environmental model is to be run were discussed in the previous section. The computational process becomes much more complicated when climatic studies are to be carried out. There are several reasons for this: (a) runs over a long time-period have to be performed, (b) many scenarios are needed in order to investigate the influence of different important input parameters on the model results and (c) the calculated data have to be stored and carefully analysed. The difficulties become enormous when fine resolution has also to be used. It was explained in the previous section that in the latter case it is necessary to handle 142,518,376 equations during 213,120 time-steps at each run. When the above conditions are satisfied then many hundreds of runs have to be performed. Therefore, the global task becomes extraordinarily difficult even when the requirements formulated after formula (4) in the previous section are satisfied. We should mention here that it took more than 2 years to compute output data from all 2688 runs (14 scenarios $\times$ 16 years $\times$ 12 months) carried out in this study. This fact illustrates the great computational difficulties that are related to the investigation of various impacts of climatic changes on pollution levels. It must be added that the storage requirements (the need for huge input and output files) are also enormous.

One can now ask an important question: **Is it necessary to run the model on such a fine grid?** Two examples are given below in an attempt to show that high precision is indeed needed, especially when the situation in some small areas is studied. In Figs. 8.2 and 8.5 emission fields in two different parts of Europe (Denmark and Bulgaria) are given. In Figs. 8.3 and 8.6 the concentration fields calculated by using a crude resolution are drawn. The corresponding fields obtained when a fine resolution is applied are given in Figs. 8.4 and 8.7. It can be seen immediately that the results shown in Figs. 8.3 and 8.6 do not reflect correctly the real situation (the highest concentrations should be greater where the emissions are biggest). On the other side, the results in Figs. 8.4 and 8.7 are at least qualitatively correct (the concentrations are highest where the biggest emission sources are located in Figs. 8.2 and 8.5).

However, it is also possible to apply another approach. One can improve the spatial resolution gradually; starting with some crude grid and zooming several times gradually to the desired sub-area by using finer and finer grids in the nested sub-regions and by calculating boundary conditions for any of the nested sub-areas by using the results calculated by using the previous sub-region, in spite of the fact that these data are less accurate because cruder resolution is used in the previous sub-regions. Then the calculations in the last sub-area will be carried out by using a sufficiently high resolution. **The big question is whether this approach should be preferred?** The answer to this question is not very easy and, in our opinion, it is not possible to answer it only with "yes" or only with "no". If there are big emission sources in the sub-region of interest, then the most important transformations will take place there and the accuracy of the boundary conditions will not be very critical. In such a situation the use of nested sub-domains will be efficient. On the other hand, if most of transformations in the sub-area of interest are due to transport from the outside, then accurate boundary conditions are required and, therefore, boundary conditions calculated by using the less accurate concentrations calculated in the previous sub-domain will most probably not be sufficient to ensure the required accuracy. The results presented in Fig. 8.8 show that the transport of pollutants to some parts of Europe (in this particular case to the Balkan Peninsula) is rather considerable. Two runs with UNI-DEM were performed in order to calculate the results shown in this figure. The Basic Scenario with meteorological data and emissions for 1997 is used in the first run. All human-made (anthropogenic) emissions in the Balkan countries are set to zero in the second run (the emissions in the remaining part of Europe are not changed). Then the quantities $100(B - A)/B$ are calculated for each surface cell, where A is the ozone concentration obtained during the second run, while B is the corresponding concentrations calculated during the first run. This means that the contributions caused by transport to the Balkan countries from outside measured in percent are presented in Fig. 8.8. It is clearly seen that these contributions are rather high; more than 50 % nearly everywhere in the Balkan Peninsula. This is why we prefer the other approach: to run every time when it is possible the model on a fine grid in the whole spatial domain. It should be mentioned here that this approach has a very valuable advantage: it becomes possible to concentrate our attention to each particular sub-domain: there is no need

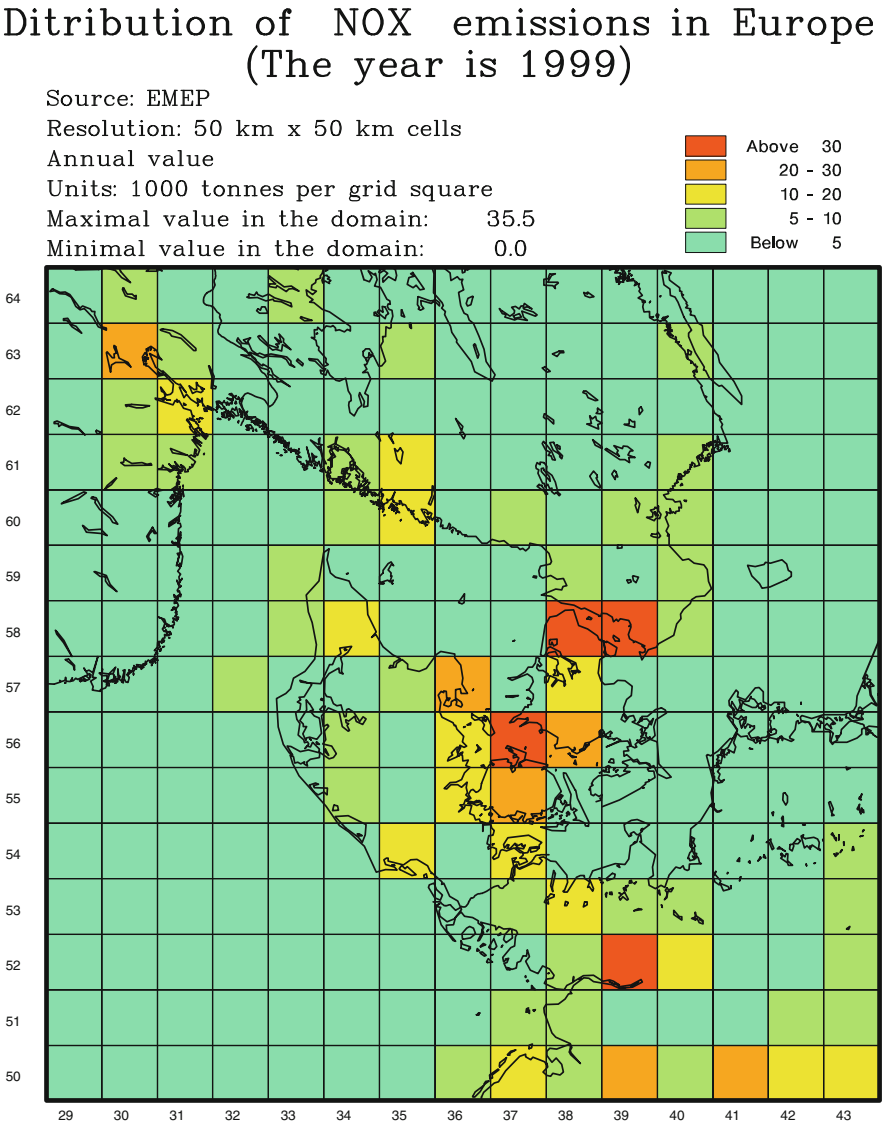

Fig. 8.2 Distribution of the annual averaged human-made NO_2 emissions in Denmark and its surroundings. It is clearly seen that the biggest emissions are around the capital Copenhagen and the big Swedish city Malmö as well as around Aarhus and Odense, the second largest and the third largest cities in Denmark

to carry out additional runs with other nested sub-domains when it is necessary to change the sub-domain which is of interest. This is demonstrated by presenting results both for the Danish area and for the Bulgarian area (Figs. 8.2–8.8).

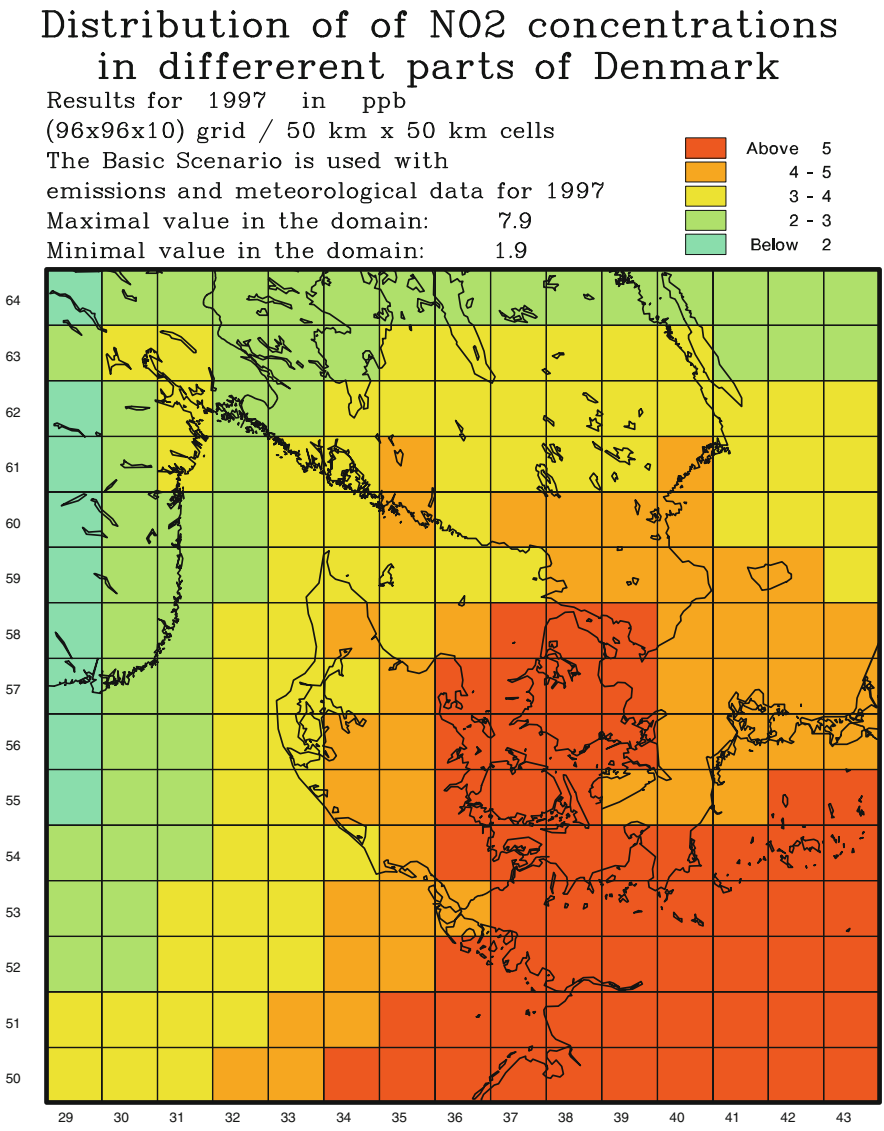

Fig. 8.3 Distribution of the annual averaged NO_2 concentrations in Denmark and its surroundings when UNI-DEM is run on a 96 × 96 horizontal grid resulting in 50 km × 50 km surface cells

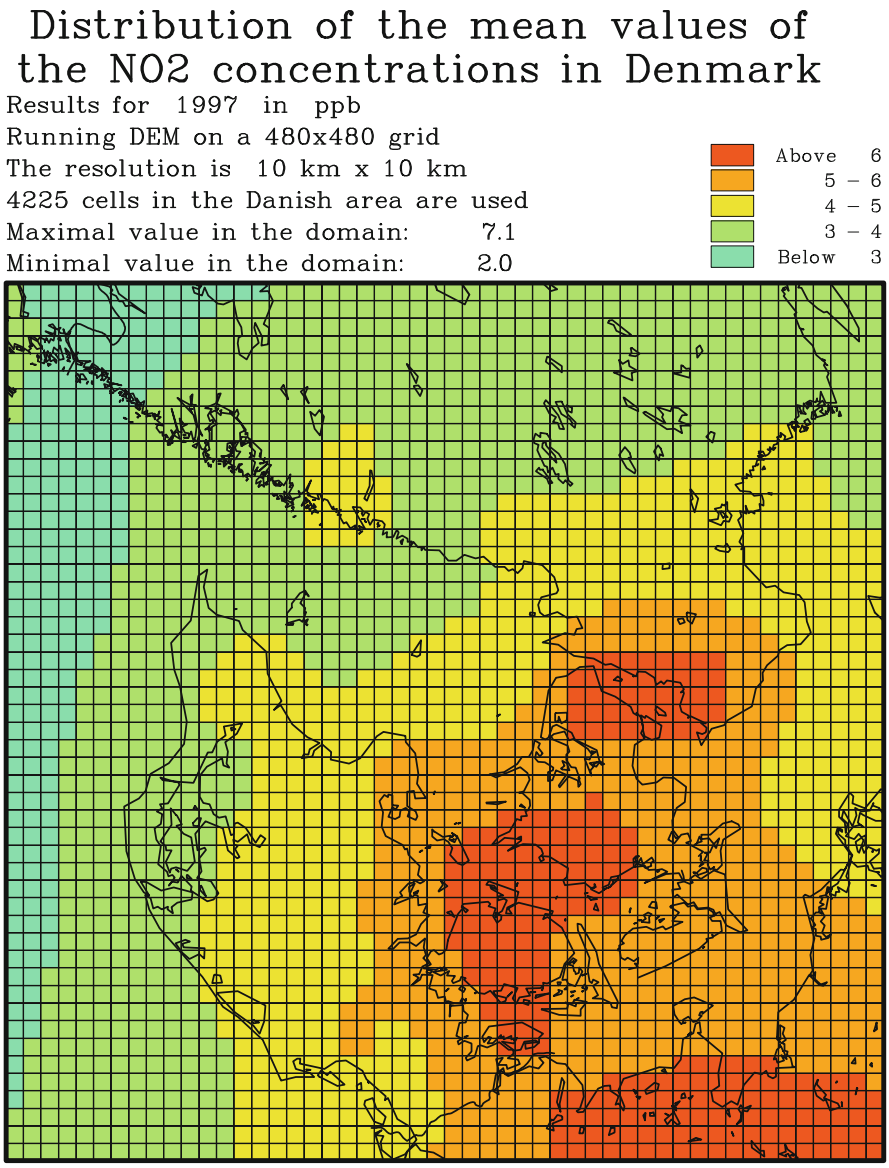

Fig. 8.4 Distribution of the annual averaged NO_2 concentrations in Denmark and its surroundings when UNI-DEM is run on a 480 × 480 horizontal grid resulting in 10 km × 10 km surface cells

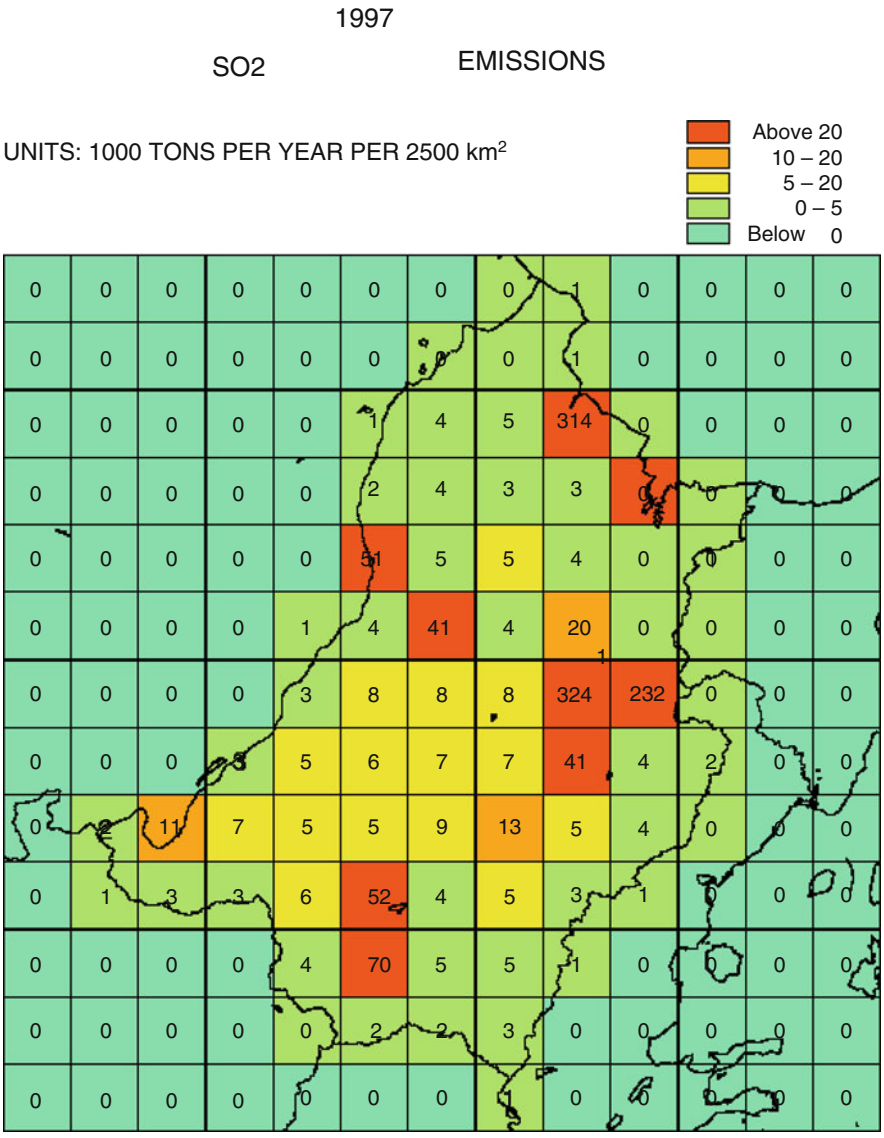

Fig. 8.5 Distribution of the annual averaged human-made SO_2 emissions in Bulgaria and its surroundings

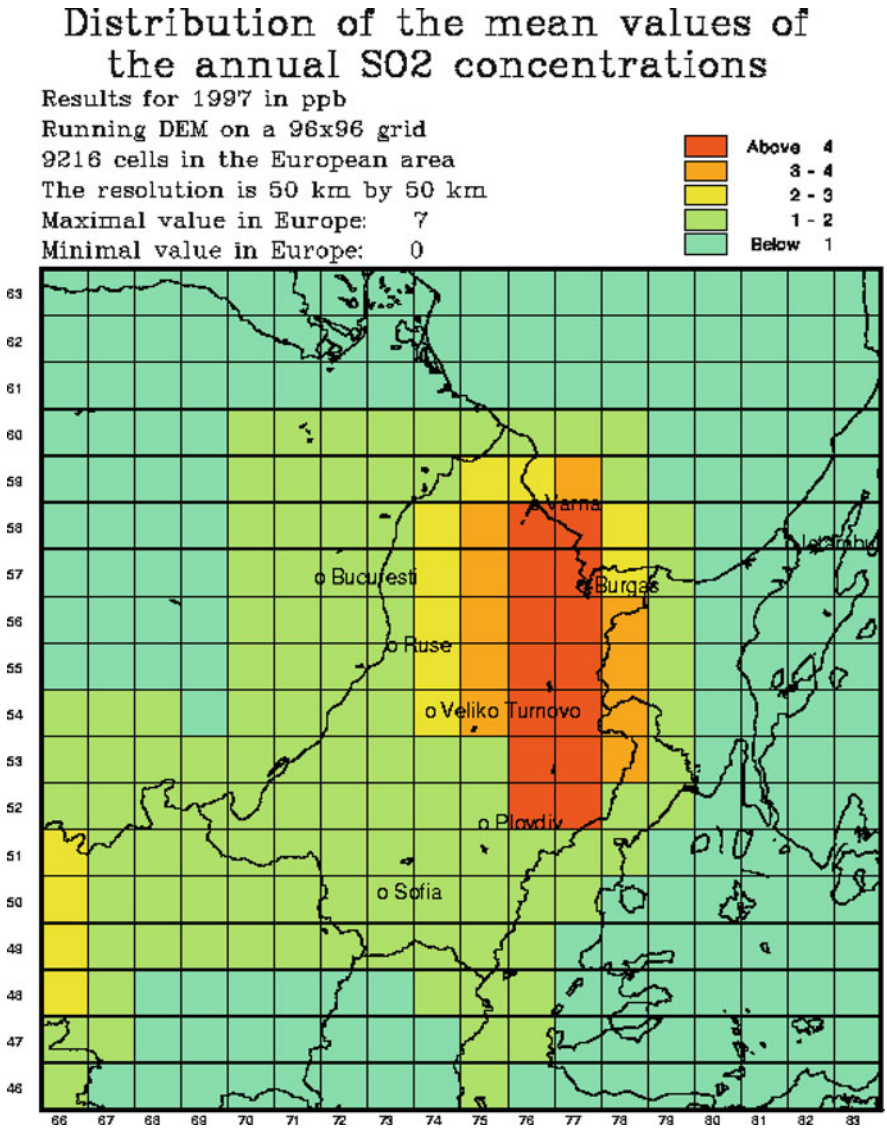

Fig. 8.6 Distribution of the annual averaged SO_2 concentrations in Bulgaria and its surroundings when UNI-DEM is run on a 96 × 96 horizontal grid resulting in 50 km × 50 km surface cells

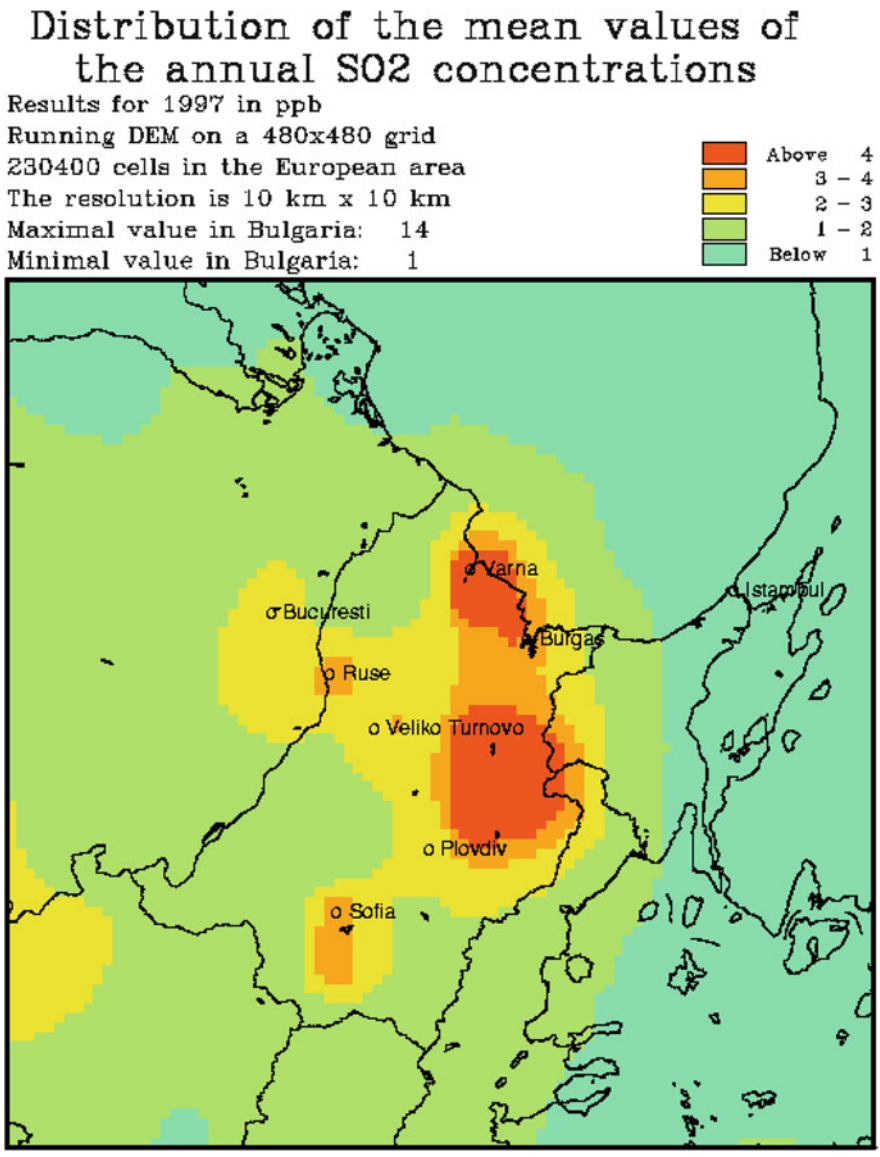

Fig. 8.7 Distribution of the annual averaged SO_2 concentrations in Bulgaria and its surroundings when UNI-DEM is run on a 480 × 480 horizontal grid resulting in 10 km × 10 km surface cells

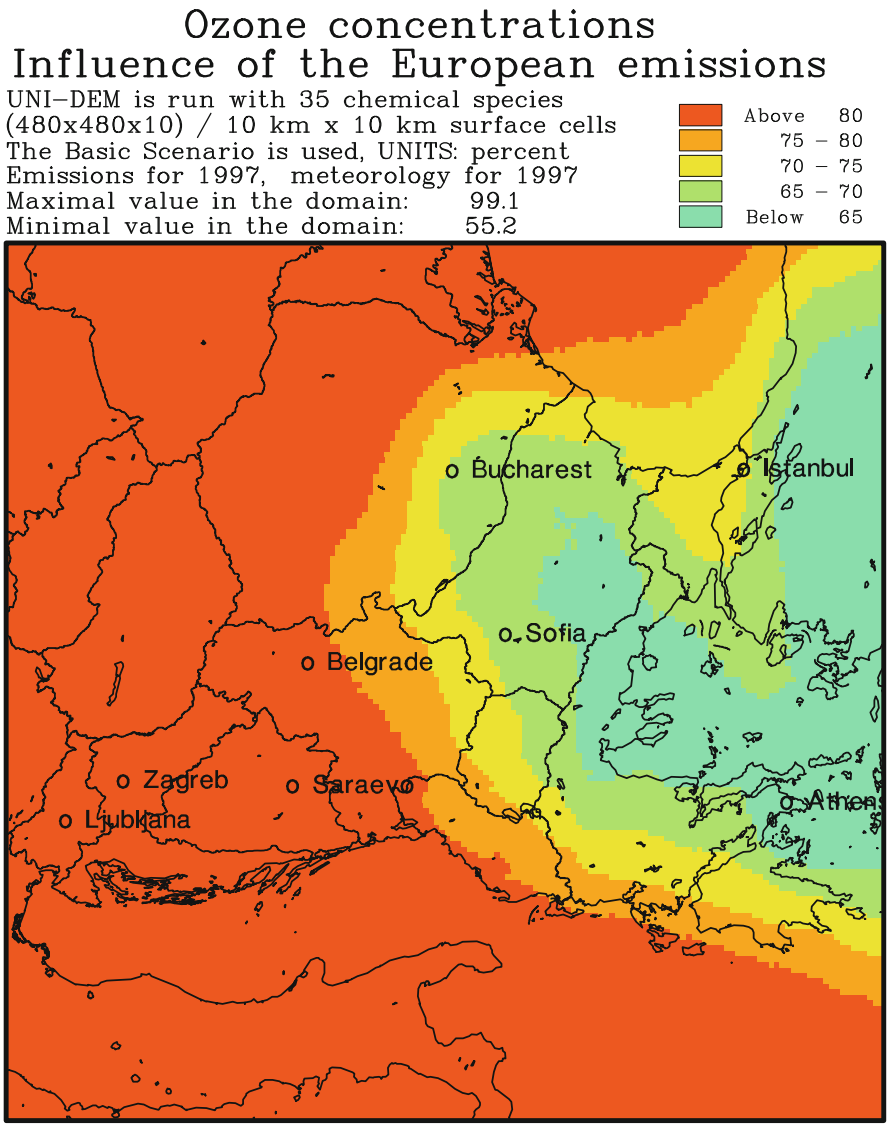

Fig. 8.8 Influence of the transport of ozone from European countries to Bulgaria obtained by running UNI-DEM on a 480 × 480 × 10 grid resulting in 10 km × 10 km surface cells

8.5 Inter-Annual Variations of the Meteorological Conditions and Some Other Issues

It is shown in this section that the inter-annual variations of the meteorological conditions and some other issues that are related to the emissions, both the human-made (anthropogenic) emissions and the natural (biogenic emissions) must be carefully taken into account during the preparation of the scenarios. This leads to an increase of the scenarios, but it allows us to draw more and better conclusions.

Very often one runs an air pollution model over several years with the actual meteorology and emissions. A second run with meteorology and emissions prescribed by a climatic model is performed. Then one compares the average concentrations received in the two runs. The conclusion is nearly always that the pollution levels do not depend too much on the climatic changes. We shall explain in this section that this is not a very correct approach. Annual variations of both meteorological conditions and the emissions must be carefully incorporated in the used scenarios.

8.5.1 Why Are the Inter-Annual Variations of the Meteorological Conditions Important?

First we shall demonstrate the necessity to take the inter-annual variations into account. The great inter-annual variations of the averaged daily ozone maxima around the Bulgarian capital Sofia are demonstrated in Fig. 8.9. It should be pointed out that rather large variations of annual averages of concentrations were observed also in other parts of Europe and for other pollutants too; see [4, 6, 11, 12, 32–36, 41–43].

The variations of the ammonium + ammonia levels in the Danish area are shown in Fig. 8.10. Results obtained with five different scenarios are shown in this figure. The Basic Scenario is run with the actual emissions and meteorological conditions. Two other scenarios are also used. The 2010 Scenario is run by using levels of the anthropogenic emissions, which were prescribed (in the end of the twentieth century) for year 2010. The MFR (Maximum Feasible Reduction) Scenario assumes that the anthropogenic emissions will be reduced very significantly (up to 90 % in some countries). Both scenarios were developed at IIASA (the International Institute for Applied System Analysis in Laxenburg, Austria; see more details in [3]).The two corresponding climatic scenarios are based on the use of the recommendations proposed in the IPCC SRES A2 Scenario in Scenario 2010 and in the MFR Scenario. The following conclusions can be drawn from the results presented in Fig. 8.10 as well as from results presented in some previous studies [4, 6, 11, 12, 32–36, 41–43]: (a) the inter-annual variations remain for all five scenarios, (see again

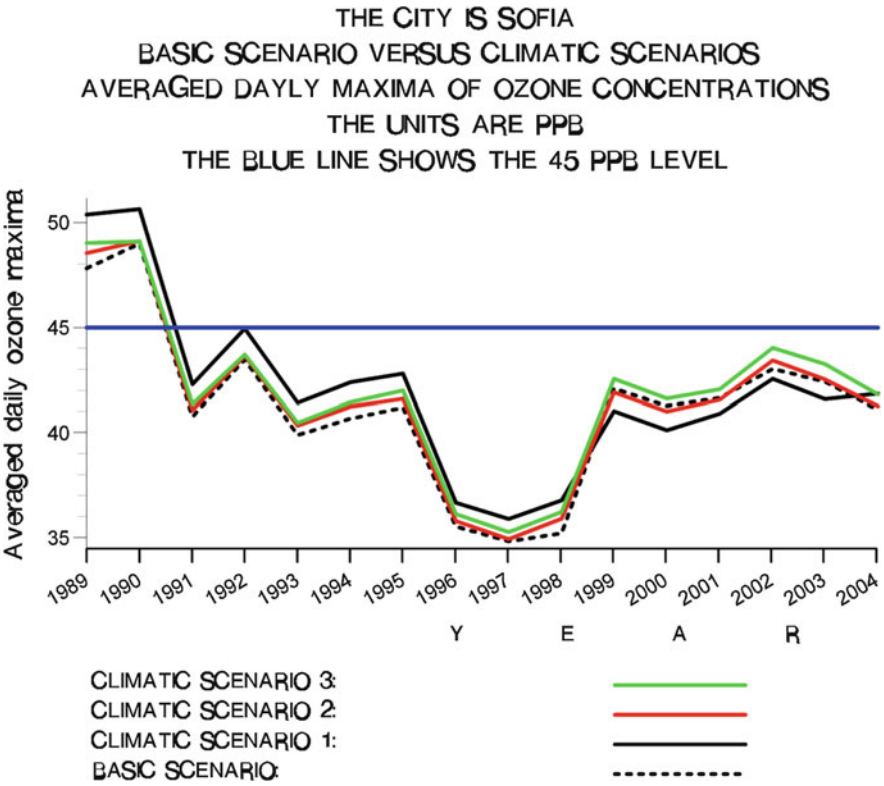

Fig. 8.9 Variations of the averaged daily maxima of the ozone concentrations during a period of 16 years

[4, 6, 11, 12, 32–36, 41–43]), (b) the differences between the results obtained by the Basic Scenario and those found when Scenario 2010 and Climate Scenario 2010 are used are rather small for this pollutant, while the MFR Scenario leads to a large decrease of the pollution levels and (c) the influence of the climate changes is not very significant when annual values of ammonia + ammonium concentrations are studied.

8.5.2 Need for Scenarios with Human-Made and Natural Emissions

The fact that the European human-made (anthropogenic) emissions were reduced during the studied period has to be taken into account in this investigation.

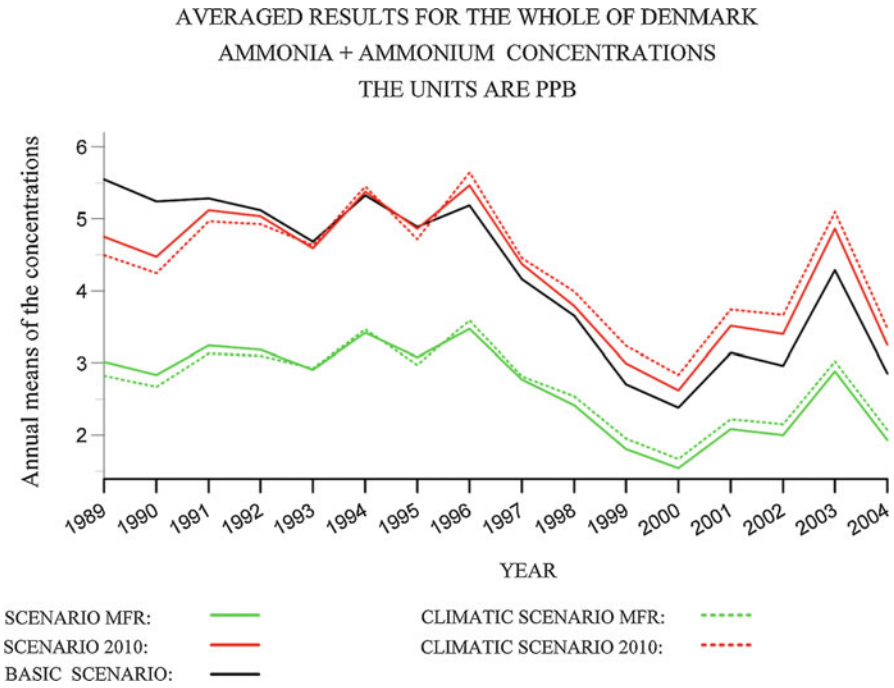

Fig. 8.10 Variations of the yearly averages of the ammonia-ammonium concentrations in Denmark

The reduction of the Bulgarian emissions is shown in Fig. 8.11. It is seen that the reduction of the emissions in this country is rather significant (up to 60 % for some of the emissions). It must be emphasized that the reduction of the Bulgarian emissions during this period was not an isolated case. The reduction of the emissions in Europe as a whole is shown in Fig 8.12. It can be seen immediately that the trend is the same. More examples, which show that the emissions in the European countries were reduced in this period are given in [11].

The decrease of the human-made (anthropogenic) emissions leads to an increase of the relative part and, thus, of the importance of the natural (biogenic) emissions. The biogenic emissions in the Unified Danish Eulerian Model are created by using ideas described in [16, 25, 29]. Similar ideas are also used in some other air pollution models. However, it should be mentioned here that some scientists claim that the natural emissions are greatly underestimated; see, for example, [5, 8, 9]. Therefore, it was also useful to develop and apply some scenarios in which the natural (biogenic) emissions are varied.

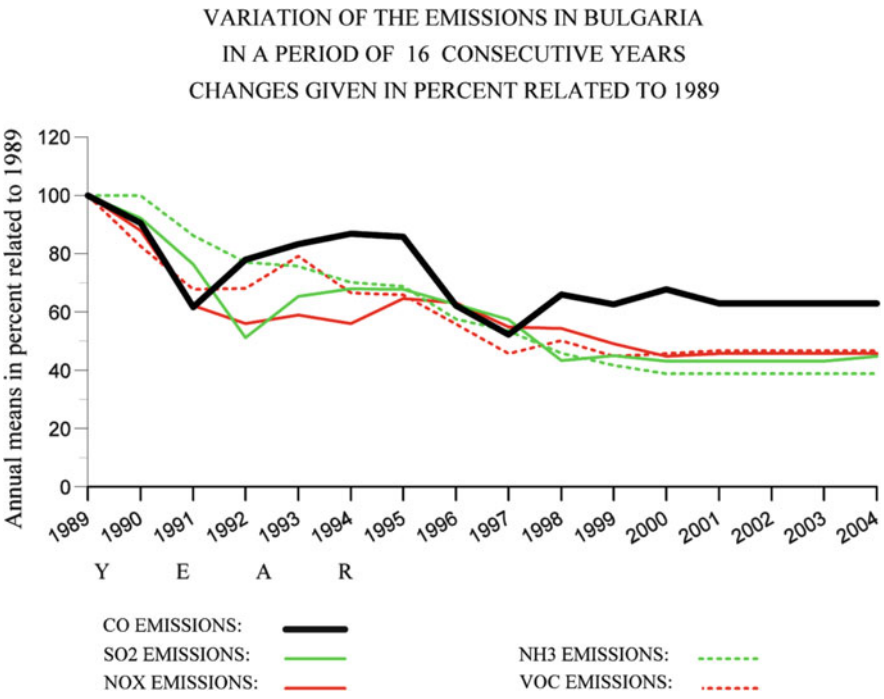

Fig. 8.11 Changes of the Bulgarian human-made emissions during the period from 1989 to 2004

It should furthermore be emphasized that both the emission sources and the meteorological data are very important. This is illustrated by the results presented in Fig. 8.13, which were obtained by running three emission scenarios. It is seen that if the emissions sources are kept constant, then one can see the annual variations but not the decreasing trend of the concentrations (caused by the decreased emissions). If the meteorological conditions are kept constant, then it is not possible to see the annual variations, but the decreasing trend is preserved. Therefore, all scenarios were run with the actual emissions and with the actual wind fields (which is also true for the climatic scenarios). This allows us both to compare the differences between the results obtained by different scenarios for every chosen year from the selected time-interval of 16 years and to demonstrate very clearly the fact that there are considerably large inter-annual variations of the pollution levels.

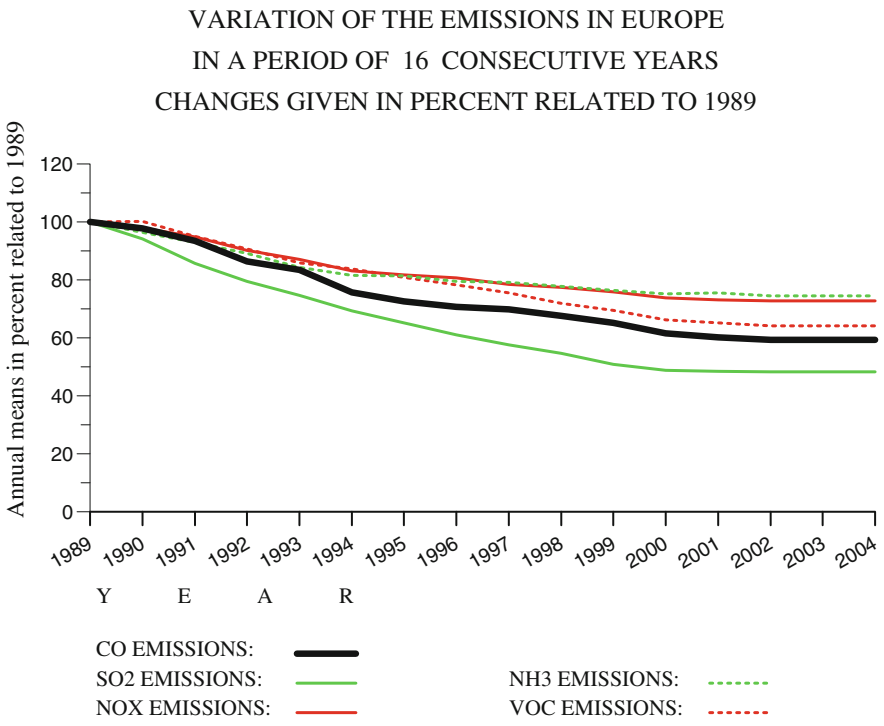

Fig. 8.12 Changes of the European human-made emissions during the period from 1989 to 2004

8.6 Influence of the Climatic Changes on Pollution Levels

The Basic Scenario was extensively compared with the three climatic scenarios that were discussed in the previous section. Some results from this comparison are presented in Figs. 8.9 and 8.10. Much more results for other parts of Europe can be found in [11, 12, 31–36, 41, 43]. All results indicate that (a) the daily maxima of the ozone concentrations obtained when the climatic scenarios are used are often (but not always) greater than those obtained by the Basic Scenarios and (b) the differences between the daily maxima of the ozone concentrations obtained with the climatic scenarios and those obtained with the Basic Scenario are rather small. It is shown in this section that the second statement, statement (b), is not necessarily true when "**bad days**" (to be defined below), which might cause damages on human beings, are considered instead of averaged annual concentrations. In the latter case the differences can be considerably larger. The main conclusion is that it is much more relevant to consider not the annual means of the concentrations but directly the

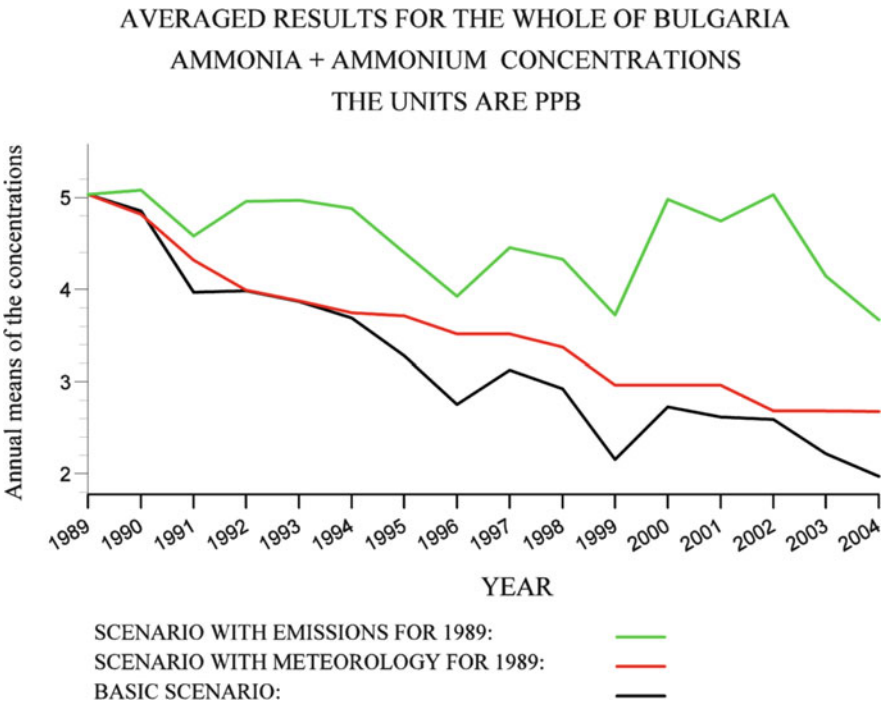

Fig. 8.13 The Basic Scenario versus scenarios with constant emissions and meteorological conditions

numbers of "**bad days**", which can be dangerous for our environment when exceed certain limits. Furthermore, it is important to establish whether the critical levels for these quantities, the "**bad days**", which are established by the EU Directive [15], are really exceeded or not. Assume that c_{max} is the maximum of the 8-h averages of the ozone concentrations calculated by some model or measured at some station in a given day at some site A. If the condition $c_{max} > 60$ ppb is satisfied at least once during the day under consideration, then the expression a "**bad day**" will be used for such a day at site A. "**Bad days**" can have damaging effects on some groups of human beings (people who suffer from asthmatic diseases). Therefore, the number of such days should be reduced as much as possible. Two important aims are stated in the Ozone Directive issued by the EU Parliament issued in 2002, [15]. **Target aim:** The number of "**bad days**" in any site of the European Union should in principle not exceed 25 after year 2010 and **Long-term aim:** No "**bad day**" should occur in the European Union.

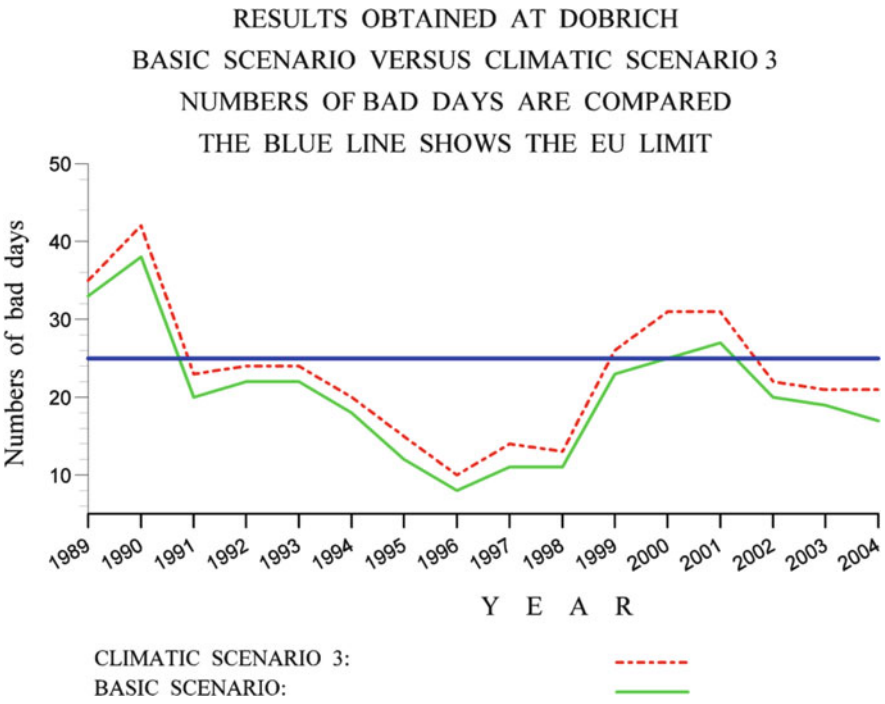

Fig. 8.14 Comparing numbers of "bad days" obtained by using the Basic Scenario and Climatic Scenario 3

The model results (including here model results reported in previous papers) indicate that these critical levels are greatly overestimated.

The numbers of "**bad days**" obtained in Dobrich (a town in the north-eastern part of Bulgaria, which is not very polluted) are given in Fig. 8.14. It is seen that the numbers of "**bad days**" for the Climatic Scenario 3 are always greater than the corresponding numbers for the Basic Scenario. Moreover, the critical level of no more than 25 "**bad days**" is exceeded for many years of the studied period of 16 years.

One may ask the question whether the increases shown in Fig. 8.14 are big or small. The differences of the bad days obtained by the two scenarios were calculated and plotted in Fig. 8.15. It is seen that for the town Dobrich these differences vary in the interval from three to seven. It is quite clear that such differences are at least considerable, because they show that sometimes the critical level may be exceeded in the Climatic Scenario 3, while the results for the Basic Scenario are acceptable. Results presented in [34] indicate that the situation is the same (or at least similar) in many other parts of Europe. This fact is demonstrated in Fig. 8.16.

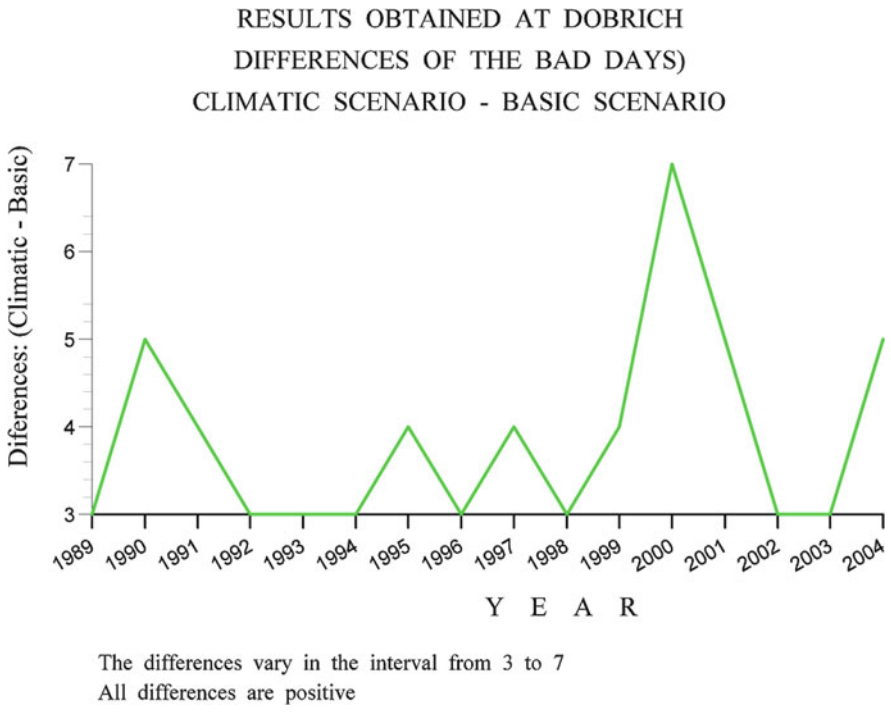

Fig. 8.15 Comparing differences of "bad days" obtained by using the Basic Scenario and Climatic Scenario 3

The distribution of the numbers of "bad days" in the Balkan Peninsula for the last year in the studied period, year 2004, is shown in Fig. 8.17. It is seen that the critical level prescribed in the directive issued by the European Union is exceeded in all regions of the Balkan Peninsula. It should also be noted that the numbers of "bad days" in the western part of the studied area are in general larger than those in the eastern part. This is caused by the transportation of ozone pollutants from European sources and, thus, should be expected. The increases (in percent) of the numbers of "bad days" in 2004 on the territory of the Balkan Peninsula when the Climatic Scenario 3 is used instead of the Basic Scenario are shown in Fig. 8.18. It is clearly seen that in a very large part of the peninsula the increases are greater than 15 %, which is a rather considerable amount.

Some scenarios with increased biogenic emissions (including here not only increases of the biogenic emissions created by forest trees, but also assuming the existence of biogenic emissions created by crops) were developed and tested. The changes were made by following some recommendations made in [5, 8, 9]. One of the 14 scenarios, the Climatic Scenario 3 combined with Increased Biogenic

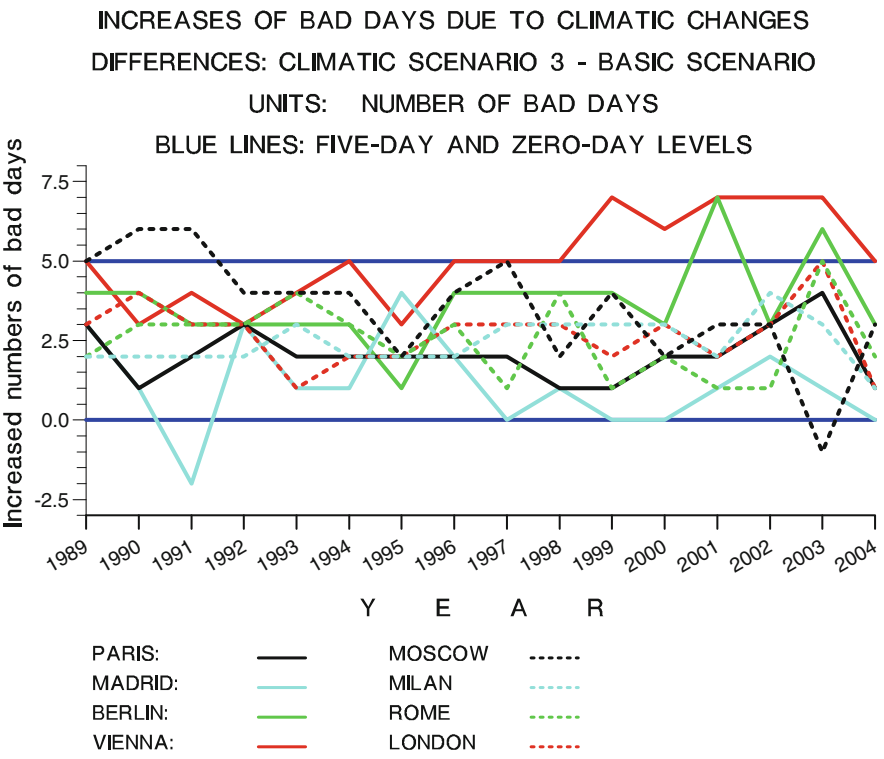

Fig. 8.16 Comparing differences of "bad days" in the surroundings of eight big European cities which are obtained by using the Basic Scenario and Climatic Scenario 3

Emissions was compared with the Basic Scenario. Results obtained in runs for 2004 are presented in Fig. 8.19. It is seen that now the percentages of "bad days" found in the comparison of the results from this scenario with those calculated with the Basic scenario are greater than 15 % in nearly the whole territory of the Balkan Peninsula. This indicates that if the claims that the biogenic emissions are underestimated are correct, then the climatic changes will cause much greater increases of some pollution levels.

It must be emphasized here that the results shown in Figs. 8.17, 8.18 and 8.19 are for year 2004. The code was run (as stated in the previous sections) for all 16 years in the period from 1989 to 2004 and the trend remains the same for every year. In fact, for many years the increases are even bigger than those shown in these three figures.

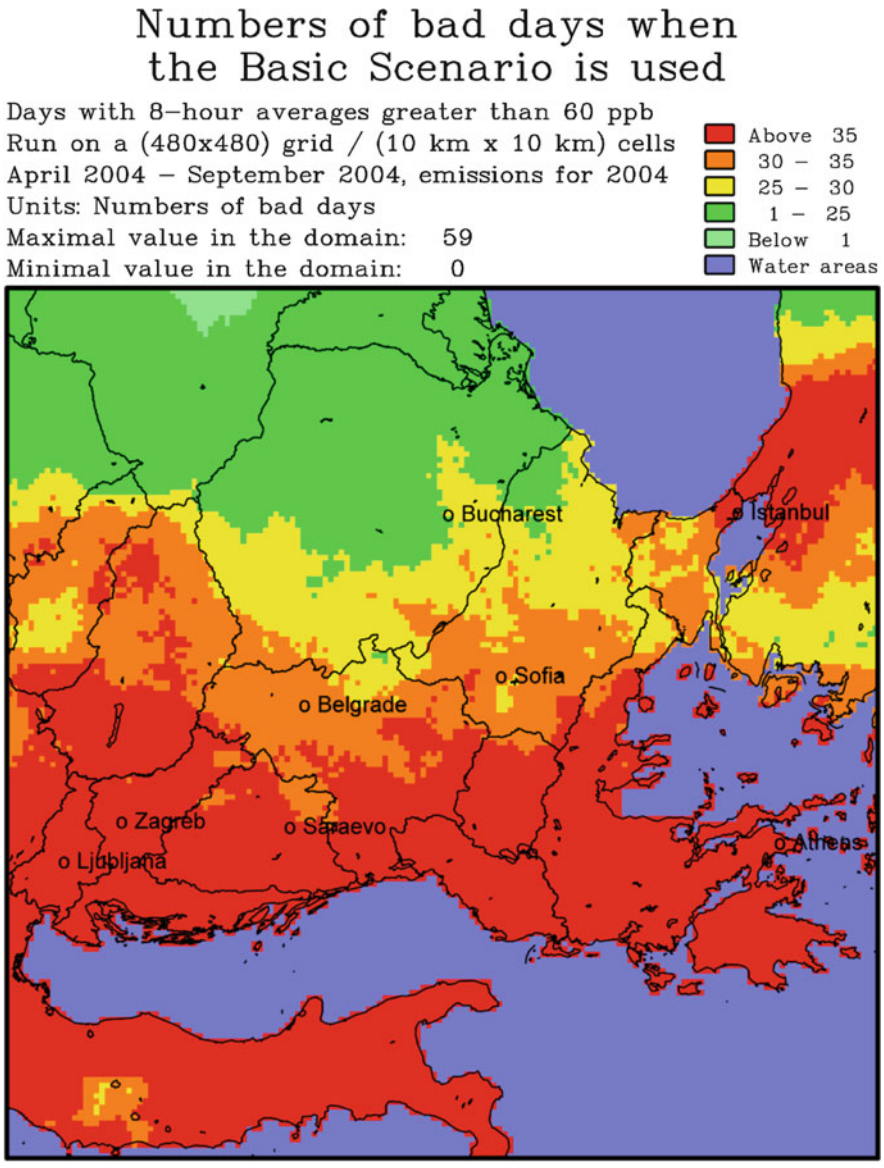

Fig. 8.17 Distribution of the numbers of "bad days" in the different regions of Balkan Peninsula

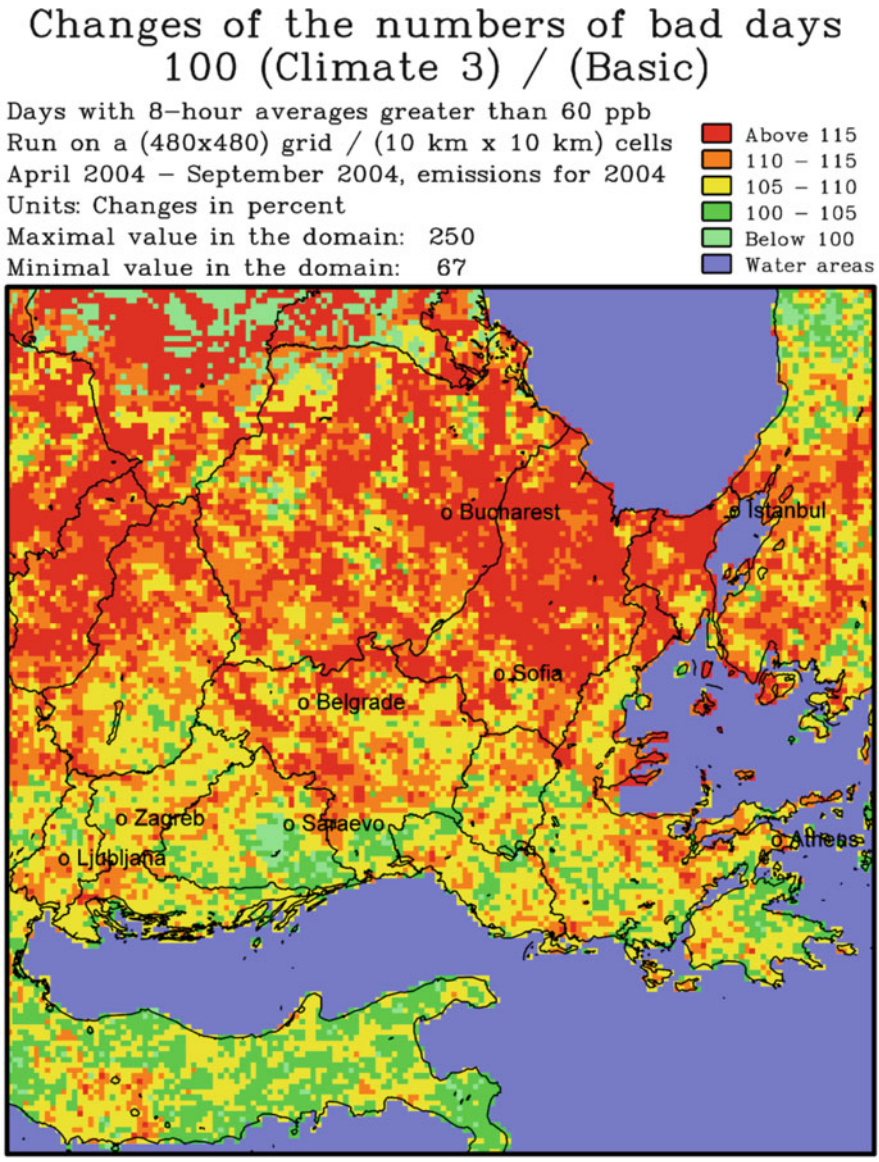

Fig. 8.18 Climatic Scenario 3 versus the Basic Scenario: increases (in percent) of the numbers of bad days

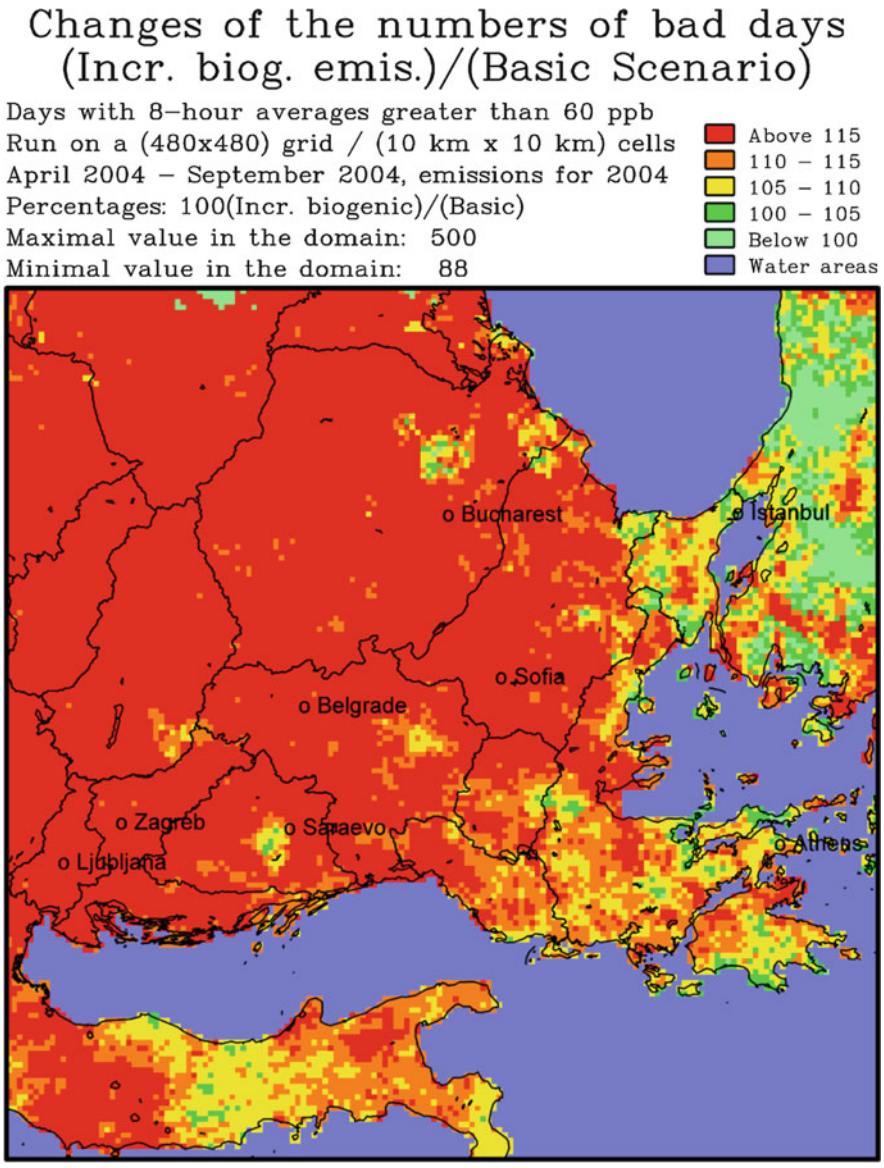

Fig. 8.19 Additional increases when the biogenic emissions are increased

8.7 Conclusions

The results presented in this chapter indicate very clearly that the climatic changes will lead to an increase of the pollution levels related to ozone in many parts of Europe. Similar results were reported in [11, 12], and [29–36, 41–43] for many other parts of the continent and also for other pollutants. The important fact is that the general trend does not change too much. Indeed, results obtained for areas from Russia and Ukraine to England and Spain and from Sweden and Denmark to Italy and Greece show clearly that independently of the fact that the pollution levels vary a lot in the different countries, the general tendency remains the same: the increase of the temperature will cause increases of many pollution levels. Therefore, the policy-makers must take into account the global warming effect during the preparation of strategies for keeping the future pollution levels under the prescribed critical levels. It is interesting to find a reliable answer of the following question: By how much the amount of the anthropogenic emissions should be reduced in order to keep the pollution levels under the prescribed in the EU Ozone Directive [15] critical levels?

It should also be noted that a systematic application of algorithms based on advanced sensitivity analysis will improve very much both the presentation of the results and the understanding of the trends related to the increase of the pollution levels.

It must be emphasized here that better definitions related to critical levels of potentially dangerous pollutants are needed. Indeed, many of the critical levels, including here most of the critical levels that are required in the EU Ozone Directive [15], are not very carefully defined. For example, the determination of the quantity used in this chapter, the "bad days", might be an extremely unstable process because in some situations it might be enormously sensitive to very small (even negligible) errors of model results or measurements. This fact creates difficulties in the preparation of reliable and robust control strategies. Therefore, it is necessary to try to stabilize somehow the definitions used in the definitions of the critical levels. In connection with the "bad days", the use of the sharp limit of 60 ppb is clearly not a very good decision (in an extreme situation, the transition of the 8-h average of the ozone concentration from 59.99 to 60.01 ppb will cause a shift from a "good day" to a "bad day"). It would be much more appropriate to introduce an uncertainty zone (let us call it, as in [34], a "grey zone"). For example, if the maximal 8-h averaged ozone concentration is in the range from 40 to 80 ppb then the day under consideration should be considered as belonging to the "grey zone". If this number is under 40 ppb it will be appropriate to declare the day as a "good day", while it will certainly be a "bad day" if this number is greater that 80 ppb. By applying this procedure, all the uncertain cases will be accumulated in the "grey zone". The question is what to do with the "grey days". The simplest (but perhaps not the best) strategy will be to declare that n "grey days" are equivalent to one "bad day". It will be necessary to perform a long series of systematic experiments in order to decide what value of n should be chosen. More elaborated strategies can also be tried. For example, it is possible to use some weight coefficients (smaller weight coefficients

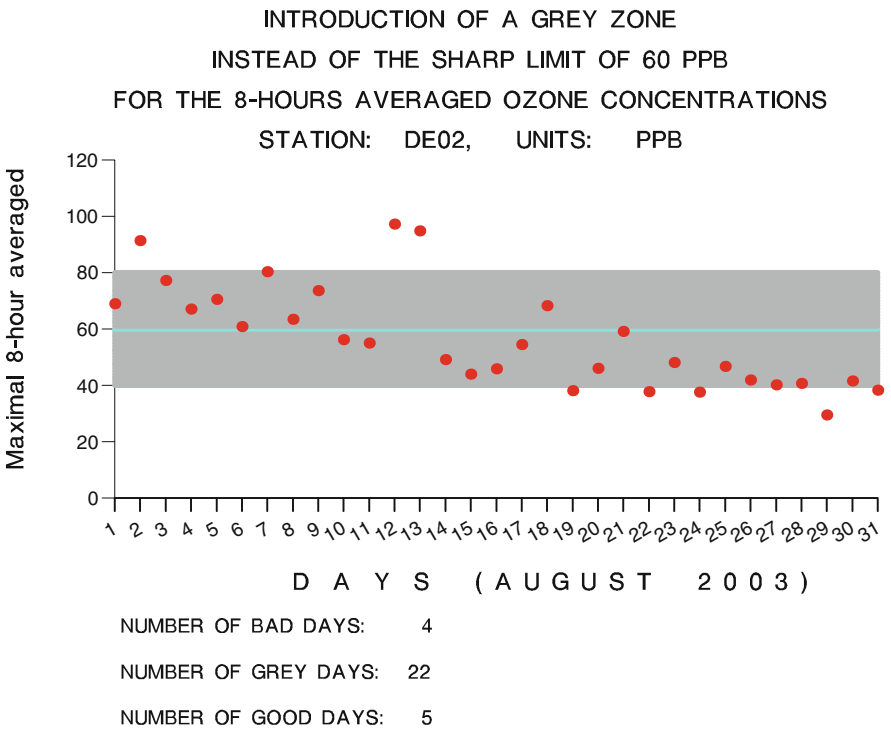

Fig. 8.20 The *grey zone* which appears in connection with the German station in Langebrugge

should be used when the maximal 8-h averaged ozone concentration is closer to the lower limit of 40 ppb and larger weight coefficients in the opposite case). Finally, it is also possible to apply two upper limits: one for the "proper bad days" (say, zero days) and one for the "grey days" (say 50 days). An illustration of the fact that most of the "bad days" are in fact in the "grey zone" is given in Fig. 8.20.

Acknowledgements I. Faragó was supported by the Hungarian Scientific Research Fund OTKA under grant No. K112157.

References

1. Abdalmogith, S., Harrison, R.M., Zlatev, Z.: Intercomparison of inorganic aerosol concentrations in the UK with predictions of the Danish Eulerian model. J. Atmos. Chem. **54**, 43–66 (2006)
2. Alexandrov, V., Owczarz, W., Thomsen, P.G , Zlatev, Z.: Parallel runs of large air pollution models on a grid of SUN computers. Math. Comput. Simul. **65**, 557–577 (2004)
3. Amann, M., Bertok, I., Cofala, J., Gyarfas, F., Heyes, C., Klimont, Z., Makowski, M., Schöpp, W., Syri, S.: Cost-effective control of acidification and ground-level ozone. Seventh Interim

Report, International Institute for Applied System Analysis (IIASA), A-2361 Laxenburg, Austria (1999)
4. Ambelas Skjøth, C., Bastrup-Birk, A., Brandt, J., Zlatev, Z.: Studying variations of pollution levels in a given region of Europe during a long time-period. Syst. Anal. Model. Simul. **37**, 297–311 (2000)
5. Anastasi, C., Hopkinson, L., Simpson, V.J.: Natural hydrocarbon emissions in the United Kingdom. Atmos. Environ. **25A**, 1403–1408 (1991)
6. Bastrup-Birk, A., Brandt, J., Uria, I., Zlatev, Z.: Studying cumulative ozone exposures in Europe during a 7-year period. J. Geophys. Res. **102**, 23917–23035 (1997)
7. Bell, M.L., Goldberg, R., Hogrefe, C., Kinney, P.L., Knowlton, K., Lynn, B., Rosenthal, J., Rosenzweig, C., Patz, A.: Climate change, ambient ozone, and health in 50 US cities. Clim. Chang. **82**, 61–76 (2007)
8. Bouchet, V.S., Laprise, R., Torlaschi, E., McConnel, J.C.: Studying ozone climatology with a regional climate model, 1. Model description and evaluation. J. Geophys. Res. **104**, 30351–30371 (1999)
9. Bouchet, V.S., Laprise, R., Torlaschi, E., McConnel, J.C., Plummer, D.A.: Studying ozone climatology with a regional climate model, 2 climatology. J. Geophys. Res. **104**, 30373–30385 (1999)
10. Carvalho, A., Monteiro, A., Solman, S., Miranda, A.I., Borrego, C.: Climate-driven changes in air quality over Europe by the end of the 21st century, with special reference to Portugal. Environ. Sci. Pol. **13**, 445–458 (2010)
11. Csomós, P., Cuciureanu, R., Dimitriu, G., Dimov, I., Doroshenko, A., Faragó, I., Georgiev, K., Havasi, Á., Horváth, R., Margenov, S., Ostromsky, Tz., Prusov, V., Syrakov, D., Zlatev, Z.: Impact of climate changes on pollution levels in Europe. Final report for a NATO Linkage Project (Grant 980505). Available at:http://www.cs.elte.hu/~faragois/NATO.pdf,http://www2.dmu.dk/atmosphericenvironment/Climate%20and%20Pollution,http://www.umfiasi.ro/NATO.pdf,http://www.personal.rdg.ac.uk/~sis04itd/MyPapers/climatic_scenarios_NATO.pdf,http://www.softasap.net/ips/climatic_scenarios_NATO.pdf,http://www.meteo.bg/bulair/NATO.pdf (2006)
12. Dimov, I., Geernaert, G., Zlatev, Z.: Impact of future climate changes on high pollution levels. Ann. Mat. Pura. Appl. **32**(2), 200–230 (2008)
13. EMEP: Emission Data: Status Report, EMEP/MSC-W Report 1/99, July 1999, Meteorological Synthesizing Centre - West, Norwegian Meteorological Institute, P. O. Box 43 - Blindern, N-0313 Oslo 3, Norway (1999)
14. EMEP Home Web-page: http://www.emep.int/index_data.html (2006)
15. European Parliament: Directive 2002/3/EC of the European Parliament and the Council of 12 February 2002 relating to ozone in ambient air. Off. J. Eur. Communities **L67**, 14–30 (2002)
16. Geernaert, G., Zlatev, Z.: Studying the influence of the biogenic emissions on the AOT40 levels in Europe. Int. J. Environ. Pollut. **23**(1–2), 29–41 (2004)
17. Georgiev, K., Zlatev, Z.: Parallel sparse matrix algorithms for air pollution models. Parallel Distrib. Comput. Pract. **2**, 429–442 (2000)
18. Harrison, R.M, Zlatev, Z., Ottley, J.C.: A comparison of the predictions of an Eulerian atmospheric transport chemistry model with experimental measurements over the North Sea. Atmos. Environ. **28**, 497–516 (1994)
19. Hass, H., van Loon, M., Kessler, C., Stern, R., Mathijsen, J., Sauter, F., Zlatev, Z., Langner, J., Foltescu, V., Schaap, M.: Aerosol modelling: results and intercomparison from European regional-scale modelling systems. GSF-National Research Center for Environment and Health, International Scientific Secretariat, EUROTRAC, Münich. http://www.trumf.fu-berlin.de/veranstaltungen/events/glream/GLOREAM_PMmodel-comparison.pdf (2004)
20. Havasi, Á., Bozó, L., Zlatev, Z.: Model simulation on transboundary contribution to the atmospheric sulfur concentration and deposition in Hungary. Időjárás **105**, 135–144 (2001)
21. Havasi, Á., Zlatev, Z.: Trends of Hungarian air pollution levels on a long time-scale. Atmos. Environ. **36**, 4145–4156 (2002)

22. Hertel, O., Ambelas Skjøth, C., Frohn, L.M., Vignati, E., Frydendall, J., de Leeuw, G., Schwarz, U., Reis, S.: Assessment of the atmospheric nitrogen and sulphur inputs into the North Sea using a Lagrangian model. Phys. Chem. Earth **27**, 1507–1515 (2002)
23. Houghton, J.T., Ding, Y., Griggs, D.J., Noguer, M., van der Linden, P.J., Dai, X., Maskell, K., Johnson, C.A. (eds.): Climate Change 2001: The Scientific Basis. Cambridge University Press, Cambridge/New York/Melbourne/Madrid/Cape Town (2001)
24. Jacobson, M.Z.: On the causal link between carbon dioxide and air pollution mortality. Geophys. Res. Lett. **35**, L03809, 4145–4156 (2008). doi:10.1029/2007GL031101
25. Lübkert, B., Schöpp, W.: The OECD-map emission inventory for, and in Western Europe. Report No. WP-89-082. International Institute for Applied Systems and Analysis (IIASA), Laxenburg (1989)
26. Owczarz, W., Zlatev, Z.: Running a large-scale air pollution model on an IBM SMP computer. Int. J. Comput. Res. **10**, 485–500 (2001)
27. Owczarz, W., Zlatev, Z.: Parallel matrix computation in air pollution modelling. Parallel Comput. **28**, 355–368 (2002)
28. Roemer, M., Beekman, M., Bergsröm, R., Boersen, G., Feldmann, H., Flatøy, F., Honore, C., Langner, J., Jonson, J.E., Matthijsen, J., Memmesheimer, M., Simpson, D., Smeets, P., Solberg, S., Stevenson, D., Zandveld, P., Zlatev, Z.: Ozone trends according to ten dispersion models. GSF-National Research Center for Environment and Health, International Scientific Secretariat, EUROTRAC, Münich http://www.mep.tno.nl/eurotrac/EUROTRAC-trends.pdf (2004)
29. Simpson, D., Guenther, A., Hewitt, C.N., Steinbrecher, R.: Biogenic emissions in Europe: I. Estimates and uncertainties. J. Geophys. Res. **100**, 22875–22890 (1995)
30. Stocker, T. F., Qin, D., Plattner, G.-K., Tignor, M., Allen, S.K., Boschung, J., Nauels, A., Xia, Y., Bex, V., Midgley, P.M. (eds.): Climate Change 2013: The Physical Basis, Contribution of the Working Group I of the Intergovernmental Panel on Climate Change. Cambridge University Press, Cambridge/New York (2013)
31. Zlatev, Z.: Application of predictor-corrector schemes with several correctors in solving air pollution problems. BIT **24**, 700–715 (1984)
32. Zlatev, Z.: Computer Treatment of large Air Pollution Models. Kluwer Academic Publishers (at present Springer), Dordrecht/Boston/London (1995)
33. Zlatev, Z.: Partitioning ODE systems with an application to air pollution models. Comput. Math. Appl. **42**, 817–832 (2001)
34. Zlatev, Z.: Impact of future climate changes on high ozone levels in European suburban areas. Clim. Chang. **101**, 447–483 (2010)
35. Zlatev, Z.: Broy, M.: Massive data sets issues in air pollution modelling. In: Abello, J., Pardalos, P.M., Resende, M.G.C. (eds.) Handbook on Massive Data Sets in Science and Engineering, pp. 1169–1220. Kluwer Academic Press, Dordrecht/Boston/London (2002)
36. Zlatev, Z., Dimov, I.: Computational and Numerical Challenges in Environmental Modelling. Elsevier, Amsterdam (2006)
37. Zlatev, Z., Moseholm, L.: Impact of climate changes on pollution levels in Denmark. Environ. Model. **217**, 305–319 (2008)
38. Zlatev, Z., Syrakov, D.: A fine resolution modelling study of pollution levels in Bulgaria. Part 1: SOx and NOx pollution. Int. J. Environ. Pollut. **22**(1–2), 186–202 (2004)
39. Zlatev, Z., Syrakov, D.: A fine resolution modelling study of pollution levels in Bulgaria. Part 2: High ozone levels. Int. J. Environ. Pollut. **22**(1–2), 203–222 (2004)
40. Zlatev, Z., Wasniewski, J., Schaumburg, K.: Numerical treatment of models arising in nuclear magnetic resonance spectroscopy. Adv. Eng. Softw. **8**, 223–233 (1986)
41. Zlatev, Z., Dimov, I., Ostromsky, Tz., Geernaert, G., Tzvetanov, I., Bastrup-Birk, A.: Calculating losses of crops in Denmark caused by high ozone levels. Environ. Model. Assess. **6**, 35–55 (2001)
42. Zlatev, Z., Havasi, Á., Faragó, I.: Influence of climatic changes on pollution levels in Hungary and its surrounding countries. Atmosphere **2**, 201–221 (2011)
43. Zlatev, Z., Georgiev, K., Dimov, I.: Influence of climatic changes on pollution levels in the Balkan Peninsula. Comput. Math. Appl. **65**, 544–562 (2013)

Part III
Meteorological Data Assimilation and Probabilistic Forecasting

Numerical modelling of the Earth system is one of the most rapidly evolving field in meteorology. Numerical Weather Prediction (NWP) and climate models are able to provide realistic estimates of the future states of the atmosphere/climate system and they are essential tools for serving forecast information for decision makers. In the last decade enormous progress was achieved in the quantification of uncertainties in weather forecasts and climate projections in the form of probabilistic forecast information and the users understand and appreciate more and more the added value of uncertainty estimates attached to the forecasts/projections.

The intrinsic characteristic of the atmosphere and the climate system is that they behave as chaotic systems. Consequently, meteorological forecasts sensitively depend on the initial conditions, in other words small errors in the model initial conditions might lead to large forecast errors. The NWP data assimilation systems provide initial conditions for the numerical model. The determination of model initial conditions is a complex mathematical optimisation problem and the initial state of the atmosphere can be estimated only with some uncertainties. These uncertainties must be taken into account, while constructing Ensemble Prediction Systems (EPS), where not only a single forecast, but an ensemble of forecasts is exploited having each model integration differing (at least) in its initial conditions. The ensemble method is now far more extended, since not only the initial condition uncertainties, but all the quantifiable atmospheric/climate uncertainties are taken into account, while designing and producing an EPS.

Due to the application of ensemble data assimilation methods the data assimilation and probabilistic forecasting research and development efforts cannot be fully disentangled any more. Initial condition uncertainties are described by the adequate initial condition perturbations of an ensemble prediction system and EPS can provide valuable information on the background error characteristics used in the data assimilation process. This makes the two areas inseparable in modern meteorological research.

In Part III, both data assimilation and probabilistic forecasting in meteorology are introduced and also several examples are shown to demonstrate the interplay between these two NWP modelling areas.

Chapter 9 gives an introduction to the basic data assimilation methods. It aims at presenting the mathematical derivation of the various methods and their application to test problems.

Chapter 10 provides the mathematical study of data assimilation methods, and suggests the use of a novel cost function.

Chapter 11 introduces the idea of ensemble forecasting, and shows how it is used in NWP models. The authors also present how ensemble forecasting can be applied in meteorological data assimilation.

Chapter 12 is dedicated to specify the leading uncertainties in climate projections on different time scales, geographical areas and meteorological variables.

Chapter 9
An Invitation to Meteorological Data Assimilation

Ágnes Bodó and Petra Csomós

Abstract The chapter introduces the basic data assimilation methods used in meteorological modelling. After briefly recalling the mathematical notions and tools needed, we present the optimal interpolation, the variational methods, and the Kálmán Filter techniques in one and more dimensions. In order to illustrate the use of the methods introduced, we present the results of numerical experiments done for simple models.

Keywords Data assimilation • Ensemble transform Kálmán filter • Kálmán filter • Optimal interpolation • Variational method

9.1 Introduction

The present chapter serves as an introduction to data assimilation methods used in meteorological modelling. Our aim is to present the mathematical derivation of the various methods and their applications to simple test models. Data assimilation literally means that one aims at combining information from several sources leading to a result which is better in some sense than the original data. Since we are after the best weather forecast possible, meteorological data assimilation aims at combining all the information being gathered about the present state of the atmosphere: observations, numerical prediction, climatological data, etc. The mathematical question is then how to combine all these data in order to get a result being nearest to the true state of atmosphere. For a detailed introduction in this field we refer to Kalnay [13] and Evensen [5] and the references therein.

Á. Bodó
Department of Applied Analysis and Computational Mathematics, Eötvös Loránd University, Pázmány Péter sétány 1/C, H-1117 Budapest, Hungary
e-mail: bodoagi@cs.elte.hu

P. Csomós (✉)
Department of Applied Analysis and Computational Mathematics & MTA–ELTE Numerical Analysis and Large Networks Research Group, Eötvös Loránd University, Pázmány Péter sétány 1/C, H-1117 Budapest, Hungary
e-mail: csomos@cs.elte.hu

A. Bátkai et al. (eds.), *Mathematical Problems in Meteorological Modelling*, Mathematics in Industry 24, DOI 10.1007/978-3-319-40157-7_9

For the sake of simplicity, we consider only two information sources being typical in meteorology: observations and numerical forecast obtained by a numerical prediction model. Both of them can be considered as vectors containing the values of the seven meteorological variables, that is, temperature, wind velocity in three directions, pressure, density, and relative humidity, at each point of a certain three-dimensional spatial mesh covering the whole atmosphere or its smaller region. Let $x \in \mathbb{R}^n$ denote the vector of numerical forecast and $y \in \mathbb{R}^m$ the vector of observations. In practice we usually have $m \ll n$ (nowadays $n \approx 10^7$, $m \approx 10^5$). Hence, we are looking for that combination of x and y, called *analysis* in meteorology, which approximates best the true state of the atmosphere. Since the analysis at time t is the best approximation of the true state of the atmosphere at that time, it plays two roles. On one hand, it serves as the weather forecast for time t, being presented to the public. On the other hand, it is the best candidate for the initial value of a numerical weather prediction model computing the numerical forecast for the next time level, that is, for time $t + \Delta t$ with some time step $\Delta t > 0$. Due to its latter role, it should be compatible with the model's variables, that is, it should be a vector of size n. Hence, we denote the analysis by $x_a \in \mathbb{R}^n$.

In the present chapter we introduce the basic data assimilation methods used in numerical weather prediction models, such as optimal interpolation, variational methods, and Kálmán Filter techniques. In Sect. 9.2 we summarise the mathematical tools needed later on. In Sects. 9.3 and 9.4 the optimal interpolation and the variational method are introduced in one and more dimensions, respectively. Section 9.5 serves as an introduction to the various Kálmán Filter techniques, and in Sect. 9.6 we present two test models and with the help of numerical experiments we compare the data assimilation methods. Section 9.7 serves as an outlook on various procedures used in nonlinear data assimilation.

9.2 Mathematical Background

In what follows we introduce the notions from mathematical statistics needed later on.

Definition 9.1 Let $\Omega \neq \emptyset$ denote the sample space being the space of all possible outcomes and let a σ-algebra $\mathcal{E}$ denote the set of all events where each event is a set containing zero or more outcomes, that is, an event is a subset of the sample space Ω. Then the function $P : \mathcal{E} \to [0, 1]$ is called a probability function if it possesses the following properties: $P(\Omega) = 1$ and it is countably additive, that is, for all $A_n \in \mathcal{E}$, $n = 1, \ldots, N$ with $A_i \cap A_j$, $i \neq j$ one has

$$P\Big(\bigcup_{n=1}^{N} A_n\Big) = \sum_{n=1}^{N} P(A_n).$$

The triple $(\Omega, \mathcal{E}, P)$ is called a probability space. The measurable function $x : \Omega \to \mathbb{R}$ is called a real-valued random variable if $\{\omega \in \Omega : x(\omega) \leq r\} \in \mathcal{E}$ for all $r \in \mathbb{R}$ meaning that the set of events ω, for which $x(\omega) \leq r$ holds, is again an event, that is, we can talk about its probability. We will use the expression vector-valued random variable $x \in \mathbb{R}^n$, if the coordinate functions of $x : \Omega \to \mathbb{R}^n$ are real-valued random variables.

By having a random variable at hand, one can define its statistical quantities which play an important role in data assimilation. From now on we suppose that Ω is the finite union of the intervals $I_j \subset \mathbb{R}$ for $j = 1, \ldots, n$ with $n \in \mathbb{N}$.

Definition 9.2 Let $(\Omega, \mathcal{E}, P)$ be a probability space and $x = (x^{(1)}, \ldots, x^{(n)}) : \Omega \to \mathbb{R}^n$ be a vector-valued random variable. We define the following quantities.

1. The cumulative distribution function $F_x : \mathbb{R}^n \to \mathbb{R}$ of the vector-valued random variable x is defined as

$$F_x(\xi^{(1)}, \ldots, \xi^{(n)}) = P(x^{(1)} < \xi^{(1)}, \ldots, x^{(n)} < \xi^{(n)})$$

   for all $\xi = (\xi^{(1)}, \ldots, \xi^{(n)}) \in \mathbb{R}^n$. Two random variables are called identically distributed if they possess the same distribution function.
2. The probability density function $f_x : \mathbb{R}^n \to \mathbb{R}$ (if exists) of the vector-valued random variable x is the function which fulfills

$$F_x(\xi) = \int_{-\infty}^{\xi^{(1)}} \ldots \int_{-\infty}^{\xi^{(n)}} f_x(t^{(1)}, \ldots, t^{(n)}) \mathrm{d}t^{(n)} \ldots \mathrm{d}t^{(1)}$$

   for any $\xi = (\xi^{(1)}, \ldots, \xi^{(n)}) \in \mathbb{R}^n$.

In what follows we define the most important notions characterising a random variable. Its expectation is intuitively the long-run average value of repetitions of the experiment it represents. The variance measures how far a set of numbers is spread out, and the covariance measures how much two random variables depend on each other.

Definition 9.3

1. The expectation $\mathbb{E}$ of the vector-valued random variable $x \in \mathbb{R}^n$ is defined as

$$\mathbb{E}(x) := \left(\mathbb{E}(x^{(1)}), \ldots, \mathbb{E}(x^{(n)})\right) \quad \text{with}$$
$$\mathbb{E}(x^{(i)}) := \int_{I_j} t f_{x^{(i)}}(t) \mathrm{d}t \quad \text{for all} \quad i = 1, \ldots, n$$

   (if exists). Let $X = (x_1, \ldots, x_k) \in \mathbb{R}^{n \times k}$ be the matrix containing the k pieces of vector-valued random variables $x_1, \ldots, x_k \in \mathbb{R}^n$ in its columns. Then the notation $\mathbb{E}(X)$ means $(\mathbb{E}(X))_{i,j} := \mathbb{E}(x_j^{(i)})$ for all $i = 1, \ldots, n$ and $j = 1, \ldots, k$, i.e., we take the expectation elementwise.

2. Let $x \in \mathbb{R}^n$ and $y \in \mathbb{R}^m$ be vector-valued random variables. Their covariance is defined as

$$\operatorname{cov}(x, y) := \mathbb{E}\big((x - \mathbb{E}(x))(y - \mathbb{E}(y))^\top\big) \in \mathbb{R}^{n\times m},$$

where $\top$ denotes the transposition, that is, $xy^\top \in \mathbb{R}^{n\times m}$ is the dyadic product of the vectors $x \in \mathbb{R}^n$ and $y \in \mathbb{R}^m$. We note that $\mathbb{V}(x) := \operatorname{cov}(x, x) \in \mathbb{R}^{n\times n}$ is called the variation of the random variable x. Since we have

$$\big(\mathbb{V}(x)\big)_{i,j} = \operatorname{cov}\big(x^{(i)}, x^{(j)}\big) \quad \text{for all} \quad i, j = 1, \ldots, n,$$

that is, the entries of $\mathbb{V}(x)$ are the covariances of the elements of x, $\mathbb{V}(x)$ is also called the *covariance matrix* of the random variable x.

The following properties will be used frequently.

1. The expectation $\mathbb{E}$ is a linear function.
2. The matrix $\mathbb{V}(x)$ is symmetric and positive semidefinite for all random variables x (whenever it exists).

One often investigates the jointly behaviour of two random variables but the knowledge of their distribution functions is usually not sufficient. Therefore, we need to define the joint distribution function of two random variables.

Definition 9.4

1. The joint distribution function $F_{x,y} : \mathbb{R}^n \times \mathbb{R}^m \to \mathbb{R}$ of the vector-valued random variables $x \in \mathbb{R}^n$ and $y \in \mathbb{R}^m$ is defined as

$$F_{x,y}(\xi, \eta) := P\big(x^{(1)} < \xi^{(1)}, \ldots, x^{(n)} < \xi^{(n)}, y^{(1)} < \eta^{(1)}, \ldots, y^{(m)} < \eta^{(m)}\big)$$

for all $\xi \in \mathbb{R}^n$, $\eta \in \mathbb{R}^m$.

2. The vector-valued random variables $x \in \mathbb{R}^n$ and $y \in \mathbb{R}^m$ are called independent if

$$F_{x,y}(\xi, \eta) = F_x(\xi) F_y(\eta) \quad \text{for all} \quad \xi \in \mathbb{R}^n,\ \eta \in \mathbb{R}^m.$$

3. The vector-valued random variables $x \in \mathbb{R}^n$ and $y \in \mathbb{R}^m$ are called uncorrelated if

$$\operatorname{cov}(x, y) = 0 \in \mathbb{R}^{n\times m}.$$

We note that if two random variables are independent, then they are uncorrelated as well.

In some cases the random variable x is unknown and it is approximated by another random variable $\tilde{x}$ called an *estimator* of x with the following properties.

Definition 9.5 Let x be a vector-valued random variable and $\tilde{x}$ one of its estimators.

1. The estimator $\tilde{x}$ is called unbiased if $\mathbb{E}(\tilde{x}) = \mathbb{E}(x)$.
2. The estimator $\tilde{x}$ is called optimal if the trace $\operatorname{tr}\mathbb{E}((\tilde{x} - x)(\tilde{x} - x)^\top)$ is minimal among all possible estimators.

We note that for a real-valued random variable $x \in \mathbb{R}$, the optimal estimator $\tilde{x}$ possesses the minimal variance $\mathbb{V}(\tilde{x})$.

The sample (or empirical) mean and the sample covariance are statistics computed from one or more random variables. These will be important later on when the data assimilation methods are introduced.

Definition 9.6

1. The sample mean $\mathbb{E}_{x_1 \dots x_k}$ of the vector-valued random variables $x_1, \dots, x_k \in \mathbb{R}^n$ is defined as

$$\mathbb{E}_{x_1 \dots x_k} := \frac{1}{k} \sum_{j=1}^{k} x_j \in \mathbb{R}^n.$$

2. The sample covariance matrix $\mathbb{V}$ of the vector-valued random variables $x_1, \dots, x_k \in \mathbb{R}^n$ is defined as

$$\mathbb{V} := \frac{1}{k-1} \sum_{j=1}^{k} (x_j - \mathbb{E}_{x_1 \dots x_k})(x_j - \mathbb{E}_{x_1 \dots x_k})^\top \in \mathbb{R}^{n \times n}.$$

When introducing the basic data assimilation methods used in meteorology, we will need the following result presented e.g. in Johnson and Wichern [11]

Proposition 9.1 *Let x be a vector-valued random variable and $x_1, \dots, x_k$ its mutually independent and identically distributed estimators. Then the following assertions hold.*

1. *The sample mean $\mathbb{E}_{x_1 \dots x_k}$ is an unbiased estimator of the expectation $\mathbb{E}(x)$.*
2. *The sample covariance matrix $\mathbb{V}$ is an unbiased estimator of the covariance matrix $\mathbb{V}(x)$.*

9.3 Optimal Interpolation and Variational Method in One Dimension

This section is devoted to the introduction of the basic data assimilation methods when applied to one-dimensional problems, for example estimating the unknown true temperature $x_t \in \mathbb{R}$ at a point. To do so we make two measurements, that is, we take the real-valued random variables x, y and look for their (in some sense best) combination, that is, the real-valued estimator x_a. In meteorological data assimilation, we always suppose the following.

Assumptions 9.1 Let x and y be real-valued random variables and let x_a be an estimator of the constant true state $x_t \in \mathbb{R}$. We suppose the following.

1. The estimator x_a is the linear combination of x and y, that is, $x_a = \alpha_1 x + \alpha_2 y$ for some constants $\alpha_1, \alpha_2 \in \mathbb{R}$.
2. The estimator x_a is unbiased, that is, $\mathbb{E}(x_a) = \mathbb{E}(x_t) = x_t$.
3. The estimator x_a is optimal, that is, the $\mathbb{E}((x_a - x_t)^2)$ is minimal.
4. The measurements x and y are unbiased, that is, $\mathbb{E}(x) = \mathbb{E}(y) = x_t$.
5. The measurements x and y are uncorrelated, that is, $\mathrm{cov}(x, y) = 0$.
6. The values of the variances $\mathbb{V}(x)$ and $\mathbb{V}(y)$ are given.

We present first the result of the *optimal interpolation* being a least mean square estimate.

Theorem 9.1 *Under Assumptions 9.1, the estimator x_a has the form*

$$x_a = x + \frac{\mathbb{V}(x)}{\mathbb{V}(x) + \mathbb{V}(y)}(y - x). \tag{9.1}$$

Proof Instead of just checking Assumptions 9.1, we present a constructive proof. From the linearity of the expectation $\mathbb{E}$ and the estimator x_a in x and y, it follows that for some $\alpha_1, \alpha_2 \in \mathbb{R}$ the following identity holds

$$\mathbb{E}(x_a) = \mathbb{E}(\alpha_1 x + \alpha_2 y) = \alpha_1 \mathbb{E}(x) + \alpha_2 \mathbb{E}(y) = (\alpha_1 + \alpha_2) x_t.$$

Since the estimator x_a is unbiased, we have that $\alpha_1 + \alpha_2 = 1$, hence, we obtain the form

$$x_a = (1 - \alpha)x + \alpha y = x + \alpha(y - x)$$

for some constant $\alpha \in \mathbb{R}$. In order to minimize the variance $\mathbb{V}(x_a)$, we note first that Definition 9.3 implies

$$\mathbb{V}(x_a) = \mathbb{E}\big((x_a - \mathbb{E}(x_a))^2\big) = \mathbb{E}\big((x_a - x_t)^2\big),$$

and similarly for $\mathbb{V}(x) = \mathbb{E}(\varepsilon_x^2)$ and $\mathbb{V}(y) = \mathbb{E}(\varepsilon_y^2)$, where $\varepsilon_x := x - x_t$ and $\varepsilon_y := y - x_t$ denote the errors of the measurements x and y, respectively, being real-valued random variables as well. Hence, we have the identity

$$\begin{aligned}
&\mathbb{V}(x_a) = \mathbb{E}((x_a - x_t)^2) = \mathbb{E}\big((x + \alpha(y - x) - x_t)^2\big) \\
=&\mathbb{E}\big((x_t + \varepsilon_x + \alpha(x_t + \varepsilon_y - x_t - \varepsilon_x) - x_t)^2\big) = \mathbb{E}\big(\varepsilon_x + \alpha(\varepsilon_y - \varepsilon_x))^2\big) \\
=&\mathbb{E}\big((1 - \alpha)^2 \varepsilon_x^2 + \alpha^2 \varepsilon_y^2 - 2\alpha(1 - \alpha)\varepsilon_x \varepsilon_y\big) \\
=&(1 - \alpha)^2 \mathbb{E}(\varepsilon_x^2) + \alpha^2 \mathbb{E}(\varepsilon_y^2) - 2\alpha(1 - \alpha)\mathbb{E}(\varepsilon_x \varepsilon_y).
\end{aligned}$$

Since the measurements x and y are unbiased and uncorrelated, we have

$$0 = \operatorname{cov}(x, y) = \mathbb{E}\big((x - \mathbb{E}(x))(y - \mathbb{E}(y))\big) = \mathbb{E}((x - x_t)(y - x_t)) = \mathbb{E}(\varepsilon_x \varepsilon_y)$$

by Definitions 9.4 and 9.5. This implies the result

$$\mathbb{V}(x_a) = (1 - \alpha)^2 \mathbb{V}(x) + \alpha^2 \mathbb{V}(y),$$

which is minimal if its derivative with respect to the parameter α vanishes:

$$0 = \tfrac{\mathrm{d}}{\mathrm{d}\alpha} \mathbb{V}(x_a) = \tfrac{\mathrm{d}}{\mathrm{d}\alpha} (1 - \alpha)^2 \mathbb{V}(x) + \alpha^2 \mathbb{V}(y) = -2(1 - \alpha)\mathbb{V}(x) + 2\alpha \mathbb{V}(y)$$

which implies

$$\alpha = \frac{\mathbb{V}(x)}{\mathbb{V}(x) + \mathbb{V}(y)}$$

completing the proof.

We note that formula (9.1) contains all the information given: the measurements x, y and their variances $\mathbb{V}(x)$, $\mathbb{V}(y)$. In cases when the formula above is not feasible to compute (e.g. in more dimensions presented later on), usually a statistical cost function is minimised. As before, let x and y be estimators for the true state x_t with probability density functions f_x and f_y, respectively. The analysis x_a is then derived by maximising the maximum likelihood function $L : z \mapsto f_x(z) f_y(z)$ for the real-valued random variable z. Such methods are called *variational methods*.

Assumptions 9.2 We suppose that the real-valued random variables x and y are equally distributed and are of normal distribution with given variances $\mathbb{V}(x)$ and $\mathbb{V}(y)$.

Theorem 9.2 *Under Assumptions 9.1 and 9.2, the solution of the maximum likelihood method leads to the same solution* (9.3) *as the optimal interpolation.*

Proof Since x and y are of normal distribution, the maximum likelihood function has the following form for any $\xi \in \mathbb{R}$:

$$\begin{aligned} L(\xi) &= f_x(\xi) f_y(\xi) \\ &= \tfrac{1}{\sqrt{2\pi \mathbb{V}(x)}} \mathrm{e}^{-\frac{1}{2} \frac{(x-\xi)^2}{\mathbb{V}(x)}} \tfrac{1}{\sqrt{2\pi \mathbb{V}(y)}} \mathrm{e}^{-\frac{1}{2} \frac{(y-\xi)^2}{\mathbb{V}(y)}} \\ &= \tfrac{1}{2\pi \sqrt{\mathbb{V}(x)\mathbb{V}(y)}} \mathrm{e}^{-\frac{1}{2} \frac{(x-\xi)^2}{\mathbb{V}(x)} - \frac{1}{2} \frac{(y-\xi)^2}{\mathbb{V}(y)}}. \end{aligned}$$

The function L is maximal if the absolute value of the exponent

$$J(\xi) := \frac{1}{2}\frac{(x-\xi)^2}{\mathbb{V}(x)} + \frac{1}{2}\frac{(y-\xi)^2}{\mathbb{V}(y)} \tag{9.2}$$

is minimal, that is, its derivative with respect to ξ vanishes. Hence, we obtain

$$x_a = \frac{\mathbb{V}(y)}{\mathbb{V}(x)+\mathbb{V}(y)}x + \frac{\mathbb{V}(x)}{\mathbb{V}(x)+\mathbb{V}(y)}y = x + \frac{\mathbb{V}(x)}{\mathbb{V}(x)+\mathbb{V}(y)}(y-x)$$

which completes the proof.

The function J defined by formula (9.2) is called *cost function* in meteorological data assimilation. We note that it is a quadratic function.

9.4 Optimal Interpolation and Variational Method in More Dimensions

In the previous section we have seen how the optimal interpolation and the variational method work in one dimension. Since in meteorology one aims at estimating the true state of the whole atmosphere, or at least the true values of the meteorological variables in the spatial grid points, the measurements x and y are (quite long) vectors. Hence, in this section we seek the best combination of the model's forecast $x \in \mathbb{R}^n$ and the observations $y \in \mathbb{R}^m$ by supposing the same as in Assumption 9.1 in the appropriate form. To do so, we introduce first the operator $\mathcal{H} : \mathbb{R}^n \to \mathbb{R}^m$, called *observation operator*, which maps the forecast vector x onto the grid of the observations' vector y.

Assumptions 9.3 Let $x \in \mathbb{R}^n$ and $y \in \mathbb{R}^m$ be vector-valued random variables with $m \leq n$ and $x_a \in \mathbb{R}^n$ be an estimator of the constant true state $x_t \in \mathbb{R}^n$.

1. The estimator x_a is a linear function of x and y, that is, there exists a matrix $K \in \mathbb{R}^{n\times m}$ such that

$$x_a = x + K(y - \mathcal{H}(x)). \tag{9.3}$$

2. The estimator x_a and the data x, y are unbiased, that is, $\mathbb{E}(x_a) = \mathbb{E}(x) = x_t$ and $\mathbb{E}(y) = \mathcal{H}(x_t)$, and are of normal distribution.
3. The estimator x_a is optimal in the sense of Definition 9.5.
4. The data are uncorrelated, that is, $\mathrm{cov}(x, y) = 0$.
5. The values of the variances $\mathbb{V}(x)$ and $\mathbb{V}(y)$ are given.
6. The observation operator $\mathcal{H} = H \in \mathbb{R}^{m\times n}$ is linear.

Remark 9.1 Let $\varepsilon_x := x - x_t \in \mathbb{R}^n$ and $\varepsilon_y := y - \mathcal{H}(x_t) \in \mathbb{R}^m$ denote the errors of x and y, respectively, being vector-valued random variables as well. Since the data x

and y are unbiased, the variances have the form

$$\mathbb{V}(x) = \mathbb{E}\big((x - \mathbb{E}(x))(x - \mathbb{E}(x))^\top\big) = \mathbb{E}\big((x - x_t)(x - x_t)^\top\big) = \mathbb{E}(\varepsilon_x \varepsilon_x^\top)$$

and similarly for $\mathbb{V}(y) = \mathbb{E}(\varepsilon_y \varepsilon_y^\top)$. Hence, they are usually called *error covariance matrices*. Moreover, since the data x and y are uncorrelated, we have

$$0 = \operatorname{cov}(x, y) = \mathbb{E}\big((x - \mathbb{E}(x))(y - \mathbb{E}(y))^\top\big) = \mathbb{E}((x - x_t)(y - x_t)^\top) = \mathbb{E}(\varepsilon_x \varepsilon_y^\top)$$

and similarly $\mathbb{E}(\varepsilon_y \varepsilon_x^\top) = 0$.

The next question is how to choose the matrix K, called Kálmán gain matrix, in order to obtain an optimal estimator x_a.

Theorem 9.3 *Under Assumptions 9.3, the Kálmán gain matrix K in formula (9.3) has the form*

$$K = \mathbb{V}(x)H^\top(\mathbb{V}(y) + H\mathbb{V}(x)H^\top)^{-1}. \tag{9.4}$$

Proof Since the vector-valued random variables $x \in \mathbb{R}^n$ and $y \in \mathbb{R}^m$ are of normal distribution, their probability density functions have the following form for any $\xi \in \mathbb{R}^n$:

$$f_x(\xi) = \frac{1}{\sqrt{2\pi|\mathbb{V}(x)|}} \mathrm{e}^{-\frac{1}{2}(x-\xi)^\top \mathbb{V}(x)^{-1}(x-\xi)},$$
$$f_y(\xi) = \frac{1}{\sqrt{2\pi|\mathbb{V}(y)|}} \mathrm{e}^{-\frac{1}{2}(y-H\xi)^\top \mathbb{V}(y)^{-1}(y-H\xi)},$$

where $|\cdot|$ denotes the determinant of the corresponding matrix. Thus, the maximum likelihood function reads as

$$\begin{aligned} L(\xi) &:= f_x(\xi) f_y(\xi) \\ &= \frac{1}{\sqrt{2\pi|\mathbb{V}(x)||\mathbb{V}(y)|}} \mathrm{e}^{-\frac{1}{2}(x-\xi)^\top \mathbb{V}(x)^{-1}(x-\xi) - \frac{1}{2}(y-H\xi)^\top \mathbb{V}(y)^{-1}(y-H\xi)}. \end{aligned}$$

The function L is maximal if the absolute value of the exponent

$$J(\xi) := \tfrac{1}{2}(x - \xi)^\top \mathbb{V}(x)^{-1}(x - \xi) + \tfrac{1}{2}(y - H\xi)^\top \mathbb{V}(y)^{-1}(y - H\xi) \tag{9.5}$$

is minimal, that is, if its derivative vanishes:

$$\tfrac{\mathrm{d}}{\mathrm{d}\xi} J(\xi) = \mathbb{V}(x)^{-1}(x - \xi) + H^\top \mathbb{V}(y)^{-1}(y - H\xi) = 0.$$

Hence, we obtain

$$x_a = x + \big(\mathbb{V}(x)^{-1} + H^\top \mathbb{V}(y)^{-1} H\big)^{-1} H^\top \mathbb{V}(y)^{-1}(y - Hx).$$

From the identities

$$\big(\mathbb{V}(x)^{-1} + H^\top \mathbb{V}(y)^{-1} H\big)^{-1} H^\top \mathbb{V}(y)^{-1} = \mathbb{V}(x) H^\top \big(\mathbb{V}(y) + H\mathbb{V}(x)H^\top\big)^{-1}$$

and

$$H^\top \mathbb{V}(y)^{-1}\big(H\mathbb{V}(x)H^\top + \mathbb{V}(y)\big) = \big(\mathbb{V}(x)^{-1} + H^\top \mathbb{V}(y)^{-1} H\big)\mathbb{V}(x)H^\top,$$

we have that

$$\big(\mathbb{V}(x)^{-1} + H^\top \mathbb{V}(y)^{-1} H\big)^{-1} H^\top \mathbb{V}(y)^{-1} = \mathbb{V}(x) H^\top \big(\mathbb{V}(y) + H\mathbb{V}(x)H^\top\big)^{-1},$$

which completes the proof.

Theorem 9.4 *Under Assumptions 9.3, for any matrix $K \in \mathbb{R}^{n\times m}$, the analysis error covariance matrix $\mathbb{V}(x_a)$ is given by*

$$\mathbb{V}(x_a) = \big(\mathrm{I} - KH\big)\mathbb{V}(x)\big(\mathrm{I} - KH\big)^\top + K\mathbb{V}(y)K^\top. \tag{9.6}$$

If the Kálmán gain matrix K has the special form defined in (9.4), the expression becomes

$$\mathbb{V}(x_a) = \big(\mathrm{I} - KH\big)\mathbb{V}(x). \tag{9.7}$$

Proof From formula (9.3), we obtain for the errors that

$$\begin{aligned}\varepsilon_a - \varepsilon_x &= x_a - x_t - x + x_t = K(y - Hx)\\ &= K(\varepsilon_y + Hx_t - Hx) = K(\varepsilon_y + H(x_t - x))\\ &= K(\varepsilon_y - H\varepsilon_x),\end{aligned}$$

which implies

$$\varepsilon_a = \varepsilon_x + K\varepsilon_y - KH\varepsilon_x = (\mathrm{I} - KH)\varepsilon_x + K\varepsilon_y.$$

Hence, the error covariance matrix $\mathbb{V}(x_a)$ of the analysis can be expressed as

$$\begin{aligned}\mathbb{V}(x_a) = \mathrm{cov}(\varepsilon_a) &= \mathbb{E}\big((\varepsilon_a - \mathbb{E}(\varepsilon_a))(\varepsilon_a - \mathbb{E}(\varepsilon_a))^\top\big)\\ &= \mathbb{E}\big(((\mathrm{I} - KH)\varepsilon_x + K\varepsilon_y)((\mathrm{I} - KH)\varepsilon_x + K\varepsilon_y)^\top\big)\\ &= (\mathrm{I} - KH)\mathbb{E}(\varepsilon_x\varepsilon_x^\top)(\mathrm{I} - KH)^\top + (\mathrm{I} - KH)\mathbb{E}(\varepsilon_x\varepsilon_y^\top)K^\top\\ &\quad + K\mathbb{E}(\varepsilon_y\varepsilon_x^\top)(\mathrm{I} - KH)^\top + K\mathbb{E}(\varepsilon_y\varepsilon_y^\top)K^\top.\end{aligned}$$

Remark 9.1 further implies

$$\begin{aligned}\mathbb{V}(x_a) &= \big(\mathrm{I} - KH\big)\mathbb{V}(x)\big(\mathrm{I} - KH\big)^\top + K\mathbb{V}(y)K^\top \\ &= \mathbb{V}(x) - \mathbb{V}(x)H^\top K^\top - KH\mathbb{V}(x) + KH\mathbb{V}(x)H^\top K^\top + K\mathbb{V}(y)K^\top \\ &= \mathbb{V}(x) - KH\mathbb{V}(x) - KH\mathbb{V}(x) + KH\mathbb{V}(x)H^\top K^\top + K\mathbb{V}(y)K^\top \\ &= (\mathrm{I} - KH)\mathbb{V}(x) + \triangle\end{aligned} \tag{9.8}$$

with $\triangle := -KH\mathbb{V}(x) + KH\mathbb{V}(x)H^\top K^\top + K\mathbb{V}(y)K^\top$. We only have to prove now that $\triangle = 0$ hold. From formula (9.4) we have

$$K = \mathbb{V}(x)H^\top\big(H\mathbb{V}(x)H^\top + \mathbb{V}(y)\big)^{-1} = \mathbb{V}(x)^\top H^\top\big((H\mathbb{V}(x)H^\top + \mathbb{V}(y))^{-1}\big)^\top,$$

which implies

$$K^\top = \big(H\mathbb{V}(x)H^\top + \mathbb{V}(y)\big)^{-1}H\mathbb{V}(x)$$

and

$$H\mathbb{V}(x) = \big(H\mathbb{V}(x)H^\top + \mathbb{V}(y)\big)K^\top = H\mathbb{V}(x)H^\top K^\top + \mathbb{V}(y)K^\top.$$

Then from the identity

$$KH\mathbb{V}(x) = KH\mathbb{V}(x)H^\top K^\top + K\mathbb{V}(y)K^\top$$

we finally conclude the proof with

$$0 = -KH\mathbb{V}(x) + KH\mathbb{V}(x)H^\top K^\top + K\mathbb{V}(y)K^\top = \triangle.$$

By inserting the form (9.4) of K into formula (9.6), one obtains the identity (9.7) which was to prove.

Besides the specific form (9.3) of the analysis x_a, we will show its optimality as well. To do so we will need the following technical Lemma.

Lemma 9.1 *Let $g : \mathbb{R}^{n\times m} \to \mathbb{R}$ be a continuously differentiable function, and $A \in \mathbb{R}^{m\times a}$, $B \in \mathbb{R}^{m\times m}$ be arbitrary fixed matrices for some $m, a \in \mathbb{N}$. Then the following holds for its derivative for any $K \in \mathbb{R}^{n\times m}$.*

1. *For $g(K) = \operatorname{tr} KA$ one has $\frac{\partial g}{\partial K} = A^\top$.*
2. *For $g(K) = \operatorname{tr} KBK^\top$ one has $\frac{\partial g}{\partial K} = KB^\top + KB$.*

Proof For the whole proof we refer to Schönemann [16]. For the conviction of the reader we note that since the function g is continuously differentiable with respect to $K = (K_{jk})_{j,k} \in \mathbb{R}^{n\times m}$ ($j = 1, \ldots, n$ and $k = 1, \ldots, m$), its derivative can be

expressed as

$$\frac{\partial g}{\partial K} = \begin{pmatrix} \frac{\partial g}{\partial K_{11}} & \cdots & \frac{\partial g}{\partial K_{1m}} \\ \vdots & \cdots & \vdots \\ \frac{\partial g}{\partial K_{n1}} & \cdots & \frac{\partial g}{\partial K_{nm}} \end{pmatrix}. \tag{9.9}$$

We can now state the main result of this section.

Theorem 9.5 *Under Assumptions 9.3, the analysis x_a, given by the formula (9.3) with the Kálmán gain matrix (9.4), is optimal in the sense of Definition 9.5.*

Proof The analysis x_a is optimal if the trace of the matrix

$$\mathbb{E}((x_a - x_t)(x_a - x_t)^\top)$$

is minimal. Since x_a is an unbiased estimate, this is equivalent to the minimisation of $\operatorname{tr} \mathbb{V}(x_a)$. Formula (9.7) in Theorem 9.4 implies that

$$\mathbb{V}(x_a) = (\mathrm{I} - KH)\mathbb{V}(x),$$

therefore, its trace is given in (9.8) as

$$\operatorname{tr} \mathbb{V}(x_a) = \operatorname{tr} \mathbb{V}(x) + \operatorname{tr} KH\mathbb{V}(x)H^\top K^\top - 2 \operatorname{tr} KH\mathbb{V}(x) + \operatorname{tr} K\mathbb{V}(y)K^\top.$$

Since the expression above is minimal if its derivative with respect to the matrix K vanishes, we need to compute $\frac{\partial \operatorname{tr} \mathbb{V}(x_a)}{\partial K}$. We use Lemma 9.1/2 first for the matrix $B := H\mathbb{V}(x)H^\top$, and obtain

$$\begin{aligned} \frac{\partial \operatorname{tr} KH\mathbb{V}(x)H^\top K^\top}{\partial K} &= K(H\mathbb{V}(x)H^\top)^\top + KH\mathbb{V}(x)H^\top \\ &= (H\mathbb{V}(x)H^\top K^\top)^\top + KH\mathbb{V}(x)H^\top. \end{aligned}$$

Similarly, for the choice $B := \mathbb{V}(y)$, Lemma 9.1/2 implies

$$\frac{\partial \operatorname{tr} K\mathbb{V}(y)K^\top}{\partial K} = (\mathbb{V}(y)K^\top)^\top + K\mathbb{V}(y).$$

Finally, for the matrix $A := H\mathbb{V}(x)$, Lemma 9.1/1 implies

$$\frac{\partial \operatorname{tr} KH\mathbb{V}(x)}{\partial K} = \mathbb{V}(x)^\top H^\top.$$

So the derivative of $\operatorname{tr}\mathbb{V}(x_a)$ is given by

$$\begin{aligned}\frac{\partial \operatorname{tr}\mathbb{V}(x_a)}{\partial K} =& (H\mathbb{V}(x)H^\top K^\top)^\top + KH\mathbb{V}(x)H^\top + K\mathbb{V}(y) \\ &+ (\mathbb{V}(y)K^\top)^\top - 2\mathbb{V}(x)^\top H^\top \\ =& 2KH\mathbb{V}(x)H^\top + 2K\mathbb{V}(y) - 2\mathbb{V}(x)H^\top,\end{aligned}$$

which is zero if and only if

$$K = \mathbb{V}(x)H^\top(H\mathbb{V}(x)H^\top + \mathbb{V}(y))^{-1}$$

holds, which completes the proof.

Since formula (9.3) together with formula (9.4) is the best linear unbiased estimate, this method is called BLUE from the initials. We note that if the observation operator $\mathcal{H}$ is nonlinear but linearisable around x_a (i.e. there exists $H \in \mathbb{R}^{m\times n}$ being the first derivative of $\mathcal{H}$ at x_a) then formula BLUE reads as

$$x_a = x + K(y - \mathcal{H}(x))$$

and together with (9.4) yield an approximatively optimal estimate to x_a, being however the only analysis which is possible to compute in practice in this way.

9.5 Kálmán Filter Techniques

In the previous section we presented the two basic data assimilation methods used in meteorology. From formulae BLUE (9.3) and (9.4) one can see how important role the error covariance matrices $\mathbb{V}(x)$ and $\mathbb{V}(y)$ play. Their computation, however, is a challenging task in practice. As a first attempt, they are usually supposed to be constant in time, however, in reality they may strongly depend on the weather situation. In the present study we focus on $\mathbb{V}(x)$ and assume that $\mathbb{V}(y)$ is constant in time. This can be supposed, because the spatial propagation of that part of x_a which causes the changes to x (called analysis increment) is based on $\mathbb{V}(x)$ solely. We present now a procedure due to Kálmán [12] to update the value of the error covariance matrix $\mathbb{V}(x)$ of the model's forecast in each time step. To do so, we need to introduce a model operator. Since the model operator describes time-dependent processes, we denote it by $\mathcal{M}_i : \mathbb{R}^n \to \mathbb{R}^n$ acting between the time levels i and $i+1$. It contains the spatially and temporally discretised version of the partial differential equations describing the atmosphere's dynamics and the physical parametrisations. By applying the BLUE data assimilation method, the numerical forecast $x^{\{i+1\}}$ at

time level $i+1$ is then obtained from the analysis $x_a^{\{i\}}$ valid at the ith time level as

$$x^{\{i+1\}} = \mathcal{M}_i(x_a^{\{i\}}),$$
$$x_a^{\{i+1\}} = x^{\{i+1\}} + K_{i+1}(y^{\{i+1\}} - \mathcal{H}(x^{\{i+1\}}))$$

for all $i \in \mathbb{N}$, where $x_a^{(0)}$ is a given initial value (e.g. from another numerical weather prediction model) and the Kálmán gain matrix is defined by formula (9.4), that is,

$$K_i = \mathbb{V}(x^{\{i\}})H_i^\top \left(\mathbb{V}(y^{\{i\}}) + H_i\mathbb{V}(x^{\{i\}})H_i^\top\right)^{-1}$$

for all $i \in \mathbb{N}$, where H_i denotes the linear observation operator. We note that if one takes the derivative of the nonlinear observation operator $\mathcal{H}$ at $x_a^{\{i\}}$ instead of $\mathcal{H}$ itself, the method described above only leads to an approximation to $x_a^{\{i+1\}}$ at the ith time level. We denote the model's error at time level i by $\varepsilon_{\mathcal{M}}^{\{i\}}$ and its error covariance matrix by $\mathbb{V}(\mathcal{M}_i(x_t^{\{i\}})) := \mathbb{E}(\varepsilon_{\mathcal{M}}^{\{i\}}(\varepsilon_{\mathcal{M}}^{\{i\}})^\top)$. As before, we suppose that the various errors are uncorrelated.

Assumptions 9.4 We suppose that the model's error and the error of the other data x and y are uncorrelated. We further suppose that the model operator and the observation operator are linear for all $i \in \mathbb{N}$, that is, $\mathcal{M}_i = M_i \in \mathbb{R}^{n\times n}$ and $\mathcal{H}_i = H_i \in \mathbb{R}^{m\times n}$.

In what follows we present the *Kálmán Filter* method for updating the error covariance matrix.

Theorem 9.6 *Under Assumptions 9.4, the update of the forecast's error covariance matrix reads as*

$$\mathbb{V}(x^{\{i+1\}}) = M_i\mathbb{V}(x_a^{\{i\}})M_i^\top + \mathbb{V}(M_i x_t^{\{i\}}) \quad \text{for all} \quad i \in \mathbb{N}. \tag{9.10}$$

Proof We consider the following two relations:

$$\begin{cases} x^{\{i+1\}} = M_i x_a^{\{i\}}, \\ x_t^{\{i+1\}} = M_i x_t^{\{i\}} - \varepsilon_{\mathcal{M}}^{\{i\}}, \end{cases}$$

where $x_t^{\{i\}}$ denotes the (unknown) true state at the ith time level. By subtracting the second equation from the first, one obtains

$$x^{\{i+1\}} - x_t^{\{i+1\}} = M_i x_a^{\{i\}} - M_i x_t^{(t)} + \varepsilon_{\mathcal{M}}^{\{i\}}.$$

Due to the linearity of the observation and the model operators, we can write

$$x^{\{i+1\}} - x_t^{\{i+1\}} = M_i\left(x_a^{\{i\}} - x_t^{(t)}\right) + \varepsilon_{\mathcal{M}}^{\{i\}}.$$

Since $x_a^{\{i\}} - x_t^{(t)} = \varepsilon_a^{\{i\}}$ for all $i \in \mathbb{N}$, we have

$$\begin{aligned}\mathbb{V}(x^{\{i+1\}}) =& \mathbb{E}\big(\varepsilon_x^{\{i+1\}}(\varepsilon_x^{\{i+1\}})^\top\big)\\ =& \mathbb{E}\Big(\big(M_i\big(x_a^{\{i\}} - x_t^{(t)}\big) + \varepsilon_{\mathcal{M}}^{\{i\}}\big)\big(M_i\big(x_a^{\{i\}} - x_t^{(t)}\big) + \varepsilon_{\mathcal{M}}^{\{i\}}\big)^\top\Big)\\ =& \mathbb{E}\Big(\big(M_i\varepsilon_a^{\{i\}} + \varepsilon_{\mathcal{M}}^{\{i\}}\big)\big(M_i\varepsilon_a^{\{i\}} + \varepsilon_{\mathcal{M}}^{\{i\}}\big)^\top\Big)\\ =& M_i\mathbb{E}\big(\varepsilon_a^{\{i\}}(\varepsilon_a^{\{i\}})^\top\big)M_i^\top + \mathbb{E}\big(\varepsilon_{\mathcal{M}}\varepsilon_{\mathcal{M}}^\top\big)\\ &+ \mathbb{E}\big(\varepsilon_{\mathcal{M}}(\varepsilon_a^{\{i\}})^\top\big)M_i^\top + M_i\mathbb{E}\big(\varepsilon_a^{\{i\}}(\varepsilon_{\mathcal{M}}^{\{i\}})^\top\big).\end{aligned}$$

Since the different kinds of data are uncorrelated and from Definition 9.3, we obtain for all $i \in \mathbb{N}$ that

$$\mathbb{V}(x^{\{i+1\}}) = M_i\mathbb{V}(x_a^{\{i\}})M_i^\top + \mathbb{V}(M_i x_t^{\{i\}}),$$

which completes the proof.

We remark that if the model operator $\mathcal{M}_i$ is nonlinear but linearisable, formula (9.10) stays valid but gives only an approximation to the update of the error covariance matrix. We note that in meteorology M_i and $M_i^\top$ are called tangent linear and adjoint model, respectively.

Formula (9.10) seems to be promising but it is absolutely not feasible for meteorological purposes. Due to the large number of grid points, $n \approx 10^7$, that is, the size n times n of the matrix M_i and its transpose makes the matrix product impossible to compute in a reasonable time. Hence, some other procedures are needed to approximate its effect. All the attempts in this direction originate from the ensemble predictions so far. Instead of taking only one initial analysis $x_a^{\{i\}}$, let us consider $k \in \mathbb{N}$ pieces of them, that is, we take $x_{a,j}^{\{i\}}$ for $j = 1, \ldots, k$. At the end of the section we list some techniques how they are generated in practice. Proposition 9.1 implies that the error covariance matrix $\mathbb{V}(x_a^{\{i\}})$ of the analysis can be estimated by

$$\mathbb{V}^{\{i\}}_{x_{a,1}\ldots x_{a,k}} := \frac{1}{k-1}\sum_{j=1}^{k}\Big(x_{a,j}^{\{i\}} - \frac{1}{k}\sum_{j=1}^{k}x_{a,j}^{\{i\}}\Big)\Big(x_{a,j}^{\{i\}} - \frac{1}{k}\sum_{j=1}^{k}x_{a,j}^{\{i\}}\Big)^\top \tag{9.11}$$

for all $i \in \mathbb{N}$. Formula (9.11) is the basic of all presented methods approximating the effect of the Kálmán Filter (9.10). In what follows we will sometimes drop the index of the time level in order to ease the notation.

Ensemble Kálmán Filter enables us to update the forecast's error covariance matrix by multiplying smaller matrices, that is, it desires much less computational effort than the original Kálmán Filter (9.10), see e.g. in Houtekamer and Mitchell [10] and Evensen [5]. Given the analysis ensemble members $x_{a,j}^{\{i\}}$ for $j = 1, \ldots, k$

we compute their sample mean from Definition 9.6 as

$$\mathbb{E}^{\{i\}}_{x_{a,1}\dots x_{a,k}} := \frac{1}{k}\sum_{j=1}^{k} x^{\{i\}}_{a,j} \quad \text{for all} \quad i \in \mathbb{N}.$$

We define the matrices $Z^{\{i\}}_a, Z^{\{i\}}_x \in \mathbb{R}^{n\times k}$ of the analysis and forecast perturbations, respectively, such that they contain the vectors

$$\tfrac{1}{\sqrt{k-1}}\big(x^{\{i\}}_{a,j} - \mathbb{E}^{\{i\}}_{x_{a,1}\dots x_{a,k}}\big) \quad \text{and} \quad \tfrac{1}{\sqrt{k-1}}\big(x^{\{i\}}_{j} - \mathbb{E}^{\{i\}}_{x_1\dots x_k}\big)$$

in their jth column, respectively, for all $j = 1,\dots,k$ and $i \in \mathbb{N}$. Proposition 9.1 implies that

$$\mathbb{V}(x^{\{i\}}_{a,j}) \approx \mathbb{V}^{\{i\}}_{x_{a,1}\dots x_{a,k}} = Z^{\{i\}}_a (Z^{\{i\}}_a)^\top \in \mathbb{R}^{n\times n} \quad \text{and}$$
$$\mathbb{V}(x^{\{i\}}_{j}) \approx \mathbb{V}^{\{i\}}_{x_1\dots x_k} = Z^{\{i\}}_x (Z^{\{i\}}_x)^\top \in \mathbb{R}^{n\times n}$$

for any $j = 1,\dots,k$, where the approximation sign means an unbiased estimate. The forecast ensemble is now generated by updating the analysis perturbations by the model, that is,

$$Z^{\{i+1\}}_x = M_i Z^{\{i\}}_x \quad \text{for all} \quad i \in \mathbb{N}. \tag{9.12}$$

Then we automatically obtain formula (9.10) for negligible $\mathbb{V}(M_i x^{\{i\}}_i)$ as

$$\begin{aligned}\mathbb{V}(x^{\{i+1\}}) &= Z^{\{i+1\}}_x \big(Z^{\{i+1\}}_x\big)^\top = M_i Z^{\{i\}}_a \big(Z^{\{i\}}_a M_i\big)^\top \\ &= M_i Z^{\{i\}}_a \big(Z^{\{i\}}_a\big)^\top M_i^\top = M_i \mathbb{V}(x^{\{i\}}_a) M_i^\top.\end{aligned}$$

Ensemble Kálmán Filter's advantage is that one needs to integrate with the model only k times in formula (9.12). We note that in the original setting the ensemble members $x_{a,j}$ stem from the application of multiply analyses, i.e., application of the BLUE estimate (9.3) multiple times with a set explicitly perturbed observations (with a perturbation size in the range of the observation error variances) and a set of implicitly perturbed forecasts. In this case the estimate is optimal. If the model $\mathcal{M}_i$ is nonlinear but linearisable, formula (9.12) reads as $Z^{\{i+1\}}_x = \mathcal{M}_i(Z^{\{i\}}_x)$, and formula (9.10) gives only an approximation to the error covariance matrix.

Ensemble Transform Kálmán Filter is a technique which not only updates the forecast's error covariance matrix but also generates ensemble members for the next assimilation step. It is based on the idea that, as in the case of Ensemble Kálmán Filter, there is a relation between the analysis's and the forecast's perturbations. From the analysis ensemble, the new forecast members $x^{\{i+1\}}_j$ are obtained by integrating with the model. By introducing the matrix $Z^{\{i\}}_x \in \mathbb{R}^{k\times k}$ as before, we

are after the transformation matrix $T \in \mathbb{R}^{k\times k}$ for which $Z_a^{\{i+1\}} = Z_x^{\{i\}} T^{\{i\}}$ holds for all $i \in \mathbb{N}$. Bishop et al. [1] showed that $T = V(\Lambda + I)^{-1/2}$ with

$$Z_x^\top H^\top \mathbb{V}(y)^{-1} H Z_x = V \Lambda V^\top.$$

Thus, matrix V contains the normalised eigenvectors and Λ the eigenvalues of the matrix on the left-hand side. Therefore, an eigenvalue decomposition has to be solved in each time step. By choosing a control member $x_{a,1}^{\{i\}}$, the columns of the matrix $Z_a^{\{i\}}$ contain the perturbations to be added to $x_{a,1}^{\{i\}}$ in order to generate the ensemble members. Given the analysis ensemble $x_{a,j}^{\{i\}}$ for $j = 1, \ldots, k$ and $i \in \mathbb{N}$, the algorithm of the Ensemble Transform Kálmán Filter together with BLUE data assimilation (9.3) and optimal Kálmán gain matrix (9.4) is the following for all $i \in \mathbb{N}$:

$$\begin{aligned}
x_j^{\{i+1\}} &:= \mathcal{M}_i(x_{a,j}^{\{i\}}) \quad \text{for} \quad j = 1, \ldots, k \\
\left(Z_x^{\{i+1\}}\right)_j &:= \tfrac{1}{\sqrt{k-1}}\left(x_j^{\{i+1\}} - \mathbb{E}_{x_1 \ldots x_k}^{\{i+1\}}\right) \quad \text{for} \quad j = 1, \ldots, k \\
(Z_x^{\{i+1\}})^\top H_{i+1}^\top \mathbb{V}(y^{\{i+1\}})^{-1} H_{i+1} Z_x^{\{i+1\}} &= V^{\{i+1\}} \Lambda^{\{i+1\}} (V^{\{i+1\}})^\top \\
T^{\{i+1\}} &:= V^{\{i+1\}} (\Lambda^{\{i+1\}} + I)^{-1/2} \\
Z_a^{\{i+1\}} &:= Z_x^{\{i+1\}} T^{\{i+1\}} \\
\mathbb{V}_{x_1 \ldots x_k}^{\{i+1\}} &:= Z_x^{\{i+1\}} (Z_x^{\{i+1\}})^\top \\
K_{i+1} &:= \mathbb{V}_{x_1 \ldots x_k}^{\{i+1\}} H_{i+1}^\top \left(\mathbb{V}(y^{\{i+1\}}) + H_{i+1} \mathbb{V}_{x_k \ldots x_k}^{\{i+1\}} H_{i+1}^\top\right)^{-1} \\
x_{a,1}^{\{i+1\}} &:= x_1^{\{i+1\}} + K_{i+1}\left(y^{\{i+1\}} - \mathcal{H}(x_1^{\{i+1\}})\right) \\
x_{a,j}^{\{i+1\}} &:= x_{a,1}^{\{i+1\}} + \left(Z_a^{\{i+1\}}\right)_j
\end{aligned}$$

generating the new analysis ensemble members $x_{a,j}^{\{i+1\}}$ and the updated approximate value $\mathbb{V}_{x_1 \ldots x_k}^{\{i+1\}}$ of the forecast's error covariance matrix.

We note again that the same procedure works for nonlinear model and observation operators $\mathcal{M}_i$ and $\mathcal{H}_i$ as well, however, it only leads to an approximative time evolution of the error covariance matrix. For more methods in the nonlinear case we refer to Sect. 9.7.

Previously, we supposed that there existed k pieces of analysis perturbations $x_{a,j}^{\{i\}}$, $j = 1, \ldots, k$ being valid at time level i. The question arises how they are generated in practice. The perturbation of the observations has already been mentioned. One can of course randomly perturb the actual analysis $x_a^{\{i\}}$ field itself. The *time-lagged approach* uses a mixture of two analyses initiated from two different time levels but being valid at the same time level, see e.g. in Hoffman and Kalnay [9]. This latter techniques will, however, not necessarily lead to perturbations being near to

the directions along that the model stretches the most, which would be one of the most beneficial requirements.

To this end, the *breeding method* was initiated where some initial random perturbations are added to the nonlinear model, and these models integrate the same initial analysis field $x_a^{\{0\}}$. The solution to the unperturbed model is then subtracted from the other solutions at each step, and the appropriately scaled differences are added to the unperturbed solution again to generate the new analysis perturbations for the next step. After some time, breeding method yields the so-called bred vectors approximating the directions in phase space where the instabilities grow fastest. The technique is described e.g. in Tóth and Kalnay [18, 19], and Kalnay [13].

Another popular perturbation generating technique is the method of *singular vectors*. The idea behind the method is the following. One considers a spatially discretised partial differential equation leading to an ordinary differential equation of the form $\frac{\mathrm{d}}{\mathrm{d}t}x(t) = \mathcal{N}(x(t))$, $t \geq t_0$ for the continuously differentiable functions $x\colon \mathbb{R}_0^+ \to \mathbb{R}^n$, $\mathcal{N}\colon \mathbb{R}^n \to \mathbb{R}^n$ for some $n \in \mathbb{N}$. If the initial value $x(t_0) = x_0$ is oppressed by a certain error e_0, a first-order approximation to the time evolution of the error term $e(t)$ can be obtained from the linearised equation $\frac{\mathrm{d}}{\mathrm{d}t}e(t) = \mathcal{J}(t)e(t)$ with the initial value $e(t_0) = e_0$, where $\mathcal{J}(t) = \mathcal{N}'(x(t))$ denotes the Jacobian of $\mathcal{N}$ taken at the state $x(t)$ for all $t \geq t_0$. Then there exists a matrix $\Psi(t) \in \mathbb{R}^{n\times n}$ such that the solution to this problem has the form $x(t) = \mathrm{e}^{\Psi(t-t_0)}x_0$ for all $t \geq t_0$. Since the matrix $\Psi(t)$ is difficult to compute exactly (it is the sum of infinitely many terms containing the integral of various commutators of $\mathcal{J}(t)$), certain approximation is computed in practice (e.g., Magnus method). By choosing the initial error term such that $\|e_0\| = \varepsilon$ for some $\varepsilon > 0$, that is, being on the surface on the n dimensional sphere of radius ε. Our aim is now to determine how this sphere evolves subject the nonlinear model $\mathcal{N}$. To this end, we denote the propagator by $E(t, t_0) := \mathrm{e}^{\Psi(t-t_0)}$ and the scalar product in $\mathbb{R}^n$ by $\langle\cdot,\cdot\rangle$. We compute now

$$\|e(t)\|^2 = \|E(t, t_0)e_0\|^2 = \langle E(t, t_0)e_0, E(t, t_0)e_0\rangle = \langle E(t, t_0)^\top E(t, t_0)e_0, e_0\rangle.$$

Due to the norm inequality we also have that

$$\|e(t)\|^2 = \|E(t, t_0)e_0\|^2 \leq \|E(t, t_0)\|^2\|e_0\|^2 = \varepsilon^2\|E(t, t_0)\|^2.$$

Altogether we have $\langle E(t, t_0)^\top E(t, t_0)e_0, e_0\rangle \leq \varepsilon^2\|E(t, t_0)\|^2$, that is,

$$\langle \mathrm{E}(t)e_0, e_0\rangle \leq 1 \tag{9.13}$$

with the matrix

$$\mathrm{E}(t) = \frac{1}{\varepsilon^2\|E(t, t_0)\|^2}E(t, t_0)^\top E(t, t_0).$$

Formula (9.13) gives the equation of an ellipsoid. The directions of its axes are given by the eigenvectors of the matrix $\mathrm{E}(t)$. These directions give, namely, the directions

along which the nonlinear model $\mathcal{N}$ stretches/compresses the error function $e(t)$ initially lying on the sphere. When generating the analysis perturbations, one is interested in that directions where the stretching the larger is. The direction of the largest stretching is given by the eigenvector belonging to the largest eigenvalue of the matrix $\mathrm{E}(t)$, and so on. Since the eigenvectors/eigenvalues of the matrix $E(t,t_0)^\top E(t,t_0)$ are called singular vectors/values of the matrix $E(t,t_0)$, we call this procedure the method of singular vectors. In order to get the singular vectors belonging to the leading singular values, one needs to integrate with the tangent linear model forward in time and then with the adjoint model backward in time many times, see e.g. in Errico [4].

We note, however, that in numerical weather prediction, the method of singular vector is always combined with either ensemble analyses with perturbed observations (EDA) or with perturbations generated by the Ensemble Transform Kálmán Filter. As we have already mentioned, Ensemble Transform Kálmán Filter generates not only the forecast's error covariance matrix $\mathbb{V}^{\{i+1\}}$ but the analysis perturbations as well. Comparisons between breeding method and Ensemble Transform Kálmán Filter, between singular vectors and EDA, and between EDA and Ensemble Transform Kálmán Filter are presented in Wang and Bishop [2, 24], and [7], respectively.

9.6 Numerical Experiments

In order to illustrate the use of the methods introduced above, we present the results of numerical experiments done for simple models. The reason of choosing these models for the experiments is twofold. On one hand, they are of low dimensions with $n = 1$ and $n = 3$, respectively, therefore, Kálmán Filter can directly be applied and there is no need to apply one of its approximations (such as Ensemble or Ensemble Transform Kálmán Filter). On the other hand, the exact solution of the first system is known, therefore, the behaviour of the data assimilation methods can easily be explained. Although the second system does not admit a known exact solution, it shares certain properties with the meteorological models (such us nonlinearity, sensitivity to the initial values, etc.), making it a perfect test model to study the performance of data assimilation methods.

9.6.1 Linear Iteration

We consider the system $x^{\{i+1\}} = x^{\{i\}}$ for $x^{\{i\}} \in \mathbb{R}$ and $i \in \mathbb{N}$ with $x^{\{0\}} = 1$. One can see that the true state equals $x_t = x^{\{0\}} = 1$. We suppose that the observations are unbiased and normally distributed perturbations of the true state:

$$y^{\{i\}} = x_t + \mathrm{N}(0, \mathbb{V}(y)) \quad \text{for all} \quad i \in \mathbb{N} \tag{9.14}$$

where $\mathbb{V}(y) = 0.3$ is given. The simulations aim at illustrating the effect of the forecast's error covariance matrix $\mathbb{V}(x)$. Since $\mathbb{V}(x)$ represents the reliability of the forecast, we can study how the solution changes depending on how much we rely on the forecast. Another goal is to show the advantage of Kálmán Filter, therefore, we present the same numerical experiments using BLUE (9.3)(9.4) and BLUE together with Kálmán Filter (9.10). This enables us to study how the analysis, being initially $x_a^{\{0\}} = 2$ far away from the true state $x_t = 1$, evolves in time in the two different cases.

In Figs. 9.1, 9.2, and 9.3 the numerical results are shown for three values of the error covariance matrix $\mathbb{V}(x) = 10^{-4}, 10^{-2}, 10$, respectively. Figure 9.1 illustrates the case when we trust the forecast very much: The results of both the BLUE and the Kálmán Filter methods are far from the true value $x_t = 1$ and follow the initial (wrong) analysis value $x_a^{\{0\}} = 2$. Figure 9.2 corresponds to the case when we treat

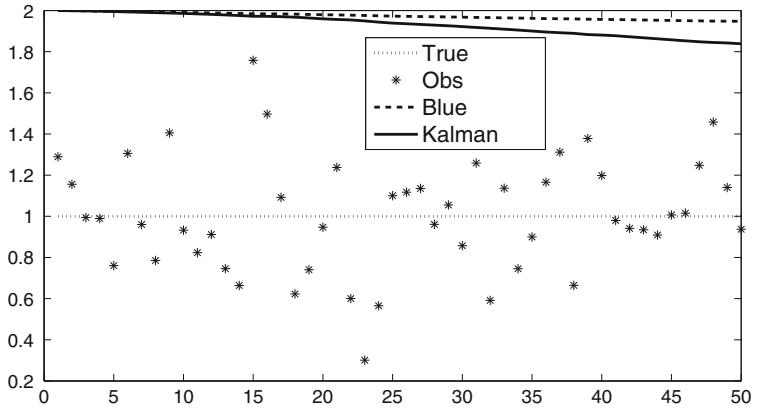

Fig. 9.1 Linear iteration with $\mathbb{V}(x) = 10^{-4}$

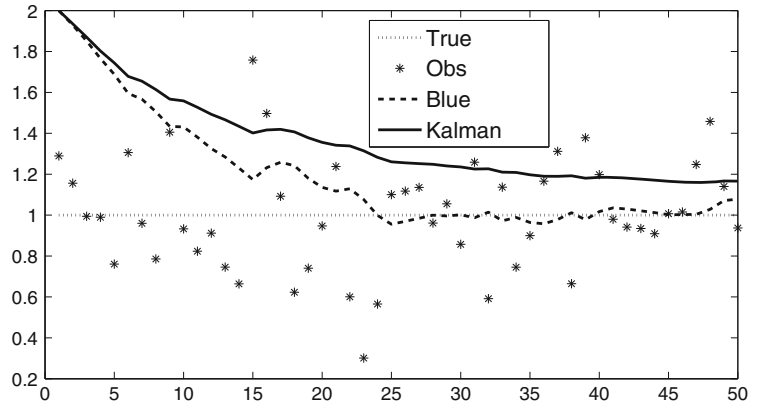

Fig. 9.2 Linear iteration with $\mathbb{V}(x) = 10^{-2}$

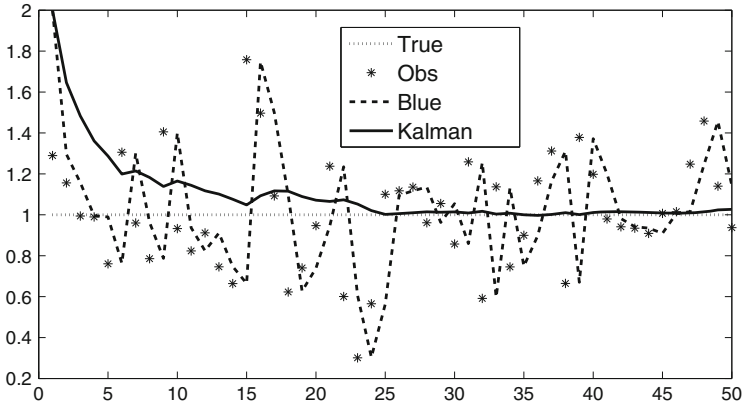

Fig. 9.3 Linear iteration with $\mathbb{V}(x) = 10$

the observations more reliable than in the latter case but still less reliable than the forecast. One can see that we obtain better results: Both methods converge to the true value $x_t = 1$. Figure 9.3 illustrates the case when $\mathbb{V}(x)$ has a much greater initial value than $\mathbb{V}(y)$, that is, we believe the observations much more reliable than the forecast. Then the numerical results of the BLUE method completely follows the observations, while the Kálmán Filter method updates $\mathbb{V}(x)$ in a perfect way: Its result finds the true solution very quickly.

9.6.2 Lorenz System

Our second example is the nonlinear three-dimensional Lorenz system. In 1963 Edward Lorenz developed a simplified mathematical model for atmospheric convection in [14]. The model is a system of three ordinary differential equations now known as the Lorenz equations:

$$\frac{\mathrm{d}}{\mathrm{d}t}x(t) = \sigma(y(t) - x(t)), \tag{9.15}$$

$$\frac{\mathrm{d}}{\mathrm{d}t}y(t) = x(t)(\rho - x(t)) - y(t), \tag{9.16}$$

$$\frac{\mathrm{d}}{\mathrm{d}t}x(t) = x(t)y(t) - \beta x(t), \tag{9.17}$$

where $x, y, z : (0, \infty) \to \mathbb{R}$ are the unknown functions, and $\sigma, \rho, \beta \in \mathbb{R}$ are parameters with specific values $\sigma = 10, \rho = 28, \beta = \frac{8}{3}$. Since its exact solution is not known, we solve the system numerically by using the first-order Euler method and the fourth-order Runge–Kutta method with time step $\Delta t = 0.01$. We consider the latter as the observations y at each time step. The solution with the Euler method is considered as the model's forecast. In the simulations we fix the covariance

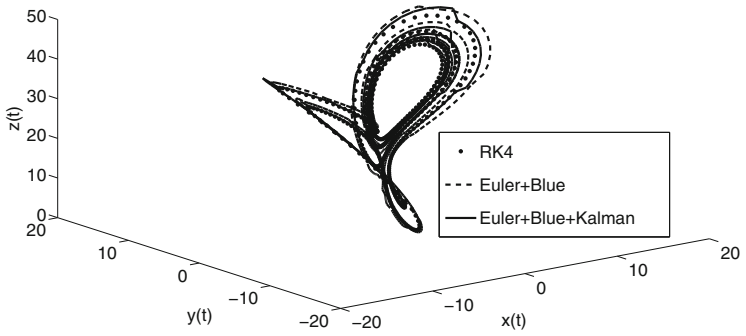

Fig. 9.4 The different trajectories in the phase space with parameters $\mathbb{V}(\mathcal{M}_i(x_t)) = 10^{-2}$, $t = 2$, $N = 10$

matrices as $\mathbb{V}(y) = (\Delta t)^8 \cdot \mathrm{I} \in \mathbb{R}^{3\times 3}$ and $\mathbb{V}(x) = \frac{1}{2}\mathbb{V}(y)$. Our aim is to investigate the role of the covariance matrix of the model's error $\mathbb{V}(\mathcal{M}_i(x_t))$, therefore, we set it to the following three value: $\mathbb{V}(\mathcal{M}_i(x_t)) = 1, 10^{-2}, 10^{-10}$. As before, we apply BLUE (9.3), (9.4) with and without Kálmán Filter (9.10).

Figure 9.4 shows the trajectories in the phase space (x, y, z) from the initial point $(2, 5, 10)$ by applying the fourth-order Runge–Kutta (RK4) method and the explicit Euler method with data assimilation method BLUE with and without Kálmán Filter. One can immediately see that the three solutions differ, a more detailed study will follow. We analyse first how the solution depends on the frequency of the data assimilation, that is, on the number N of the time steps after which the analysis x_a is computed. Figure 9.5 shows the results when the data assimilations methods are performed in each time step. One can see that all the three trajectories are closed to each other at the beginning, however, the Kálmán Filter method performs better then the BLUE method alone. Figure 9.6 illustrates the case when the data assimilation methods are performed only at every 10th time step. One can see that both methods have greater distance form the observations (RK4) as before. Furthermore, they experience "jumps" after each 10 time steps when their solutions are forced to follow the reliable observations by the data assimilation procedure. The same phenomena can be observed in Fig. 9.7 when data assimilation is performed in each 50th time steps. Both Figs. 9.6 and 9.7 show that the solutions cover each other at the beginning, hence, the Kálmán Filter benefits from the update of the error covariance matrix $\mathbb{V}(x)$ only after the first data assimilation step.

In Fig. 9.8 the relative error of BLUE

$$\mathrm{err}^{\{i\}} := \frac{\|x_a^{\{i\}} - y^{\{i\}}\|_2}{\|y^{\{i\}}\|_2}$$

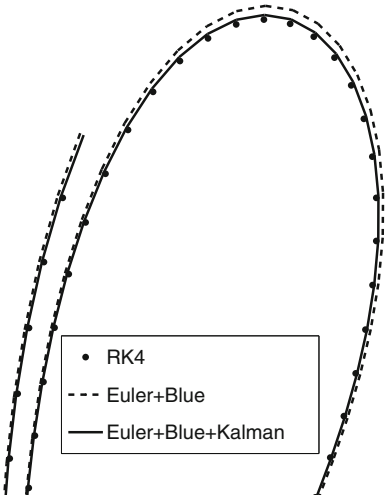

Fig. 9.5 Lorenz system with data assimilation frequency $N = 1$

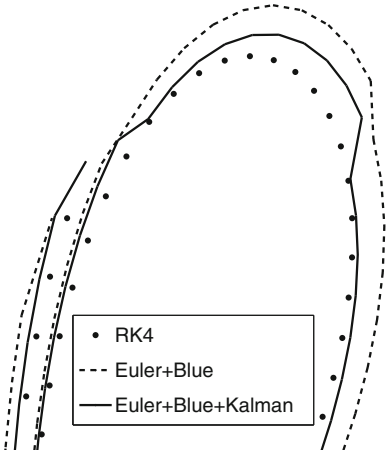

Fig. 9.6 Lorenz system with data assimilation frequency $N = 10$

with and without Kálmán Filter is shown. One can see that the Kálmán Filter always performs better then the BLUE alone.

We investigated the effect of the model's error covariance matrix $\mathbb{V}(\mathcal{M}_i(x_t))$ as well. Figure 9.9 shows our results for the values $\mathbb{V}(\mathcal{M}_i(x_t)) = 1, 10^{-8}$, and 10^{-16}, respectively. One can see that in the first case the solutions follow almost the same trajectories. The explanation is that in this case $\mathbb{V}(\mathcal{M}_i(x_t)) = 1$, that is, the model is considered unreliable, therefore, the solutions rely on the measurements (obtained by the fourth-order Runge–Kutta method RK4). If the value of $\mathbb{V}(\mathcal{M}_i(x_t))$ is decreased, the data assimilation methods treat the model more reliable and try to follow its trajectory. In the case $\mathbb{V}(\mathcal{M}_i(x_t)) = 10^{-16}$ the situation is clear: The BLUE method still follows the measurements (because $\mathbb{V}(\mathcal{M}_i(x_t))$ does not play

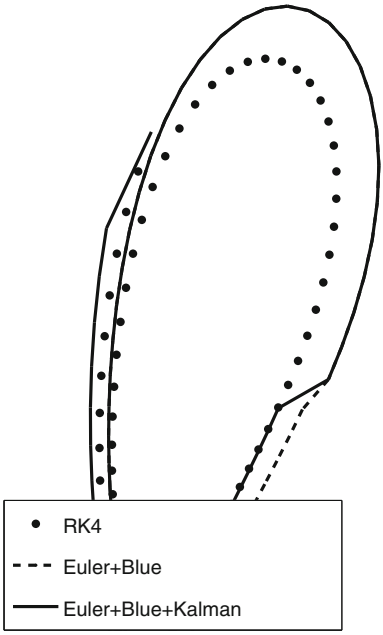

Fig. 9.7 Lorenz system with data assimilation frequency $N = 50$

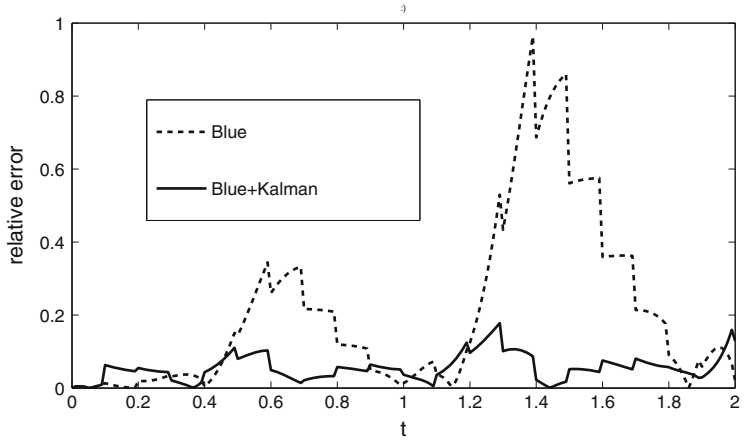

Fig. 9.8 Relative error of the BLUE method with and without Kálmán Filter technique

any role in its computation), however, the Kálmán Filter method tries to converge to the model's trajectory.

The explanation of the expected behaviour is the following. The measurements stem from the use of the fourth-order Runge–Kutta method being more accurate

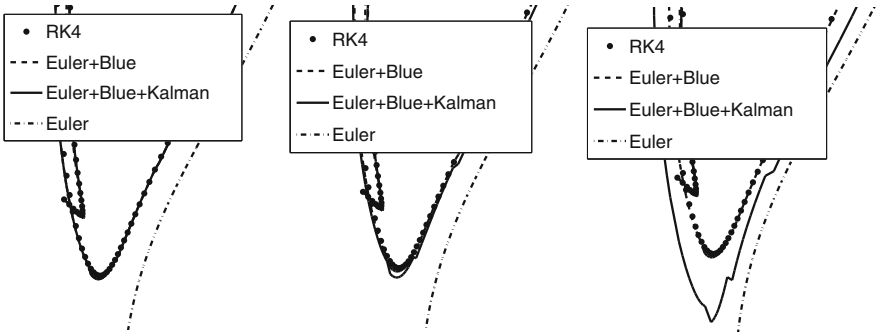

Fig. 9.9 Lorenz system with $\mathbb{V}(\mathcal{M}_i(x_t)) = 1, 10^{-8}, 10^{-16}$, respectively

than the first-order Euler method which provides the model's forecast. Without applying any data assimilation methods, the model's forecast (indicated by "Euler" in the Figures) differs very much from the (more accurate) measurements (indicated by "RK4" in the Figures). Hence, contrary to the case of the models used in numerical weather prediction where the true state of the atmosphere is somewhere "between" the measurements and the model's forecast, in this setting it is clearly known that the (unknown) exact solution is nearer to the measurements' trajectory. Application of a data assimilation method results in a more accurate solution which approaches therefore the trajectory of the measurements. Exactly this scenario can be observed in Fig. 9.9: Both data assimilation methods (BLUE and BLUE with Kálmán Filter) improves the model's forecast. In the third case, when the inaccurate model is undeservedly trusted too much (i.e. its error covariance matrix is small, $\mathbb{V}(\mathcal{M}_i(x_t)) = 10^{-16}$), the Kálmán Filter follows the trajectory of the Euler method causing a significant error in the analysis.

The results above illustrate that the use of a flow-dependent data assimilation method (e.g. Kálmán Filter or its approximate versions) itself is not enough for improving the weather forecast, setting the appropriate value of the model's error covariance matrix $\mathbb{V}(\mathcal{M}_i(x_t))$ is important as well. Since the model's error includes not only the numerical error originated from the space and time discretisation of the corresponding partial differential equations, but also the error done by the parametrisations of various physical processes and the error of the boundary conditions, very little is known about the its covariance matrix $\mathbb{V}(\mathcal{M}_i(x_t))$. It is usually modelled by adding some noise with zero mean to the forecast (or to each member of the forecast ensemble). Although there are several results related, see e.g. in Raynaud et al. [15], Trémolet [20], Düben and Palmer [3] and the references therein, the further study of this issue is highly anticipated.

The studies presented above aim at giving an insight how the parameters of the data assimilation methods effect the solution's accuracy. We showed that the analysis x_a depends very much on the frequency of the assimilation step and on the corresponding error covariance matrices. Hence, their right choice is crucial for the efficient use of data assimilation methods.

9.7 Outlook: Nonlinear Data Assimilation

We have seen previously that the solution to the linear data assimilation problem (9.3) is known and given in formula (9.4). The solution to the nonlinear data assimilation problem, that is, when the model and observation operators $\mathcal{M}$ and $\mathcal{H}$ are nonlinear, is given and studied e.g. by van Leeuven and Evensen in [21]. Since its derivation is based on Bayes' theorem, and in practice the probability density functions can be far from being Gaussian, there is a demand for new techniques which (1) do not use linearisation and (2) lead to a nonlinear analysis.

In this section we present some ideas how to proceed when the system is not linear. For a more detailed introduction, we refer the reader to van Leeuven [23]. The most common approaches of treating the nonlinearity are the use of incremental variational analysis and the particle filter methods.

We present the *incremental variational analysis* by applying it to the four-dimensional variational analysis (4D-Var), see e.g. in Talagrand and Courtier [17], Trémolet [20], which belongs to the class of variational data assimilation techniques presented in Sect. 9.4. Its cost function is similar to that presented in (9.5), however, it takes into account the effect of the various observations at their proper time levels. We consider the nonlinear model $\mathcal{M}_i$, the nonlinear observation operator $\mathcal{H}_i$, the observations $y^{\{i\}}$ at the ith time level, and the previous forecast x being valid at the time level t_0. Then the cost function $J(\xi)$ of the 4D-Var method reads as

$$\begin{aligned} J(\xi_0) :&= \tfrac{1}{2}(x-\xi)^\top \mathbb{V}(x)^{-1}(x-\xi_0) \\ &+ \tfrac{1}{2}\sum_{i=0}^{I}(y^{\{i\}}-\mathcal{H}_i(\xi^{\{i\}}))^\top \mathbb{V}(y)^{-1}(y^{\{i\}}-\mathcal{H}_i(\xi^{\{i\}})) \end{aligned} \tag{9.18}$$

with $\xi^{\{i\}}$ subject the nonlinear model $\xi^{\{i\}} = \mathcal{M}_{i-1}(\xi^{\{i-1\}})$, $i = 1, \ldots, I$. By denoting $\delta_0 := K(y - \mathcal{H}(x))$, the identity (9.1) reads as $x_a = x + \delta_0$, hence, formula (9.18) can be rewritten as

$$J(\delta_0) := \tfrac{1}{2}\delta_0^\top \mathbb{V}(x)^{-1}\delta_0 + \tfrac{1}{2}\sum_{i=0}^{I}(y^{\{i\}}-\mathcal{H}_i(\xi^{\{i\}}))^\top \mathbb{V}(y)^{-1}(y^{\{i\}}-\mathcal{H}_i(\xi^{\{i\}})).$$

The terms in the sum can be approximated by using the linearisation of the nonlinear operators $\mathcal{M}_i$ and $\mathcal{H}_i$ around the state $\xi^{\{i-1\}} := \xi^{\{i\}} - \delta^{\{i-1\}}$ with the vector-valued random variables $\delta_i \in \mathbb{R}^n$, $i = 0, \ldots, I$:

$$\begin{aligned} \mathcal{M}_i(\xi^{\{i\}}) &\approx \mathcal{M}_{i-1}(\xi^{\{i-1\}}) + \mathcal{M}'_{i-1}(\xi^{\{i-1\}})\delta^{\{i-1\}}, \quad i = 1, \ldots, I, \\ \mathcal{H}_i(\xi^{\{i\}}) &\approx \mathcal{H}_{i-1}(\xi^{\{i-1\}}) + \mathcal{H}'_{i-1}(\xi^{\{i-1\}})\delta^{\{i-1\}}, \quad i = 1, \ldots, I. \end{aligned} \tag{9.19}$$

Putting these formulas together, one obtains an approximative cost function those minimisation leads to an approximation to $\tilde{\delta}_0$. In order to take the linear operators

$\mathcal{M}_i'(\xi^{\{i\}})$ and $\mathcal{H}_i'(\xi^{\{i\}})$ at the proper time levels, one needs an outer loop to compute the linearisations (9.19) at each time level.

The inner loop contains then the minimisation of the cost function, that is, we seek that state $x_a := \xi$ for which $\frac{\mathrm{d}}{\mathrm{d}\xi}J(\xi) = 0$. This problem can be rewritten in the form $A\delta = b$ where matrix A contains the linear operators $\mathcal{M}_i'(\xi^{\{i\}})$ and $\mathcal{H}_i'(\xi^{\{i\}})$ as well, and the vector b contains the terms $y^{\{i\}} - \mathcal{H}_i(\xi^{\{i\}})$. Such problems are usually solved by the *conjugate gradient method* which global error depends on the condition number $\kappa := \|A\|\|A^{-1}\|$, that is, it converges fast if κ is small enough. There exist several preconditioning technics used to reduce the condition number of the problem and to obtain faster convergence, see e.g. in Faragó and Karátson [6]. A survey about the (pre)conditioning of the model operators appearing in meteorological modelling can be found e.g. in Haben et al. [8].

Another approach to treat nonlinearity is the *particle filtering*. The idea behind it is already presented in Sect. 9.5 about Ensemble Kálmán Filter, that is, the model's probability density function is approximated by using random ensemble members (also called as particles). More precisely, in this case we need to approximate the conditional density function which measures the probability density of the atmosphere's actual state given the specific observations. Then the conditional density function is represented as the weighted sum of Dirac functions positioned at the various particles (i.e., model states). Intuitively, we choose various particles and make them propagate with time subject the nonlinear model. For the next step we consider only those particles which "arrived" near to the observations, and by a resampling procedure we generate new particles from them. The weights in the sum correspond to the particles' distance from the observations. Then we repeat the cycle with the same amount of particles as in initial step. Since the derivation of particle filtering is based on the conditional probability theory (e.g. Bayesian statistics, stochastic filtering, Monte–Carlo methods), this is out of the scope of the present chapter, however, a detailed introduction can be found in van Leeuven [22].

Acknowledgements The authors thank Gergely Bölöni for the careful reading, the corrections, and the useful suggestions. The financial support of the "Stiftung Aktion Österreich-Ungarn" (project nr. 89öu11) is kindly acknowledged.

References

1. Bishop, C.H., Etherton, B.J., Majumdar, S.J.: Adaptive sampling with the ensemble transform Kalman filter. Mon. Weather Rev. **129**, 420–436 (2001)
2. Buizza, R., Leutbecher M., Isaksen, L.: Potential use of an ensemble of analyses in the ECMWF ensemble prediction system. Q. J. Roy. Meteorol. Soc. **134**, 2051–2066 (2008)
3. Düben, P.D., Palmer, T.N.: Benchmark tests for numerical weather forecasts on inexact hardware. Mon. Weather Rev. **142**, 3809–3829 (2014)
4. Errico, R.M.: What is an adjoint model? Bull. Am. Meteorol. Soc. **78**, 2577–2591 (1997)
5. Evensen, G.: Data assimilation. The Ensemble Kalman Filter. Springer, Berlin (2009)

6. Faragó, I., Karátson, J.: Numerical Solution of Nonlinear Elliptic Problems via Preconditioning Operators: Theory and Applications. Nova Science Publishers, New York (2002)
7. Gustafsson, N., Bojarova, J., Vigne, O.: A hybrid variational ensemble data assimilation for the HIgh Resolution Limited Area Model (HIRLAM). Nonlinear Processes Geophys. **21**, 303–323 (2014)
8. Haben, S.A., Lawless, A.S., Nichols, N.K.: Conditioning of incremental variational data assimilation, with application to the met office system. Tellus A **63**, 782–792 (2011)
9. Hoffman, R.N., Kalnay, E.: Lagged average forecasting, an alternative to Monte Carlo forecasting. Tellus A **354**, 100–118 (1983)
10. Houtekamer, P.L., Mitchell, H.L.: Data assimilation using an ensemble Kalman filter technique. Mon. Weather Rev. **126**, 797–811 (1998)
11. Johnson, R.A., Wichern, D.W.: Applied Multivariate Statistical Analysis. Pearson Prentice Hall,Upper Saddle River (2007)
12. Kalman, R.E.: A new approach to linear filtering and prediction problems. J. Basic Eng. **82**, 35–45 (1960)
13. Kalnay, E.: Atmospheric Modeling, Data Assimilation and Predictability. Cambridge University Press, Cambridge (2002)
14. Lorenz, E.N.: Deterministic nonperiodic flow. J. Atmos. Sci. **20**, 130–141 (1963)
15. Raynaud, L., Berre, L., Desroziers, G.: Accounting for model error in the Météo-France ensemble data assimilation system. Q. J. R. Meteorol. Soc. **2138**, 249–262 (2012)
16. Schönemann, P.H.: On the formal differentiation of traces and determinants. Multivar. Behav. Res. **20**, 113–139 (1985)
17. Talagrand, O., Courtier, P.: Variational assimilation of meteorological observations with the adjoint vorticity equation. I: theory. Q. J. R. Meteorol. Soc. **113**, 1311–1328 (1987)
18. Toth, Z., Kalnay, E.: Ensemble forecasting at NMC: the generation of perturbations. Bull. Am. Meteorol. Soc. **74**, 2317–2330 (1993)
19. Toth, Z., Kalnay, E.: Ensemble forecasting at NCEP and the breeding method. Mon. Weather Rev. **125**, 3297–3319 (1997)
20. Trémolet, Y.: Accounting for an imperfect model in 4D-Var. Q. J. R. Meteorol. Soc. **132**, 2483–2504 (2006)
21. van Leeuven, P.J., Evensen, G.: Data assimilation and inverse methods in terms of probabilistic formulation. Mon. Weather Rev. **124**, 2898–2913 (1996)
22. van Leeuven, P.J.: Nonlinear data assimilation in geosciences: an extremely efficient particle filter. Q. J. R. Meteorol. Soc. **136**, 1991–1999 (2010)
23. van Leeuven, P.J., Cheng, Y., Reich, S.: Nonlinear Data Assimilation. Springer, Berlin (2015)
24. Wang, X., Bishop, C.H.: A comparison of breeding and ensemble transform Kalman filter ensemble forecast schemes. J. Atmos. Sci. **60**, 1140–1158 (2003)

Chapter 10
Analysis of the Data Assimilation Methods from the Mathematical Point of View

Tamás Szentimrey

Abstract The Bayes estimation theory is the mathematical background of the data assimilation methods in meteorology. According to the Bayes theorem, the conditional density function of atmospheric state, given observations and background, can be expressed by the conditional density function of atmospheric state, given background, and the conditional density function of observations, given atmospheric state. Assuming joint normal distribution and certain premise for the conditional expectation of atmospheric state, given background, can be obtained the variation cost function applied at the data assimilation methods. We present some discussion of the above premise for conditional expectation, furthermore some examination of the background and observation error covariance matrices at the cost function. These terms are key issues at the data assimilation methods and we think them to be related to the climate statistical parameters.

Keywords Bayes estimation • Conditional covariance matrix • Conditional expectation • Cost function • Data assimilation • Interpolation • Normal conditional density function

10.1 Introduction

The author is a mathematician who is interested to develop adequate mathematics for the statistical climatology in accordance with the theory of probability and mathematical statistics. The preferred topics are the homogenization and quality control of data series, spatial interpolation etc. that with their connections between each other are presented on Fig. 10.1. Our software based on the developed mathematics are MASH and MISH. The software package MASH (Multiple Analysis of Series for Homogenization; [4, 5]) can be applied for homogenization of daily and monthly data series of several meteorological variables e.g. temperature and precipitation. The software package MISH (Meteorological Interpolation based on

T. Szentimrey (✉)
Hungarian Meteorological Service, P.O. Box 38, 1525 Budapest, Hungary
e-mail: szentimrey.t@met.hu

A. Bátkai et al. (eds.), *Mathematical Problems in Meteorological Modelling*,
Mathematics in Industry 24, DOI 10.1007/978-3-319-40157-7_10

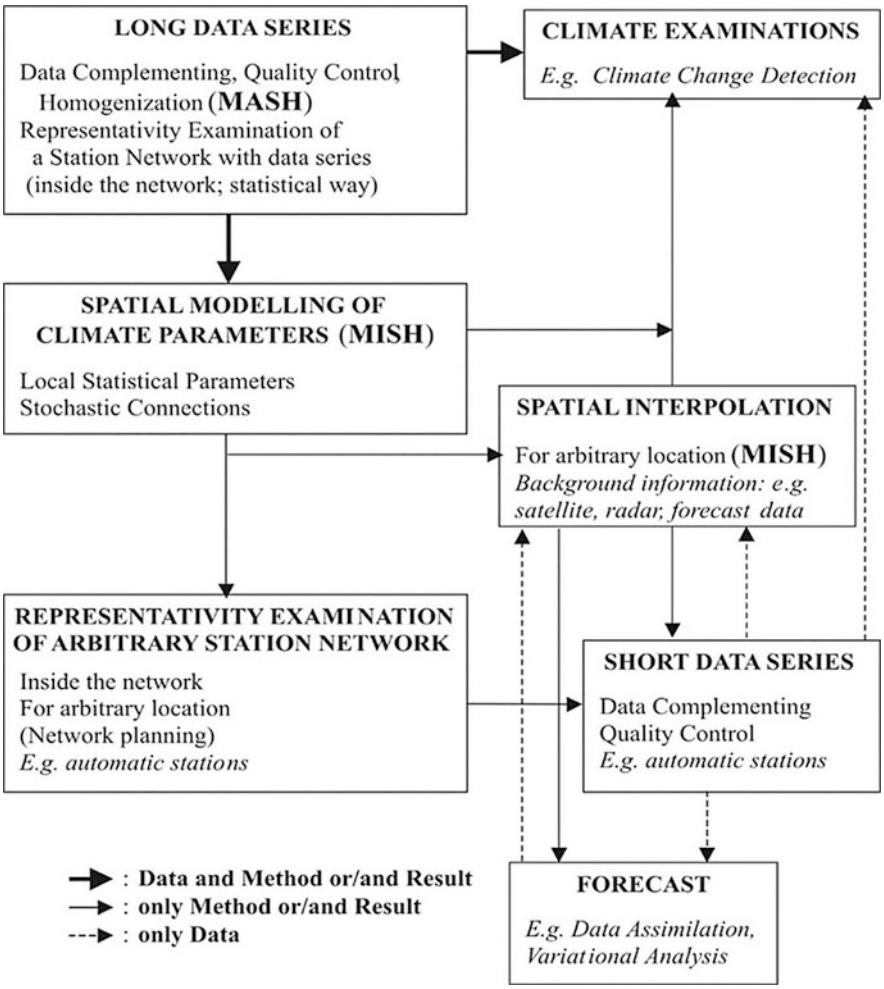

Fig. 10.1 Block diagram for the possible connections between various basic meteorological topics and systems

Surface Homogenized Data Basis; [3, 6]) is suitable for spatial interpolation of the meteorological variables.

The meteorological data assimilation is also presented on the block diagram of Fig. 10.1 since it can be considered as a cross-border procedure between the climatology and the forecast or in respect of methodology it is between mathematical statistics and the dynamics modelling. However the mathematical basis of the data assimilation is the probability theory, namely the Bayesian estimation. Therefore we will examine this basis together with the analysis of the most relevant mathematical properties, theorems since the theoretical results make possible to develop the procedures applied in the practice. The [2] is recommended for an

introduction to a general overview of the various data assimilation models and procedures.

10.2 Data Assimilation Model Applied in the Meteorological Practice

10.2.1 The Cost function of Data Assimilation

The purpose of data assimilation is to determine a best possible atmospheric state using observations and short range forecasts. The typical way applied in practice to estimate the true atmospheric state is the minimization of the following variational cost function:

$$J(\mathbf{x}) = (\mathbf{x} - \mathbf{x}_b)^{\mathrm{T}} \mathbf{B}^{-1} (\mathbf{x} - \mathbf{x}_b) + (\mathbf{y}_0 - \mathbf{H}\mathbf{x})^{\mathrm{T}} \mathbf{R}^{-1} (\mathbf{y}_0 - \mathbf{H}\mathbf{x}), \tag{10.1}$$

where the vectors and the parameter matrices are as follows:

$\mathbf{x} = [x_1, x_2, ..., x_n]^{\mathrm{T}}$: the atmospheric state, the realization of the n-dimensional random vector variable $\mathbf{X} = [X_1, \ldots, X_n]^{\mathrm{T}}$,
$\mathbf{x}_a$: analysis i.e. the solution of the minimization, $\mathbf{x}_a = \arg \min_x J(\mathbf{x})$,
$\mathbf{x}_b = [x_{b1}, x_{b2}, ..., x_{bn}]^{\mathrm{T}}$: the background i.e. short range forecasts, the realization of the n-dimensional random vector variable $\mathbf{X}_b = [X_{b1}, \ldots, X_{bn}]^{\mathrm{T}}$,
$\mathbf{y}_0 = [y_{01}, y_{02}, ..., y_{0m}]^{\mathrm{T}}$: the observations of the atmospheric state, the realization of the m-dimensional random vector variable $\mathbf{Y}_0 = [Y_{01}, \ldots, Y_{0m}]^{\mathrm{T}}$,
$\mathbf{H}$: forward operator,
$\mathbf{B}$: background error covariance matrix,
$\mathbf{R}$: observation error covariance matrix.

10.2.2 Problems with the Cost Function

The cost function (10.1) is known and referred by the forecasting community as it is based on the Bayesian estimation theory (e.g. [1] and [7]). However as we will see that there are some mathematical omissions and simplifications at the cost function (10.1). For example this formula includes implicitly the assumption that the conditional expectation of $\mathbf{X}$, given $\mathbf{X}_b = \mathbf{x}_b$ is identical with $\mathbf{x}_b$ i.e. $\mathrm{E}(\mathbf{X} \mid \mathbf{X}_b = \mathbf{x}_b) = \mathbf{x}_b$. Or the relation of the background error covariance matrix $\mathbf{B}$ and the climate is in general not well understood. Consequently the necessary climate statistical parameters are also neglected at the data assimilation procedures applied in practice. In the following sections we will overview the mathematical background of the data assimilation procedure together with the most relevant mathematical properties, theorems since the theoretical results make it possible to develop the procedures applied in the practice.

10.2.3 Problems with the Reanalysis Data Based on Data Assimilation

The data assimilation technique is used also to produce reanalysis data series in order to monitor the climate change based on past observation series. However beside the above mentioned inadequacies there are further sources of errors for reanalysis data. One of them is the inhomogeneity of the used station data series i.e. these series are often affected by artificial shifts due to changes in the measurement conditions (relocations, instrumentation). Another problem may be the little spatial representativity i.e. relatively few station data series are used for production of reanalysis data series as a consequence of the data policy between the countries.

10.3 Derivation of the Bayesian Cost Function for Data Assimilation

10.3.1 Application of the Bayes Theorem

The formula (10.1) is based on the Bayes theorem with the assumption of the joint distribution of vector variables $\mathbf{X}, \mathbf{X}_b, \mathbf{Y}_0$ being normal.

First we have to express the conditional density function of the atmospheric state, given the background and the observations.

Lemma 10.1 *The conditional density function of* $\mathbf{X}$*, given* $\mathbf{X}_b = \mathbf{x}_b,\ \mathbf{Y}_0 = \mathbf{y}_0$*, can be written as*

$$f(\mathbf{x} \mid \mathbf{x}_b,\ \mathbf{y}_0) = f(\mathbf{y}_0 \mid \mathbf{x},\ \mathbf{x}_b) \cdot f(\mathbf{x} \mid \mathbf{x}_b) \cdot \frac{1}{f(\mathbf{y}_0 \mid \mathbf{x}_b)}, \tag{10.2}$$

$f(\mathbf{y}_0 \mid \mathbf{x}, \mathbf{x}_b)$*: conditional density function of* $\mathbf{Y}_0$*, given* $\mathbf{X} = \mathbf{x}$*,* $\mathbf{X}_b = \mathbf{x}_b$*,*
$f(\mathbf{x} \mid \mathbf{x}_b)$*: conditional density function of* $\mathbf{X}$*, given* $\mathbf{X}_b = \mathbf{x}_b$*,*
$f(\mathbf{y}_0 \mid \mathbf{x}_b)$*: conditional density function of* $\mathbf{Y}_0$*, given* $\mathbf{X}_b = \mathbf{x}_b$*.*

Proof According to the Bayes theorem the joint density function of vector variables $\mathbf{X}, \mathbf{X}_b, \mathbf{Y}_0$ can be expressed equivalently as

$$f(\mathbf{x}, \mathbf{x}_b,\ \mathbf{y}_0) = f(\mathbf{y}_0 \mid \mathbf{x},\ \mathbf{x}_b) \cdot f(\mathbf{x} \mid \mathbf{x}_b) \cdot f(\mathbf{x}_b),$$

$$f(\mathbf{x}, \mathbf{x}_b,\ \mathbf{y}_0) = f(\mathbf{x} \mid \mathbf{x}_b,\ \mathbf{y}_0) \cdot f(\mathbf{y}_0 \mid \mathbf{x}_b) \cdot f(\mathbf{x}_b).$$

Consequently, $f(\mathbf{x} \mid \mathbf{x}_b,\ \mathbf{y}_0) \cdot f(\mathbf{y}_0 \mid \mathbf{x}_b) = f(\mathbf{y}_0 \mid \mathbf{x},\ \mathbf{x}_b) \cdot f(\mathbf{x} \mid \mathbf{x}_b)$.

Then using Lemma 10.1 the conditional density function of $\mathbf{X}$, given $\mathbf{X}_b = \mathbf{x}_b,\ \mathbf{Y}_0 = \mathbf{y}_0$, can be written in the following simple form:

$$f(\mathbf{x} \mid \mathbf{x}_b,\ \mathbf{y}_0) = f(\mathbf{y}_0 \mid \mathbf{x}) \cdot f(\mathbf{x} \mid \mathbf{x}_b) \cdot \frac{1}{f(\mathbf{y}_0 \mid \mathbf{x}_b)}, \tag{10.3}$$

since it can be assumed $f(\mathbf{y}_0 \mid \mathbf{x},\ \mathbf{x}_b) = f(\mathbf{y}_0 \mid \mathbf{x})$, where $f(\mathbf{y}_0 \mid \mathbf{x})$ is the conditional density function of $\mathbf{Y}_0$, given $\mathbf{X} = \mathbf{x}$.

Consequently the Bayes estimation for the realization of $\mathbf{X}$, given $\mathbf{X}_b = \mathbf{x}_b,\ \mathbf{Y}_0 = \mathbf{y}_0$, that is:

$$\mathbf{x}_a = \arg \max_{\mathbf{x}} f(\mathbf{x} \mid \mathbf{x}_b,\ \mathbf{y}_0),$$

is equivalent to the following maximization:

$$\mathbf{x}_a = \arg \max_{\mathbf{x}} f(\mathbf{y}_0 \mid \mathbf{x}) \cdot f(\mathbf{x} \mid \mathbf{x}_b). \tag{10.4}$$

10.3.2 The Normal Conditional Density Functions and their Properties

Since it is assumed that the joint distribution of vector variables $\mathbf{X}, \mathbf{X}_b, \mathbf{Y}_0$ is normal, therefore the conditional density functions $f(\mathbf{x} \mid \mathbf{x}_b)$, $f(\mathbf{y}_0 \mid \mathbf{x})$ are also normal. It means:

$$f(\mathbf{x} \mid \mathbf{x}_b) = \frac{\exp\left(-\frac{1}{2}(\mathbf{x} - \mathrm{E}(\mathbf{X} \mid \mathbf{X}_b = \mathbf{x}_b))^{\mathrm{T}} \mathbf{B}^{-1} (\mathbf{x} - \mathrm{E}(\mathbf{X} \mid \mathbf{X}_b = \mathbf{x}_b))\right)}{\sqrt{(2\pi)^n \det(\mathbf{B})}}, \tag{10.5}$$

$$f(\mathbf{y}_0 \mid \mathbf{x}) = \frac{\exp\left(-\frac{1}{2}(\mathbf{y}_0 - \mathrm{E}(\mathbf{Y}_0 \mid \mathbf{X} = \mathbf{x}))^{\mathrm{T}} \mathbf{R}^{-1} (\mathbf{y}_0 - \mathrm{E}(\mathbf{Y}_0 \mid \mathbf{X} = \mathbf{x}))\right)}{\sqrt{(2\pi)^m \det(\mathbf{R})}}, \tag{10.6}$$

where we have the following notations:

$\mathrm{E}(\mathbf{X} \mid \mathbf{X}_b = \mathbf{x}_b)$: conditional expectation of $\mathbf{X}$, given $\mathbf{X}_b = \mathbf{x}_b$,
$\mathbf{B} = \mathbf{Cov}[\mathbf{X} \mid \mathbf{X}_b = \mathbf{x}_b]$: conditional covariance matrix of $\mathbf{X}$, given $\mathbf{X}_b = \mathbf{x}_b$,
$\mathrm{E}(\mathbf{Y}_0 \mid \mathbf{X} = \mathbf{x})$: conditional expectation of $\mathbf{Y}_0$, given $\mathbf{X} = \mathbf{x}$,
$\mathbf{R} = \mathbf{Cov}[\mathbf{Y}_0 \mid \mathbf{X} = \mathbf{x}]$: conditional covariance matrix of $\mathbf{Y}_0$, given $\mathbf{X} = \mathbf{x}$.

Theorem 10.1 *The properties of the conditional covariance matrices are as follows:*

1. $\mathbf{B} = \mathbf{Cov}\left[\mathbf{X} - \mathrm{E}\left(\mathbf{X} \mid \mathbf{X}_b\right)\right]$: *covariance matrix of* $\mathbf{X} - \mathrm{E}\left(\mathbf{X} \mid \mathbf{X}_b\right)$.
2. $\mathbf{B} = \mathbf{Cov}\left[\mathbf{X} - \mathrm{E}\left(\mathbf{X} \mid \mathbf{X}_b\right)\right] = \mathbf{Cov}\left[\mathbf{X}\right] - \mathbf{Cov}\left[\mathrm{E}\left(\mathbf{X} \mid \mathbf{X}_b\right)\right]$.
3. $\mathbf{R} = \mathbf{Cov}\left[\mathbf{Y}_0 - \mathrm{E}\left(\mathbf{Y}_0 \mid \mathbf{X}\right)\right]$: *covariance matrix of* $\mathbf{Y}_0 - \mathrm{E}\left(\mathbf{Y}_0 \mid \mathbf{X}\right)$.
4. $\mathbf{R} = \mathbf{Cov}\left[\mathbf{Y}_0 - \mathrm{E}\left(\mathbf{Y}_0 \mid \mathbf{X}\right)\right] = \mathbf{Cov}\left[\mathbf{Y}_0\right] - \mathbf{Cov}\left[\mathrm{E}\left(\mathbf{Y}_0 \mid \mathbf{X}\right)\right]$.

Proof

1. $\mathbf{B} = \mathbf{Cov}\left[\mathbf{X} \mid \mathbf{X}_b = \mathbf{x}_b\right]$ and
$$\mathbf{Cov}\left[\mathbf{X} \mid \mathbf{X}_b\right] = \mathrm{E}\left(\left(\mathbf{X} - \mathrm{E}\left(\mathbf{X} \mid \mathbf{X}_b\right)\right)\left(\mathbf{X} - \mathrm{E}\left(\mathbf{X} \mid \mathbf{X}_b\right)\right)^{\mathrm{T}} \mid \mathbf{X}_b\right) = \\ = \mathrm{E}\left(\left(\mathbf{X} - \mathrm{E}\left(\mathbf{X} \mid \mathbf{X}_b\right)\right)\left(\mathbf{X} - \mathrm{E}\left(\mathbf{X} \mid \mathbf{X}_b\right)\right)^{\mathrm{T}}\right) = \mathbf{Cov}\left[\mathbf{X} - \mathrm{E}\left(\mathbf{X} \mid \mathbf{X}_b\right)\right],$$
since in case of normal distribution the arbitrary functions $g\left(\mathbf{X} - \mathrm{E}\left(\mathbf{X} \mid \mathbf{X}_b\right)\right)$ and $\mathbf{X}_b$ are independent, consequently the conditional expectations are $\mathrm{E}\left(g\left(\mathbf{X} - \mathrm{E}\left(\mathbf{X} \mid \mathbf{X}_b\right)\right) \mid \mathbf{X}_b\right) = \mathrm{E}\left(g\left(\mathbf{X} - \mathrm{E}\left(\mathbf{X} \mid \mathbf{X}_b\right)\right)\right)$.
2. $$\mathbf{Cov}\left[\mathbf{X}\right] = \mathrm{E}\left(\left(\mathbf{X} - \mathrm{E}\left(\mathbf{X}\right)\right)\left(\mathbf{X} - \mathrm{E}\left(\mathbf{X}\right)\right)^{\mathrm{T}}\right) = \\ = \mathrm{E}\Big(\left(\left(\mathbf{X} - \mathrm{E}\left(\mathbf{X} \mid \mathbf{X}_b\right)\right) + \left(\mathrm{E}\left(\mathbf{X} \mid \mathbf{X}_b\right) - \mathrm{E}\left(\mathbf{X}\right)\right)\right) \\ \left(\left(\mathbf{X} - \mathrm{E}\left(\mathbf{X} \mid \mathbf{X}_b\right)\right) + \left(\mathrm{E}\left(\mathbf{X} \mid \mathbf{X}_b\right) - \mathrm{E}\left(\mathbf{X}\right)\right)\right)^{\mathrm{T}}\Big) = \\ = \mathrm{E}\left(\left(\mathbf{X} - \mathrm{E}\left(\mathbf{X} \mid \mathbf{X}_b\right)\right)\left(\mathbf{X} - \mathrm{E}\left(\mathbf{X} \mid \mathbf{X}_b\right)\right)^{\mathrm{T}}\right) \\ + \mathrm{E}\left(\left(\mathrm{E}\left(\mathbf{X} \mid \mathbf{X}_b\right) - \mathrm{E}\left(\mathbf{X}\right)\right)\left(\mathrm{E}\left(\mathbf{X} \mid \mathbf{X}_b\right) - \mathrm{E}\left(\mathbf{X}\right)\right)^{\mathrm{T}}\right) = \\ = \mathbf{Cov}\left[\mathbf{X} - \mathrm{E}\left(\mathbf{X} \mid \mathbf{X}_b\right)\right] + \mathbf{Cov}\left[\mathrm{E}\left(\mathbf{X} \mid \mathbf{X}_b\right)\right],$$
since $\mathbf{X} - \mathrm{E}\left(\mathbf{X} \mid \mathbf{X}_b\right)$, $\mathrm{E}\left(\mathbf{X} \mid \mathbf{X}_b\right) - \mathrm{E}\left(\mathbf{X}\right)$ are independent with $\mathbf{0}$ expectations, therefore $\mathrm{E}\left(\left(\mathbf{X} - \mathrm{E}\left(\mathbf{X} \mid \mathbf{X}_b\right)\right)\left(\mathrm{E}\left(\mathbf{X} \mid \mathbf{X}_b\right) - \mathrm{E}\left(\mathbf{X}\right)\right)^{\mathrm{T}}\right) = \mathrm{E}\left(\left(\mathrm{E}\left(\mathbf{X} \mid \mathbf{X}_b\right) - \mathrm{E}\left(\mathbf{X}\right)\right)\left(\mathbf{X} - \mathrm{E}\left(\mathbf{X} \mid \mathbf{X}_b\right)\right)^{\mathrm{T}}\right) = \mathbf{0}$.
3. The proof is the same as 1.
4. The proof is the same as 2.

10.3.3 The General Form of the Cost Function

Returning to the Bayes estimation for the realization of $\mathbf{X}$, given $\mathbf{X}_b = \mathbf{x}_b$, $\mathbf{Y}_0 = \mathbf{y}_0$, at Eq. (10.4), the following maximization can be obtained by logarithmization:

$$\mathbf{x}_a = \arg\max_{\mathbf{x}} \left(\ln f\left(\mathbf{x} \mid \mathbf{x}_b\right) + \ln f\left(\mathbf{y}_0 \mid \mathbf{x}\right)\right). \tag{10.7}$$

Substituting the conditional density functions (10.5) and (10.6) in the formula (10.7), the final general form of the cost function to be minimized with respect

to $\mathbf{x}$ is:

$$J(\mathbf{x}) = (\mathbf{x} - \mathrm{E}(\mathbf{X} \mid \mathbf{X}_b = \mathbf{x}_b))^{\mathrm{T}} \mathbf{B}^{-1} (\mathbf{x} - \mathrm{E}(\mathbf{X} \mid \mathbf{X}_b = \mathbf{x}_b)) + \\ + (\mathbf{y}_0 - \mathrm{E}(\mathbf{Y}_0 \mid \mathbf{X} = \mathbf{x}))^{\mathrm{T}} \mathbf{R}^{-1} (\mathbf{y}_0 - \mathrm{E}(\mathbf{Y}_0 \mid \mathbf{X} = \mathbf{x})), \tag{10.8}$$

and the analysis is, $\mathbf{x}_a = \arg \min_{\mathbf{x}} J(\mathbf{x})$.

The conditional expectations and the parameter matrices are as follows:

$\mathrm{E}(\mathbf{X} \mid \mathbf{X}_b = \mathbf{x}_b)$: conditional expectation of $\mathbf{X}$, given $\mathbf{X}_b = \mathbf{x}_b$,
$\mathbf{B} = \mathbf{Cov}[\mathbf{X} - \mathrm{E}(\mathbf{X} \mid \mathbf{X}_b)]$: covariance matrix of $\mathbf{X} - \mathrm{E}(\mathbf{X} \mid \mathbf{X}_b)$,
$\mathrm{E}(\mathbf{Y}_0 \mid \mathbf{X} = \mathbf{x})$: conditional expectation of $\mathbf{Y}_0$, given $\mathbf{X} = \mathbf{x}$,
$\mathbf{R} = \mathbf{Cov}[\mathbf{Y}_0 - \mathrm{E}(\mathbf{Y}_0 \mid \mathbf{X})]$: covariance matrix of $\mathbf{Y}_0 - \mathrm{E}(\mathbf{Y}_0 \mid \mathbf{X})$.

Remark 10.1 According to the theorems of the probability theory the conditional expectations $\mathrm{E}(\mathbf{X} \mid \mathbf{X}_b)$, $\mathrm{E}(\mathbf{Y}_0 \mid \mathbf{X})$ are linear functions if the joint distribution of vector variables $\mathbf{X}, \mathbf{X}_b, \mathbf{Y}_0$ is normal:

$$\mathrm{E}(\mathbf{X} \mid \mathbf{X}_b = \mathbf{x}_b) = \mathrm{E}(\mathbf{X}) + \mathbf{C}\ (\mathbf{x}_b - \mathrm{E}(\mathbf{X}_b)), \tag{10.9}$$

$$\mathrm{E}(\mathbf{Y}_0 \mid \mathbf{X} = \mathbf{x}) = \mathrm{E}(\mathbf{Y}_0) + \mathbf{H}\ (\mathbf{x} - \mathrm{E}(\mathbf{X})), \tag{10.10}$$

where $\mathrm{E}(\mathbf{X}), \mathrm{E}(\mathbf{X}_b), \mathrm{E}(\mathbf{Y}_0)$ are the expectations and $\mathbf{C}, \mathbf{H}$ are certain coefficient matrices.

A special case is the cost function (10.1) where the identity $\mathrm{E}(\mathbf{X} \mid \mathbf{X}_b = \mathbf{x}_b) = \mathbf{x}_b$ is assumed implicitly. However this assumption seems to be doubtful, therefore we will analyze the possibilities for modelling of the statistical relationship between the atmospheric state and the forecast.

10.4 The Properties of the General Cost Function

10.4.1 *Examination of* $\mathbf{E}(\mathbf{X} \mid \mathbf{X}_b = \mathbf{x}_b)$ *and* $\mathbf{B} = \mathbf{Cov}[\mathbf{X} - \mathbf{E}(\mathbf{X} \mid \mathbf{X}_b)]$

In the following theorem some basic properties are formulated.

Theorem 10.2

1. *If the expectations of* $\mathbf{X}$ *and* $\mathbf{X}_b$ *are identical* i.e. $\mathrm{E}(\mathbf{X}_b) = \mathrm{E}(\mathbf{X}) \iff \mathrm{E}(\mathbf{X} - \mathbf{X}_b) = \mathbf{0}$ *then according to Eq. (10.9):*

$$\mathrm{E}(\mathbf{X} \mid \mathbf{X}_b = \mathbf{x}_b) = \mathrm{E}(\mathbf{X}) + \mathbf{C}\ (\mathbf{x}_b - \mathrm{E}(\mathbf{X})).$$

2. *If 1, and* $\mathrm{E}\left(X_i \mid \mathbf{X}_b = \mathbf{x}_b\right) = \mathrm{E}\left(X_i \mid X_{b,i} = x_{b,i}\right) \quad (i = 1, \ldots, n)$ *then*

$$\mathrm{E}\left(X_i \mid \mathbf{X}_b = \mathbf{x}_b\right) = \mathrm{E}\left(X_i\right) + \beta_i \left(x_{b,i} - \mathrm{E}\left(X_i\right)\right) .$$

3. *If 2, and* $\beta_i = \beta \ \left(i = 1, \ldots, n\right)$ *then*

$$\mathrm{E}\left(\mathbf{X} \mid \mathbf{X}_b = \mathbf{x}_b\right) = \mathrm{E}\left(\mathbf{X}\right) + \beta \cdot \left(\mathbf{x}_b - \mathrm{E}\left(\mathbf{X}\right)\right).$$

Special case applied at cost function (10.1): $\beta = 1 \Rightarrow \mathrm{E}\left(\mathbf{X} \mid \mathbf{X}_b = \mathbf{x}_b\right) = \mathbf{x}_b$.

4. *If 3, that is* $\mathrm{E}\left(\mathbf{X} \mid \mathbf{X}_b\right) = \mathrm{E}\left(\mathbf{X}\right) + \beta \cdot \left(\mathbf{X}_b - \mathrm{E}\left(\mathbf{X}\right)\right)$ *then according to equation Theorems 10.1 and 10.2:*

$$\mathbf{B} = \mathbf{Cov}\left[\mathbf{X} - \mathrm{E}\left(\mathbf{X} \mid \mathbf{X}_b\right)\right] = \mathbf{Cov}\left[\mathbf{X}\right] - \mathbf{Cov}\left[\mathrm{E}\left(\mathbf{X} \mid \mathbf{X}_b\right)\right] = \mathbf{Cov}\left[\mathbf{X}\right] - \beta^2 \cdot \mathbf{Cov}\left[\mathbf{X}_b\right].$$

5. *If 4, and the covariance matrices of* $\mathbf{X}$ *and* $\mathbf{X}_b$ *are identical* i.e.*:*

$$\mathbf{Cov}\left[\mathbf{X}_b\right] = \mathbf{Cov}\left[\mathbf{X}\right] \ \textit{then} \ \mathbf{B} = \left(1 - \beta^2\right) \ \mathbf{Cov}\left[\mathbf{X}\right] \ \left(\beta^2 \leq 1\right) .$$

Remark 10.2 If we have the natural assumptions of Theorem 10.2 then the obtained model is:

$$\mathrm{E}\left(\mathbf{X} \mid \mathbf{X}_b = \mathbf{x}_b\right) = \mathrm{E}\left(\mathbf{X}\right) + \beta \cdot \left(\mathbf{x}_b - \mathrm{E}\left(\mathbf{X}\right)\right), \ \mathbf{B} = \left(1 - \beta^2\right) \ \mathbf{Cov}\left[\mathbf{X}\right], \quad (10.11)$$

where expectations E(**X**), covariance matrix **Cov**[**X**] are climate statistical parameters!

This result implies that more climate information should be used for the data assimilation! The expectations and the covariance structure of the atmospheric state should be built in the data assimilation model.

In practice the special case $\mathrm{E}\left(\mathbf{X} \mid \mathbf{X}_b = \mathbf{x}_b\right) = \mathbf{x}_b$ i.e. $\mathrm{E}\left(\mathbf{X} \mid \mathbf{X}_b\right) = \mathbf{X}_b$ is assumed implicitly according to the cost function (10.1). Let us assume further the forecast variable $\mathbf{X}_b$ has the same covariance structure as the variable $\mathbf{X}$ of the atmospheric state. Then we have the following unexpected result.

Theorem 10.3 *The conditional expectation of* $\mathbf{X}$*, given* $\mathbf{X}_b$ *is identical with* $\mathbf{X}_b$ i.e. $\mathrm{E}\left(\mathbf{X} \mid \mathbf{X}_b\right) = \mathbf{X}_b$ *and* $\mathbf{Cov}\left[\mathbf{X}_b\right] = \mathbf{Cov}\left[\mathbf{X}\right]$ *if and only if* $\mathbf{X}_b = \mathbf{X}$*, that is the forecast values are always perfect!*

Proof If $\mathrm{E}\left(\mathbf{X} \mid \mathbf{X}_b\right) = \mathbf{X}_b$ and $\mathbf{Cov}\left[\mathbf{X}_b\right] = \mathbf{Cov}\left[\mathbf{X}\right]$ then formulas (10.11) can be used, where $\beta = 1$. Consequently $\mathbf{0} = \mathbf{B} = \mathbf{Cov}\left[\mathbf{X} - \mathrm{E}\left(\mathbf{X} \mid \mathbf{X}_b\right)\right] = \mathbf{Cov}\left[\mathbf{X} - \mathbf{X}_b\right]$ that is possible if and only if $\mathbf{X}_b = \mathbf{X}$ since $\mathrm{E}\left(\mathbf{X} - \mathbf{X}_b\right) = \mathbf{0}$.

10.4.2 Examination of the Structure of Cost Function

At this examination we assume that we have forecasts also for the locations of observations $\mathbf{y}_0$ i.e. $\mathbf{x}_{b,0} \subset \mathbf{x}_b$ and the appropriate atmospheric data are $\mathbf{x}_0 \subset \mathbf{x}$. The appropriate random variables having the realizations $\mathbf{x}_{b,0}$, $\mathbf{x}_0$ are $\mathbf{X}_{b,0} \subset \mathbf{X}_b$, $\mathbf{X}_0 \subset \mathbf{X}$.

Then the difference $\mathbf{y}_0 - \mathbf{x}_0$ can be taken as an observation error vector with the properties

$$\mathrm{E}\left(\mathbf{Y}_0 \mid \mathbf{X} = \mathbf{x}\right) = \mathbf{x}_0, \mathbf{R} = \mathbf{Cov}\left[\mathbf{Y}_0 - \mathrm{E}\left(\mathbf{Y}_0 \mid \mathbf{X}\right)\right] = \mathbf{Cov}\left[\mathbf{Y}_0 - \mathbf{X}_0\right] = \sigma^2\, \mathbf{I},$$

where $\mathbf{I}$ is the identity matrix.

Then according to Eq. (10.8) using the assumptions of Theorem 10.2, the cost function for $\mathbf{x}$ is:

$$J(\mathbf{x}) = \left(\mathbf{x} - \mathrm{E}\left(\mathbf{X} \mid \mathbf{X}_b = \mathbf{x}_b\right)\right)^{\mathrm{T}} \mathbf{B}^{-1} \left(\mathbf{x} - \mathrm{E}\left(\mathbf{X} \mid \mathbf{X}_b = \mathbf{x}_b\right)\right) + \frac{1}{\sigma^2} \|\mathbf{y}_0 - \mathbf{x}_0\|^2, \tag{10.12}$$

where $\mathrm{E}\left(\mathbf{X} \mid \mathbf{X}_b = \mathbf{x}_b\right) = \mathrm{E}\left(\mathbf{X}\right) + \beta \cdot \left(\mathbf{x}_b - \mathrm{E}\left(\mathbf{X}\right)\right)$ and $\mathbf{B} = \left(1 - \beta^2\right)\ \mathbf{Cov}\left[\mathbf{X}\right]$ $\left(\beta^2 < 1\right)$.

Moreover since it can be assumed that $\mathrm{E}\left(\mathbf{Y}_0 \mid \mathbf{X}_0, \mathbf{X}_{b,0}\right) = \mathrm{E}\left(\mathbf{Y}_0 \mid \mathbf{X}_0\right)$, therefore $\mathrm{E}\left(\mathbf{Y}_0 \mid \mathbf{X}_{b,0}\right) = \mathrm{E}\left(\mathrm{E}\left(\mathbf{Y}_0 \mid \mathbf{X}_0, \mathbf{X}_{b,0}\right) \mid \mathbf{X}_{b,0}\right) = \mathrm{E}\left(\mathrm{E}\left(\mathbf{Y}_0 \mid \mathbf{X}_0\right) \mid \mathbf{X}_{b,0}\right) = \mathrm{E}\left(\mathbf{X}_0 \mid \mathbf{X}_{b,0}\right)$ that is:

$$\mathrm{E}\left(\mathbf{Y}_0 \mid \mathbf{X}_{b,0} = \mathbf{x}_{b,0}\right) = \mathrm{E}\left(\mathbf{X}_0 \mid \mathbf{X}_{b,0} = \mathbf{x}_{b,0}\right) = \mathrm{E}\left(\mathbf{X}_0\right) + \beta \cdot \left(\mathbf{x}_{b,0} - \mathrm{E}\left(\mathbf{X}_0\right)\right). \tag{10.13}$$

Then again the analysis is:

$$\mathbf{x}_a = \arg\min_{\mathbf{x}} J(\mathbf{x}). \tag{10.14}$$

The second term of cost function (10.12) is a quality control for $\mathbf{y}_0$, while the first term is an interpolation.

10.4.2.1 Examination of the First Term $\left(\mathbf{x} - \mathrm{E}\left(\mathbf{X} \mid \mathbf{X}_b = \mathbf{x}_b\right)\right)^{\mathrm{T}} \mathbf{B}^{-1} \left(\mathbf{x} - \mathrm{E}\left(\mathbf{X} \mid \mathbf{X}_b = \mathbf{x}_b\right)\right)$

Let us assume for this part of analysis $\mathbf{x}_{a,0} \subset \mathbf{x}_a$ that $\mathbf{x}_{a,0} = \hat{\mathbf{y}}_0$, where $\hat{\mathbf{y}}_0$ is the corrected $\mathbf{y}_0$. Then the solution $\mathbf{x}_a$ given at Eq. (10.14) may be written as:

$$\mathbf{x}_a = \arg\min_{\mathbf{x}} J(\mathbf{x}) = \arg\min_{\mathbf{x} \text{ if } \mathbf{x}_0 = \mathbf{x}_{a,0}} \left(\mathbf{x} - \mathrm{E}\left(\mathbf{X} \mid \mathbf{X}_b = \mathbf{x}_b\right)\right)^{\mathrm{T}} \mathbf{B}^{-1} \left(\mathbf{x} - \mathrm{E}\left(\mathbf{X} \mid \mathbf{X}_b = \mathbf{x}_b\right)\right),$$

that is equivalent with an interpolation:

$$\mathbf{x}_a = \mathrm{E}\left(\mathbf{X} \mid \mathbf{X}_b = \mathbf{x}_b\right) + \mathbf{\Lambda}\left(\mathbf{x}_{a,0} - \mathrm{E}\left(\mathbf{X}_0 \mid \mathbf{X}_{b,0} = \mathbf{x}_{b,0}\right)\right),$$

where coefficient matrix $\mathbf{\Lambda}$ depends on $\mathbf{Cov}[\mathbf{X}]$ according to Eq. (10.12).

This interpolation can be also written as:

$$\mathbf{x}_a = \mathbf{x}_c + \beta \cdot (\mathbf{x}_b - \mathbf{x}_{b,c}) \tag{10.15}$$

where $\mathbf{x}_c$ is the climatological interpolation with predictors $\mathbf{x}_{a,0} = \hat{\mathbf{y}}_0$:

$$\mathbf{x}_c = \mathrm{E}(\mathbf{X}) + \mathbf{\Lambda}\left(\mathbf{x}_{a,0} - \mathrm{E}(\mathbf{X}_0)\right) = \mathrm{E}(\mathbf{X}) + \mathbf{\Lambda}\left(\hat{\mathbf{y}}_0 - \mathrm{E}(\mathbf{X}_0)\right), \tag{10.16}$$

and $\mathbf{x}_{b,c}$ is the same interpolation with predictors $\mathbf{x}_{b,0}$:

$$\mathbf{x}_{b,c} = \mathrm{E}(\mathbf{X}) + \mathbf{\Lambda}\left(\mathbf{x}_{b,0} - \mathrm{E}(\mathbf{X}_0)\right). \tag{10.17}$$

10.4.2.2 Interpolation with Background Information in Climatology

We emphasize the strong relationship with climatology. For example at our software MISH the climatological interpolation module is Eq. (10.16) with quality controlled observations $\hat{\mathbf{y}}_0$, while in case of having background information—e.g. forecast, satellite, radar data—just the interpolation procedure (10.15) is applied using Eqs. (10.16) and (10.17). The necessary interpolation parameters are calculated from modelled values of the statistical parameters $\mathrm{E}(\mathbf{X})$, $\mathbf{Cov}[\mathbf{X}]$, while the coefficient β can be estimated by using the following equality obtained from (10.13):

$$\mathrm{E}\left(\hat{\mathbf{Y}}_0 \mid \mathbf{X}_{b,0} = \mathbf{x}_{b,0}\right) = \mathrm{E}\left(\mathbf{X}_0 \mid \mathbf{X}_{b,0} = \mathbf{x}_{b,0}\right) = \mathrm{E}(\mathbf{X}_0) + \beta \cdot \left(\mathbf{x}_{b,0} - \mathrm{E}(\mathbf{X}_0)\right), \tag{10.18}$$

where $\hat{\mathbf{Y}}_0$ is the random variable of the controlled observations with the realization $\hat{\mathbf{y}}_0$.

10.5 The Problem of Conditional Expectation of Atmospheric State, Given Forecasts

As it was mentioned the identity $\mathrm{E}\left(\mathbf{X} \mid \mathbf{X}_b = \mathbf{x}_b\right) = \mathbf{x}_b$ i.e. $\mathrm{E}\left(\mathbf{X} \mid \mathbf{X}_b\right) = \mathbf{X}_b$ is assumed implicitly at the cost function (10.1) applied in the practice generally. This assumption seems to be doubtful and unrealistic especially in the light of the Theorem 10.3. In addition an interesting counterexample can be constructed

mathematically. Let us assume we have different forecast fields $\mathbf{X}_{b,k}$ with the above property:

$$\mathrm{E}\left(\mathbf{X} \mid \mathbf{X}_{b,k}\right) = \mathbf{X}_{b,k} \quad (k = 1, \ldots K).$$

Let an ensemble prediction be: $\overline{\mathbf{X}}_{b,p} = \sum_{k=1}^{K} p_k \mathbf{X}_{b,k}, \sum_{k=1}^{K} p_k = 1, p_k > 0.$

The expected mean square errors (MSE) are:

$$H_k^2 = \mathrm{E}\left(\|\mathbf{X} - \mathbf{X}_{b,k}\|^2\right), \quad H_p^2 = \mathrm{E}\left(\left\|\mathbf{X} - \overline{\mathbf{X}}_{b,p}\right\|^2\right).$$

Theorem 10.4 *If* $\mathbf{X}_{b,k}$ $(k = 1, \ldots K)$ *are not identical i.e.* $\mathrm{P}\left(\mathbf{X}_{b,1} = ... = \mathbf{X}_{b,K}\right) < 1$ *then*

1. $H_p^2 < \sum_{k=1}^{K} p_k H_k^2$, *consequently if* $H_k^2 = H^2 \quad (k = 1, \ldots K)$ *then* $H_p^2 < H^2$.
2. *But the assumption used generally is not true:* $\mathrm{E}\left(\mathbf{X} \;\middle|\; \overline{\mathbf{X}}_{b,p}\right) \neq \overline{\mathbf{X}}_{b,p}$!

Proof

1. $H_p^2 = \mathrm{E}\left(\left\|\mathbf{X} - \overline{\mathbf{X}}_{b,p}\right\|^2\right) = \mathrm{E}\left(\left\| \sum_{k=1}^{K} p_k \left(\mathbf{X} - \mathbf{X}_{b,k}\right) \right\|^2\right) <$

   $< \mathrm{E}\left(\sum_{k=1}^{K} p_k \|\mathbf{X} - \mathbf{X}_{b,k}\|^2\right) = \sum_{k=1}^{K} p_k H_k^2$, as a consequence of Lemma 10.2 below and Markov inequality, if $\mathbf{X}_{b,k}$ $(k = 1, \ldots K)$ are not identical.
2. If $\mathrm{E}\left(\mathbf{X} \mid \mathbf{X}_{b,k}\right) = \mathbf{X}_{b,k}$ then $\mathrm{E}\left(\mathbf{X}_{b,k}^{\mathrm{T}}\mathbf{X} \mid \mathbf{X}_{b,k}\right) = \mathbf{X}_{b,k}^{\mathrm{T}}\mathrm{E}\left(\mathbf{X} \mid \mathbf{X}_{b,k}\right) = \mathbf{X}_{b,k}^{\mathrm{T}}\mathbf{X}_{b,k}$. Consequently $\mathrm{E}\left(\mathbf{X}_{b,k}^{\mathrm{T}}\mathbf{X}\right) = \mathrm{E}\left(\mathrm{E}\left(\mathbf{X}_{b,k}^{\mathrm{T}}\mathbf{X} \mid \mathbf{X}_{b,k}\right)\right) = \mathrm{E}\left(\mathbf{X}_{b,k}^{\mathrm{T}}\mathbf{X}_{b,k}\right)$. Similarly, if $\mathrm{E}\left(\mathbf{X} \;\middle|\; \overline{\mathbf{X}}_{b,p}\right) = \overline{\mathbf{X}}_{b,p}$ then $\mathrm{E}\left(\overline{\mathbf{X}}_{b,p}^{\mathrm{T}}\mathbf{X}\right) = \mathrm{E}\left(\overline{\mathbf{X}}_{b,p}^{\mathrm{T}}\overline{\mathbf{X}}_{b,p}\right)$. However,

$$\mathrm{E}\left(\overline{\mathbf{X}}_{b,p}^{\mathrm{T}}\mathbf{X}\right) = \mathrm{E}\left(\left(\sum_{k=1}^{K} p_k \mathbf{X}_{b,k}\right)^{\mathrm{T}}\mathbf{X}\right) = \mathrm{E}\left(\sum_{k=1}^{K} p_k \mathbf{X}_{b,k}^{\mathrm{T}}\mathbf{X}\right) = \mathrm{E}\left(\sum_{k=1}^{K} p_k \mathbf{X}_{b,k}^{\mathrm{T}}\mathbf{X}_{b,k}\right) =$$
$$= \mathrm{E}\left(\sum_{k=1}^{K} p_k \|\mathbf{X}_{b,k}\|^2\right) > \mathrm{E}\left(\left\| \sum_{k=1}^{K} p_k \mathbf{X}_{b,k} \right\|^2\right) = \mathrm{E}\left(\overline{\mathbf{X}}_{b,p}^{\mathrm{T}}\overline{\mathbf{X}}_{b,p}\right),$$

as a consequence of the next, well-known Lemma 10.2 and Markov inequality, if $\mathbf{X}_{b,k}$ $(k = 1, \ldots K)$ are not identical, that is a contradiction was obtained.

Lemma 10.2 *Let us suppose* $\overline{\mathbf{z}}_p = \sum_{k=1}^{K} p_k \mathbf{z}_k, \sum_{k=1}^{K} p_k = 1, \; p_k > 0.$

Then $\left\|\overline{\mathbf{z}}_p\right\|^2 \leq \sum_{k=1}^{K} p_k \|\mathbf{z}_k\|^2$ *with equality if and only if* $\mathbf{z}_k = \overline{\mathbf{z}}_p \ \ (k = 1, \ldots K)$.

Proof

$$0 \leq \sum_{k=1}^{K} p_k \left\|\mathbf{z}_k - \overline{\mathbf{z}}_p\right\|^2 = \sum_{k=1}^{K} p_k \left(\|\mathbf{z}_k\|^2 - \mathbf{z}_k^{\mathrm{T}} \overline{\mathbf{z}}_p - \overline{\mathbf{z}}_p^{\mathrm{T}} \mathbf{z}_k + \left\|\overline{\mathbf{z}}_p\right\|^2 \right) =$$
$$= \sum_{k=1}^{K} p_k \|\mathbf{z}_k\|^2 - 2\, \overline{\mathbf{z}}_p^{\mathrm{T}} \overline{\mathbf{z}}_p + \left\|\overline{\mathbf{z}}_p\right\|^2 = \sum_{k=1}^{K} p_k \|\mathbf{z}_k\|^2 - \left\|\overline{\mathbf{z}}_p\right\|^2.$$

10.6 Summary and Conclusion

Referring to Eq. (10.12) we suggest considering the following cost function:

$$J(\mathbf{x}) = (\mathbf{x} - \mathrm{E}(\mathbf{X} \mid \mathbf{X}_b = \mathbf{x}_b))^{\mathrm{T}} [\mathbf{Cov}[\mathbf{X}]]^{-1} (\mathbf{x} - \mathrm{E}(\mathbf{X} \mid \mathbf{X}_b = \mathbf{x}_b)) + \gamma^2 \cdot \|\mathbf{y}_0 - \mathbf{x}_0\|^2,$$

where $\mathrm{E}(\mathbf{X} \mid \mathbf{X}_b = \mathbf{x}_b) = \mathrm{E}(\mathbf{X}) + \beta \cdot (\mathbf{x}_b - \mathrm{E}(\mathbf{X}))$ and $\gamma^2 = \frac{1-\beta^2}{\sigma^2}$, $\left(\beta^2 \leq 1\right)$.

Then the expectation vector E(**X**) and the covariance matrix **Cov**[**X**] are climate statistical parameters that must be modelled by statistical climatological procedures based on long term observed data series. Modelling at least the first two moments of the present climate should be a basic task of the statistical climatology as it is indicated at the second block on Fig. 10.1. As regards the other unknown parameters the coefficient β can be estimated by using $\mathbf{y}_0$ and $\mathbf{x}_{b,0}$ on the basis of the formula (10.13) and it can characterize the quality of the forecast. The estimation of σ can be based on long-term experience related to the expected observation error.

References

1. Lorenc, A.C.: Analysis methods for numerical weather prediction. Q. J. R. Meteorol. Soc. **112**, 1177–1194 (1986)
2. Nodet, M.: Introduction to data assimilation. https://team.inria.fr/moise/files/2012/03/Nodet_Intro_DataAssimilation.pdf (2012)
3. Szentimrey, T., Bihari, Z., Lakatos, M., Szalai, S.: Mathematical, methodological questions concerning the spatial interpolation of climate elements. Időjárás **115**(1–2), 1–11 (2011)
4. Szentimrey, T.: Theoretical questions of daily data homogenization. Időjárás **117**(1), 113–122 (2013)
5. Szentimrey, T.: Manual of homogenization software MASHv3.03, Hungarian Meteorological Service, 70 pp. (2014)

6. Szentimrey, T., Bihari, Z.: Manual of interpolation software MISHv1.03, Hungarian Meteorological Service, 58 pp. (2014)
7. WMO: Data Assimilation in Meteorology and Oceanography: Theory and Practice. A Collection of Papers Presented at the WMO Second International Symposium on Assimilation of Observations in Meteorology and Oceanography, 13–17 March 1995, Tokyo, Japan, J. Meteorol. Soc. Japan, 75, No IB, pp. 496 (1997)

Chapter 11
Ensemble Methods in Meteorological Modelling

Mihály Szűcs, András Horányi, and Gabriella Szépszó

Abstract Numerical modelling is a continuously developing discipline in meteorology, which provides meteorological forecasts and climate change projections based on the numerical solutions of the set of equations describing the processes in the atmosphere and the related spheres. The progress in numerical weather prediction (NWP) and climate modelling has been enormous in the last few decades thanks to the improved theoretical understanding of the meteorological processes, the growing number of observations and the increasing available computer power. In spite of the steady progress, meteorological forecasts cannot be fully perfect due to the intrinsic characteristics of the atmosphere and the climate system. Weather forecast uncertainties exist in initial conditions and in the model formulations themselves and evolve rapidly with lead time. In climate change projections the initial conditions have negligible role, but the internal climate variability and the unknown future evolution of the anthropogenic activity are additional sources of uncertainties. Since they cannot be avoided (just minimized), their representation and quantification are essential tasks both in numerical weather prediction and climate research. Currently the only feasible way to challenge this problem is the ensemble approach, which delivers probabilistic information and attributes uncertainty information to the numerical weather forecasts and climate projections. This additional uncertainty estimation is a valuable bonus for the users and can be efficiently applied in decision-making.

Keywords Climate projections • Ensemble prediction • Probabilistic forecasting • Uncertainty

M. Szűcs (✉) • G. Szépszó
Hungarian Meteorological Service, Kitaibel Pál street 1, 1024 Budapest, Hungary
e-mail: szucs.m@met.hu; szepszo.g@met.hu

A. Horányi
Erdőalja utca 1/C, 2083 Solymár, Hungary
e-mail: Andras.Horanyi@ecmwf.int

MTA-ELTE Numerical Analysis and Large Networks Research Group Budapest, Hungary

A. Bátkai et al. (eds.), *Mathematical Problems in Meteorological Modelling*,
Mathematics in Industry 24, DOI 10.1007/978-3-319-40157-7_11

11.1 Introduction

The main objective of this chapter is to give a general overview of the present state of ensemble forecasting methods based on already existing references. Ensemble approaches applied in short-range and climate time scale are introduced in detail, together with ensemble visualization and interpretation possibilities, which are used at the Hungarian Meteorological Service (HMS).

The present chapter contains five sections. After the introduction, Sect. 11.2 provides a general description of uncertainties in atmospheric weather prediction models and climate models and gives motivation for using probabilistic forecasts. Sect. 11.3 focuses on ensemble designs that are quantifying the previously described uncertainties. Specific techniques are detailed which define different kinds of perturbations in an ensemble system. Section 11.4 represents how operational ensemble systems can be constructed and how ensemble methods can be applied in the practice of climate modelling research. Furthermore, this section gives examples for the interpretation and visualization of ensemble probabilistic products. Section 11.5 is a short summary of the chapter.

11.2 Uncertainties in Numerical Weather Predictions and Climate Projections

Theoretically, the error sources in NWP can be divided into two main groups [39]. First group is called “God-given errors” which refers to the intrinsic chaotic characteristic of the atmosphere and the climate system. Similarly to simple low-dimensional systems described by non-linear equations [30], the atmosphere is also very sensitive to its initial conditions. Small differences in the current initial states can cause large differences among the future ones. In other words, even small uncertainties can grow rapidly and might have significant impact on the weather forecast outputs. Since perfect initial conditions cannot be given, predictability has been always limited in numerical weather predictions. Evolution of the climate system also has sensitivity to its initial state, however, within this initial condition description of the oceans and ice sheets is also included. The other group of errors can be called “man-made errors” which refers to the incomplete human knowledge about the system to be described and technical limitations about its modelling. Numerical models are not perfect counterparts of the Earth system and they contain many approximations, for instance the underlying mathematical equations are solved numerically with temporal and spatial discretization. In practice these two main types of errors cannot be separated and they affect each other in a very complex way.

The initial conditions of NWP models are mostly produced by complex data assimilation methods which are using observations and background information. This background is usually a short-range forecast valid at the analysis time and consequently imperfect. Observations can also contain errors, since there might be

instrument errors or they might not be representative for their vicinity. Additionally, there might be significant spatial and temporal inhomogeneities in the observations. The assimilation algorithms themselves also use approximations providing another source of errors. Specifying initial conditions for climate simulations faces similar challenges, but it requires measurements and background information about the climate system, (e.g., the deep ocean) making the data assimilation procedure even more complex.

Governing model equations are partial differential equations which cannot be solved analytically, thus they are discretized and then solved numerically. Taking the available computer resources into account, the discretization is limited. In spite of the fact that the current supercomputers are extremely powerful, the model grid is still unable to directly resolve all the meteorological phenomena at the desired spatial scales, consequently some of the processes have to be parameterized. These parametrizations can only give an estimation of the net effect of sub-grid scale processes. Models also need lower and upper boundary conditions and their specification can be particularly difficult for the surface. Additionally, in limited area models the proper treatment of lateral boundary conditions (LBCs), which are used to connect the processes inside and outside the regional domain, is non-trivial and a potential source of error. In climate modelling, not only natural processes are represented in approximate way but also human activity has to be taken into account as the forcing factor of future climate change. Anthropogenic activity is quantified in climate model simulations via hypothetic emission scenarios (discussed in Sect. 11.3.3).

It is important to underline that atmospheric predictability is highly varying and affected by the weather situation (Fig. 11.1a, b), meaning that it is higher in stable conditions. It also depends on the forecasted parameter. For instance, 500 hPa geopotential field describes the large synoptic-scale motions and it is more predictable than precipitation, which is influenced by local effects and small-scale phenomena like convection. Although non-hydrostatic models can describe convection explicitly, predictability is overall lower towards smaller scales.

All these uncertainties reveal the necessity of providing not only single-forecasts and single-projections but probabilistic information corresponding to the predictability of the given atmospheric state and limitations of modelling. Since smaller-scale phenomena have lower predictability, the importance of probabilistic forecasts is growing along with the increased model resolution and continuous model improvements.

11.3 Ensemble Methods

Nowadays the only feasible way to produce probabilistic forecasts is to conduct an ensemble of model integrations. In ensemble prediction systems (EPS) not only a single model run predicts the future state, but an ensemble of forecasts gives many possible realizations of the atmospheric (climate) system. The members of

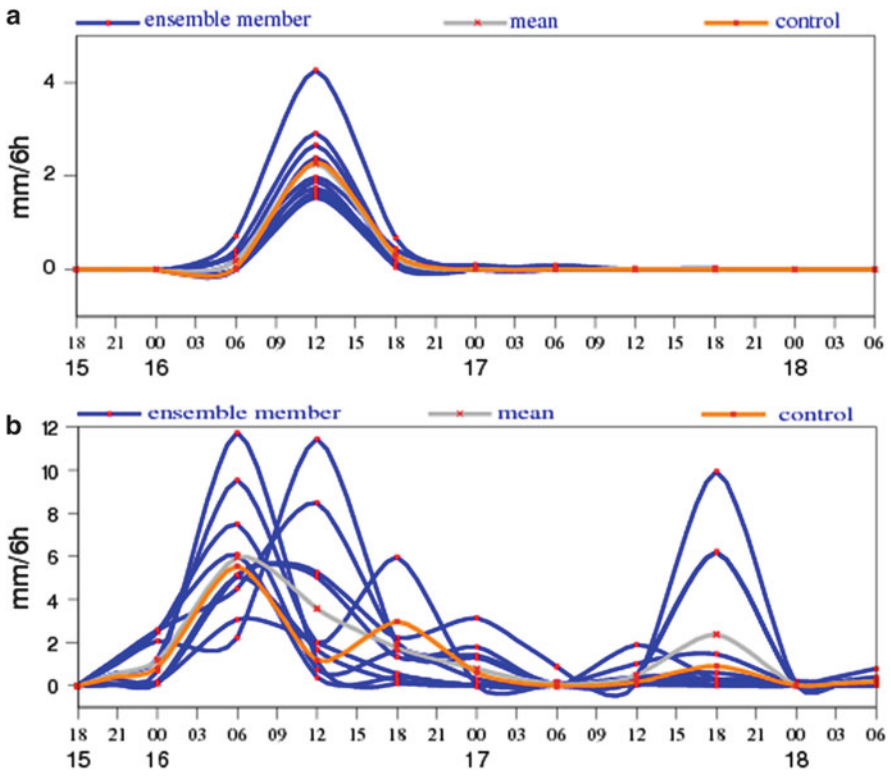

Fig. 11.1 (**a**) An example of the plume diagram from the results of LAMEPS at the HMS. It shows the time evolution of the 6 h total precipitation values predicted by the ensemble members. Forecasts were run at 18UTC 15 March 2014. *Blue curves* belong to the perturbed members while *orange* denotes the control member and *grey* is the ensemble mean. (**b**) The same as (**a**) but forecast was started at 18UTC 15 May 2014

such ensemble in NWP can differ slightly from each other in their initial conditions or model formulations. These small differences are called perturbations and they are supposed to be large enough to produce sufficient ensemble spread within the existing uncertainties. There are many perturbation generation methods that are dedicated for special types of possible uncertainties mentioned in the previous section. These methods are divided into two main groups: the first one focuses on initial condition perturbations (see Sect. 11.3.1), while the second one represents model uncertainties (see Sect. 11.3.2). There are some practical ways to generate ensemble systems, which are detailed in Sects. 11.3.2–11.3.4.

Generally an EPS contains 10–50 members, which would make an enormous computational growth if the high resolution operational model versions were applied in the ensemble system. To avoid this extraordinary cost, a compromise is needed and EPS members run usually at a coarser resolution. The member using unperturbed initial condition and model formulation is called control. Usually EPS

is designed in a way that perturbed initial conditions have a symmetric structure around the control.

Let us present the partial differential equation system of the atmosphere in a very schematic way for the better understanding of the perturbation generation methods detailed in the present section.

$$\begin{aligned} \tfrac{dx}{dt} &= F(x;t) \\ x(t=0) &= x_0 \end{aligned} \tag{11.1}$$

In Eq. (11.1) vector x contains the state variables (e.g., pressure, temperature, wind component, humidity) describing the atmospheric state, $\boldsymbol{F}$ denotes the forecast model and x_0 is the corresponding initial condition of the equation. The model state at time T is the time integral of Eq. (11.1):

$$x(T) = \int_{t=0}^{T} F(x;t)\,dt = \int_{t=0}^{T} (A(x;t) + P(x;t))dt \tag{11.2}$$

In Eq. (11.2) $\boldsymbol{F}$ can be divided into two parts: the explicitly handled non-parameterized ($\boldsymbol{A}$) and the parameterized small-scale processes ($\boldsymbol{P}$). The latter processes are typically convection in non-hydrostatic models, turbulence, microphysics and radiation. This separation is important because the second term ($\boldsymbol{P}$) is more uncertain than the first one ($\boldsymbol{A}$). The unperturbed control member of an ensemble system can be directly described by Eqs. (11.1) and (11.2), while modified equations are needed to explain the various perturbation generation methods.

11.3.1 Initial Condition Perturbations

Historically the first and currently the most commonly used methods to create ensemble prediction systems are perturbing the initial conditions of NWP models. These methods are mostly based on either finding the most unstable perturbations, which are growing fastest during the model forecasts, or determining and quantifying the model initial condition (analysis) error sources. In the next sections the most popular methods are briefly summarized, like the computation of Singular Vectors (SV), the determination of the Breeding Vectors (BV) and the application of the Ensemble of Data Assimilations (EDA) method.

If these methods are applied then the initial condition equation of Eq. (11.1) should be modified with an additional perturbation term. Consequently, the initial condition of an arbitrary j-th ensemble member can be written as

$$x_j(t=0) = x_0 + y_j(t=0)\,. \tag{11.3}$$

Below different ways of defining y_j are explained.

11.3.1.1 Singular Vectors

The computation of singular vectors is one of the first perturbation generation methods and was developed at the European Centre for Medium-Range Weather Forecasts (ECMWF) in the early 1990s [6]. The basic idea is to find such directions of the phase space (defined by the state variables of the model), where perturbations can grow fastest in the early forecast evolution when the linear approximation is still valid, normally the first 12–48 h of the forecast.

Let us consider the system described by Eq. (11.1) and its initial condition perturbation $y(t=0)$ as defined by Eq. (11.3) which will result in the solution $x(t)+y(t)$ at time t. If $y(t)$ is sufficiently small then the Taylor-series of the right-hand-side function $\boldsymbol{F}$ around $x(t)$ can be written as

$$F\left(x(t)+y(t)\right)=F\left(x(t)\right)+\frac{dF}{dX}y(t)+O\left(y^2(t)\right). \tag{11.4}$$

Equations (11.1) and (11.4) can be combined as

$$\frac{d\left(x(t)+y(t)\right)}{dt}=\frac{dx(t)}{dt}+\frac{dF}{dX}y(t)+O\left(y^2(t)\right), \tag{11.5}$$

which can be further simplified into the tangent linear equation considering the linear approximation:

$$\frac{dy(t)}{dt}=\frac{dF}{dX}y(t). \tag{11.6}$$

The general solution of the tangent-linear equation can be also formulated by the propagator matrix (denoted as $\boldsymbol{M}$ in Eqs. (11.7)–(11.11)), which holds the relationship between perturbations at the initial t_0 and final t_1 instants:

$$y\left(t_1\right)=My\left(t_0\right). \tag{11.7}$$

As mentioned above, the main idea of the SV method is to find the fastest growing perturbations in a linear system (so the assumption of linearity is important while considering the SVs). This linear perturbation growth in the $[t_0; t_1]$ time-interval can be quantified with a properly selected norm. For the perturbation growth the ratio described by Eq. (11.8) must be maximized.

$$\frac{\|y\left(t_1\right)\|_E}{\|y\left(t_0\right)\|_E}=\frac{\|My\left(t_0\right)\|_E}{\|y\left(t_0\right)\|_E} \tag{11.8}$$

The proper choice of the norm E is crucial in practice. Note that the norm defined in the initial and final time instants might be different. This norm can be defined in association with an inner product $<;>_E$ as follows:

$$\|y\|_E^2 = \langle y; Ey \rangle_E. \tag{11.9}$$

In Eq. (11.9) $\boldsymbol{E}$ is a positive definite Hermitian matrix. In case of Euclidean norm this $\boldsymbol{E}$ matrix becomes the identity and consequently all the state vector variables are combined with the same weight. The use of Euclidean norm provides an unphysical metric since the state variables with larger units would dominate in the norm, e.g., temperature. Therefore, a norm is desirable which has physical meaning when combining the various model state variables. For instance, the total energy is widely used as a physically sound norm, where the weights are provided according to the contribution of the given variable to the total energy. There are also experiments with CAPE (convective available potential energy) norm in limited area models [42].

It can be noted that the norm might also contain a geographic projection operator calculated over a given area of interest. The definition of such target areas can help to focus e.g. on the tropics, where the perturbations are often improperly represented by the global models [40]. Targeted SVs also allow to focus on such areas where dynamically downscaled limited area ensemble systems run (see in the next section).

If in Eq. (11.9) the size of the initial perturbation $||y(t_0)||_E$ is defined as a unit, then the goal is to find the maximum of $||y(t_1)||_E$. The formula of Eq. (11.9) can be deduced after considering the propagator Eq. (11.7) and transforming the norms into scalar products and using the definition of the adjoint of the propagator matrix $\boldsymbol{M}^*$:

$$\|y(t_1)\|_E^2 = \|My(t_0)\|_E^2 = \langle My(t_0); My(t_0) \rangle_E = \langle M * My(t_0); y(t_0) \rangle_E. \tag{11.10}$$

Equation (11.10) shows that the search of the fastest growing perturbations is equivalent to finding the $v_i(t_0)$ eigenvectors of the $\boldsymbol{M}^*\boldsymbol{M}$ matrix having the largest eigenvalue of ${\sigma_i}^2$:

$$M * Mv_i(t_0) = \sigma_i^2 v_i(t_0). \tag{11.11}$$

The square roots of the ${\sigma_i}^2$ eigenvalues are called singular values and the eigenvectors $v_i(t_0)$ are the singular vectors of $\boldsymbol{M}$. The eigenvectors belonging to the largest eigenvalues show those directions of the phase space, where the perturbations have the largest growth in the $[t_0;t_1]$ time interval based on the E norm. In realistic atmospheric models the dimension of the eigenvalue problem is huge, therefore its solution is non-trivial and it is obtained through special numerical algorithms. In meteorology generally the Lanczos-algorithm is applied [29]. The initial condition perturbations of Eq. (11.3) can be computed as one solution with combining the

largest singular vectors of the different target areas:

$$x_j = x_0 + y_{SV} = x_0 + \sum_{k=1}^{N_{TA}} \sum_{i=1}^{N_{SV}} \alpha_{ki} v_{ki}. \tag{11.12}$$

In Eq. (11.12) N_{TA} is the number of target areas, N_{SV} is the number of used singular vectors and α is a parameter scaling the perturbation to the size of the estimated analysis error.

11.3.1.2 Breeding Method and Kalman Filter

The breeding method [46] was developed in the US simultaneously to the above-mentioned singular vector technique. The main conceptual difference of the breeding method with respect to the singular vectors is that the largest uncertainties are sought in the past (in the assimilation cycle) and not in the near future. This is achieved by "breeding" of past perturbations with retaining only the most unstable ones. The applied procedure is iterative. First, some small, random perturbations are generated and added to the NWP analysis. Then short range numerical forecasts are run based on the unperturbed control and the perturbed initial conditions. The evolution of these initial perturbations is monitored by tracking the differences between the control and perturbed forecasts. Cyclically, these perturbations are rescaled and then added again to a new analysis. After that new forecasts are started from the newly perturbed initial condition and the process restarts. In such an iterative procedure after few steps the system is able "to breed" the necessary perturbations (Fig. 11.2), with selecting the perturbations growing fastest during the assimilation cycle. They can be used for perturbing the model initial conditions and create a forecast ensemble.

The original implementation of the breeding method was built on the top of a data assimilation cycle, so forecast perturbations were rescaled in every 6 h having the same size as in initial time and they were added to a regular analysis. In further tests even longer time periods were applied (12 or 24 h) to find the fastest growing modes

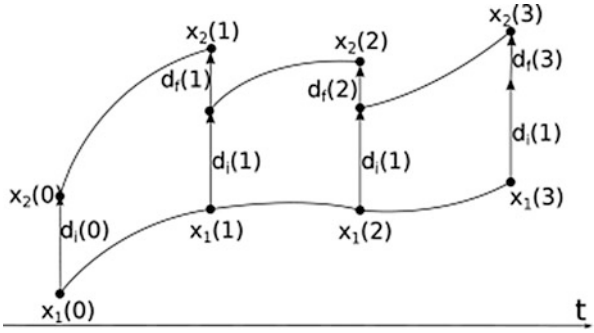

Fig. 11.2 The schematic description of the breeding method in case of two members. x_1 denotes the unperturbed and x_2 the perturbed member, d_i refers to the rescaled perturbations and d_f to the bred perturbations at the end of each breeding cycle

of the perturbations [47]. These tests also underlined the weakness of the method, namely that a globally constant rescaling factor is not able to reflect geographical variation and accuracy of the observing system. One possible solution can be the so called masked breeding method where a latitude and longitude dependent rescaling factor is defined. Although none of the above described breeding method realizations can correctly take into account the forecast error variances.

This problem can be handled by Kalman Filter (KF) based methods. The classic KF concept provides relationship between forecast and analysis error covariances via the linear model, its transposed version and the model error covariance matrix. Such a relationship can help to iteratively evolve the analysis and background error covariance matrices through the data assimilation cycles and take into account flow dependent errors. While the classic KF method is computationally expensive the Ensemble Transform Kalman Filter (ETKF) was introduced. In ETKF a special transformation matrix is defined by the estimation of background error covariance matrix (given by the forecast perturbations of an ensemble system) and the observation error covariance matrix. Such a transformation matrix can be used to upgrade the error covariance matrices in a data assimilation system, but moreover it is possible to use it to transform forecast perturbations into analysis perturbations again [1]. Such a transformation has the advantage against the breeding method that it can reflect the background error variances.

The Ensemble Kalman Filter (EnKF) can be also mentioned as a data assimilation related application of ensemble systems. In EnKF both the forecast and the analysis error covariances are estimated from the spread of the forecast and analysis perturbations, respectively. Unlike to KF, EnKF uses the nonlinear model operator to evolve the analysis state into the forecast state [20].

11.3.1.3 Ensemble of Data Assimilations

The main idea behind the Ensemble of Data Assimilations technique is the simultaneous execution of more data assimilation cycles [24]. The differences among these data assimilation cycles are provided by the quantified uncertainties in the data assimilation system. The knowledge of these uncertainties provides a clue about the realistic error sources of the system and makes possible to compute analysis and short range error statistics. The analysis error statistics can be used to define suitable perturbations to an ensemble prediction system and the short range error statistics can be used for computing the background error covariances for the data assimilation system.

For the better understanding, first we will show how a variational data assimilation system can be formulated by defining a cost function, which measures the deviations of the analysis from the various information sources used in the assimilation process. The solution of the variational problem can be obtained by minimization of a cost function ensuring that the meteorological analysis is optimally near to all the ingredients of the assimilation system taking into account their corresponding reliabilities. The two most important sources of information in

a data assimilation system are the observations and the background fields (short range NWP forecasts valid at the analysis time). The cost function of the variational system can be written as:

$$J(x) = (x - x_b)^T B^{-1} (x - x_b) + (o - H(x))^T R^{-1} (o - H(x)) . \tag{11.13}$$

In Eq. (11.13) x is the model state, $\boldsymbol{B}$ is the background error covariance matrix, x_b is the background state, o contains the observations, $\boldsymbol{R}$ is the observation error covariance matrix and $\boldsymbol{H}$ is the observation operator (which establishes relationship between model space and observation space). The $\boldsymbol{B}$ and $\boldsymbol{R}$ covariance matrices are essential ingredients of the system, providing proper weighting between the observation and background information.

In such data assimilation system considering the linear approximation the analysis update can be defined as follows:

$$\begin{aligned} x_a^k &= x_b^k + K_k \left(o^k - H_k x_b^k\right) \\ x_b^{k+1} &= M_k x_a^k . \end{aligned} \tag{11.14}$$

In Eq. (11.14) superscript k refers to the assimilation cycling and the gain matrix $\boldsymbol{K_k}$ can be written as:

$$K_k = B_k^b H_k^T \left(H_k B_k^b H_k^T + R_k\right)^{-1} . \tag{11.15}$$

In practice the uncertainties taken into account in EDA are related to the observations, to the background fields, to the model formulation and to the lower boundary conditions. In an EDA system, the observations are usually perturbed by a random number η_k drawn from a Gaussian distribution which has zero mean (no systematic errors are assumed) and its standard deviation equals to the estimated standard deviation of the observation error. Consequently, the formula of the perturbed analysis can be written as a modification of Eq. (11.14):

$$\begin{aligned} (\tilde{x})_a^k &= (\tilde{x})_b^k + K_k \left(o^k + \eta_k - H_k (\tilde{x})_b^k\right) \\ \eta_k &\in N(0; R) . \end{aligned} \tag{11.16}$$

The background fields are not explicitly perturbed since they will be automatically different during the assimilation cycles through the evolved perturbations coming from the previous step (Fig. 11.3). Additionally, model uncertainties can be also quantified in the assimilation cycle by perturbing the model formulation ($\boldsymbol{M'}$) and consequently the modified equation of the forecast step of the analysis Eq. (11.14) can be written as:

$$(\tilde{x})_b^{k+1} = M' (\tilde{x})_a^k . \tag{11.17}$$

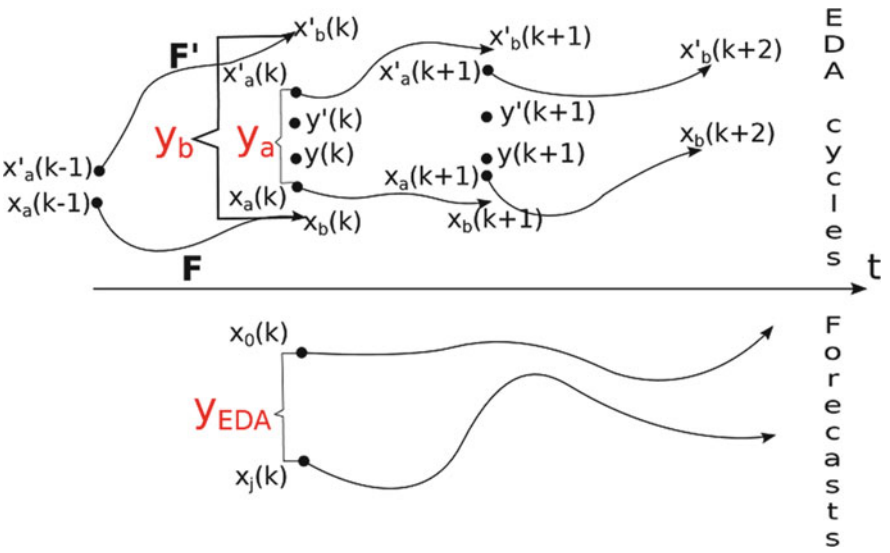

Fig. 11.3 The schematic representation of the Ensemble of Data Assimilations (EDA) system. Only the control member (x) and an arbitrary perturbed member (x′) are visualized with the corresponding unperturbed (y) and perturbed (y′) observations

Model error representation methods will be detailed in Sect. 11.3.2. It has to be noted that boundary condition uncertainties can be taken into account in the above-mentioned forecast step. A possible lower boundary condition perturbation method is described and the perturbed lateral boundary conditions of the limited area models are mentioned in Sect. 11.4.1.

If the $\boldsymbol{R}$ observation error covariance matrix is properly estimated and the perturbed $\boldsymbol{M}'$ model formulation gives back the model errors correctly, then the perturbations of the data assimilation system realistically represent the uncertainties of the system.

$$\begin{aligned} y_a &\equiv \tilde{x}_a - x_a \\ y_b &\equiv \tilde{x}_b - x_b \end{aligned} \tag{11.18}$$

In practice perturbed EPS members can be directly initialized by the perturbed analysis. In this case Eq. (11.3) can be rewritten in a very simple way:

$$x_j = \mathrm{x}_0 + y_{EDA} = x_a + y_a. \tag{11.19}$$

Another possibility is to define EDA perturbations as a difference between the perturbed background fields and their ensemble mean. These perturbations can be added to an analysis, which is produced independently from the EDA system (let us denote as x_A). This procedure has the advantage that this additional analysis can

have better quality (finer resolution or created by a more sophisticated assimilation method) and there is no need to wait for the most recent analysis of the EDA members. In this case the perturbed initial condition of the arbitrary j-th member of an EPS containing N members can be written as:

$$x_j = x_0 + y_{EDA} = x_A + \left(\tilde{x}_j - \overline{x}_b\right) = x_A + \tilde{x}_j - \frac{1}{N}\sum_{i=1}^{N} \tilde{x}_{bi}. \tag{11.20}$$

If the perturbations of EDA are correctly defined using adequate observation and background error statistics then EDA shows those directions of the phase space, where the data assimilation uncertainties are the largest. Therefore these perturbations can effectively contribute to the initial condition perturbations used for an EPS. Some more details of the ECMWF specific application is described in Sect. 11.4.1.

11.3.2 Representation of Model Uncertainties

As already mentioned in Sect. 11.2 there are many sources of uncertainties related to the atmospheric models. Although in principle, inflated initial condition perturbations can partly account for model imperfections, they are not designed for that goal and therefore other methods should be used to represent model-related uncertainties. For that purpose, generally model formulations are not identical for every ensemble member and their variety will result in such perturbations which represent the model uncertainties in an ensemble system. Based on these model formulation differences Eq. (11.2) can be modified for perturbed ensemble members as follows:

$$x_j(T) = \int_{t=0}^{T} F'\left(x_j; t\right) dt. \tag{11.21}$$

In Eq. (11.21) the $\boldsymbol{F}$ forecast model is replaced by its perturbed counterpart $\boldsymbol{F}'$. The multi-model method simply uses more types of models and then combine their results, which means that in Eq. (11.21) $\boldsymbol{F}'$ represents a set of the applied NWP models (see below). Other methods try to identify perturbations from the most uncertain parts of the model, which are the various parameterizations of the sub-grid scale processes. Following this concept the parts of $\boldsymbol{F}'$ can be separated like it was the case in Eq. (11.2).

$$x_j(T) = \int_{t=0}^{T} F'\left(x_j; t\right) dt = \int_{t=0}^{T} \left(A\left(x_j; t\right) + P'\left(x_j; t\right)\right) dt \tag{11.22}$$

In Eq. (11.22) $\boldsymbol{P}'$ represents the perturbed contribution of the parametrization schemes while the contribution of non-parametrized processes $\boldsymbol{A}$ remains unchanged. Similarly to the multi-model method, these perturbations can be generated simply by using more parametrization schemes (multi-physics method, see below) or using the same scheme but with perturbed settings (perturbed parameter method, see below) or applying identical schemes with stochastic modifications in their net contribution (stochastic physics, see below).

11.3.2.1 Multi-Model, Multi-Physics and Perturbed Parameter Method

In current NWP modelling practice there is no superior model, which performing best in all conditions: all models have strengths and weaknesses. Different models are better or worse depending on multiple factors like the current weather situation or forecasted variable for instance. This variety of model performances motivates experts to use several numerical models at the same time and provide information from all of them to the users of forecast and climate model outputs (e.g., forecasters, end users). The integrations of these models can be handled as members of an ensemble system and they can provide information about forecast uncertainty [10]. This ensemble generation method is called multi-model approach which is rather a practical way to express model uncertainties without defining model perturbations in a scientifically rigorous manner. This technique is often applied to estimate uncertainties in climate projections, since running simulations on decadal or longer time frame requires huge computational capacity, especially on global scale. Therefore, climate ensembles are usually created by merging single (or at best a few) climate experiments of individual institutes. Results of the most typical multi-model climate ensemble are published in assessment reports of the Intergovernmental Panel on Climate Change (IPCC; e.g., IPCC AR5 WGI, 2013), however, several ensemble systems composed of regional climate simulations are also available (see Sect. 11.4.1).

It should be mentioned that even inside an NWP model there are more available parameterization schemes which performance is also situation and variable dependent. As already mentioned and described by Eq. (11.22) these parameterized processes are the most uncertain parts of the model formulations and they can be perturbed while non-parameterized processes stay unchanged. A practical way to take into account this uncertainty is provided by multi-physics method where different parameterization schemes are paired to different members of an ensemble system [51].

A practical disadvantage of the multi-model and multi-physics methods is that forecast centres cannot easily maintain many models at the same time or construct large number of equally reliable parametrization schemes and consequently ensure the sufficient ensemble population.

In a well-designed model and parametrization system there are large number of tuning parameters which are empirically defined and their precise tuning is uncertain. The main idea behind the perturbed parameter approach is to keep the

same model and physical parameterization schemes for every ensemble member and perturb only the most uncertain parameters. These parameters can be set differently for all members or their value can vary stochastically between realistic thresholds [8].

11.3.2.2 Stochastic Physics

The original stochastic physics scheme was developed in ECMWF and later it was referred to as BMP scheme [5]. Similarly to the previously described approaches it is supposed that sub-grid scale processes (described by model physics) are more uncertain than the large-scale motions (described by the model dynamics on the model grid). Due to this reason the total contribution of parametrization schemes is perturbed by multiplying its original value with a random number. In this case $\boldsymbol{P}'$ of Eq. (11.22) can be described as follows:

$$P'\left(x_j;t\right) = \left\langle r_j\left(\lambda,\phi,t\right)\right\rangle_{D,T} * P\left(x_j;t\right). \tag{11.23}$$

In the BMP scheme r_j values are uniformly distributed in the $[1-\beta;\ 1+\beta]$ interval. β is an important parameter of the scheme which can control the scale of the perturbation and in practice it is usually set to 0.5. The r_j values are kept constant in several grid boxes over a $D \times D$ large geographical domain and for more time steps over a T time interval. Their typical values vary between some hundreds of kilometers for D and between 3 and 12 h for T. A disadvantage of the BMP scheme is that r_j values are independently picked random numbers which might lead to unphysical spatial and temporal jumpiness in the perturbed tendency fields.

This deficiency is addressed by the revised version of stochastic physics scheme which is called as Stochastically Perturbed Parameterized Tendencies (SPPT) scheme. Its main aim is to ensure well-defined temporal and spatial correlation between the r_j values of the different model grid boxes.

$$P'\left(x_j;t\right) = \left(1+\alpha r_j\right) * P\left(x_j;t\right) \tag{11.24}$$

If the SPPT scheme is applied in spectral models, then r_j fields can be generated in spectral space and then transformed to grid point space where the actual parameterization computations are performed. Therefore r_j is described by spherical harmonics in a spectral global model [38] and by bi-Fourier functions in a spectral limited area model [3]. The r_j field is evolved by a so-called spectral pattern generator where its spectral coefficients $(r_j')_{mn}$ are described by a first order auto-regressive [AR(1)] process which ensures the temporal correlation.

$$\begin{gathered}\left(r_j'\right)_{mn}(t+\Delta t) = \varphi r'_{mn}(t) + \sigma\mu_{mn}(t) \\ \varphi = \exp\left(-\Delta t/\tau\right)\end{gathered} \tag{11.25}$$

In the AR(1) process described by Eq. (11.25) all the new $(r_j')_{mn}$ values are calculated from two parts. The first part is the previous value multiplied by φ which is the one-timestep correlation set by the decorrelation-timescale τ. In the second part μ values are independent random numbers picked from a Gaussian distribution with 0 mean, 1 variance and bounded into the $[-2; 2]$ interval. These values are multiplied by the σ parameter which is responsible for the size of the perturbations and it is (similarly to the original BMP scheme) most commonly set to 0.5. While r_j fields are represented in spectral space, the horizontal correlation of grid-point values are ensured after the spectral transformation. In the spectral pattern generator the so-called space correlation length (L) can control the "smoothness" of r_j fields (Fig. 11.4). In practice horizontal and temporal correlation are set according to the characteristic scale of the errors in the atmospheric processes which is represented by the scheme. There are experiments where two r_j fields are combined [38]: one of them represents fast evolving synoptic-scale errors ($\sigma = 0.5$, $\tau = 6$ h, $L = 500$ km) and the other one represents slow evolving planetary-scale errors ($\sigma = 0.2$, $\tau = 30$ days, $L = 2500$ km).

In Eq. (11.24) α is an additional height-dependent function which can modify the vertical structure of the perturbations. In the recent implementations it is set to

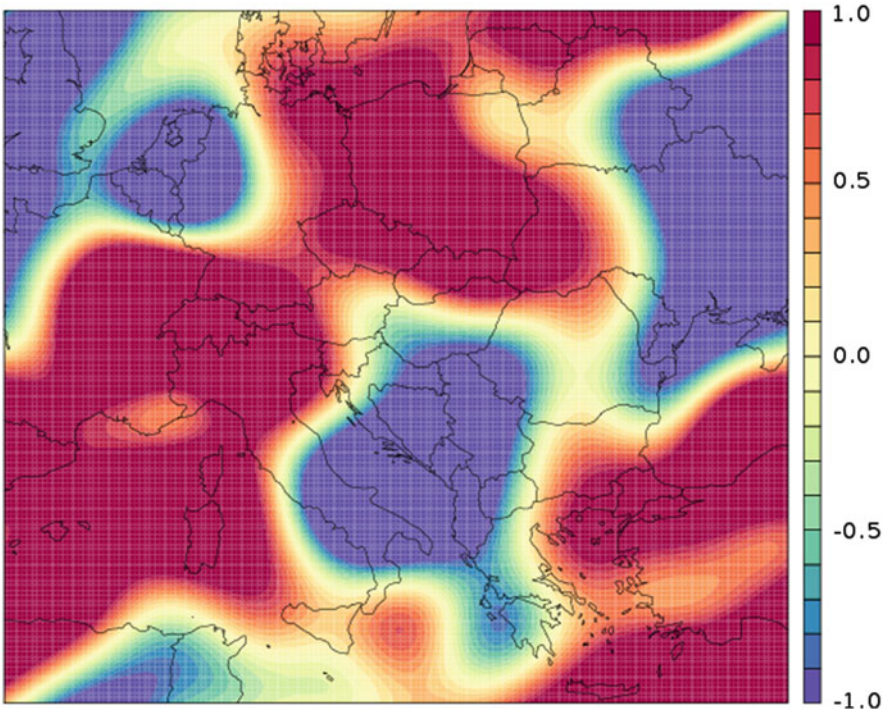

Fig. 11.4 An example for r_j field used in SPPT scheme and evolved by the spectral pattern generator of the ALADIN model. The horizontal correlation length is set to 500 km

1 except near to the surface and near to the model top where it smoothly relaxes to 0. This relaxation is necessary to avoid numerical instabilities coming from inconsistencies between the surface (top of the model) and the perturbed low-level (high-level) atmospheric tendencies. Although experiments are started recently to apply SPPT also in boundary layer [37].

As it is expected and experienced, SPPT scheme is able to improve ensemble systems by ensuring sufficient spread through the model integration by the perturbed model formulations. It can be also noted that its positive impact can be measured in the quality improvement of model climatology (especially in the case of precipitation and in the tropics; [38]). It is related to the fact that SPPT not only takes into account the model uncertainty but it can recover the variety of the sub-grid scale process tendencies which is often hidden by the "deterministic" nature of the parameterization schemes.

11.3.3 Representation of Uncertainties Related to Anthropogenic Activity

On multi-decadal and longer time scales, besides the natural drivers, anthropogenic activity is also an important forcing of the climate system, consequently, climate models must take them into account. Human activity can contribute to the climate change in several ways: e.g., through the emissions of greenhouse gases (GHG) and aerosol particles, land use or demographic change. These effects can be considered in climate models uniquely through meteorological parameters, e.g., via equivalent carbon dioxide concentration as external forcings. An important type of climate simulations is when CO_2 level is changed to a fixed value (e.g., to its double) and the model is run until a new equilibrium. Such an experiment does not provide information about the temporal evolution and the dynamics of climate change, however, it allows exploring (and possibly explaining) the sensitivity of different models to a given radiative forcing.

With the increasing computational capacity, the so-called *transient method* was introduced: climate model integrations are forced with time-dependent atmospheric greenhouse gas and aerosol concentration levels. Transient model runs can simulate a number of important aspects of climate variability, like North Atlantic Oscillation, monsoon systems, El Nino events. Most importantly, it can be applied to study the future climate change trends and their impacts. Time series of concentrations derived by Integrated Assessment Models (IAMs), which calculate GHG concentrations as response to the assumed environmental and economic processes (and vice versa). Since there are several possible pathways of the global future socio-economic developments, the most likely future concentration equivalents can be described only with limitations. Therefore, climate simulations based on these scenarios are called and treated as projections (instead of forecasts).

An important scenario family is SRES (Special Report on Emissions Scenarios; [36]) which consists of four basic scenario sets distinct in assumed global population change and main features of the economic and technological developments from 2001 onwards along the twenty-first century. It was widely applied in global climate model (GCM) experiments providing scientific basis for the third and fourth assessment reports of Intergovernmental Panel on Climate Change [21, 22]. Measurements of the anthropogenic emissions in the last decade urged the need to review the SRES scenarios. The RCP (Representative Concentration Pathways; [35]) scenarios were constructed following a new methodology: using selected pathways of radiative forcings or equivalent CO_2 concentration levels, Earth System Models (i.e., climate models) and IAMs are integrated simultaneously and interactively to estimate the future response of climate and socio-economic conditions to the varying atmospheric and radiative forcings. RCPs cannot be identified with any given socio-economic scenario: they are referred to their radiation forcing value for 2100, which can be resulted along several socio-economic development paths. RCPs have four representative versions depending on their radiative forcing levels considered for 2100 from pre-industrial value (Fig. 11.5). The RCP scenario family has been used in the GCM simulations serving results for [23].

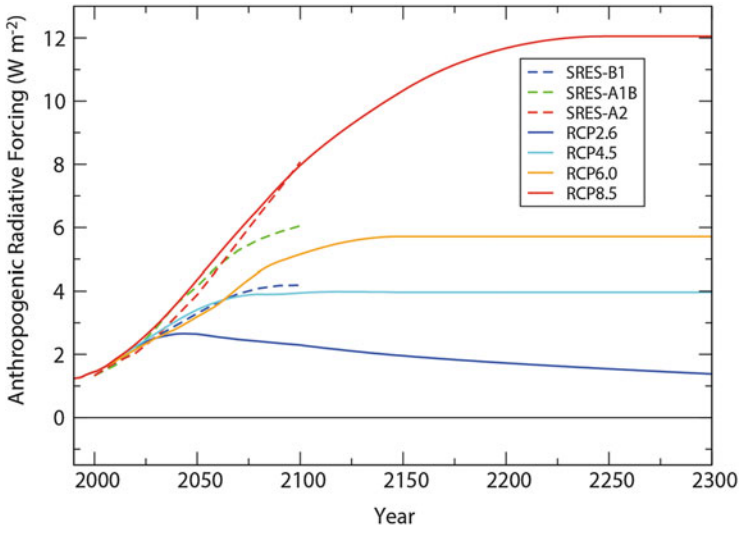

Fig. 11.5 Time evolution of the total anthropogenic radiative forcing relative to pre-industrial (about 1765) level between 2000 and 2300 for RCP scenarios, and SRES scenarios (until 2100) as computed by the Integrated Assessment Modelling Consortium (IAMC) [23]

11.3.4 Other Methods

Multi-model and multi-physics methods have already been described in Sect. 11.3.2. This list can be supplemented with other methods following a similar basic idea. For instance multi-analysis methods start forecasts from various analyses computed by different forecast centres. This technique can be also combined with the multi-model method or with the multi-LBC approach used in limited area ensemble systems, where EPS members can be coupled to different global models [10, 12]. Such multi-LBC methods are addressing uncertainties of the lateral boundary conditions.

Considering that many meteorological services and forecast centres run their own EPS, a logical step can be combining them and generating a more populous ensemble. Such systems are able to represent many types of uncertainties due to the big variety of the applied methods and the large number of EPS members. In practice, the setup of multi-ensembles (ensemble of ensembles) can be technically challenging because of the significant data transfers between forecast centres. In case of limited area ensembles, the different integration domains can add additional difficulties. Due to the mentioned issues multi-ensembles are more used for research and quality control purposes [14].

11.4 Applications of Ensemble Forecasts

In the past decades ensemble systems have become increasingly popular tools to provide probabilistic forecasts and projections both in numerical weather prediction and in climate applications.

The ensemble method was first implemented in medium-range global models (see below). Later many national meteorological services started to run ensembles with their limited area models (LAMEPS) to refine global probabilistic forecasts on a shorter time range and for a smaller area of interest (see below). Recently the focus of research and development is shifted towards the so-called convection-permitting ensembles, where such fine-resolution, non-hydrostatic models are used and are able to resolve deep convection explicitly [12, 34, 50]. The prediction of small-scale meteorological events is very uncertain due to their low predictability. This fact motivates the use of probabilistic forecasts on finer resolution even more.

Adaptation to climate change impacts requires high-cost efforts from the economics and societies. Therefore, credibility of the climate information providing input for these actions has great importance. Due to long-term consequences of the adaptation strategies, the most essential aspect of this credibility is to quantify the uncertainties of climate model simulations. In climate projections targeting multi-decadal and centennial time scales, uncertainties are mainly originated from approximations used in description of physical and anthropogenic processes. It means in practice that climate ensembles are constructed with choosing different anthropogenic scenarios and different climate models. The huge computational

requirements and the limited national resources motivate the international co-operations in establishing climate ensembles. The first climate ensemble system was composed of GCM simulations in 1995. Although limited area models have been used for climate purpose since the 1990s [13], the first ensemble system consisting of regional climate model simulations was organized only in mid-2000s.

11.4.1 Some Examples of Ensemble Systems

11.4.1.1 The ECMWF Ensemble Prediction System

The ECMWF operational Ensemble Prediction System (ENS) produces 51 forecasts (1 control and 50 perturbed members) for the quantification of the forecast uncertainties in the Integrated Forecasting System (IFS). The forecast uncertainties are quantified as the result of initial and model perturbations.

The initial perturbations of the ENS are determined by adding a combination of EDA and SV perturbations to the unperturbed analysis (which is the high resolution ECMWF analysis) described by Eq. (11.26).

$$x_j = x_0 + y_{EDA} + y_{SV} \tag{11.26}$$

EDA perturbations (y_{EDA}) are generated by computing differences between the 6 h EDA forecasts and the EDA mean, like in Eq. (11.20). The 6 h EDA forecasts are chosen since the latest EDA is not yet available at the time of analysis. The SVs are computed by the optimization of the total energy growth in a 48 h time interval using various target areas for the extra-tropics and the tropics. The SVs are linearly combined (see Eq. (11.12)) and the perturbations are scaled to have an amplitude locally similar to the analysis error estimation obtained from 4D-Var (4- dimensional variational data assimilation).

The uncertainties of the lower boundary conditions can be also considered in an ensemble of data assimilation cycles. The method applied in ECMWF generates perturbations with errors correlated with the sea surface temperature fields [49]. Model uncertainties are taken into account by adding stochastic perturbations to the physics parameterization tendencies using SPPT (see Sect. 11.3.2) and Spectral Kinetic Energy Backscatter (SKEB) schemes [38].

11.4.1.2 Limited Area EPS Activity at Hungarian Meteorological Service

The operational regional EPS of the Hungarian Meteorological Service (HMS) is based on the hydrostatic ALADIN model [18] and runs with 8 km horizontal resolution over a continental European domain (Fig. 11.6a). The system has a control and 10 perturbed members which are the dynamical downscaling of the first 11 members of the French global EPS, called PEARP (Prévision d'Ensemble

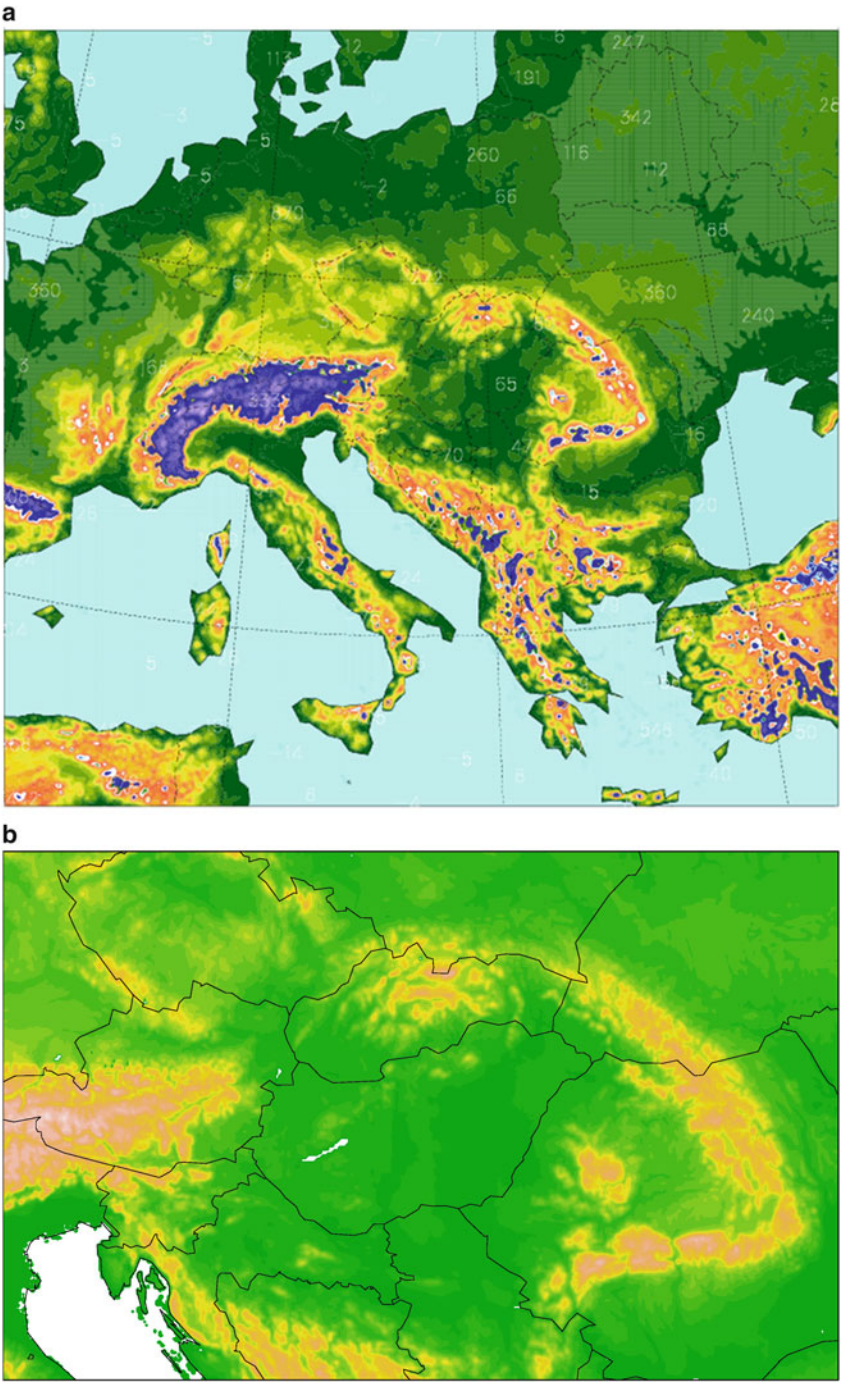

Fig. 11.6 (**a**) ALADIN model domain. (**b**) AROME model domain

ARPEGE). In that global system initial condition perturbations are generated as a combination of EDA and SV perturbations and model uncertainty is taken into account by the multi-physics approach [11]. Global perturbations have impact in the limited area system through the downscaled initial and lateral boundary conditions. The operational LAMEPS can provide useful probabilistic guidance for the forecasters and the end-users as it is shown on some examples in Sect. 11.4.2. Some experiments showed the efficiency of targeted singular vectors which can inject locally efficient perturbations into the global system. These perturbations can also penetrate into the limited area model domain through the downscaling process [15]. The slightly positive impact of an EDA implementation was also shown where only near-surface observations were perturbed in an ensemble of surface optimal interpolations [19].

HMS has also started its convection-permitting ensemble research based on the AROME non-hydrostatic model [41, 44]. Integrations run with 2.5 km horizontal resolution over a domain covering the Carpathian Basin (Fig. 11.6b). Most of the tests were launched (similar to the operational LAMEPS) with 10+1 members coupled to the PEARP or in some cases to the ECMWF's EPS. Such a convection-permitting ensemble system is able to properly describe the small-scale structure of thunderstorms and help in the early warning of hazardous events as will be demonstrated in Sect. 11.4.2.

The EDA scheme was extensively tested and its positive impact was quantified [44]. In the applied configuration 10+1 EDA members were used to initialize the 10+1 EPS members in accordance with Eq. (11.19). During the data assimilation cycles all the observations were perturbed both in atmospheric variational assimilation and in surface optimal interpolation. The quality of the single members were improved by the impact of data assimilation itself and the spread of the ensemble system was increased by the injected initial condition perturbations.

The influence of the SPPT scheme was also examined in AROME-EPS [44]. The parameters of the SPPT scheme were tuned in a way to attribute smaller scale errors to the perturbations which are adequate to the finer model resolution of a non-hydrostatic model ($\sigma = 0.5$, $\tau = 2$ h, $L = 500$ km or 125 km). The impact of the scheme proved to be more neutral than generally in global systems.

11.4.1.3 Coupled Model Intercomparison Projects (CMIPs)

The climate system is composed of atmosphere, hydrosphere, cryosphere, land surface and biosphere, including highly non-linear feedbacks between them. Weather prediction is concentrating primarily on short- and medium-range description of the atmosphere, which is the most well-known and rapidly changing part of the Earth system. Climate models simulate the asymptotic behaviour of the complex climate system, where their components have a variety of adjustment time scales changing from years to hundreds of thousand years. Consequently, response of the climate system to an external forcing can be determined by coupled models, which incorporate mainly atmospheric and ocean model components, simulating not

only the atmospheric and ocean motions but also sea-ice processes and interactions between them. Even though the first realistic atmosphere–ocean general circulation model (AOGCM) experiment dates back to 1975 [31], systematic collection of AOGCM output of leading climate centres was started in mid-1990s by the Working Group on Coupled Modelling of WCRP.[1] Simulations were based on a common protocol in order to establish a database supporting the climate community to study, validate, evaluate and intercompare AOGCM results. While CMIP1[2] [28] and CMIP2 [9] were composed of control runs (i.e., experiments for the past climate with observed forcing) and idealized forcing scenario runs (i.e., experiments with 1 % CO_2 concentration increase per year), respectively, series of realistic climate change simulations were started with CMIP3 [32] in 2005. These model runs described not only the natural forcings for the past, but the future projections were preceded by comprehensive scenario constructions resulted in SRES emission scenarios. Experiments focused on three emission scenarios (SRES A2, A1B and B1), each of them representing a substantially different future pathway of anthropogenic activity (indicating approximately 850, 700, 550 ppm CO_2 concentration by 2100, respectively). Results are freely available in CMIP3 database and provided input to the IPCC Fourth Assessment Report [22]. CMIP3 was followed directly by CMIP5 [45] in 2010; a new numbering was introduced referring to the corresponding IPCC reports (since CMIP5 results served as input for IPCC AR5; [23]). CMIP5 model simulations have already applied RCP scenarios for prescribing future anthropogenic forcings. Experiments addressed three main issues: (1) to assess the scientific background of model differences in carbon cycle and clouds feedbacks, (2) to examine climate predictability on decadal time scales, (3) to identify reasons for different responses produced by similarly forced models. The sixth phase of CMIP [33] is still under design: simulations will be carried out with Earth System models extended with additional model components and their main focus will be on model biases, predictability and uncertainty issues.

11.4.1.4 Ensembles of Regional Climate Model Simulations

The first ensemble of regional climate model simulations in Europe were produced in the PRUDENCE[3] FP5[4] project [7]. The time horizon of the RCM experiments was 2071–2100 and 1961–1990 was chosen as reference. Due to limited computer resources, *time-slice simulations* were achieved, meaning that RCM runs concentrated only on the selected two time frames. This is scientifically sound in regional modelling (especially if the RCM contains exclusively an atmospheric

[1] World Climate Research Programme

[2] First phase of Coupled Model Intercomparison Project

[3] Prediction of Regional scenarios and Uncertainties for Defining EuropeaN Climate change risks and Effects

[4] 5th Framework Programme of European Union

model component), since regional models provide dynamical downscaling of GCM outputs and the downscaled outcomes are basically independent of initial date of the integration. The regional experiments focused on Europe with 50 km horizontal resolution using two largely different SRES emission scenarios (A2 and B2, with approx. 850 and 600 ppm CO_2 concentration levels in 2100, respectively). Contrary to PRUDENCE, in the ENSEMBLES FP6 project (2004–2009) *transient climate simulations* (cf. transient method in Sect. 11.3.3) were accomplished for the period of 1951–2100 covering Europe on 25 km horizontal resolution [48]. The simulations were conducted with various RCMs driven by outputs of various GCMs. More focus was put on precipitation projections: the finer resolution and the improved model features led to better representation of related fine scale structures and temporal distribution [2]. The main target of studies was 2021–2050, and it is known based on Hawkins and Sutton [16, 17] that choice of emission scenario has no significant impact to the range of climate projection uncertainties in this time frame. Therefore, the same scenario forcing was applied in most RCM experiments, which is SRES A1B considered as a medium scenario by the end of the century. Consequently, ensemble of ENSEMBLES represents the model uncertainties, which is of key essence in case of precipitation projections (see also Chap. 12 of Szabó and Szépszó in the same volume, [43]). At the same time, this ensemble was not fully well-balanced, because the majority of the RCMs were driven only by two GCMs. Since lateral boundary conditions have great importance on regional outcomes, over-representation of 1 or 2 selected GCMs in the ensemble may bias the probabilistic information.

Recently, the most important cooperation in regional climate modelling is CORDEX [26], initiated by WCRP in 2009. Its original objective was to cover the poorly researched continents (especially Africa) with high- (12–50 km) resolution regional climate model experiments. Nowadays, CORDEX has lots of branches focusing on different regions of the Earth, for instance EURO-CORDEX [25] for Europe. The unprecedented fine-resolution simulations with most recent climate models show improved performance over Europe with respect to the ENSEMBLES outputs [27]. Forcings and lateral boundary conditions for CORDEX RCM experiments are provided by CMIP5 results using different RCP scenarios. As a result, the CORDEX ensemble represents both model and scenario uncertainties, moreover it makes possible to study the impact of emission scenario families (through inter-comparisons with earlier results obtained by PRUDENCE or ENSEMBLES).

11.4.2 Visualization Methods

In this section some visualization methods are shown which are connected to the above-described applications. The primary aim of these interpretation methods is generally to concisely summarize all the information which is provided by the ensemble members. They can for instance quantify the uncertainty of the

forecasts or represent them in a probabilistic way or underline the likelihood of any meteorological event of interest.

11.4.2.1 Plume Diagram

Plume diagrams have been already referred to in Sect. 11.2 as the demonstration of flow-dependent uncertainty. These plots show the values of a given meteorological variable in all the ensemble members as a function of time for a given geographic location. They are very informative about the growth of the forecast uncertainty and the range of possible future values of a given variable.

The precipitation values predicted by the LAMEPS of the HMS can be compared in a forecast started from 18UTC on 15th of March 2014 (Fig. 11.1a) and in another case, exactly 2 months later (Fig. 11.1b). In the first case a light cold front crossed Hungary which precipitation pattern was rather certain and consequently similar in all the EPS members. In the second case the so-called Yvette storm hit the whole Central European region causing damages by its strong wind gusts and large precipitation amounts. A very complex precipitation field belonged to this cyclone which had low predictability and therefore the ensemble members showed large spread.

Climate projections can also be visualized similarly to the plume diagrams. Figure 11.7 shows the evolution of global mean annual temperature as projected by an ensemble of climate models. The first panel depicts temperature change relative to 1961–1990 based on results of 15 GCM simulations, in which the future CO_2 concentration values were uniquely prescribed according to SRES A1B emission scenario. So the 15 projections were conducted with different global climate models taking the same external forcing into account. The annual mean temperature change is foreseen to be in the ranges of 1.0–2.2 °C by 2050 and 2.2–3.8 °C by 2100. In the second panel of Fig. 11.7, projections are extended with outputs of 30 additional experiments achieved with the same GCMs, but applying two additional SRES emission scenarios, A2 and B1. It can be noticed that uncertainty is growing using significantly different scenarios. This enhancement is not uniform in time, scenario choice has greater impact during the second part of the twenty-first century: the projected interval of mean temperature change does not increase significantly (0.5–2.2 °C) until 2050, while warming is expected to be between 1.7 and 4.5 °C until 2100 considering all the three emission scenarios. This means that in projections for the next few decades there is larger departure between results of simulations obtained with different GCMs but with the same emission scenario than vice versa. (What is not surprising considering that CO_2 concentration levels in different scenarios start to diverge from around 2030.)

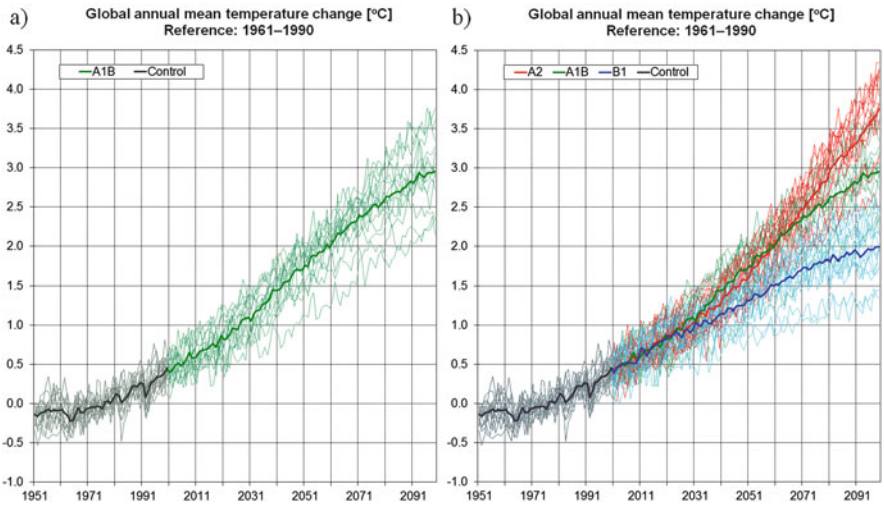

Fig. 11.7 (**a**) Global annual mean temperature change (°C) relative to 1961–1990 based on results of 15 global climate model simulations using SRES A1B emission scenario for description of future anthropogenic activity. (**b**) Same as (**a**), but results are based on 45 global climate model simulations using three different SRES emission scenarios (*red*: A2, *green*: A1B, *blue*: B1). *Thick curves* represent the multi-model means within the given scenarios, *grey and black curves* indicate the results of control runs and their multi-model mean, respectively

11.4.2.2 Probabilistic Map

Probabilities can be computed based on the individual EPS members, where mostly the members are taken into account with equal weight. First a meteorological variable (or a climate parameter) and a corresponding threshold value should be defined; for instance temperature below zero degree (or mean precipitation change over zero percent, i.e., precipitation increase). Then the probability of reaching such a threshold can be calculated from the ensemble members at every point of a given domain. The geographical visualization of those probabilities represents the likelihood of the occurrence of a given meteorological event or a climatological tendency.

Probabilistic maps can draw attention to extreme or dangerous meteorological events. On 14th of March, 2013 the probability of a devastating snowstorm was studied in the LAMEPS of the HMS (see Fig. 11.8). The probability of this event can be defined by the joint probability distribution of more meteorological variables (such as temperature, the amount of fresh snow and wind gust) which provide the necessary conditions for the occurrence of a snowstorm. For every variable a different threshold can be defined and some of their combinations can be used. In this way the probability and strength of such complex weather event can be determined together with its geographic extension. From the top left panel to the bottom right panel of Fig. 11.8 the thresholds of fresh snow amount and wind gust

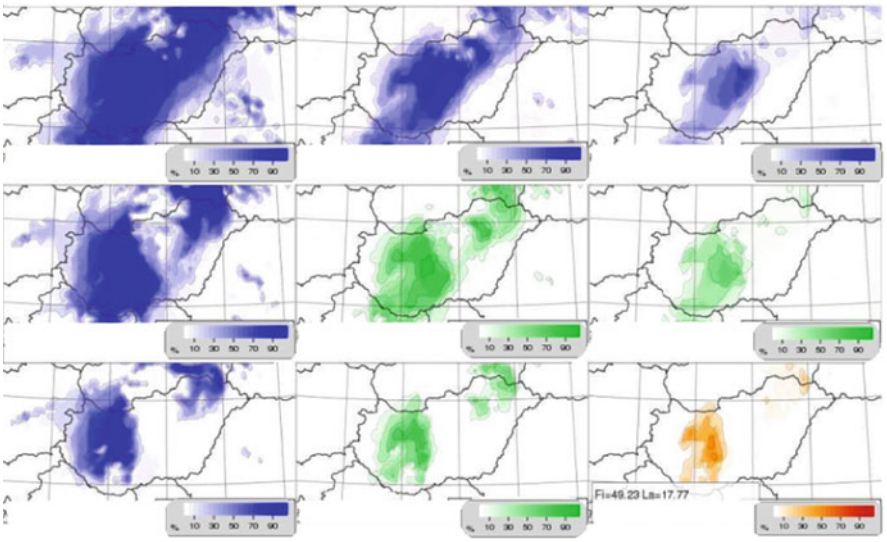

Fig. 11.8 Probability of devastating snowstorm defined as joint probability reaching given thresholds for temperature, fresh snow and wind gust. On all the maps the threshold of temperature was set to 0°, while the amount of fresh snow in 12 h is increasing from *left* to *right* (5, 10, 15 cm) and wind gust is increasing from *top* to *bottom* (10, 15, 20 m/s). *Colors* refer to the level of the threat and *orange* shows the probability of reaching the highest thresholds. Figures were drawn from a 12h forecast of LAMEPS run at 18UTC 14 March 2013

values increase, i.e., the joint probabilities show the likelihood of conditions with increased threat.

A probabilistic map can also be used in climate applications and its construction is based on the same methodology. Nevertheless, one has to be careful with interpreting this information in the same way as in weather prediction: while ensemble members in NWP represent equally likely forecasts, this cannot be considered for climate projections. In long-term projections, uncertainty due to scenario-type description of anthropogenic activity becomes more and more important with increasing lead time. However, probabilities cannot be associated to these scenarios, since future aspects of human activity strongly depend on socio-economic decisions and cannot be specified with any accuracy [4]. Consequently, the resulted projections are evaluated rather as *possible* (instead of *probable*) outcomes with given conditions. Figure 11.9 was created using results of 17 RCM simulations of ENSEMBLES, each of them applied 25 km horizontal resolution and the A1B emission scenario. Percentage values correspond to the ratio between the numbers of model experiments producing winter mean precipitation increase and decrease from 1961–1990 to 2021–2050. Assuming A1B emission pathway as realistic and probable emission pathway, it can be stated that probability of winter mean precipitation increase exceeds 70 % North from Hungary, whereas in Southern and Eastern Europe increase and decrease are equally likely.

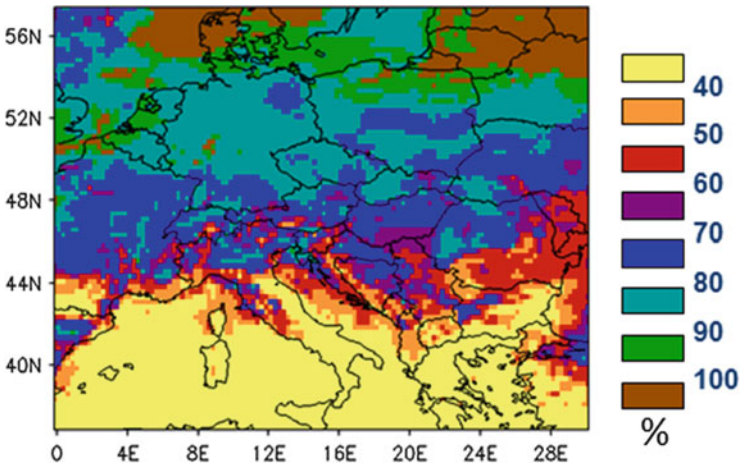

Fig. 11.9 Probability of winter mean precipitation increase (%) for 2021–2050 with respect to 1961–1990 based on results of 17 RCM experiments available in ENSEMBLES database

11.4.2.3 Stamp Diagram

It is possible to visualize all the ensemble members next to each other for a given meteorological variable. These diagrams cannot be informative about the details but they are able to warn forecasters on the possibility of hazardous weather, even if it appears only in a limited number of members.

As it was already mentioned the predictability of such small-scale phenomena like thunderstorms is rather low but at the same time they might mean risk in terms of disaster management. That was the case on the evening of 20th of August, 2013 when several events with mass public participation were held in Hungary and which were threatened by the convective activity. In the test version of convection-permitting EPS of HMS (AROME-EPS, see Sect. 11.4.1) almost all the members predicted thunderstorms with small-scale structure (Fig. 11.10). While the existence of precipitation seemed very certain its localization and intensity showed a large variability from member to member. Stamp diagram can easily warn the decision-makers if any of the members predicts hazardous thunderstorm for a given area and possibly suggest the cancellation or postponement of an event.

11.5 Summary

In this work the recent ensemble approaches have been reviewed both in the numerical weather prediction and climate projection fields. The uncertainties of atmospheric and Earth system modelling were underlined giving the motivation for using probabilistic forecasts. Ensemble methods were presented as the only feasible

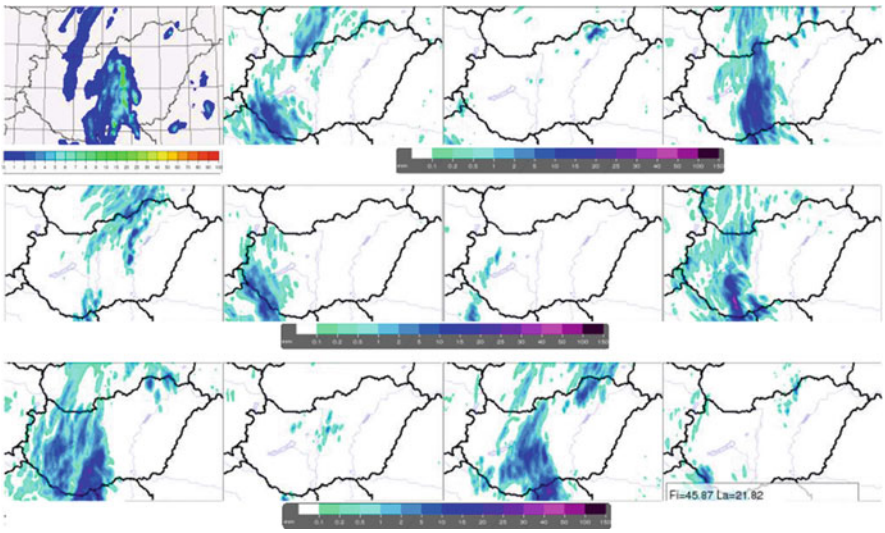

Fig. 11.10 The stamp diagram of forecast for 3-h precipitation amount between 21 UTC on 20th and 00UTC on 21st of August, 2013. *Top left panel* shows precipitation estimated from radar measurements, while *other panels* represent the members of convection-permitting ensemble system tested at the HMS (AROME-EPS)

way to get probabilistic information, meaning not only a single but an ensemble of model runs are taken into account.

The key issue in ensemble prediction systems is how differences between the members of an ensemble are defined. Various methods can perturb the initial conditions of the atmosphere, while other methods can represent the model formulation uncertainties. In climate projections, the initial state of the system is less important, but anthropogenic activity is an additional source of uncertainty taken into account through different emission scenarios.

Some examples have been given how the described ensemble approaches can be used in NWP and climate projection systems. It was noted that despite the recent model improvements, uncertainties cannot be neglected. As the resolution of the applied models is getting finer, the smaller-scale motions are resolved explicitly in the dynamical equations. Predictability of these motions is also limited resulting that probabilistic forecasts will be important in the future.

Acknowledgments We were delighted to have a possibility to contribute in the present volume of European Consortium for Mathematics in Industry. We are very thankful to the editors for their patient cooperation. We appreciate the report and suggestions of the reviewer of the chapter. We are very grateful to our colleagues at the Hungarian Meteorological Service and especially to *Péter Szabó* for his careful English review.

References

1. Bishop, C.H., Etherton, B.J., Majumdar, S.: Adaptive sampling with the ensemble transform Kalman filter. Part I: theoretical aspects. Mon. Weather Rev. **129**, 420–436 (2001)
2. Boberg, F., Berg, P., Thejll, P., Gutowski, W.J., Christensen, J.H.: Improved confidence in climate change projections of precipitation further evaluated using daily statistics from ENSEMBLES models. Clim. Dyn. **35**, 1509–1520 (2010)
3. Bouttier, F., Vié, B., Nuissier, O., Raynaud, L.: Impact of stochastic physics in a convection-permitting ensemble. Mon. Weather Rev. **140**, 3706–3721 (2012)
4. Bray, D., von Storch, H.: 'Prediction' or 'projection'? The nomenclature of climate science. Sci. Commun. **30**, 534–543 (2009). doi:10.1177/1075547009333698
5. Buizza, R., Miller, M., Palmer, T.N.: Stochastic representation of model uncertainties in the ECMWF Ensemble Prediction System. Q. J. R. Meteorol. Soc. **125**, 2887–2908 (1999)
6. Buizza, R., Palmer, T.N.: The singular-vector structure of the atmospheric global circulation. J. Atmos. Sci. **52**, 1434–1456 (1995)
7. Christensen, J.H., Carter, T.R., Rummukainen, M., Amanatidis, G.: Evaluating the performance and utility of climate models: the PRUDENCE project. Clim. Chang **81** (PRUDENCE Special Issue), 1–6 (2007)
8. Christensen, H.M., Moroz, I.M., Palmer, T.N.: Stochastic and perturbed parameter representations of model uncertainty in convection parameterization. J. Atmos. Sci. **72**, 2525–2544 (2015)
9. Covey, C., Achuta Rao, K.M., Cubasch, U., Jones, P., Lambert, S.J., Mann, M.E., Phillips, T.J., Taylor, K.E.: An overview of results from the Coupled Model Intercomparison Project (CMIP). Global Planet. Change **37**, 103–133 (2003)
10. García-Moya, J.-A., Callado, A., Escribá, P., Santos, C., Santos-Munoz, D., Simarro, J.: Predictability of short-range forecasting: a multimodel approach. Tellus A **63**, 550–563 (2011)
11. Descamps, L., Labadie, C., Joly, A., Bazile, E., Arbogast, P., Cébron, P.: PEARP, the Météo-France short-range ensemble prediction system. Q. J. R. Meteorol. Soc. **140**, 846–854 (2014). doi:10.1002/qj.2469
12. Gebhardt, C., Theis, S., Krahe, P., Renner, V.: Experimental ensemble forecasts of precipitation based on a convection-resolving model. Atmos. Sci. Lett. **9**, 67–72 (2008)
13. Giorgi, F., Bates, G.: The climatological skill of a regional model over complex terrain. Mon. Weather Rev. **117**, 2325–2347 (1989)
14. Hagedorn, R., Buizza, R., Hamill, T.M., Leutbecher, M., Palmer, T.N.: Comparing TIGGE multimodel forecasts with reforecast-calibrated ECMWF ensemble forecasts. Q. J. R. Meteorol. Soc. **138**, 1814–1827 (2012). doi:10.1002/qj.1895
15. Hágel, E., Horányi, A.: The ARPEGE/ALADIN limited area ensemble prediction system: the impact of global targeted singular vectors. Meteorol. Z. **16**(6), 653–663 (2007)
16. Hawkins, E., Sutton, R.: The potential to narrow uncertainty in regional climate predictions. Bull. Am. Meteorol. Soc. **90**, 1095–1107 (2009)
17. Hawkins, E., Sutton, R.: The potential to narrow uncertainty in projections of regional precipitation change. Clim. Dyn. **37**, 407–418 (2011)
18. Horányi, A., Kertész, S., Kullmann, L., Radnóti, G.: The ARPEGE/ALADIN mesoscale numerical modeling system and its application at the Hungarian Meteorological Service. Időjárás **110**, 203–227 (2006)
19. Horányi, A., Mile, M., Szűcs, M.: Latest developments around the ALADIN operational short-range ensemble prediction system in Hungary. Tellus **63A**, 642–651 (2011)
20. Houtekamer, P.L., Mitchell, H.L.: Ensemble Kalman filtering. Q. J. R. Meteorol. Soc. **131**, 3269–3289 (2005)
21. Houghton, J.T., Ding, Y., Griggs, D.J., Noguer, M., van der Linden, P.J., Dai, X., Maskell, K., Johnson, C.A. (eds.): IPCC TAR WGI: Climate Change 2001: The Scientific Basis. Contribution of Working Group I to the Third Assessment Report of the Intergovernmental Panel on Climate Change. Cambridge University Press, Cambridge, United Kingdom and New York, NY, USA, 881 p. (2001)

22. Solomon, S., Qin, D., Manning, M., Chen, Z., Marquis, M., Averyt, K.B., Tignor, M., Miller, H.L. (eds.): IPCC AR4 WGI: Climate Change 2007: The Scientific Basis. Contribution of Working Group I to the Fourth Assessment Report of the Intergovernmental Panel on Climate Change. Cambridge University Press, Cambridge, 946 p. (2007)
23. Stocker, T.F., Qin, D., Plattner, G.-K., Tignor, M., Allen, S.K., Boschung, J., Nauels, A., Xia, Y., Bex, V., Midgley, P.M. (eds.): IPCC AR5 WGI: Climate Change 2013: The Physical Science Basis. Contribution of Working Group I to the Fifth Assessment Report of the Intergovernmental Panel on Climate Change. Cambridge University Press, Cambridge, United Kingdom and New York, NY, USA, 1535 p. (2013)
24. Isaksen, L., Bonavita, M., Buizza, R., Fisher, M., Haseler, J., Leutbecher, M., Raynaud, L.: Ensemble of Data Assimilations at ECMWF. Tech. Rep. ECMWF RD Tech. Memo. **636**, 45 p. (2010)
25. Jacob, D., Petersen, J., Eggert, B., Alias, A., Christensen, O.B., Bouwer, L.M., Braun, A., Colette, A., Déqué, M., Georgievski, G., Georgopoulou, E., Gobiet, A., Nikulin, G., Haens-ler, A., Hempelmann, N., Jones, C., Keuler, K., Kovats, S., Kröner, N., Kotlarski, S., Kriegsmann, A., Martin, E., van Meijgaard, E., Moseley, C., Pfeifer, S., Preuschmann, S., Radtke, K., Rechid, D., Rounsevell, M., Samuelsson, P., Somot, S., Soussana, J.F., Teich-mann, C., Valentini, R., Vautard, R., Weber, B.: 2014: EURO-CORDEX: new high-resolution climate change projections for European impact research. Reg. Environ. Chang. **14**, 563–578 (2013)
26. Jones, C., Giorgi, F., Asrar, G.: The Coordinated Regional Downscaling Experiment: CORDEX. An international downscaling link to CMIP5. CLIVAR Exchanges **56**, 16 (2), 34–40 (2011)
27. Kotlarski, S., Keuler, K., Christensen, O.B., Colette, A., Déqué, M., Gobiet, A., Goergen, K., Jacob, D., Lüthi, D., van Meijgaard, E., Nikulin, G., Schär, C., Teichmann, C., Vautard, R., Warrach-Sagi, K., Wulfmeyer, V.: Regional climate modelling on European scales: A joint standard evaluation of the EURO-CORDEX RCM ensemble. Geosci. Model Dev. **7**, 1297–1333 (2014)
28. Lambert, S.J., Boer, G.J.: CMIP1 evaluation and intercomparison of coupled climate models. Clim. Dyn. **17**(2–3), 83–106 (2001)
29. Lanczos, C.: Applied Analysis. Prentice-Hall, Englewood Cliffs, NJ, USA, 539 p. (1956). Reprinted by Dover New York, 1988, ISBN 0-486-65656-X
30. Lorenz, E.: Deterministic nonperiodic flow. J. Atmos. Sci. **20**, 130–142 (1963)
31. Manabe, S., Wetherald, R.T.: The effects of doubling the CO_2-concentration on the climate of a general circulation model. J. Atmos. Sci. **32**, 3–15 (1975)
32. Meehl, G.A., Covey, C., Delworth, T., Latif, M., McAvaney, B., Mitchell, J.F.B., Stouffer, R.J., Taylor, K.E.: The WCRP CMIP3 multi-model dataset: a new era in climate change research. Bull. Am. Meteorol. Soc. **88**, 1383–1394 (2007)
33. Meehl, G.A., Moss, R., Taylor, K.E., Eyring, V., Stouffer, R.J., Bony, S., Stevens, B.: Climate model intercomparison: preparing for the next phase. EOS Trans. Am. Geophys. Union **95**, 77–78 (2014)
34. Migliorini, S., Dixon, M., Bannister, R., Ballard, S.: Ensemble prediction for nowcasting with a convection-permitting model. I: description of the system and the impact of radar-derived surface precipitation rates. Tellus **63A**, 468–496 (2011)
35. Moss, R.H., Edmonds, J.A., Hibbard, K.A., Manning, M.R., Rose, S.K., van Vuuren, D.P., Carter, T.R., Emori, S., Kainuma, M., Kram, T., Meehl, G.A., Mitchell, J.F.B., Nakicenovic, N., Riahi, K., Smith, S.J., Stouffer, R.J., Thomson, A.M., Weyant, J.P., Wilbanks, T.J.: The next generation of scenarios for climate change research and assessment. Nature **463**, 747–756 (2010)
36. Nakicenovic, N., Alcamo, J., Davis, G., de Vries, B., Fenhann, J., Gaffin, S., Gregory, K., Grübler, A., Jung, T.Y., Kram, T., La Rovere, E.L., Michaelis, L., Mori, S., Morita, T., Pepper, W., Pitcher, H., Price, L., Raihi, K., Roehrl, A., Rogner, H. H., Sankovski, A., Schlesinger, M., Shukla, P., Smith, S., Swart, R., van Rooijen, S., Victor, N., Dadi, Z.: IPCC Special Report on Emissions Scenarios. Cambridge University Press, Cambridge (2000)

37. Ollinaho, P., Leutbecher, M., Beljaars, A., Sandu, I.: Stochastic parametrization of boundary layer processes in ENS. EMS Annual Meeting Abstracts **12**, EMS2015-224 (2015)
38. Palmer, T.N., Buizza, R., Doblas-Reyes, F., Jung, T., Leutbecher, M., Shutts, G., Steinheimer, M., Weisheimer, A.: Stochastic parametrization and model uncertainty. Tech. Rep., ECMWF Tech. Memo. **598**, 42 p. (2009)
39. Palmer, T.N., Tibaldi, S.: On the prediction of forecast skill. Mon. Weather Rev. **116**, 2453–2480 (1988)
40. Puri, K., Barkmeijer, J. Palmer, T.N.: Ensemble prediction of tropical cyclones using targeted diabatic singular vectors. ECMWF Tech. Memo. **298**, 31 p. (1999)
41. Seity, Y., Brousseau, P., Malardel, S., Hello, G., Bénard, P., Bouttier, F., Lac, C., Masson, V.: The AROME-France convective-scale operational model. Mon. Weather Rev. **139**, 976–991 (2011)
42. Stappers, R., Barkmeijer, J.: HIRLAM CAPE singular vectors. HIRLAM Newsl. **54**, 76–80 (2008)
43. Szabó, P., Szépszó, G.: Quantifying sources of uncertainty in temperature and precipitation projections over different parts of Europe. In: Mathematical problems in meteorological modelling, pp. 239–261. Springer, Heidelberg (2016)
44. Szintai, B., Szűcs, M., Randriamampianina, R., Kullmann, L.: Application of the AROME non-hydrostatic model at the Hungarian Meteorological Service: physical parameterizations and ensemble forecasting. Időjárás **119**, 241–266 (2015)
45. Taylor, K.E., Stouffer, R.J., Meehl, G.A.: An overview of CMIP5 and the experiment design. Bull. Am. Meteorol. Soc. **93**, 485–498 (2012). doi:10.1175/BAMS-D-11-00094.1
46. Toth, Z., Kalnay, E.: Ensemble forecasting at NMC: the generation of perturbations. Bull. Am. Meteorol. Soc. **74**, 2317–2330 (1993)
47. Toth, Z., Kalnay, E.: Ensemble forecasting at NCEP and the breeding method. Mon. Weather Rev. **125**, 3297–3319 (1997)
48. van der Linden P., Mitchell, J.F.B. (eds.): ENSEMBLES: Climate Change and Its Impacts: Summary of Research and Results from the ENSEMBLES Project. Met Office Hadley Centre, Exeter, United Kingdom, 160 p. (2009)
49. Vialard, J., Vitart, F., Balmaseda, M., Stockdale, T., Anderson, D.: An ensemble generation method for seasonal forecasting with an ocean-atmosphere coupled model. Mon. Weather Rev. **133**, 441–453 (2005)
50. Vié, B., Nuissier, O., Ducrocq, V.: Cloud-resolving ensemble simulations of Mediterranean heavy precipitating events: uncertainty on initial conditions and lateral boundary conditions. Mon. Weather Rev. **139**, 403–423 (2011)
51. Wang, Y., Bellus, M., Wittmann, C., Steinheimer, M., Weidle, F., Kann, A., Ivatek-Šahdan, S., Tian, W., Ma, X., Tascu, S., Bazile, E.: The Central European limited-area ensemble forecasting system: ALADIN-LAEF. Q. J. R. Meteorol. Soc. **137**, 483–502 (2011). doi:10.1002/qj.751

Chapter 12
Quantifying Sources of Uncertainty in Temperature and Precipitation Projections over Different Parts of Europe

Péter Szabó and Gabriella Szépszó

Abstract In this study, uncertainties emerging from natural climate variability, the description of physical processes in models and future anthropogenic activity are quantified for mean temperature and precipitation projections over various regions in Europe. Results of global climate models from CMIP3 dataset were used for 1951–2100 with SRES emission scenarios over the twenty-first century. We are concentrating on three main issues: (1) fractions of total uncertainty and its seasonal variation over the Carpathian Basin, Northern and Southern Europe; (2) limitations in theoretically reducible uncertainty through model development; (3) quantifying the ratio of projected change and total uncertainty (signal-to-noise ratio, when results are significant) and time horizons when changes exceed natural variability (time of emergence, when major impacts happen more likely). Internal variability is the dominant uncertainty factor for the Carpathian Basin, especially in winter due to the intensive circulation activity. Scenario uncertainty has lower impact for the Carpathian Basin than for Northern and Southern Europe, where it has importance for temperature results in the second half of the century. For precipitation, emission scenarios are less meaningful. Fraction of model uncertainty is continuously growing by 2100, especially for precipitation. The smaller the area, the later the mean temperature change surpasses total uncertainty. Signal-to-noise ratio is not significant for precipitation projections over Southern Europe and Carpathian Basin, and over Northern Europe it is only for winter and spring. Seasonal temperature changes exceed natural variability between 2020 and 2045 for the Carpathian Basin, and one-two decades earlier over Northern and Southern Europe. Precipitation projections do not emerge from natural variability over the Carpathian Basin; they do only in summer over Southern Europe, and all the other seasons over Northern Europe by the end of the century.

Keywords Global climate projections • Internal variability • Model uncertainty • Scenario uncertainty • Signal-to-noise • Time of emergence

P. Szabó (✉) • G. Szépszó
Regional Climate Modelling Group, Kitaibel Pál street 1, H-1024 Budapest, Hungary
e-mail: szabo.p@met.hu; szepszo.g@met.hu

A. Bátkai et al. (eds.), *Mathematical Problems in Meteorological Modelling*,
Mathematics in Industry 24, DOI 10.1007/978-3-319-40157-7_12

12.1 Introduction

The establishment of an ensemble of global climate model (GCM) results was initiated in the 1990s: the Working Group on Coupled Modelling of WCRP[1] elaborated a common simulation protocol in order to build up a database from atmosphere–ocean general circulation model (AOGCM) outputs of leading climate centers. The main objective of CMIP[2] was to support the climate researchers to study and compare the AOGCM results. CMIP3 [16] was the first in the CMIP phases where future simulations were based on a variety of emission scenarios allowing to assess the impact of different socio-economic pathways and possible future evolution of climate change.

The quantification of uncertainties has been naturally a key focus of climate modelling research since the construction of the first ensemble of global climate model results. Focusing on CMIP3 data, Hawkins and Sutton [7] carried out a comprehensive analysis for temperature projections based on 15 coupled models and 3 different SRES[3] emission scenarios [19]. They quantified uncertainties as from three independent sources: (1) internal variability existing in climate system without any external forcing; (2) model uncertainty resulting by different formulation of climate models; (3) scenario uncertainty due to various greenhouse gas emission pathways used for description of future anthropogenic activity. The main conclusions of Hawkins and Sutton were as follows: (1) decadal internal variability and model uncertainty are the competing leading uncertainty factor in projections for the next decades, particularly on continental scales, whereas the role of the scenario uncertainty starts to increase in the second half of the twenty-first century; (2) GCMs provide valuable temperature projections over most investigated region measured quantitatively by the ratio of decadal-averaged climate change signal and total uncertainty. A similar assessment was done for precipitation projections [8] indicating that they have different uncertainty characteristics as found for temperature. The main difference is the low impact of emission scenario choice, which is especially minor on continental scale. Consequently, uncertainties in precipitation projections are chiefly caused by decadal internal variability and model uncertainty (in the latter case by the parameterization schemes applied for description of precipitation-related physical processes; [6]). The background of internal variability and the role of internally versus externally forced climate change was extensively discussed by Deser et al. [3]. It is found based on the CMIP3 multi-model ensemble that internal variability accounts for at least half of the inter-model spread in projected climate trends before 2060s and forced (i.e., scenario-driven) changes can be detected earlier in temperature than in atmospheric circulation and precipitation. The dominant source of natural variability is the coupled ocean–atmosphere variability in the

[1] World Climate Research Programme

[2] Coupled Model Intercomparison Project

[3] Special Report on Emissions Scenarios

tropics and the internal atmospheric variability associated with the annular modes of circulation variability in the extratropics. Further studies [1, 4] proved that role of natural variability is varying over different geographical regions and there are areas with low climate predictability due to large variability and vice versa (spatial scope of assessments in [5] was North America).

Hawkins and Sutton made fundamental assumptions such as the independence of the abovementioned three sources of uncertainty or that the ensemble of CMIP3 is a collection of independent GCMs. Yip et al. [25] showed that globally the model–scenario interaction effect is an important contribution to uncertainty with long lead time. Masson and Knutti [15] investigated the confidence of climate projections considering their performances over a control period. Study of Pennell and Reichler [20] indicated that due to similarities in GCM error patterns CMIP3 does not represent and underestimates the full range of projection uncertainty. Sanderson et al. [21] concluded the same for the newest available global projections (CMIP5; [23]) and proposed a weighting method for filtering out the co-dependence among the GCMs. Zubler et al. [26] also assessed dependence of CMP5 outputs focusing on the Alpine region and proved that temperature change signal over this territory is largely sensitive to the selection methods (e.g., clustering or averaging results of similar GCMs).

Coupled general circulation models (and earth system models) are the only scientific tool to explore the response of climate system to any assumed external forcing. The development of GCMs is continuous, today they are providing more and more realistic description of features related to climate variability on large scale: they are able to reproduce mean temperature variance on interannual to centennial time scales, the statistics of the global monsoon, the North Atlantic Oscillation, the El Niño-Southern Oscillation, the Quasi-Biennial Oscillation etc. [22]. It is naturally raising the question whether improvement of GCMs is accompanied by a reduction of uncertainty ranges in projections, or at least by change of its decomposition. This chapter makes some effort to partly answer this question. In the present chapter we intend to investigate the following issues:

1. Carpathian Basin is largely influenced by climate change [13] and the Hungarian Meteorological Service provides information about the future changes based on regional climate model (RCM) results for the users. According to multi-model results of the ENSEMBLES project [24], future precipitation change over Europe is substantially different over Northern and Southern Europe. Present study is addressing the question what the key uncertainty factor is in GCM projections (driving the RCMs) for seasonal temperature and precipitation over Northern and Southern Europe. To go further in investigation of this issue, we examine the composition of projection uncertainties over the zone of zero precipitation change with focus on the territory of Carpathian Basin. In the assessment the above-mentioned methodology of [7], hereafter HS, was adapted with some applied modifications.
2. It was shown by outcomes of HS, that continental-scale GCM projections are characterized by less significance than on global scale even considering decadal

change. Is there any limit of spatial and time-scales on which GCM results do not contain valuable information about climate change any more? Two measures were calculated for seasonal temperature and precipitation data: (1) signal-to-noise ratio quantifying the ratio of projected change and total uncertainty (defined as sum of the internal variability, model uncertainty and scenario uncertainty) is a measure whether the information is valuable for users; (2) time of emergence showing the year when projected change exceeds magnitude of the internal variability (i.e., natural and unavoidable part of the uncertainty) is a useful sign when an act is needed since the change is not due to variability. Another important aspect of the second question is in what extent development of global climate models is able to potentially reduce the uncertainty range of projections.

The chapter is structured as follows: Sect. 12.2 gives a detailed overview about the utilized procedure specifying the differences compared to method of HS. Section 12.3 introduces the GCM data involved in the analysis and the spatial scope of the study. Results are presented in Sect. 12.4: different uncertainties are explored first through raw temperature and precipitation time series; their contributions to the total uncertainty are analyzed in quantitative way over Northern and Southern Europe and the Carpathian Basin; a calculation was made in order to test what the theoretical range is to reduce the uncertainties via model development or following rigorously an emission scenario; finally we calculated some measures (signal-to-noise ratio, time of emergence) interesting for decision making. The chapter is closed with a short summary and a brief outlook.

12.2 Methods

The methods following the article of HS to quantify uncertainty of climate model results were implemented with some minor changes at the Hungarian Meteorological Service. Below the methodology used in our study is introduced with indicating the modifications applied on HS.

1. A fourth-order polynomial fit was adjusted to the raw temperature ($X_T(t)$, T index refers to temperature) and precipitation ($X_P(t)$, P index refers to precipitation) data from 1951 to 2100 following Eqs. (12.1) and (12.2):

$$X_T(t) = \Delta T(t) + \bar{T} + \varepsilon(t) \tag{12.1}$$

$$X_P(t) = \left(\frac{\Delta P(t) + 100}{100}\right) * \bar{P} * \left(\frac{\varepsilon(t) + 100}{100}\right), \tag{12.2}$$

where $\bar{T}$ and $\bar{P}$ are the temperature and precipitation polynomial averages for the reference period of 1971–2000, $\Delta T(t)$ and $\Delta P(t)$ denote the departure of polynomial values from this reference with t time (years) and $\varepsilon(t)$ values are the residuals of raw model results from the polynomial fits, representing the

variability component. Note that units in Eq. (12.1) are all degrees Celsius, while in Eq. (12.2) $X_P(t)$ and $\bar{P}$ are in mm, $\Delta P(t)$ and $\varepsilon(t)$ in percentage. Conventionally, percentage change is usually taken when providing precipitation information for the impact studies or end-users, thus we decided to use relative changes.

2. Internal variability $[V(t)]$ is quantified as the variance of the residuals:

$$V(t) = var_{m,s,t}\varepsilon(t) \Big| \; t = \left(\overline{1951 \ldots 1980}\right) \rightarrow \left(\overline{2071 \ldots 2100}\right), \tag{12.3}$$

where m stands for models, s represents scenarios. Contrary to HS, internal variability was not taken constant through the whole analyzed time period, in our study it was re-calculated in every year for the previous 30-year period. This was needed since internal variability is found not to be constant according to the observations over the Carpathian Basin. Applying the same fitting method for the E-OBS data set [10] from 1951 to 2010, it is concluded that seasonal range of internal variability within this period is 0.6–1.7 K for temperature and 19–29 % for precipitation. Fourth-order polynomial fits appeared to be the best choice since it conserves the signal while eliminates the variability. Furthermore, fluctuation in the internal variability also appears in the future model results for the Carpathian Basin (see Fig. 12.4c). It should be noted that internal variability results were smoothed with a moving average applying a 10-year window to get rid of small fluctuations. This smoothing was also applied for the Northern and Southern European results to stay consistent.

3. Model uncertainty $[M(t)]$ and scenario uncertainty $[S(t)]$ were calculated after Eqs. (12.4) and (12.5), respectively, while the sum of Eqs. (12.3), (12.4) and (12.5) provides total uncertainty $[T(t)]$ in Eq. (12.6). Note that in Eqs. (12.4), (12.5) and later in (12.7) for precipitation calculations, $\Delta P(t)$ should be applied instead of $\Delta T(t)$.

$$M(t) = \frac{1}{N_s}\sum_s var_m \, \Delta T(t) \tag{12.4}$$

$$S(t) = var_s \left(\frac{1}{N_m}\sum_m \Delta T(t)\right) \tag{12.5}$$

$$T(t) = V(t) + M(t) + S(t) \tag{12.6}$$

where Ns is the number of scenarios (i.e., 3), N_m is the number of models (i.e., 15 or 14); s and m indices in summa run from 1 to N_s and N_m, respectively; var_m and var_s represent variance across the results of different models for a given scenario and of different scenarios for the multi-model average, respectively. Concerning temporal evolution of the different uncertainty factors, yearly annual and seasonal means were applied instead of the decadal averages used by HS. The uncertainties were calculated without weighting of models, i.e., time series were treated as equally possible realizations for the future. On the one

hand, weighting could be specified based on validation results, however, model performance is not necessarily preserved for the future and HS proved for global results that validation-based model weighting does not have big influence on the uncertainties. On the other hand, weighting could also be done through model dependence with putting less emphasize to the results of models derived from the same model family (e.g., using same physical parameterizations) in order to receive a more robust estimation of model uncertainty related to differences between model formulations [26]. We did not apply this either since same weights are not ensured over different regions. Nevertheless, this chapter has no intention to study this issue.

4. An important score, signal-to-noise ratio [STN(t), Eq. (12.8)] is the rate of the average temperature or precipitation change [G(t), Eq. (12.7)] against the root mean of total uncertainty (noise) per se. We introduce a differently defined measure with a slightly distinctive meaning, the time of emergence [TOE, Eq. (12.9)]. TOE (in actual years) is the first year when the ratio of the average change and only the root mean of the internal variability as the adherent part of the total noise is larger than a selected threshold.

$$G(t) = \frac{1}{N_m N_s} \sum_{m,s} \Delta T(t) \tag{12.7}$$

$$STN(t) = \frac{G(t)}{\sqrt{T(t)}} \tag{12.8}$$

$$TOE = t, \; when \frac{G(t)}{\sqrt{V(t)}} \geq \theta, \tag{12.9}$$

where θ is a certain threshold appropriate for impacts, usually $+1$ or -1.

In HS, the STN was concerned with significance test with a 90 % confidence level. In our study it was neglected since for precipitation over smaller regions very large total noise would occur against the average change of the polynomial fits mainly as result of large internal variability. STN ratio would never be significant for precipitation results, and we dismissed it for temperature results to keep consistency. Concordantly, we neglected significance for TOE as well.

12.3 Data

We used annual and seasonal temperature and precipitation time series of 45 and 42 CMIP3 experiments for 1951–2100 carried out by 15 (for temperature) and 14 (for precipitation) different global models driven by three SRES emission scenarios (A2, A1B and B1) from 2001. The reference period was selected as the last available 30 years before the scenario runs, thus 1971–2000 was used in all runs (which is

Table 12.1 List of selected CMIP3 models, with horizontal resolution of their atmospheric component (degrees) and number of their gridpoints over the Carpathian Basin

Model	Institution	Resolution (X × Y)	Points
BCM2.0[a]	Bjerknes Centre for Climate Research (Norway)	2.8 × 2.8	6
CCSM3	National Center for Atmospheric Research (USA)	1.4 × 1.4	21
CGCM3.1	Centre for Climate Modeling and Analysis (Canada)	3.75 × 3.75	3
CNRM-CM3	Météo France (France)	2.8 × 2.8	6
CSIRO-Mk3.0	CSIRO Marine and Atmospheric Research (Australia)	1.9 × 1.9	15
ECHAM5/MPI-OM	Max-Planck Institute for Meteorology (Germany)	1.9 × 1.9	15
ECHO-G	Meteorological Institute of Bonn University (Germany)	3.75 × 3.75	3
GFDL-CM2.0	Geophysical Fluid Dynamics Laboratory (USA)	2.5 × 2.0	12
GFDL-CM2.1	GFDL (USA)	2.5 × 2.0	12
HadCM3	Hadley Centre for Climate Prediction and Research (UK)	3.75 × 2.5	6
INM-CM3.0	Institute for Numerical Mathematics (Russia)	5.0 × 4.0	2
IPSL-CM4	Institut Pierre Simon Laplace (France)	3.75 × 2.5	6
MIROC3.2 (med)	Center for Climate System Research (Japan)	2.8 × 2.8	6
MRI-CGCM2.3.2	Meteorological Research Institute (Japan)	2.8 × 2.8	6
PCM1	NCAR (USA)	2.8 × 2.8	6

[a]The model results were not available for precipitation

still common in the observational community as well). All results in the chapter are presented after 2000. Note that there was no selection of models, but taking all available information. The horizontal resolution of the atmospheric component in single models varies from 1.4 × 1.4 degrees to 5 × 4 degrees (Table 12.1).

All calculations were done for Northern and Southern Europe and for a domain over the Carpathian Basin, as well (Fig. 12.1). Investigations of HS were repeated also for global scale in order to check the reproducibility: results were quantitatively almost equivalent to HS ones (not shown). Europe was divided into Northern and Southern Europe due to their largely different precipitation change signal (both in direction and magnitude). Based on the ENSEMBLES results [24] where the annual ensemble mean for the end of the twenty-first century shows zero precipitation change zone between 45 and 50°N (seasonally varying between 40 and 55°N), precipitation increase on higher latitudes and decrease on lower latitudes, we decided to separate Northern Europe and Southern Europe at 47°N in our study. Our main area of interest is the Carpathian Basin including our country

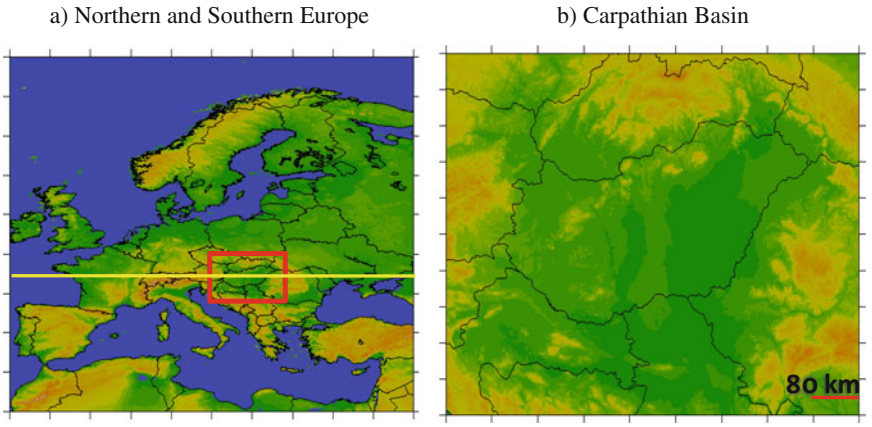

Fig. 12.1 The analysis domains for (**a**) Northern and Southern Europe (separated by the *yellow line*) and (**b**) the Carpathian Basin (also *red rectangle* on panel a)

(Hungary). Its area is over 400,000 km^2 with varying elevation features. Regarding seasonal precipitation changes, this territory is located in the zero change zone of ENSEMBLES results implying the large uncertainty in regional projections. Therefore, we aim at studying this issue in global climate model results.

12.4 Results

12.4.1 Future Temperature and Precipitation Trends

Temperature projections of the investigated global models show a clear increasing annual trend for the twenty-first century for all the analyzed regions including Northern (N) and Southern (S) Europe and the Carpathian Basin (Fig. 12.2). The mean regional warming for 2071–2100 over the Carpathian Basin is almost as big (3.1 K) as one over the halves of the continent (3.1 K over N-Europe and 2.8 K over S-Europe). Results over the Carpathian Basin derived from four locally-run regional climate models driven by SRES A1B and B2 scenarios are showing slightly larger signal than resulted from the global models: the projected change by the end of the century is 3.5 K [13]. European RCM results can only qualitatively be compared with the GCM results, but for S-Europe warming signal projected by ENSEMBLES models is definitely larger than by GCMs.

We cannot easily distinct the regional mean values calculated from different emission scenario-driven experiments unlike in case of global means. The multi-model mean of simulations driven by optimistic (B1) scenario sharply deviates from the other two around the middle of the century, while the results with medium (A1B) and the pessimistic (A2) scenarios evolve together and start to diverge

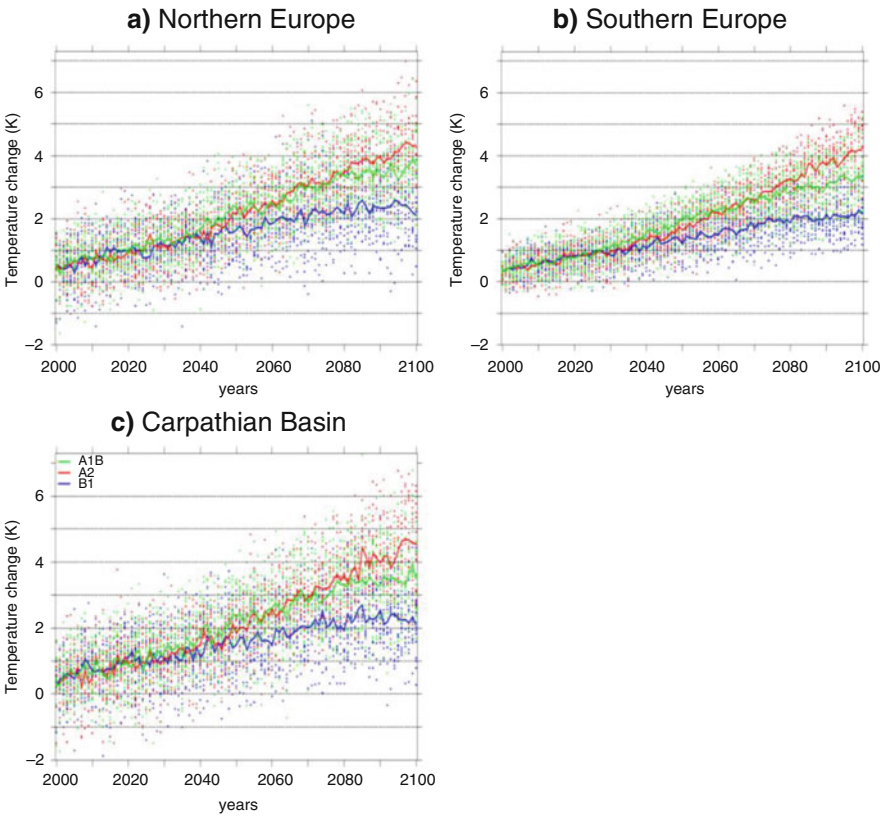

Fig. 12.2 Annual temperature change (in K) between 2001 and 2100 with respect to the reference period of 1971–2000 over 3 regions obtained from results of 45 CMIP3 simulations achieved by 15 GCMs driven with three SRES scenarios. Anthropogenic forcings were taken from SRES A2, A1B and B1 emission scenarios, and the multi-model means for each scenario are represented with *curves*

only around 2070–2080 regardless of the investigated area. Model results spread through the different scenarios even around the end of the century, especially over N-Europe and Carpathian Basin. Cooler temperature values than in the reference period could occur in some years until the middle of the century over S-Europe, but even afterwards over N-Europe and Carpathian Basin. Warming shows similar seasonality over Southern Europe and the Carpathian Basin and the opposite over Northern Europe. Temperature rise is the highest for the first two regions in JJA (June–July–August, 4.1 K), while the lowest in DJF (December–January–February, 2.7 K) and MAM (March–April–May). On the contrary, biggest warming over N-Europe can be seen in DJF and lowest in JJA can be seen in DJF and lowest in JJA, 4.3 and 3 K, respectively (not shown).

Dispersion of raw model results increases with lead time, but N-Europe and Carpathian Basin has already bigger spread than S-Europe. Annual results for

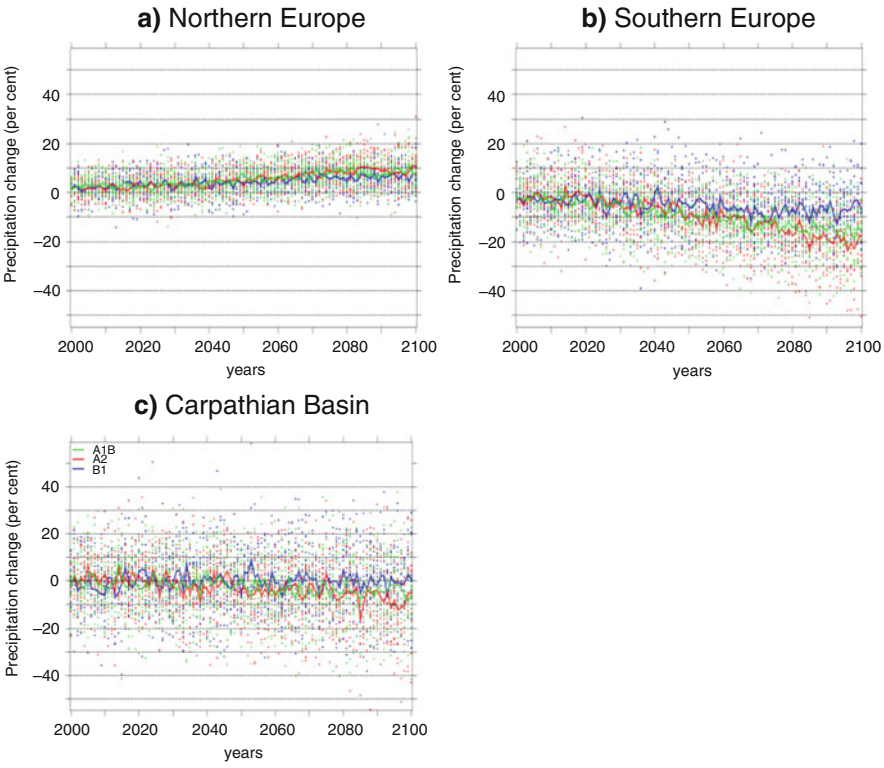

Fig. 12.3 Same as Fig. 12.2 but for precipitation change (in %) using results of 42 CMIP3 simulations

S-Europe have 1–4 K spread from the beginning to the end of the century, while over N-Europe and Carpathian Basin have 3–6 K. This time-dependent increase in uncertainty stems both from the scenario diversity and from the changing (or already larger) natural variability after detrending the data.

Annual precipitation projections (Fig. 12.3) are very much different for Northern and Southern Europe. Precipitation means for N-Europe show a small positive trend for all three scenarios, and the average change reaches 9 % by 2100 with respect to 1971–2000, in agreement with the ENSEMBLES results. Distinction in the three analyzed scenarios never occurs. Annual projections for S-Europe show a significant decrease, on average reaching −14 % by 2100. Scenarios cannot be clearly separated from each other, only to a certain extent in the last decades. Seasonally, DJF precipitation for N-Europe is projected to have the highest increase (10–20 %), while in JJA no change is foreseen. Results for S-Europe are clearly different: means for DJF are slightly below zero and the greatest decrease is expected in JJA with (−40)–(−20) % (not shown).

Results for the Carpathian Basin are somewhat between the two European domain ones, giving relevance for its separate analysis. No apparent up- or

downward trend can be concluded for the Carpathian Basin, but there is a slight negative annual change of −4 % by 2100 thanks to mainly the significant JJA decrease (between −5 and −20 % by 2100). Average change of other seasons by the end of the century is around zero, while in DJF a 5–20 % increase is projected (not shown). This corresponds with the locally-run RCM results [13].

The model spread is different for precipitation results than in case for temperature: basically the models span through the three scenarios (except for S-Europe around the end of the century, when medium and pessimistic scenario outputs project larger reduction). We can clearly see that the magnitude of variability increases with lead time over S-Europe and the Carpathian Basin. Their amounts almost double from 30–40 % to 70–75 % from the beginning to the end of the century, which can stem also from scenario uncertainty over S-Europe. In case of Northern Europe, increase of the spread is much less (from 20 to 30 % from the beginning to the end of the century), even though scenarios stick together.

12.4.2 Internal Variability

Internal variability is an important feature of the climate system and it is evolving over time, according to both observations for the past and climate simulations for the future. Using gridded E-OBS measurements for the Carpathian Basin, seasonal temperature variability before 2000 is overestimated in the GCMs except DJF (not shown). The variance of seasonal temperature values between 2001 and 2100 is around 0.5–0.7 K for Southern Europe (Fig. 12.4b), and it does not vary much with time. For Northern Europe (Fig. 12.4a), the highest values of internal variability also occur in DJF (with double values than for S-Europe) mainly caused by the more intensified large-scale circulation. The lowest values are in JJA which may be due to the fact that large-scale synoptic situations are more stable and affect little the temperature variability in summer, while effect of the local convective activity occurring mostly in summer is described weakly by GCM parameterization. Based on the investigated GCM results, internal variability of future temperature averaged over the Carpathian Basin has similar design with even higher values than over N-Europe (Fig. 12.4c). The measured trend of the temperature variability between 1951 and 2010 was increasing for JJA and SON (September–October–November), while in other seasons no trend was apparent (not shown). According to [1], natural variability of temperature is decreasing with warming mainly for all extratropical latitudes, resulting in a better scenario- and model-dependent predictability in those areas. This is valid for N-Europe and the Carpathian Basin except in JJA: internal variability shows a decrease of −5 to −20 % in MAM, SON and DJF, while JJA values increase with 10–30 % (meaning +0.06 K for N-Europe and +0.33 K for the Carpathian Basin) by the end of the twenty-first century. For S-Europe, only variability is decreasing in DJF to some extent, whereas in other seasons it is not changing for the future.

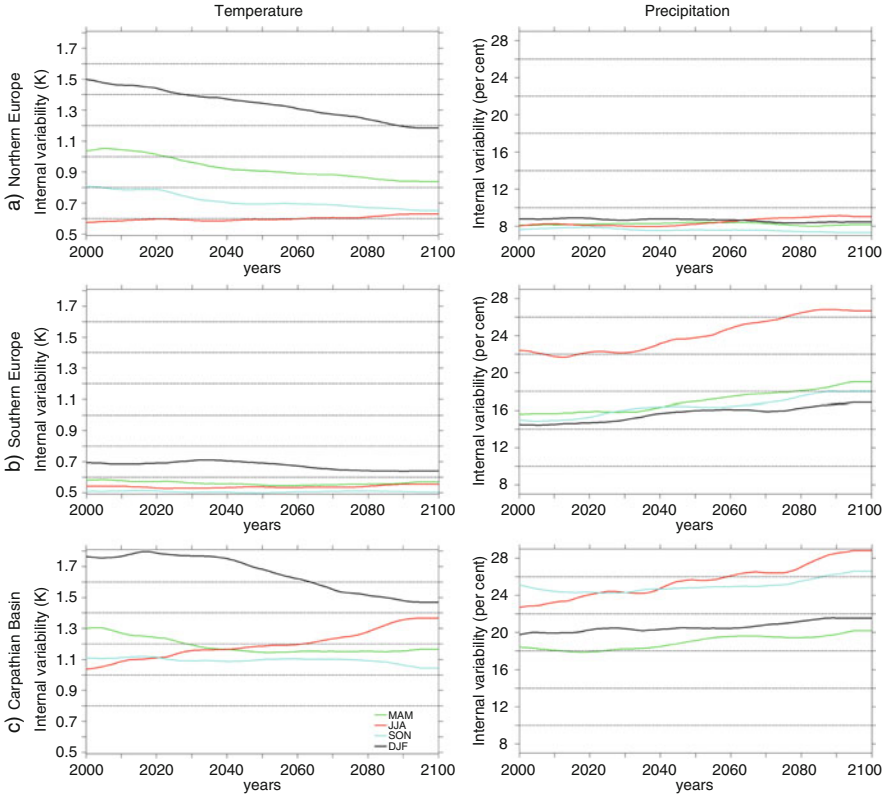

Fig. 12.4 Internal variability of seasonal temperature and precipitation change (in K and %) over 3 regions based on results of the analysed 45 and 42 CMIP3 simulations, respectively. Note that the variances were calculated on a 30-year moving window and the results are smoothed with a 10-year moving average

Taking E-OBS precipitation observations for the Carpathian Basin, internal variability is overestimated in JJA, while in SON and DJF it is underestimated by the GCMs (not shown). Even though variability of global precipitation is almost constant in time, it was proved that regional variability enhances parallel with warming over most extratropical areas [1]. It is the case for S-Europe and the Carpathian Basin, as well: natural seasonal fluctuations are around 14–25 % in 2001 and 5–25 % relative increase is foreseen by 2100, with higher variability in JJA (Fig. 12.4b, c). In contrast, a fully flat interannual precipitation variability is shown for the future over N-Europe: it is just around 8 % regardless of the season, possible due to the more stable circulation patterns throughout the year (Fig. 12.4a). Consequently, there is no trend over N-Europe apart from JJA (relative change 10 %), which results in a slightly more variable precipitation in JJA by 2100 than in DJF.

12.4.3 Fractions of Uncertainty

The fractions of total temperature uncertainty are different over Northern and Southern Europe compared to global temperature outcomes. On the one hand, magnitude of internal variability is naturally higher since a smaller area is assessed and taking annual means instead of decadal ones naturally results in higher variability. As a consequence, the contributions of model and scenario uncertainties are smaller than in global case. Even though seasonal natural variability is significantly higher in absolute terms for N-Europe than for S-Europe, it has almost the same fraction within total uncertainty over the two regions by the end of the century (Fig. 12.5a, d). Scenario uncertainty grows higher for all seasons over Southern Europe than over North. For northern part of Europe it is smaller than model uncertainty in DJF and JJA. Over southern part of Europe, the warmer the season is, the earlier the scenario surpasses the role of model uncertainty (around 2075, Fig. 12.5b, e). Model uncertainty is very significant in JJA for both regions, and it peaks around 2070 for N-Europe and 2050 for S-Europe (in other seasons it has no peak). The latter region shares lower values for model importance for all seasons than N-Europe, which can

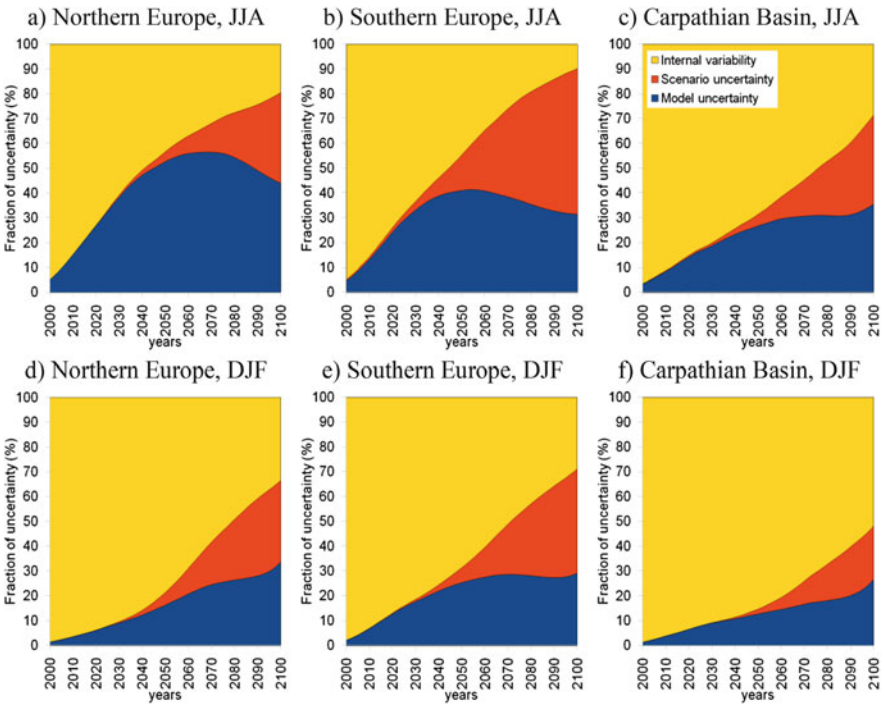

Fig. 12.5 Fractions of total uncertainty (in %) in mean JJA and DJF temperature projections explained by the 3 sources of uncertainty based on results of the analysed 45 CMIP3 simulations over 3 regions

be caused by the larger model sensitivity in the North to more intense circulation changes.

Temperature projections over the Carpathian Basin are more similar to N-European temperature results than to the S-European ones, but have significantly higher natural variability than at larger continental scales. It is the most important source of uncertainty for all seasons and almost all lead times (Fig. 12.5c, f). Scenario uncertainty emerges with a fraction of 10 % between 2060 and 2070, and its ratio does not exceed 35 % even in JJA (when the highest values occur) by 2100. The fraction of model uncertainty is small compared to the results over either part of Europe and has no peak during the twenty-first century, may be due to the lower importance of the scenario uncertainty appearing from 2050s. The proportion of model uncertainty increases slowly and almost continuously with lead time, reaching maximum with 25–35 % fraction by the end of the century.

The main differences between temperature and precipitation projections are that internal variability plays for precipitation a more important role and scenario uncertainty becomes less dominant. This implies that for few decades ahead we can only conclude for decision makers that high natural variability is the main source of uncertainty in global precipitation projections.

Seasonal precipitation results over Southern Europe show much higher fractional values for internal variability than over Northern Europe (Fig. 12.6a, b and Fig. 12.6d, e, JJA and DJF are shown), and it is responsible in both regions for the largest part of the uncertainty for all seasons and for all lead times. Even though fraction of scenario uncertainty is mainly zero or very small for MAM, JJA and SON over N-Europe, it is still a relevant factor (accounting for 15 %) in DJF at the end of the century (Fig. 12.6d). Results show the opposite for S-Europe: scenario choice is not important for DJF (Fig. 12.6e), but in the other seasons this uncertainty has 10 % contribution to the total uncertainty by 2100. Model uncertainty plays significantly bigger role for either parts of Europe: its fraction shows a continuously increasing trend without a peak, and its contribution is the highest (20 and 40 %) in JJA over both European areas, and the lowest (maximum 20 %) for DJF and MAM over N-Europe. Note that there is no remarkable difference between the different seasons regarding the proportion of model uncertainty in S-Europe, while it has in North. In general, using several global models seems more important in Northern Europe than in Southern Europe to portray a better spectrum of the uncertainties.

Over the Carpathian Basin, internal variability is the dominant source of uncertainty for seasonal precipitation projections during the entire twenty-first century with the highest values in JJA (Fig. 12.6c) and SON. Values are similar, but slightly lower than for S-Europe. Scenario uncertainty is literally zero for DJF (Fig. 12.6f), and even with the highest proportion it is only 5 % in JJA at the end of the century. Due to the significantly dominant internal variability, model uncertainty accounts only for 30 % of the total uncertainty in JJA and less in the other seasons, without any peak. Therefore, on continental and regional level, global climate model outputs should be handled and interpreted with care since internal variability is a significant uncertainty factor. Socio-economic scenarios are basically negligible in the precipitation projections, consequently, model improvements are very much

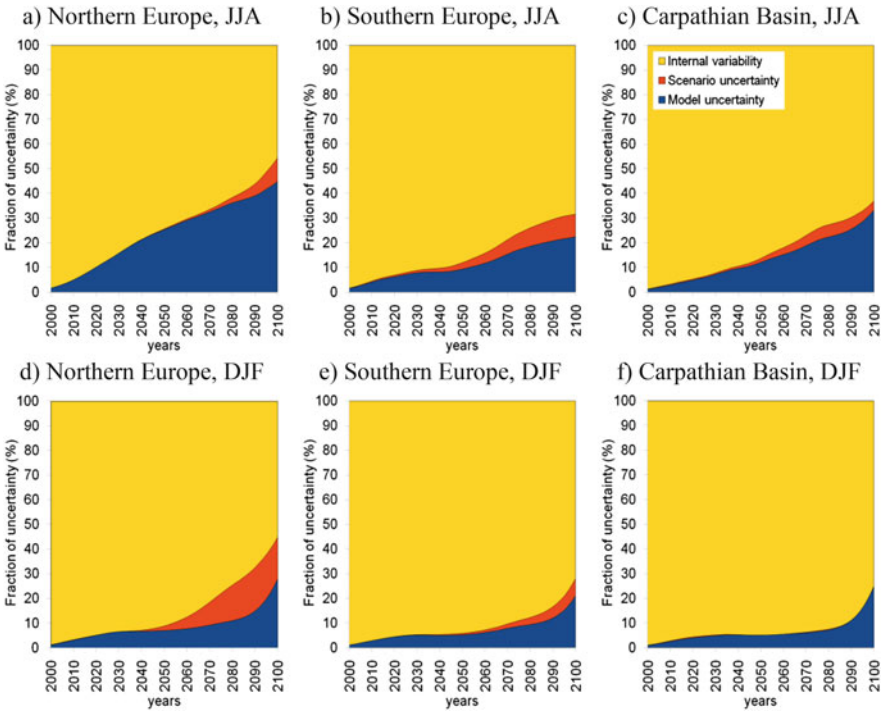

Fig. 12.6 Same as Fig. 12.5 but for precipitation and based on results of the analysed 42 CMIP3 simulations

needed, especially in the field of parameterisations of physical processes related to precipitation formation.

12.4.4 Potentially Reducible Uncertainty

Internal variability cannot be omitted from the climate system, neither its resulted uncertainty from the projection results (apart from initial years of the integration; [7]). In this section we show two short theoretical studies raised by HS, focusing on how the total uncertainty could be reduced to the largest extent:

1. Having a perfect model: we selected one climate model from the 14/15-member ensemble, considered its 3 simulations driven by the 3 scenarios and took their variance. We made this calculation for every model and picked the GCMs with maximum and minimum spread among scenarios. This study gives information on model sensitivity to the anthropogenic forcings.
2. Rigorously following a scenario: we selected one emission scenario, considered 14/15 model simulations driven within the chosen scenario and took their variance. We made this calculation for each scenario and picked the ones with

Table 12.2 Spread difference between maximum and minimum variance using a single model and a single scenario in temperature and precipitation change (in K and %) for 2050 and 2100 over the Carpathian Basin

		Temperature (K)		Precipitation (%)	
		Single model	Single scenario	Single model	Single scenario
MAM	2050	0.4	0.1	5	1
	2100	2.0	0.7	15	7
JJA	2050	0.6	0.1	12	2
	2100	2.5	0.7	18	7
SON	2050	0.5	0.2	5	3
	2100	1.3	0.3	14	7
DJF	2050	0.5	0.1	3	2
	2100	1.7	0.3	10	1

maximum and minimum model spread. This alternative provides information on sensitivity of spread in model ensemble to scenario choice.

The outcomes indicate that model sensitivity to scenarios is more influential in the total uncertainty, than how the model ensemble spreads with a given anthropogenic forcing. For the Carpathian Basin, substantial reduction of total uncertainty in temperature and precipitation projections could be obtained by cautiously selecting (and developing) a single model than following a scenario both for 2050 and 2100, disregard the seasons. Model sensitivity to scenarios in temperature change response in 2100 is the highest for JJA (2.5 K) and lowest in SON (1.3 K), while in precipitation change response in 2100 it is the highest in JJA (18 %) and lowest in DJF (10 %) (Table 12.2). Comparing to the model ensemble spread within a scenario, we have considerably lower values: 0.3–0.7 K for temperature and 1–7 % for precipitation throughout the different seasons. Even though results are shown only for the Carpathian Basin, Northern and Southern Europe share the same direction of outcomes and conclusions.

In the above study we aimed at exploring in what extent model improvement or following a given scenario could *potentially* reduce the uncertainty. Nevertheless, we must note that it is a very theoretical question which practically can be never answered for several reasons. Firstly, we cannot guarantee that model improvement achieved for the past climate will be valid in the changing future climate. Secondly, significant reduction of the model uncertainty in the total uncertainty is feasible with using a prefect model. To approach a perfect model via improvements does not seem realistic within next decades considering the large number of the difficulties in description of the physical processes acting in the climate system. Nevertheless, first part of the above study gives hints about the range of the sensitivity of existing GCMs to different anthropogenic forcings over a region. However, we do not know what magnitude the real sensitivity should be and it could be even out of the range concluded. Consequently, it is still fundamental to use different and several GCMs in climate model ensembles to depict the real model uncertainty.

12.4.5 Signal-to-Noise Ratio and Time of Emergence

The commonly used signal-to-noise ratio [STN, Eq. (12.8)] measures the significance and robustness of climate projections. An important threshold for the STN is when the projected change signal based on the multi-model mean equals the degree of total uncertainty (STN = 1, for temperature and precipitation increase or STN = −1 for precipitation decrease). A climate change signal is considered robust when the signal is at least twice as much as the total uncertainty in the results [18].

For temperature projections over Northern and Southern Europe, STN ratio exceeds the threshold of 1 between 2010 and 2030, and it becomes robust between 2030 and 2070 (Fig. 12.7a, b). STN ratios for S-Europe exceed the thresholds slightly before than for N-Europe, and peaks around 2060–2080. This peak is due to the balance between the continuously growing temperature and the divergence of the projections driven by different scenarios. STN ratios are lower for the Carpathian Basin mainly caused by higher internal variability (Fig. 12.7c). For JJA, when the strongest warming is expected, STN ratio exceeds 1 after 2025. For DJF, this happens 20 years later, mostly due to high internal variability. For this region STN ratio stays below the threshold of 2 (robustness) through the whole century, showing its peak between 2080 and 2100.

Seasonal precipitation results have substantially different characteristics. Besides 1 and 2, −1 and −2 are important thresholds for STN, since precipitation projections show also negative trends. Positive STN ratio stands for Northern Europe (for JJA around zero; Fig. 12.7a) reaching 1 in DJF around 2060 and in MAM around 2080. Southern Europe has only negative STN ratios (Fig. 12.7b) but they are never below −1. For the Carpathian Basin, seasonal STN ratios are positive in DJF and negative in JJA and SON during the entire century (Fig. 12.7c). None of the thresholds is reached in any of the seasons for this small region. All this means, that precipitation projections have lower significance and robustness compared to the temperature projections. Even if we theoretically omitted the internal variability as the largest uncertainty in future precipitation results over the Carpathian Basin (not shown), signal-to-noise containing only scenario and model uncertainty will reach 1 only for DJF season (and not −1 for JJA decrease). This implies that not only the natural variability is responsible for low "trust" in the GCM results over a smaller region.

Time of emergence [TOE, Eq. (12.9)] is slightly different, but yet a useful measure for policy makers and risk assessments, meaning when the warming or precipitation change from the mean of 1971–2000 is higher than internal variability, which cannot be eliminated from the model results [9]. When rate of the change and the internal variability is above 1 (below −1 in case of negative change), it is drawing the attention of decision makers that an act is needed since the so-far measured change is not solely caused by the internal variability. Threshold of 2 (a more radical signal) could be interpreted as an "urgent act" since major impacts are most likely to arise rapidly, depending on the impacts even more thresholds could be specified [14]. Even though there is also a large uncertainty in TOE between different models [12], their average is shown in Table 12.3. The actual years are simply estimated warnings for the expected rate of change from the reference period.

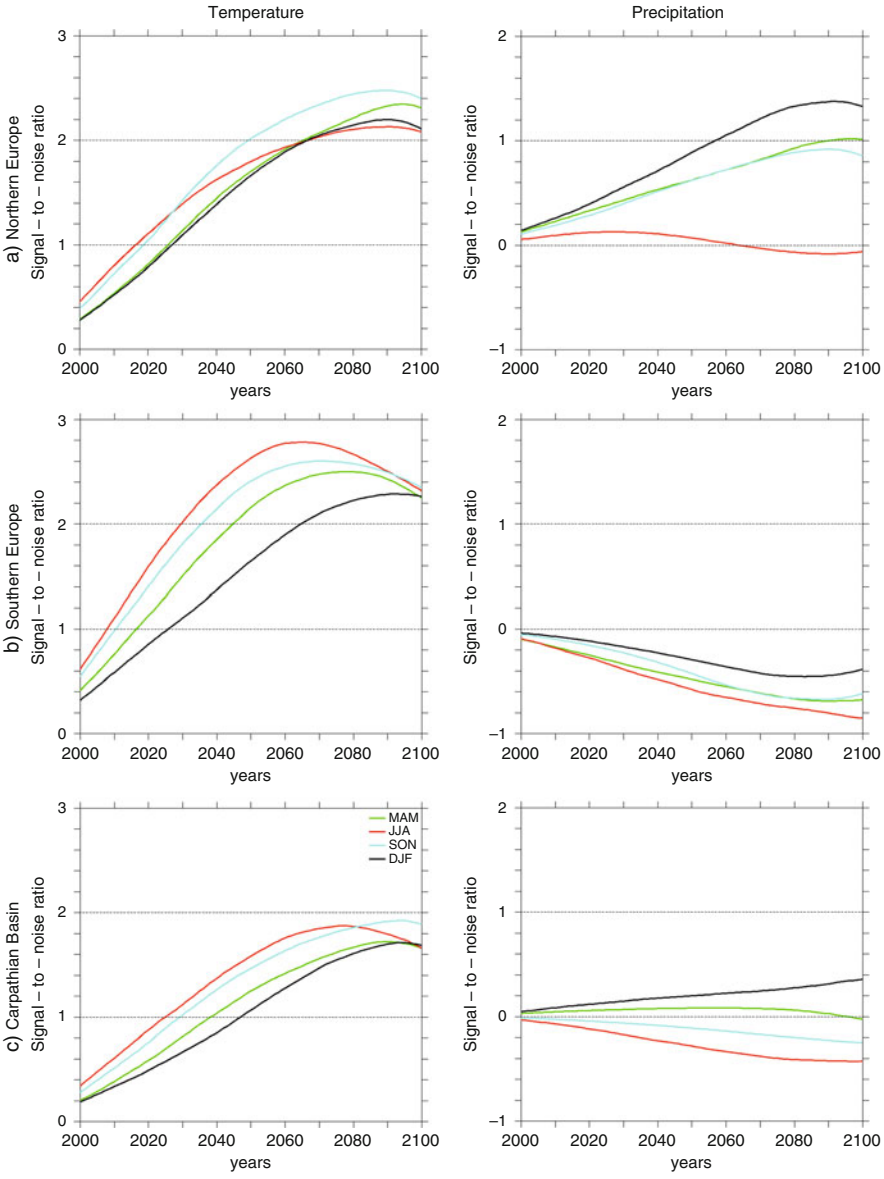

Fig. 12.7 Seasonal signal-to-noise ratio (without unit) taking into account all three sources of uncertainty based on temperature and precipitation results of the analysed 45/42 CMIP3 simulations

Consequently, TOE like other measures in the study is also highly dependent on the choice of the reference period. Note that TOE for global temperature change signal has already happened before the analyzed twenty-first century. Over Northern

Table 12.3 Time (year) of emergence when ratio of mean (temperature and precipitation) change and internal variability is above/below a threshold of 1/−1 or 2

	Northern Europe		Southern Europe		Carpathian Basin	
Temperature	**>1**	**>2**	**>1**	**>2**	**>1**	**>2**
Annual	2012	2029	2003	2017	2015	2038
MAM	2024	2049	2015	2036	2035	2073
JJA	2013	2034	2007	2022	2021	2053
SON	2017	2037	2009	2027	2027	2059
DJF	2026	2053	2023	2050	2044	2082
Precipitation	**>1**	**<−1**	**>1**	**<−1**	**>1**	**<−1**
Annual	2040	No[a]	No	2062	No	No
MAM	2076	No	No	No	No	No
JJA	No	No	No	2095	No	No
SON	2080	No	No	No	No	No
DJF	2054	No	No	No	No	No

[a]The ratio did not reach the threshold until the last analyzed year of 2100

Europe, due to higher internal variability TOE has a bit of delay (around 3–9 years) compared to S-Europe. Naturally, annual means reach the threshold earlier than seasonal ones thanks to its smaller fluctuation: TOE is the earliest for JJA and the latest for DJF seasons. The delay induced by enhanced variability (since change is similar to the European means) is much larger for the Carpathian Basin: TOE in DJF and MAM is around 2040, while in JJA and SON around 2025. It means practically when providing information about regional temperature change in periods earlier than 2021–2050 for local policymakers, scientists should communicate with users that internal variability is a meaningful component. Urgent act is needed for the Carpathian Basin in the second half of the century (after 2050 and 2080).

The time of emergence for the precipitation change signal differs from that of temperature, since precipitation shows high variation both in space and in time. Globally, TOE is reached after the first decade. Over Northern Europe, in MAM, SON and DJF (when positive changes are projected) TOE (≥ 1) happens in the second half of the century, while in JJA (when decrease is foreseen) no TOE (≤ -1) happens until 2100. It is rather the opposite for Southern Europe: we must draw the attention of policymakers only for summer decrease around the end of the century, in the other season projected precipitation increase/decrease does not exceed the internal variability. For the Carpathian Basin, seasonal and annual precipitation change signals do not go beyond internal variability, i.e., there is no TOE until 2100. On the one hand, it means that precipitation results from global models for a smaller area should be considered reservedly since they might be insufficient to provide valuable information above such a small and complex region. On the other hand, the fact that internal variability is higher than the precipitation signal can be detected also in E-OBS (although for a shorter time period, from 1951 to 2010, not shown). This could lead to the conclusion that it is the behaviour of the climate

system itself and the Carpathian Basin belongs to regions of the Earth characterized with low predictability in precipitation.

12.5 Summary

In the recent chapter we quantitatively assessed the uncertainties of temperature and precipitation projections, which are (1) the unavoidable natural climate variability, resulted by feedbacks in the climate system; (2) the scenario uncertainty, emerging from different socio-economic paths; (3) and the model uncertainty, stemming from various climate model formulations. This study is based on the methodology of Hawkins and Sutton [7, 8]. We used all possible global climate model results from the CMIP3 multi-model data set, available for 3 different SRES emission scenarios. Fourth-order polynomials were fitted onto the raw time series then the different kinds of uncertainties were calculated: internal variability as variance of the residuals, model uncertainty as variance of model spread within a scenario and scenario uncertainty as variance of scenario spread for model average. We applied some modifications compared to the reference articles, though. Namely, all models were considered equal without any weighting; internal variability were re-calculated in 30 years instead of taking a constant value throughout the whole 150-year time period; annual and seasonal means were computed instead of decadal averages; no confidence level was applied during the calculation of signal-to-noise ratio. In HS annual and DJF results were mainly published, our analysis was completed with investigation of seasonal time series. Besides signal-to-noise ratio, we estimated time of emergence providing information about necessity of an urgent act as response to the climate change. Applying this coherently modified method, assessments were made for four different geographical areas: for global average for testing the implementation (not shown here), for Northern and Southern Europe to have continental scale results (since their future climate signal is different) and for the Carpathian Basin (Central Europe) to investigate usefulness of GCM results at local scale.

Our key findings are the followings:

1. Internal variability is the most important uncertainty factor in projections for the Carpathian Basin (especially for DJF) irrespective of taking precipitation or temperature results. It is also the dominant source of uncertainty for temperature over Northern and Southern Europe until the middle of the century and for precipitation until 2100.
2. Scenario uncertainty is considerable for temperature results in the second half of the century over both parts of Europe and it is less important in precipitation results, furthermore, it is even less emphasized at local scales.
3. Model uncertainty is relatively large compared to scenario one for precipitation results. On the one hand, it has higher proportion within the total uncertainty for temperature results, on the other hand, it is comparable with scenario uncertainty

proportion around the end of the century (and slightly higher for Northern Europe and the Carpathian Basin than scenario uncertainty by 2100).

4. Selecting a multi-model ensemble driven with the same emission scenario generates larger uncertainty range regarding both precipitation and temperature change than forcing the same GCM with more scenarios (both for continental and at regional scales). Selecting hypothetically the model with the lowest sensitivity to scenarios against the model with highest sensitivity, the range of uncertainty could be narrower by 10–18 % for precipitation and by 1.3–2.5 K for temperature (depending on the seasons) over the Carpathian Basin by 2100. All this could show the potential reducibility of the total uncertainty via model improvement. However, the conclusions can be interpreted just very conditionally assuming that with current developments we will reach a perfect model in the future.
5. Climate model results are often considered valuable after a certain lead time, since the smaller the area, the later the mean temperature change (signal) surpasses total uncertainty (noise). A stricter criteria is when seasonal temperature changes exceed natural variability (i.e., time of emergence). Time of emergence is between 2020 and 2040 for the Carpathian Basin, and 1–2 decades earlier in the European results (earlier over Southern Europe). During the analyzed time period, this significance is never reached in precipitation results over the Carpathian Basin due to high internal variability. Over Northern Europe, adaptation steps and act are needed in seasons with precipitation increase in the second half of the century, while for Southern Europe results demand serious action only in the driest season (JJA) at the end of the century.

It was shown that CMIP3 global model ensemble might be limited in assessing the real extent of the climate change uncertainty even on a global scale since models cannot be treated independently [20]. Thus our next step is to continue the assessment with results of the newest available global projections (CMIP5, [23]) with taking into account both performance and dependency of GCMs [26]. In CMIP5 experiment, a new set of scenarios was developed for describing future anthropogenic activity. RCPs (Representative Concentration Pathways; [17]) have four representative scenarios and in CMIP5 model simulations two of them were applied widely.

The outcomes above are based on global model outputs, confirming that their 100–500 km horizontal resolution and physical parameterizations are not sufficient to result in significant or robust precipitation projections beyond a continental scale of Europe. Nevertheless, the results point out the key uncertainty factors on regional scale. Regional climate models are the sound options for dynamical downscaling of the global climate model response over a target area, though Déqué et al. [2] showed that lateral boundary conditions have key role in performance of regional estimations. Our further step is to investigate the results of RCMs focusing to assess which uncertainties are represented by the ensembles of RCMs available for Europe (e.g., ENSEMBLES and EURO-CORDEX; [11]).

Acknowledgments The authors are grateful to the anonymous reviewer for thorough revision of the chapter. His or her detailed suggestions and good questions inspired us to think even more intensively on the interesting issues of the topic and helped us significantly improve the article.

References

1. Boer, G.J.: Changes in interannual variability and decadal potential predictability under global warming. J. Clim. **22**, 3098–3109 (2009). doi:10.1175/2008JCLI2835.1
2. Déqué, M., Rowell, D.P., Luethi, D., Giorgi, F., Christensen, J.H., Rockel, B., Jacob, D., Kjellstrőm, E., de Castro, M., van den Hurk, B.J.J.M.: An intercomparison of regional climate simulations for Europe: assessing uncertainties in model projections. Clim. Chang. **81**, 53–70 (2007).
3. Deser, C., Phillips, A., Bourdette, V., Teng, H.: Uncertainty in climate change projections: the role of internal variability. Clim. Dyn. **38**(3–4), 527–546 (2012). doi:10.1007/s00382-010-0977-x
4. Deser, C., Knutti, R., Solomon, S., Phillips, A.S.: Communication of the role of natural variability in future North American climate. Nat. Clim. Chang. **2**(11), 775–779 (2012). doi:10.1038/nclimate1562
5. Deser, C., Phillips, A., Alexander, M.A., Smoliak, B.V.: Projecting North American climate over the next 50 years: uncertainty due to internal variability. J. Clim. **27**, 2271–2296 (2014). doi:10.1175/JCLI-D-13-00451.1
6. Dobler, C., Hagemann, S., Wilby, R.L., Stötter, J.: Quantifying different sources of uncertainty in hydrological projections in an Alpine watershed. Hydrol. Earth Syst. Sci. **16**, 4343–4360 (2012). doi:10.5194/hess-16-4343-2012
7. Hawkins, E., Sutton, R.: The potential to narrow uncertainty in regional climate predictions. Bull. Am. Meteorol. Soc. **90**, 1095–1107 (2009). doi:10.1175/2009BAMS2607.1
8. Hawkins, E., Sutton, R.: The potential to narrow uncertainty in projections of regional precipitation change. Clim. Dyn. **37**, 407–418 (2011). doi:10.1007/s00382-010-0810-6
9. Hawkins, E., Sutton, R.: Time of emergence of climate signals. Geophys. Res. Lett. **39**, L01702, 6 (2012). doi:10.1029/2011GL050087
10. Haylock, M.R., Hofstra, N., Klein Tank, A.M.G., Klok, E.J., Jones, P.D., New, M.: A European daily high-resolution gridded dataset of surface temperature and precipitation. J. Geophys. Res. (Atmos.) **113**, D20119 (2008). doi:10.1029/2008JD010201
11. Jacob, D., Petersen, J., Eggert, B., Alias, A., Christensen, O. B., Bouwer, L. M., Braun, A., Colette, A., Déqué, M., Georgievski, G., Georgopoulou, E., Gobiet, A., Nikulin, G., Haensler, A., Hempelmann, N., Jones, C., Keuler, K., Kovats, S., Kröner, N., Kotlarski, S., Kriegsmann, A., Martin, E., van Meijgaard, E., Moseley, C., Pfeifer, S., Preuschmann, S., Radtke, K., Rechid, D., Rounsevell, M., Samuelsson, P., Somot, S., Soussana, J. F., Teichmann, C., Valentini, R., Vautard, R., Weber, B.: EURO-CORDEX: new high-resolution climate change projections for European impact research. Reg. Environ. Chang. **14**, 563–578 (2014). doi:10.1007/s10113-013-0499-2
12. Knutti, R., Furrer, R., Tebaldi, C., Cermak, J., Meehl, G.A.: Challenges in combining projections from multiple climate models. J. Clim. **23**, 2739–2758 (2010). doi:10.1175/2009JCLI3361.1
13. Krüzselyi, I., Bartholy, J., Horányi, A., Pieczka, I., Pongrácz, R., Szabó, P., Szépszó, G., Torma, C.S.: The future climate characteristics of the Carpathian Basin based on a regional climate model mini-ensemble. Adv. Sci. Res. **6**, 69–73 (2011). doi:10.5194/asr-6-69-2011
14. Mahlstein, I., Knutti, R., Solomon, S., Portmann, R.: Early onset of significant local warming in low latitude countries. Environ. Res. Lett. **6**, 034009 (2011). doi:10.1088/1748-9326/6/3/034009

15. Masson, D., Knutti, R.: Spatial scale dependence of climate model performance in the CMIP3 ensemble. J. Clim. **24**, 2680–2692 (2011). doi:10.1175/2011JCLI3513.1
16. Meehl, G.A., Covey, C., Delworth, T., Latif, M., McAvaney, B., Mitchell, J.F.B., Stouffer, R.J., Taylor, K.E.: The WCRP CMIP3 multi-model dataset: a new era in climate change research. Bull. Am. Meteorol. Soc. **88**, 1383–1394 (2007). doi:10.1175/BAMS-88-9-1383
17. Moss, R.H., Edmonds, J.A., Hibbard, K.A., Manning, M.R., Rose, S.K., van Vuuren, D.P., Carter, T.R., Emori, S., Kainuma, M., Kram, T.: The next generation of scenarios for climate change research and assessment. Nature **463**, 747–756 (2010). doi:10.1038/nature08823
18. Murphy, J.M., Sexton, D.M.H., Barnett, D.N., Jones, G.S., Webb, M.J., Collins, M., Stainforth, D.A.: Quantification of modelling uncertainties in a large ensemble of climate change simulations. Nature **429**, 768–772 (2004). doi:10.1038/nature02771
19. Nakicenovic, N., Alcamo, J., Davis, G., de Vries, B., Fenhann, J., Gaffin, S., Gregory, K., Grübler, A., Jung, T.Y., Kram, T., La Rovere, E.L., Michaelis, L., Mori, S., Morita, T., Pepper, W., Pitcher, H., Price, L., Raihi, K., Roehrl, A., Rogner, H.H., Sankovski, A., Schlesinger, M., Shukla, P., Smith, S., Swart, R., van Rooijen, S., Victor, N., Dadi, Z.: IPCC special report on emissions scenarios. Cambridge University Press, Cambridge (2000)
20. Pennell, C., Reichler, T.: On the effective number of climate models. J. Clim. **24**, 2358–2367 (2011). doi:10.1175/2010JCLI3814.1
21. Sanderson, B.M., Knutti, R., Caldwell, P.: A representative democracy to reduce interdependency in a multimodel ensemble. J. Clim. **28**, 5171–5194 (2015). doi:10.1175/JCLI-D-14-00362.1
22. Stocker, T.F., Qin, D., Plattner, G.-K., Tignor, M., Allen, S.K., Boschung, J., Nauels, A., Xia, Y., Bex, V., Midgley, P.M. (eds.): IPCC AR5 WGI: Climate Change 2013: The Physical Science Basis. Contribution of Working Group I to the Fifth Assessment Report of the Intergovernmental Panel on Climate Change. Cambridge University Press, Cambridge, United Kingdom and New York, NY, USA, 1535 pp. (2013). doi:10.1017/CBO9781107415324
23. Taylor, K.E., Stouffer, R.J., Meehl, G.A.: An overview of CMIP5 and the experiment design. Bull. Am. Meteorol. Soc. **93**, 485–498 (2012). doi:10.1175/BAMS-D-11-00094.1
24. van der Linden, P., Mitchell, J. (eds.): ENSEMBLES: climate change and its impacts: summary of research and results from the ENSEMBLES Project. Met Office Hadley Centre, Exeter, p. 160 (2009)
25. Yip, S., Ferro, C., Stephenson, D., Hawkins, E.: A simple, coherent framework for partitioning uncertainty in climate predictions. J. Clim. **24**, 4634–4643 (2011). doi:10.1175/2011JCLI4085.1
26. Zubler, E.M., Fischer, A.M., Fröb, F., Liniger, M.A.: Climate change signals of CMIP5 general circulation models over the Alps—impact of model selection. Int. J. Climatol. (2015). doi:10.1002/joc.4538

Index

A. Bátkai et al. (eds.), *Mathematical Problems in Meteorological Modelling*,
Mathematics in Industry 24, DOI 10.1007/978-3-319-40157-7